CASE FILE
COPY,

SIGNIFICANT
ACCOMPLISHMENTS
IN SCIENCES

Goddard Space Flight Center, 1972

A symposium held at

GODDARD SPACE FLIGHT CENTER

November 7-8, 1972

NATIONAL AERONAUTICS AND SPACE ADMINISTRATION

SIGNIFICANT ACCOMPLISHMENTS IN SCIENCES

Goddard Space Flight Center, 1972

The proceedings of a symposium held at the NASA
Goddard Space Flight Center, November 7-8, 1972

Prepared by Goddard Space Flight Center

FOREWORD

This is an almost-verbatim transcript of a symposium held at Goddard Space Flight Center (GSFC) on November 7 and 8, 1972. No attempt has been made to introduce editorial or stylistic uniformity; on the contrary, an effort has been made to retain the informality of the proceedings. The text of the papers is substantially as given; but in some instances where a more detailed paper has been prepared for publication, this paper has been substituted for the transcript.

A major change results from NASA policy, which now requires in all formal publications the use of international metric units according to the Systeme International d'Unites (SI). However, in certain cases, utility requires the retention of other systems of units in addition to the SI units. The conventional units stated in parentheses following the computed SI equivalents are the basis of the measurements and calculations reported here.

CONTENTS

CONTENTS (Continued)

CONTENTS (Continued)

CONTENTS (Continued)

CONTENTS (Continued)

INTRODUCTION

This document presents the papers on scientific achievements at Goddard Space Flight Center delivered at the annual Science and Technology Review on November 7 and 8, 1972. The overall objective of the symposium was the presentation summarizing the major advances at Goddard Space Flight Center during the past year.

The presentations for this review were selected from a considerably larger number of proposed presentations. Unfortunately, time did not permit including the many other advancements of which Goddard Space Flight Center is equally proud.

The papers were presented in five groups: High Energy and Solar Astronomy, with an overview by Frank B. McDonald; Optical and UV Astronomy, with an overview by Anne B. Underhill; Planetary, Lunar, and Cometary Studies, with an overview by Norman F. Ness; Earth Observations, with an overview by William Nordberg and presented by William R. Bandeen; and Earth Physics, with an overview by Friedrich O. von Bun.

The audience consisted of scientists and engineers who had interest in and responsibility for the direction of space applications research and development. In addition to the many Goddard Space Flight Center scientists and engineers, members of the audience came from NASA Headquarters, other NASA Centers, and other Government agencies.

OPENING REMARKS

John F. Clark
Director, Goddard Space Flight Center

Welcome to Goddard's annual Science and Technology Presentation. This title is hardly a complete description, because of the nine sessions; three are science oriented, two concern technology, one involves ground operations, and finally, we will have three sessions in applications disciplines. So, one might, in order of the number of sessions, more appropriately call this "science, applications, technology, and ground operations."

These talks are winnowed out from a considerably larger number of proposed talks; the only rule is not more than five minutes and not more than three slides. When we started this, five years ago, a lot of people said it was not possible to present anything of much value in five minutes. But experience has taught us otherwise, and each year these sessions have been more effective.

I would like to note that tomorrow's session will be under the chairmanship of Mr. Robert Bourdeau, Director of Space Applications and Technology, and now let me introduce today's chairman, Dr. George Pieper, Director of Space and Earth Sciences.

REMARKS

George F. Pieper
Director of Space and Earth Sciences

In past years, we have adhered very closely to a rule which is a rough equivalent to the rule for writing a sonnet — five minutes, three slides. You will find that this year there are some variations on the theme; this is by direction, not by a random occurrence. In particular the overview talks and one or two others have not been held to our usually strict rule.

The first session this morning deals with the subjects of high energy and solar astronomy. The director of our Laboratory for High Energy Astrophysics will present an overview of this area to introduce the subject to us.

SECTION I

HIGH ENERGY AND SOLAR ASTRONOMY

As we go to cosmic rays, the crucial problems become, "What is the interstellar energy density of galactic cosmic rays? What is the charge spectrum?" And the most important question is, "What is happening in the charge spectrum as we go to very high energies?" I think one of the things we're seeing from Pioneer-10 is that the size of the modulation region is far greater than what we've previously believed. The Pioneer-10 data indicate that we are going to need the type of extended sweeps available, for instance, from a Mariner Jupiter-Saturn mission that goes out even farther than Pioneer-10.

Another interesting development is that one can look at these same processes essentially in a microcosm when one looks at large solar flares such as the giant flares of August 1972. One sees there the X-ray burst, probably coinciding with the initial particle acceleration. One sees nuclear gamma rays as the particles collide with the ambient plasma. And finally one sees one AU, the great flux of particles coming from the event. It appears that solar flares offer us one of the best ways of studying high energy astrophysics, and of understanding the nature of at least one mechanism of how particles get accelerated.

I would also like to point out one feature of our program this morning. Three of the presentations, those by David Thompson, Axel Briskin, and Robert Silverberg, are based on doctoral theses which these men have undertaken. They have been using the facilities here at Goddard. We've found that this has been useful for them, but more useful for us. The interaction with students, we feel, is what a laboratory like ours needs, and so we decided that it would be worthwhile this morning to let you see that part of Goddard, too.

8

POSITRON ANNIHILATION RADIATION FROM NEUTRON STARS

Gerhard A. Borner

The work I'm going to report on was done jointly with R. Ramaty and Jeffrey Cohen. It is concerned with an interpretation of balloon observations done by R. Haynes and co-workers at Rice University. They observed a low-energy gamma-ray line from the galactic center region, which was centered around 470 keV. The flux in the line was about 2×10^{-3} photons $cm^{-2}\,s^{-1}$.

We interpret that observation as the positron annihilation radiation line, which occurs at 511 keV, but we suggest that it occurs on the surface of old neutron stars, and is thus red-shifted by the gravitational field of the stars.

The surface of these old neutron stars will consist mainly of iron, but then they will accrete interstellar material, possibly at a rate of about 10^{11} grams per second, and the particles from interstellar matter hitting the surface of the star will induce spallation reactions and produce quite a different surface composition.

From Table 1, column 3 (or Figure 1) you can see the energies that are gained just from the gravitational field of the neutron stars. If you have protons falling down onto a neu-

Table 1
Surface Redshifts, Incident Proton Energies, and Gamma-Ray
Yields as Functions of Neutron Star Mass

$M/M_\odot$	Z	E_p (MeV)	Q^+	$Q^{(4.43)}$	$Q^{(6.14)}$
0.37	0.053	39	0.0062	0.003	0.002
0.55	0.085	57	0.015	0.005	0.003
0.77	0.13	77	0.028	0.006	0.004
1.00	0.18	103	0.048	0.007	0.005
1.24	0.24	130	0.070	0.008	0.006
1.44	0.31	160	0.095	0.009	0.007
1.56	0.38	184	0.12	0.01	0.008
1.68	0.45	208	0.14	0.011	0.008
1.72	0.51	230	0.18	0.012	0.009

Per proton of given energy, Q^+, $Q^{(4.43)}$, and $Q^{(6.14)}$ are the yields for positron annihilation radiation, 4.43 MeV carbon line, and 6.14 MeV oxygen line, respectively.

tron star, then the energy that the proton gains is determined by the mass of the star, and you see that the energies can go up as high as 200 meV per proton for neutron stars of about 1.6 solar masses.
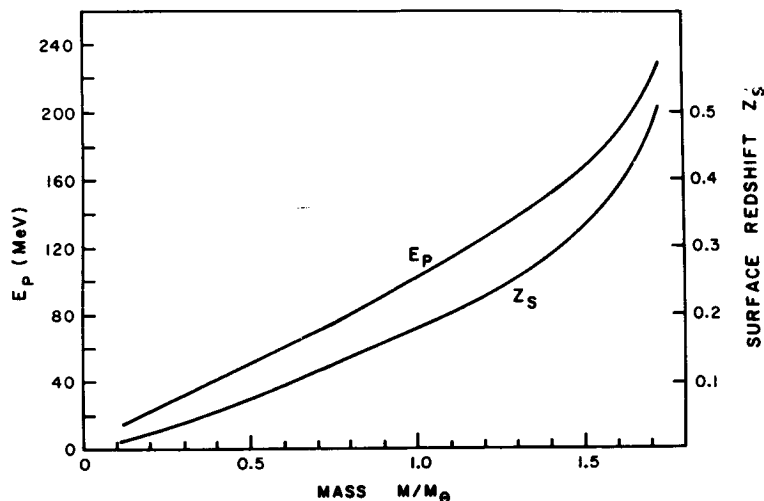
Figure 1. Accreted proton energy and surface redshift
as function of neutron star mass.

Furthermore, the mass of a star determines the redshift of any radiation escaping from the surface (column 2 in Table 1). The observation gives us a redshift of about 0.1. You see that this corresponds to a neutron star mass of around 0.6 solar masses. The energy that the protons gain would be in the vicinity of 60 MeV.

Now for neutron stars of that mass and incident particle energies of that order, we made a rough model of what the yield of positrons would be per incident proton. If one assumes a surface composition consisting mainly of elements heavier than carbon, we find that we get 0.02 positrons per incident proton (the Q^+ column in Table 1), and then you get about 10^{33} photons per second from one neutron star.

To explain the observed flux, one needs many neutron stars in the galactic center; one needs about 0.2 neutron stars per 3×10^{49} cubic meters (0.2 neutron stars per cubic parsec), if one assumes that the disk thickness is about 1.5×10^{19} meters (500 parsecs).

Near the sun, one estimates that there are about 0.03 neutron stars per cubic parsec, and so in our model, one needs an increase of the neutron star density towards the galactic center region. The fact that a line has been observed has the interesting consequence that the spread in mass of the neutron stars in the galactic center region is small; most of them are centered around 0.6 $m_\odot$.

Good tests of that model would be the observation of other lines of which two are enumerated in the last two columns of Table 1. But to precisely determine what flux to expect for these lines, one would have to know the precise surface composition, and we are just working on that problem now. The flux would probably be on the order of 10^{-4} photons $cm^{-2}s^{-1}$. Thus the very interesting possibility of a gamma spectroscopy of these distant neutron stars emerges.

A second test would be the observation of a redshifted line from the galactic disk, with a flux of the order of 10^{-4} photons $cm^{-2}s^{-1}$. From the galactic disk, one should also see a nonredshifted positron annihilation line with a similar flux which would come from the annihilation of positrons in the galactic cosmic rays. So one has to wait for future measurements to see if this idea really stands up to the expectations we have.

X-RAY OBSERVATIONS OF THE SUPERNOVA REMNANTS CAS A AND TYCHO

Axel Brisken

One of the best understood X-ray sources, the Crab Nebula, is a supernova remnant about 1000 years old. The pulsar in the Crab is believed to be the energy source for the nebular X-ray emission. Using the Crab as a model, two younger supernova remnants, Cas A and Tycho, may also have a pulsar or rotating neutron star responsible for their X-ray emission. The present observation of Cas A and Tycho is the most sensitive undertaken in the 1.5 to 10 keV X-ray band, utilizing a rocket-borne multilayer multianode proportional counter experiment launched from White Sands, New Mexico, on May 19, 1972.

Since both Cas A and Tycho are younger than the Crab, one might expect pulsars with higher frequencies. The data, however, show no evidence for periodic emission from either Cas A or Tycho in the period range of 1 millisecond to 13 seconds. Figure 1 shows 99-percent-confidence upper limits to the pulsed fraction as determined by two independent algorithms, direct fast-folding and Cooley-Tukey harmonic analysis. Here we define the pulse fraction, f, as the ratio of events in the pulsed component to those in the temporarily stable component. The pulse duty cycle, β, is the fractional width of the pulsed component over one period. Note that the harmonic analysis (represented by the solid lines) is not dependent on β, while the fast-fold analysis (represented by the dashed line) is, and provides significantly lower limits for sharper pulses. These upper limits are more stringent than the results of Gorenstein, and also cover a larger temporal range. In a previous rocket flight by the Goddard X-ray group, the Crab was observed with a pulsed fraction of 18 percent and a duty cycle of approximately 40 percent.

The fact that no periodicities were observed does not exclude a pulsar model for Cas A or Tycho. Even though they are younger than the Crab, they could have a slower pulsar, which would most probably have a 1 percent or less pulsed fraction. Also, the earth could be out of the pulsar beam.

Figure 2 shows the inferred incident photon spectra, dN/dE, for Cas A and Tycho, as a function of energy, E. It is immediately apparent that the spectra are complex and cannot be represented by a simple model. Attempts to fit the data with a single power law or thermal bremsstrahlung model resulted in failure. This is in contrast to the Crab, which can be represented by a one-component power law model. Taking just the 2 to 5 keV data, however, both Cas A and Tycho can be fit very well with a power law as shown. In addition, Tycho can also be fit with a thermal bremsstrahlung model at 4.6×10^6 K. The rounding of the data at 2 keV and below represents absorption in the sources and galaxy. The significant structure around 7 keV does not appear to be an artifact of the detector,
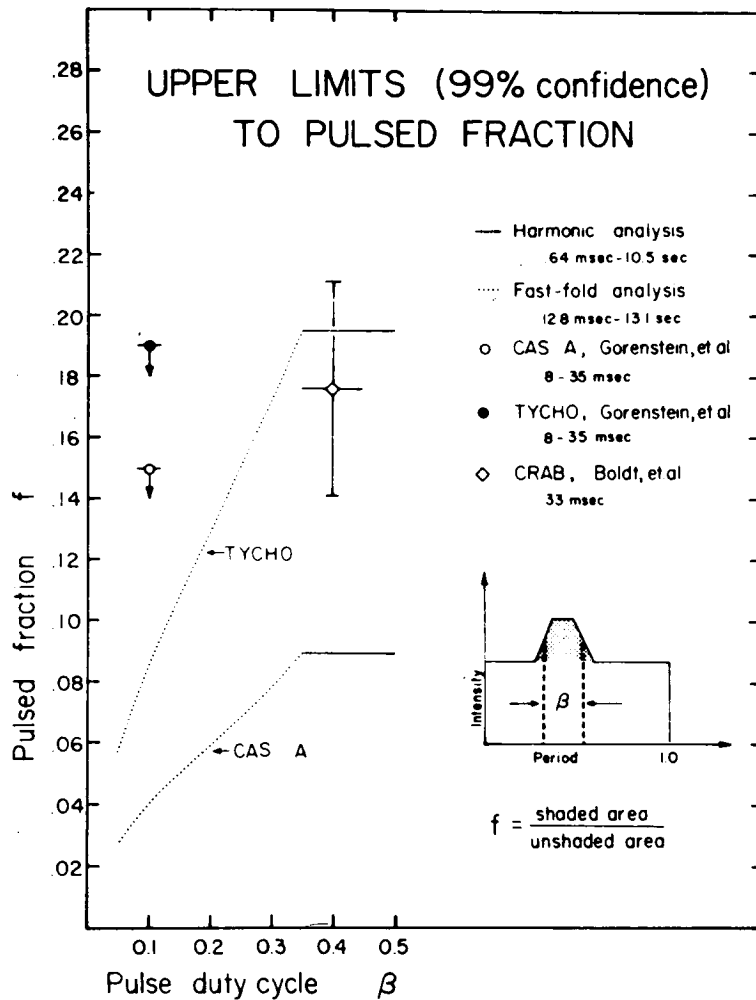
Figure 1. Upper confidence limits (99 percent) to the pulsed fraction, f, for Cas A and Tycho as determined by direct fast-folding and Cooley-Tukey harmonic analysis.

as such an effect did not appear in calibrations or previous experiments. It does require that another component be added to the spectral model.

The steep slopes observed take on increased interest when compared with radio observations. Figure 3 shows the electromagnetic flux intensity as a function of frequency. The best radio data for the Crab, Cas A, and Tycho are plotted on the left, with extrapolations represented by the shaded areas. On the right, the best X-ray results for the Crab, plus the new results for Cas A and Tycho are plotted. The usually accepted model for the Crab, Cas A, and Tycho is a synchrotron source – continuous injection model which could have a break in the spectrum, but only by one-half power, as is approximately the

case for the Crab. The spectral breaks observed here are 2.3 for Cas A and 5.7 for Tycho. If the injection of electrons ceased at some time in the past, one could still observe a synchrotron source type power law with such steep spectra. However, these steep slopes should be connected to the extrapolated radio observations by smooth rounded curves covering several decades of intensity and energy, and most certainly should not be close to or exceed the extrapolated radio data. In addition, ages of these supernovae and best estimates of their magnetic fields suggest that the spectral breaks should occur at about 100 eV.

Consequently, on the basis of these data, simple synchrotron or isothermal models for both Cas A and Tycho are ruled out. There appears to be no way of simply connecting the radio and X-ray emission from these remnants, as one could for the Crab. There must still be a contemporary source of energy in the source region, or else the steep spectra would be inconsistent with their intensity. In the case of the Crab, the pulsar led to the identification of the energy source, while with these data the additional structure in the spectra may provide the clue.
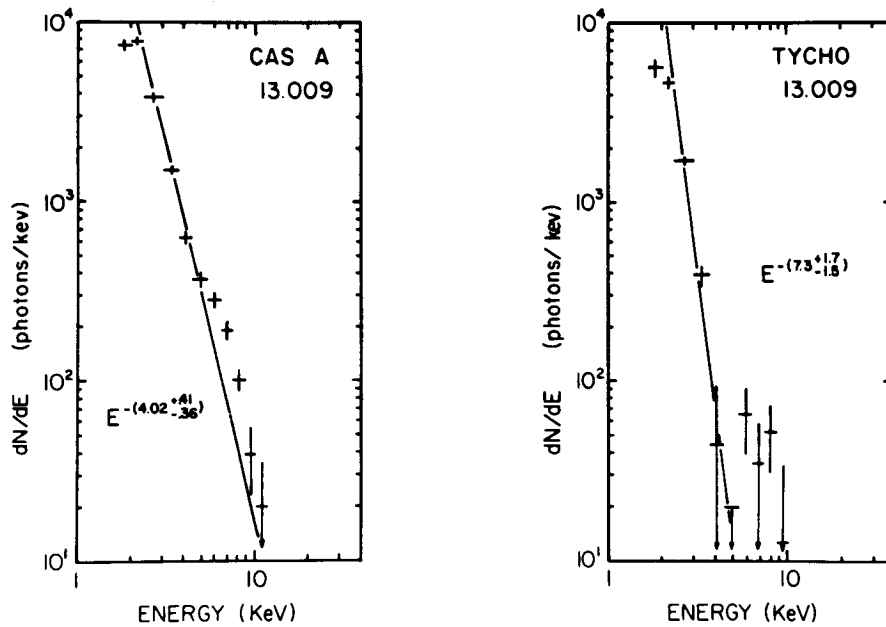
Figure 2. Inferred incident photon spectra, dN/dE, for Cas A and Tycho, as a function of energy, E.
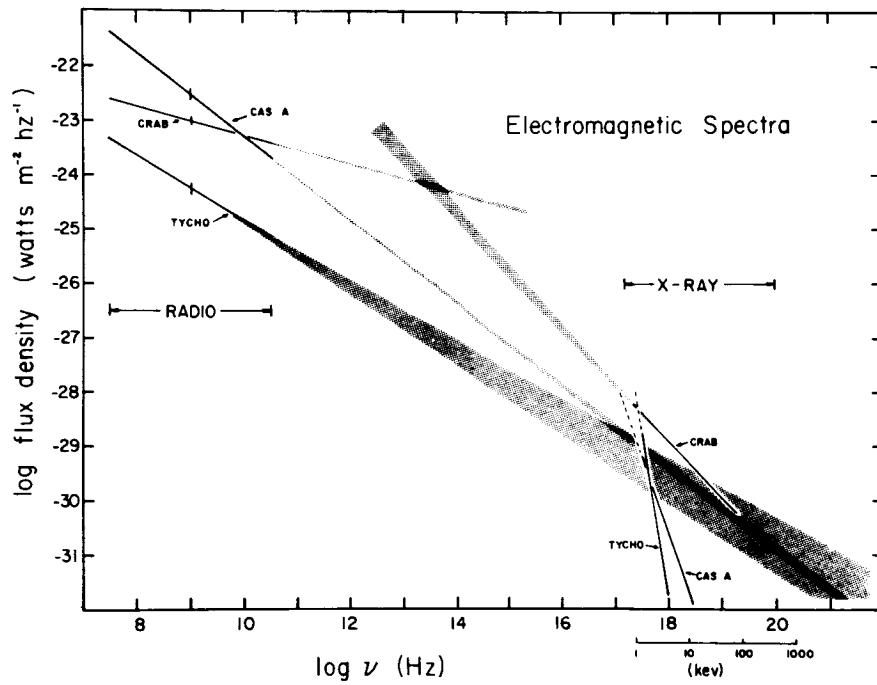
Figure 3. Electromagnetic flux intensity as a function of frequency
for the Crab, Cas A, and Tycho.

ATMOSPHERIC SECONDARY GAMMA RADIATION

David J. Thompson

The field of gamma ray astronomy has been recognized for many years as a research area of great potential, but the development of experimental gamma ray astronomy has been very slow. In fact, virtually the only points of general agreement among gamma ray astronomers today are first, that cosmic gamma rays do exist, and second, that cosmic gamma rays are very scarce.

The rarity of gamma rays outside the earth's atmosphere is the principal reason for the slow development of astronomy in the high energy range. Nearly all cosmic gamma ray detection experiments have been flown on high-altitude research balloons; and except at the highest altitudes which can be reached, the flux of atmospheric secondary gamma rays is considerably larger than the flux of incoming cosmic gamma rays.

Figure 1 is a schematic representation of how atmospheric secondary gamma rays are produced. An incoming cosmic ray such as a proton interacts in the upper atmosphere, producing a shower of secondary particles. These in turn either interact or decay. Notice the wavy lines on the left side of the diagram; these lines denote gamma rays, which come from decay of the neutral pi meson, or bremsstrahlung by an electron or positron.

This is the basic origin of the atmospheric secondary gamma radiation. Now, one way to deal with the problem of atmospheric background gamma rays is to go to satellite detectors such as the SAS-B experiment, which will be launched, we hope, in the next couple of weeks.

In addition to this approach, our research group has been working for some time on trying to gain a better understanding of the origin of gamma rays in the atmosphere. We've attacked this problem from two directions.

On the one hand, we've used one of our balloon-borne detectors to study the atmospheric radiation as a function of altitude, energy, and zenith angle. On the other hand we have developed a theoretical model which is in the form of a three-dimensional Monte Carlo calculation that starts with known cosmic ray flux at the top of the atmosphere and follows particles as they interact within the atmosphere. This model enables us to predict the atmospheric secondary gamma radiation again as a function of altitude, energy, and zenith angle.

Our experimental work is nearly complete, but we're having some problems with the Monte Carlo calculation. The theoretical results I have here today are only preliminary, and time permits only a sample of our experimental results.

16

The detector we used is a 15-centimeter-square digitized wire-grid spark chamber. This was the original prototype of the SAS-B experiment. The spark chamber is sensitive to gamma rays of energies above about 30 Mev, and measures both the energy and arrival direction for each gamma ray.

Figure 1. Cosmic-ray interactions in the atmosphere.

Figure 2 shows the total flux of downward-moving gamma rays with energy greater than 30 Mev as a function of depth in the atmosphere — the top of the atmosphere is to the left of the figure. The bars represent experimental data, while the triangles are the points predicted by the theory.
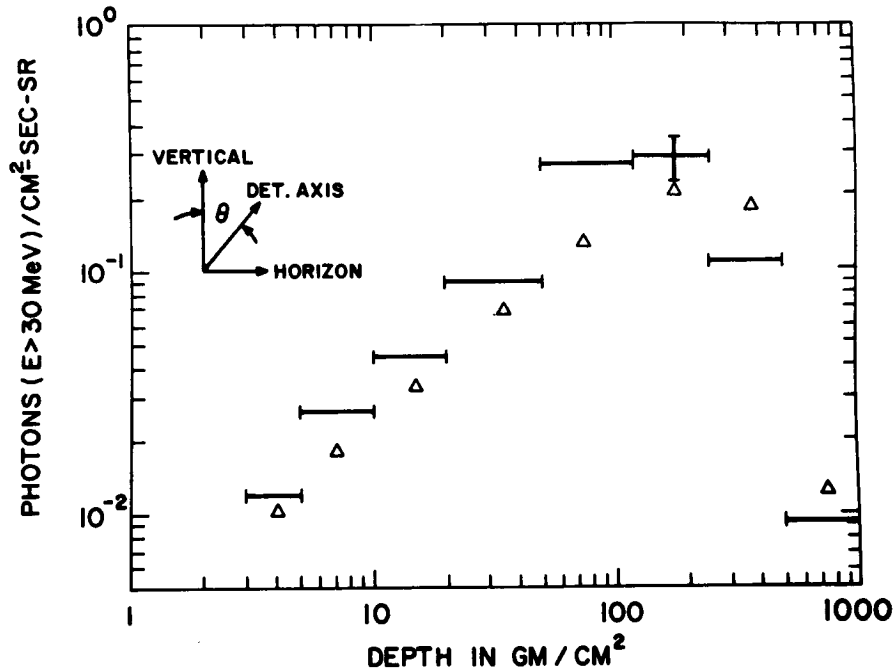
Figure 2. Photon flux versus depth in atmosphere ($\theta = 16°$).

As you can see, the theoretical maximum falls deeper in the atmosphere than we have found experimentally, but the results are still in fairly good agreement. As a point of comparison in showing the importance of these atmospheric results, the OSO—3 measurement of the cosmic gamma ray flux lies nearly two orders of magnitude below the lowest point on this graph.

Figure 3 shows the gamma ray energy spectrum at one of the points in the atmosphere. This is downward-moving gamma rays at a depth of 35 grams per square centimeter. The X's are experimental values, while the dots are the results of the Monte Carlo calculation.

Except for the absolute flux, you can see that the theory predicts the energy spectrum quite well. We have every reason to expect that the problems in the theory will be straightened out in the very near future. When they are, we will be able to go back and apply the results to the background problem for balloon gamma ray astronomy results.

18

Also, since this is a three-dimensional calculation, we will know the upward-moving, as well as the downward-moving, gamma ray flux. This gives us the only practical in-flight calibration source for satellite gamma ray detectors — that is, the secondary gamma rays escaping upward from the earth's atmosphere.

In summary, the results of this work have given us a better understanding of the atmospheric secondary gamma radiation, and should be a valuable asset in future gamma ray astronomy.
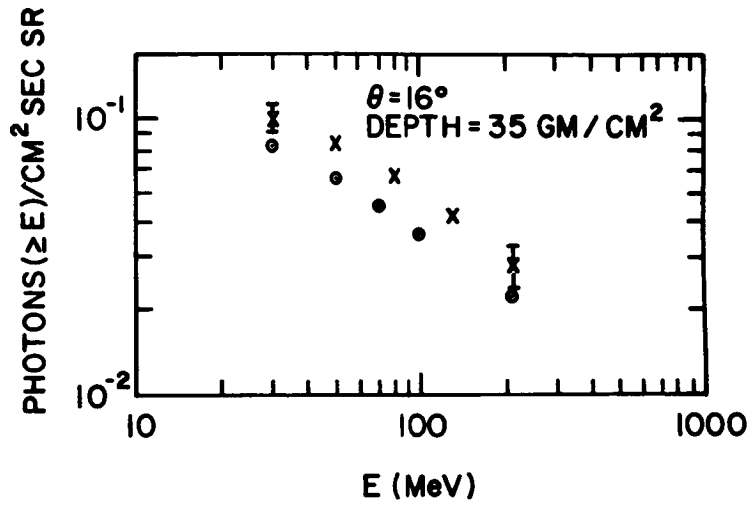
Figure 3. Energy spectrum.

PRIMARY AND SECONDARY NUCLEI IN
HIGH-ENERGY COSMIC RAYS

Jonathan F. Ormes

For several years now, we have thought that the composition of cosmic rays was independent of energy. We thought that the spectral exponent that describes the energy spectra was a property of the cosmic ray acceleration mechanism, and that all cosmic rays come from the same type sources. I want to tell you about some recent results which will greatly alter this simple picture.

Last year at this symposium, I described a balloon-borne experiment we used to determine the cosmic ray composition above a few gev per nucleon. The energy of the particles was measured with a 5000-pound block of iron, called an "ionization spectrometer." Four separate detectors were used for measuring charge, and a spark chamber was used for measuring particle trajectories and for rejecting background events.

The charge resolution is shown in Figure 1. The abundance of the elements lithium, berillium, and boron is large relative to any known possible source abundance. They are always interpreted as being produced by spallation reactions of carbon and oxygen on interstellar hydrogen and helium atoms. In a similar manner, most nuclei in the charge range 15 to 23 are thought to be produced by spallation of iron. We interpret carbon, oxygen, and iron as coming directly from the sources and as reflecting source characteristics.

If one compares the abundance of carbon and oxygen to iron in the cosmic rays, and in the universal abundance as derived from meteorites and observations of the sun, one finds that iron is relatively more abundant in cosmic rays. This has been used as one piece of evidence to suggest that cosmic rays originate in stars with a highly advanced evolutionary state, such as supernovae and pulsars.

The result is that the enhancement of iron increases with increasing energy. This is shown in Figure 2 where the ratio of carbon plus oxygen to iron is plotted versus energy. The more iron, the lower the ratio. Over the range of our experiment – the solid dots – the ratio decreases by a factor of three. And when lower-energy data is included, the change in ratio becomes a factor of five or six.

In Figure 3 this can be seen in a different way. We have plotted the differential intensities of these primary nuclei. The low-energy points are strongly affected by geomagnetic cutoff, but above a few gev per nucleon, the spectra can be fitted to power laws. If these spectra continue, then iron will become as abundant as carbon plus oxygen at a few hundred gev per nucleon, just off this scale.
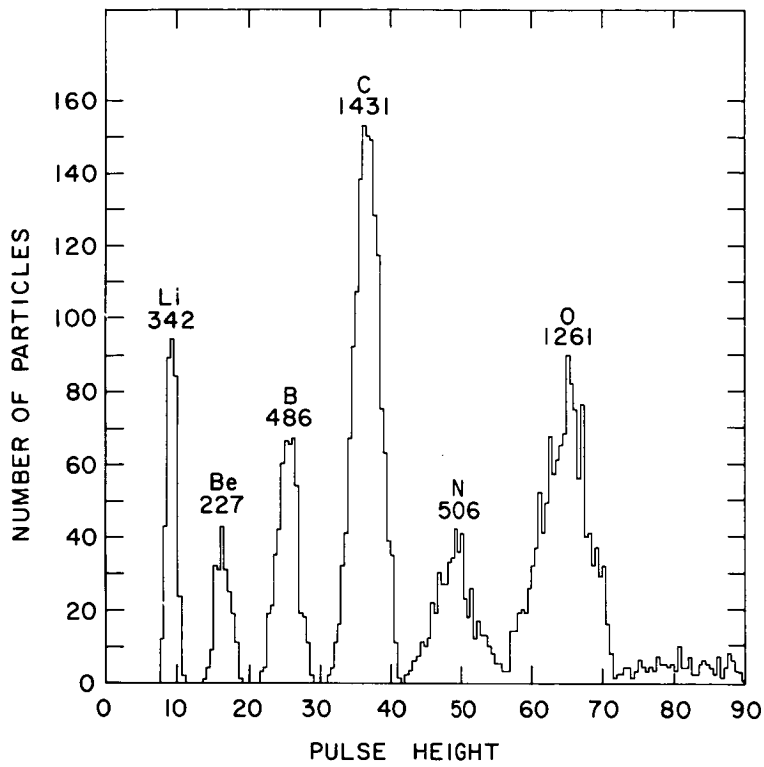
Figure 1. Charge resolution.
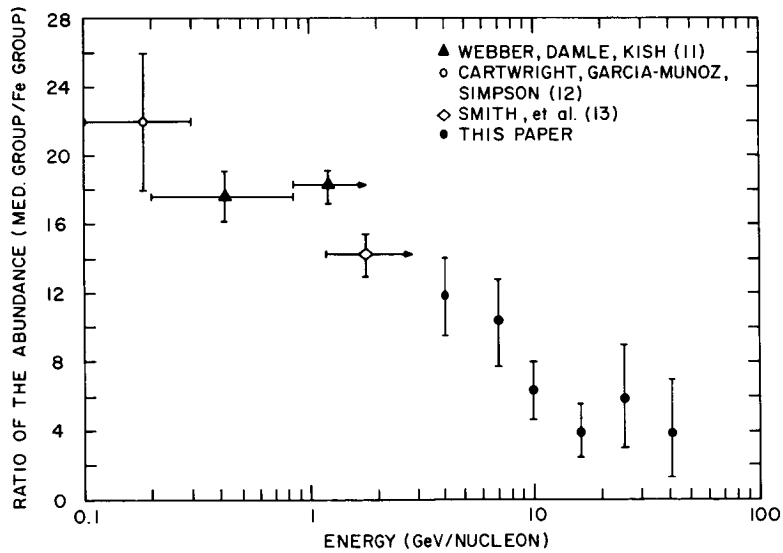
Figure 2. Ratio of carbon plus oxygen to iron plotted versus energy.

COSMIC RAY SPECTRA ABOVE 3 GeV/NUCLEON

$$dN/dE = kE^{-\gamma}$$

INTENSITY (PARTICLES / M² · SR · SEC · GeV/NUC)

ENERGY (GeV/NUC)
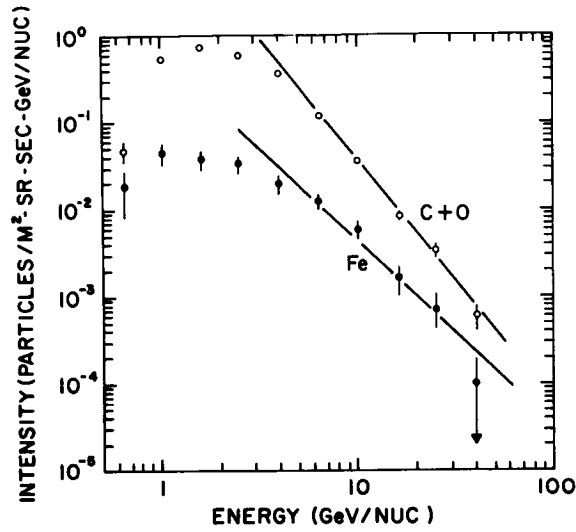
	PRIMARY	SECONDARY	$\Delta\gamma$
γ	C+O 2.61±0.04	Be+B+N 2.74±0.06	0.13±0.07
	Fe 2.1±0.15	15≤Z≤23 2.3±0.15	0.2±0.2
$\Delta\gamma$	0.5±0.2	0.44±0.2	

Figure 3. Cosmic ray spectra above 3 GeV/Nucleon
$$dN/dE = kE^{-\gamma}$$

We can speculate that at the highest air shower energies, iron nuclei might even pre-dominate over protons. In the table in Figure 3, we show the spectral exponents for various nuclei of both primary and secondary origin. The nuclei in the column labeled "secondary" are produced by spallation of the nuclei in the column just to their left labeled "primary." The numbers in the boxes are the exponents for those nuclei.

In the last column, the spectral differences between the primaries and secondaries are shown. They are just on the edge of being significant, and both Alvarez's group at Berkeley and Meyer's group at Chicago have recently reported similar results. These results can be understood in terms of a propagation effect by assuming an energy-dependent length for particles to leak out of the galaxy.

In the bottom row of the table, the spectral differences between the two groups of primary nuclei, carbon plus oxygen and iron, are shown. The difference between carbon plus oxygen and iron is large, about half a power, and is confirmed in the

difference between their secondary products. It is difficult to explain so large a difference as being due solely to propagation effects.

The gyroradii of these particles in interstellar fields are much smaller than the scale of the spiral arms, which is the smallest trapping region usually considered. The fragmentation parameters which produced the secondary nuclei are energy-independent of these energies, and the particles have only gone through a few grams per square centimeter of material.

Therefore, we conclude that we are observing a source effect. If all cosmic rays come from the same source, then preferential acceleration of heavy nuclei is implied. Maybe the acceleration process itself is charge dependent. Maybe different nuclei are produced in different sources. Only detailed examination of the spectra of individual nuclei will resolve these questions.

We believe that this is major evidence that cosmic ray energy spectra are different for different nuclei. Many of the questions that we can ask based on this data will have to await answers from the cosmic ray composition experiment on the HEAO-A satellite. At any rate, we expect these results to have a major impact on our understanding of cosmic ray acceleration and propagation.

PROGRESS IN THE MEASUREMENT OF HIGH-ENERGY GALACTIC COSMIC RAY ELECTRONS

Robert F. Silverberg

The study of cosmic electrons has been going on since the existence of a finite flux of them was established in 1961. Because they interact strongly with photons and magnetic fields, electrons are an excellent probe into the galactic environment.

A detailed knowledge of the cosmic electron spectrum and the electron to positron ratio could yield information about the energy balance in the galaxy and about sources of cosmic rays. In particular, the extremely rapid energy depletion of high-energy electrons should cause a break in the energy spectrum of cosmic electrons. The energy at which that break occurs gives an accurate estimate of the mean age of cosmic electrons.

Any measurement of cosmic electrons is made in an environment filled with energetic protons. The protons interact with matter in an explosive way, blowing nuclei apart. Electrons also interact with matter, but in a more predictable fashion.

In the detector, the high energy electrons are scattered by nuclei, as shown in Figure 1. Gamma rays are given off as a result of the acceleration experienced in the nuclear collision. The gamma rays then interact in the detector, and produce electron-positron pairs, which may again interact, producing more gamma rays and more electrons and positrons. The number of particles begins to fall when the gamma rays produced in collisions are no longer energetic enough to produce electron-positron pairs, or Compton electrons. The electrons and positrons are dissipated in ionization loss.

A sample electromagnetic shower is indicated on the right-hand side of Figure 1. The detector samples the shower and records points on the curve in sufficient detail to reproduce the curve illustrated on the right.

Proton interactions are generally of a different character, but a fraction of them may closely simulate electron showers. Since protons outnumber electrons by a factor of one hundred or more, the fraction of proton interactions which do simulate electron showers is a cause for serious concern in cosmic electron measurements. A large number of these false electron-like showers are eliminated in this experiment by placing thresholds on individual detector elements. Further discrimination against protons is provided by fitting individual events to electromagnetic shower curves. Data obtained from a calibration of our experiment at the Stanford linear electron accelerator has given us a measure of the goodness of fit that typical electrons show. Flight particles which deviate excessively from these shower curves are rejected as proton-induced events. Even further proton rejection is provided by using the apparent starting point of these showers to discriminate against interacting protons.
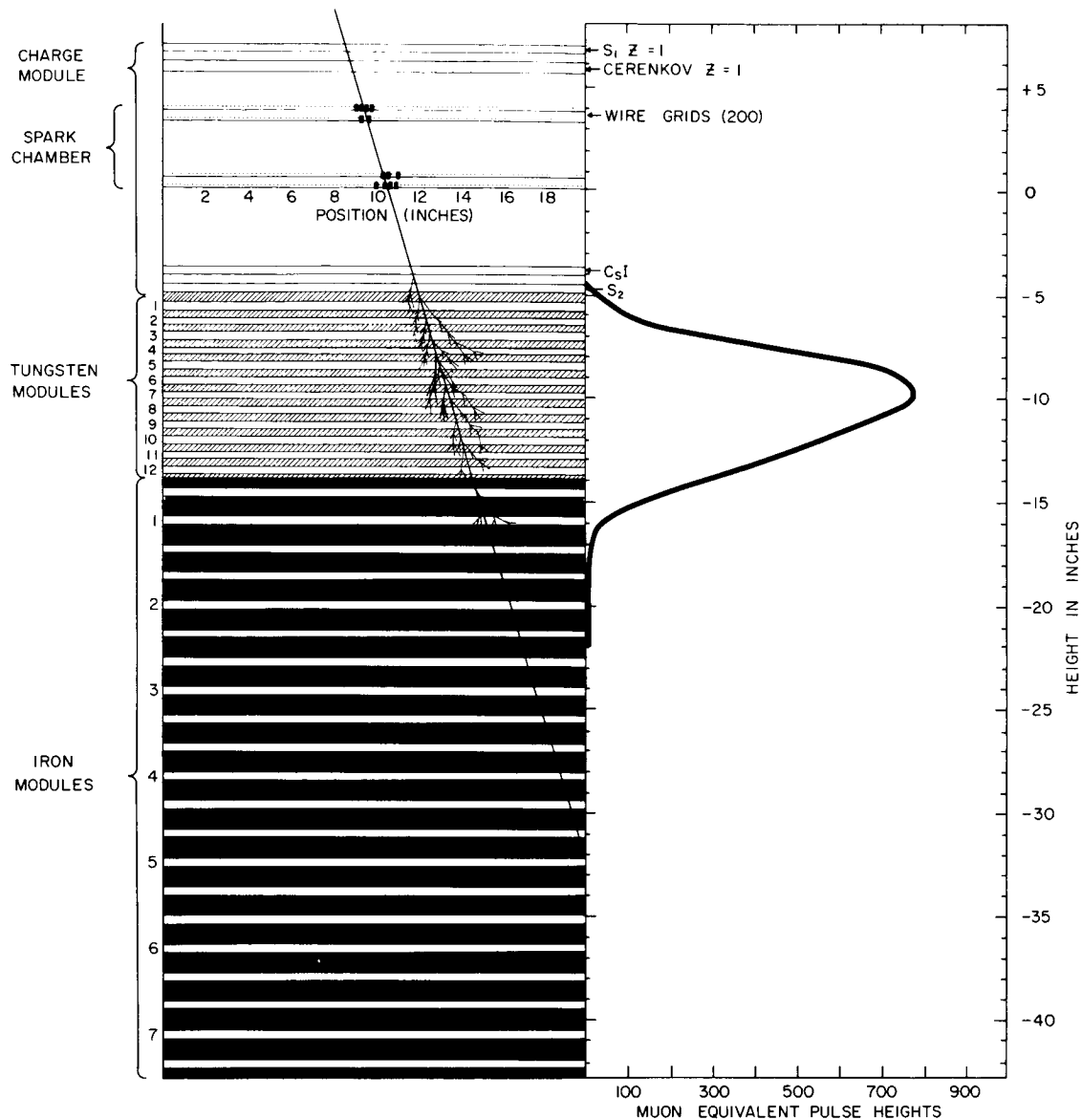
Figure 1. Schematic of detector and curve produced by a sample electromagnetic shower.

Figure 2 shows the starting point distribution of some inflight protons and some accelerator positrons. Because of the distinct difference in these distributions, another large segment of the remaining proton background can be eliminated, by demanding that acceptable events be in the starting-point range observed at the Stanford accelerator.

The appearance of structure in the proton distribution gives an indication of the accuracy of our fitting procedure. Some proton interactions in the plastic scintillator produce a large pulse, which makes the showers appear to be well developed; thus there is a valley

STARTING POINT DISTRIBUTION OF 16 GeV SLAC POSITRONS

STARTING POINT DISTRIBUTION OF
FLIGHT 3 SINGLE PARTICLES DEPOSITING ≥ 40-GeV IN IRON & ≥ 5-GeV IN TUNGSTEN

(ARROWS INDICATE POSITIONS OF SCINTILLATORS)
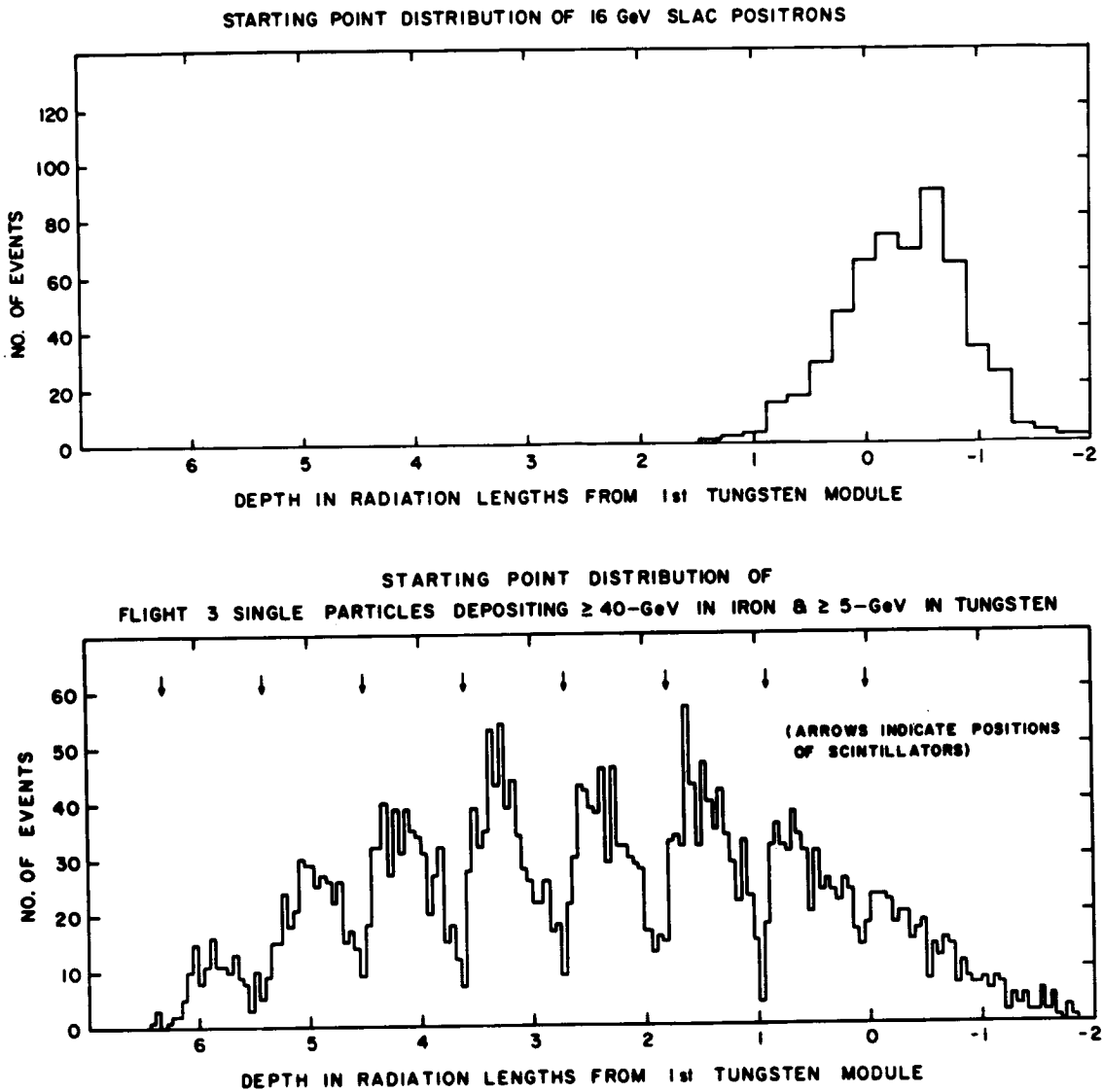
Figure 2. Starting point of some inflight protons and some accerator positrons.

created near each scintillator due to the shift of the starting point away from scintillators.

The unique feature of this experiment is the total depth of four nuclear mean-free paths. This allows the nuclear interaction secondaries to interact again, revealing themselves as proton-initiated events. After all corrections are made, it is found that about 30 percent of our electron-like showers are really proton-initiated events.

The final spectrum obtained is shown in Figure 3. While the agreement with the findings of other researchers at about 10 GeV is quite good, the spectrum shows a consistent dropoff, leading to a best fit at a power law of spectral index −3.2. Other researchers have measured

26

spectral indices in the 2.6 to 2.8 range, which is close to the proton spectral index of −2.7. Our data does not fit a power law very well, but indicates a consistent dropoff in intensity. This may be in agreement with any of several theories which indicate that a break in the cosmic electron spectrum should occur above 10 GeV.

A recent paper, however, has shown that any such break in the electron spectrum is likely to occur over two orders of magnitude in the spectrum. Although current data is insufficient to fix precisely the energy of a break, steepening of a half a power, which we observed, may indicate that a full power will occur over the next decade so that the break is centered about 100 GeV. This could indicate a cosmic electron lifetime of about 3×10^6 years.
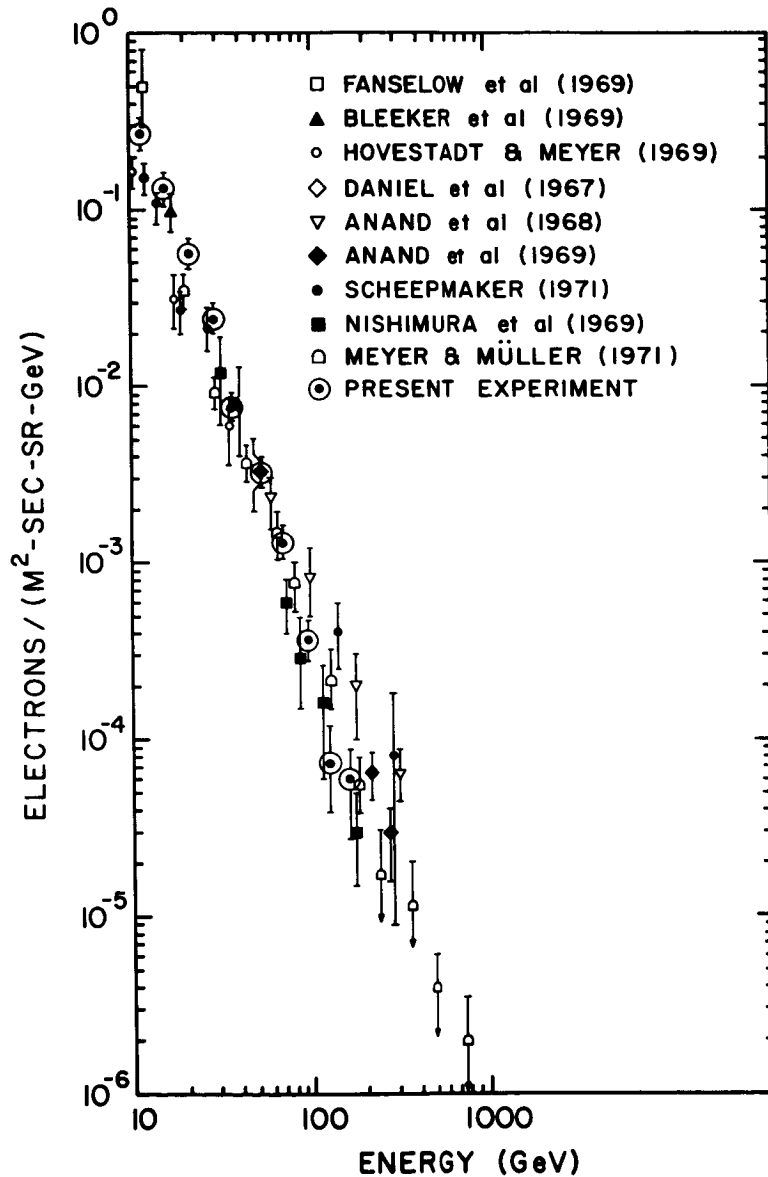
Figure 3. Final spectrum.

27

This is in good agreement with the age of cosmic rays as deduced from the lithium-berillium-boron abundances. Further study of the cosmic ray electron spectrum is required to resolve this break, or in fact, to verify that the break is indeed present. The HEAO-A spacecraft is to contain an improved version of the detector we used for this experiment, and hopefully we will gain more specific data about cosmic electrons.

THE FIRST INTEGRATED INTERPLANETARY ELECTRON SPECTRUM

Thomas L. Cline

I wish to report the first observations of a quiet-time interplanetary electron component in the 20 keV to 2 MeV energy range. The measurements fill in the gap between the highest-energy known solar wind and the lowest-energy previously observed electron populations, and connect for the first time the entire solar-quiet interplanetary electron spectrum over a dynamic range of nearly 10^{12} in energy.

The measurements come from experiments on the IMP-6 spacecraft, made in Mid-1971 at apogee, outside the magnetosphere and in the solar direction ahead of the shock front. Our detector (Figure 1) was designed to make a two-parameter measurement, analogous to $\triangle E$ versus E, but in the very low-energy region where the electrons cannot penetrate two individual sensors. It accomplishes this with a stilbene crystal, inside the CsI anti-coincidence, in which each stopping particle has both its energy loss and its rate of ionization determined by measuring its pulse height and pulse shape. A sample of data, also shown in the figure, includes a minimum-ionization line out of the noise, and a very few protons. It indicates complete proton versus electron separation for all electron energies above 50 keV, an order of magnitude lower than was previously possible. It also indicates the low intensity of on-scale protons, as compared, for example, with a flare event. The pulse decay in CsI is much slower than either lightly or heavily ionizing particles in stilbene, so that all components in the entire arrangement can be resolved with one photomultiplier tube. A second scintillator system was used to investigate the positron component by observing annihilation gammas; and a third phototube views a separate stilbene system, symmetrically placed but closed off from incident electrons. This was used to evaluate the local compton electron background, which was found to be a small effect. The resulting spectrum of quiet-time electrons is shown as the Goddard points of Figure 2, and is compared with the lower-energy data from K. Anderson and R. P. Lin's University of California experiment on the same satellite. The excellent agreement of the differential spectra observed by the two experiments is evident. In addition, each one independently observed a bump in the 100 to 300 keV region, which is seen to prevent the description of the spectrum by a single power law. Since the evidence for this feature is in good mutual agreement, we view it as unlikely that the bump can be due to systematic errors. It happens to occur at the appropriate energy interval for somewhat energy-degraded neutron-decay electrons, since the neutron beta spectrum peaks at 280 keV and ends at about 780 keV. Theoretical studies, however, have ruled out the possibilities of an interplanetary component of the observed electron

I = > 10
— = > 100
☐ = > 1000

CsI
STILBENE
LUCITE
CsI
PLASTIC SCINT.
P.M.
P.M.
P.M.
EXP PANEL
STILBENE
CsI
LUCITE

0
INCHES

J↓

→ E
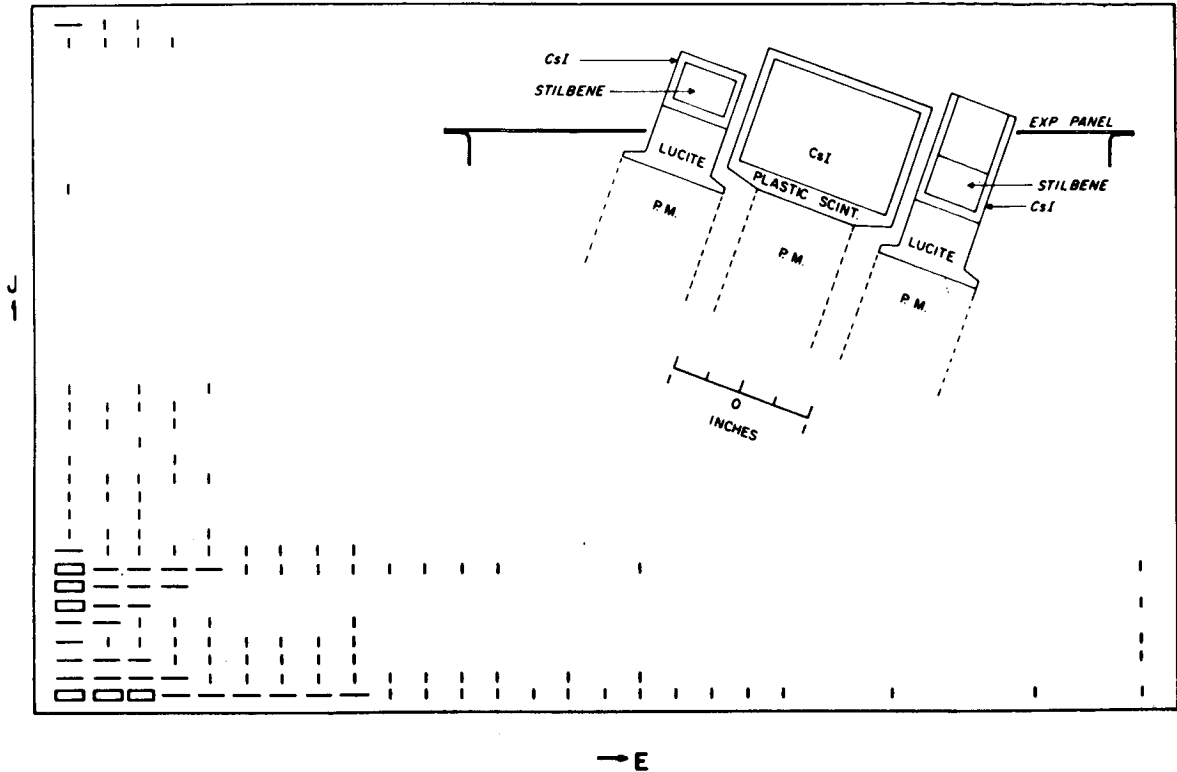
Figure 1. The electron detector on IMP-6, and a sample of raw data.

intensity from neutrons of either a terrestrial or a solar origin. It may, therefore, be preferable to consider this bump as a shelf or cutoff between two power-law regions.

In order to provide the big picture, the quiet-time interplanetary spectrum, over all available energies is compiled in Figure 3, covering a range of 10^{26} in differential intensity. Solar wind electron data departing from the theoretical 150,000 degree Maxwellian (dashed line) are shown in the 100 eV region, continuing into the higher energy range (using data from the Apollo 15 Subsatellite, which are not strictly quiet time as indicated by the IMP-6 measurements, shown with diamonds, taken in the same period). In the 20 keV to 2 MeV region, the results presented here are the only quiet-time data, except for two New Hampshire points in the several hundred keV region, which may represent either a disagreement or a time variation, since they are from a period two years closer to solar maximum. Our IMP spectrum joins smoothly onto the older IMP-4 and OGO-5 spectra at 2 MeV, which then continues with the high-energy cosmic-ray electron data up to 1 TeV. This plot ranks as one of the widest dynamic-range measurements of any single space phenomenon.

30

Figure 2. The quiet-time electron spectra from Goddard and University of California IMP-6 experiments.
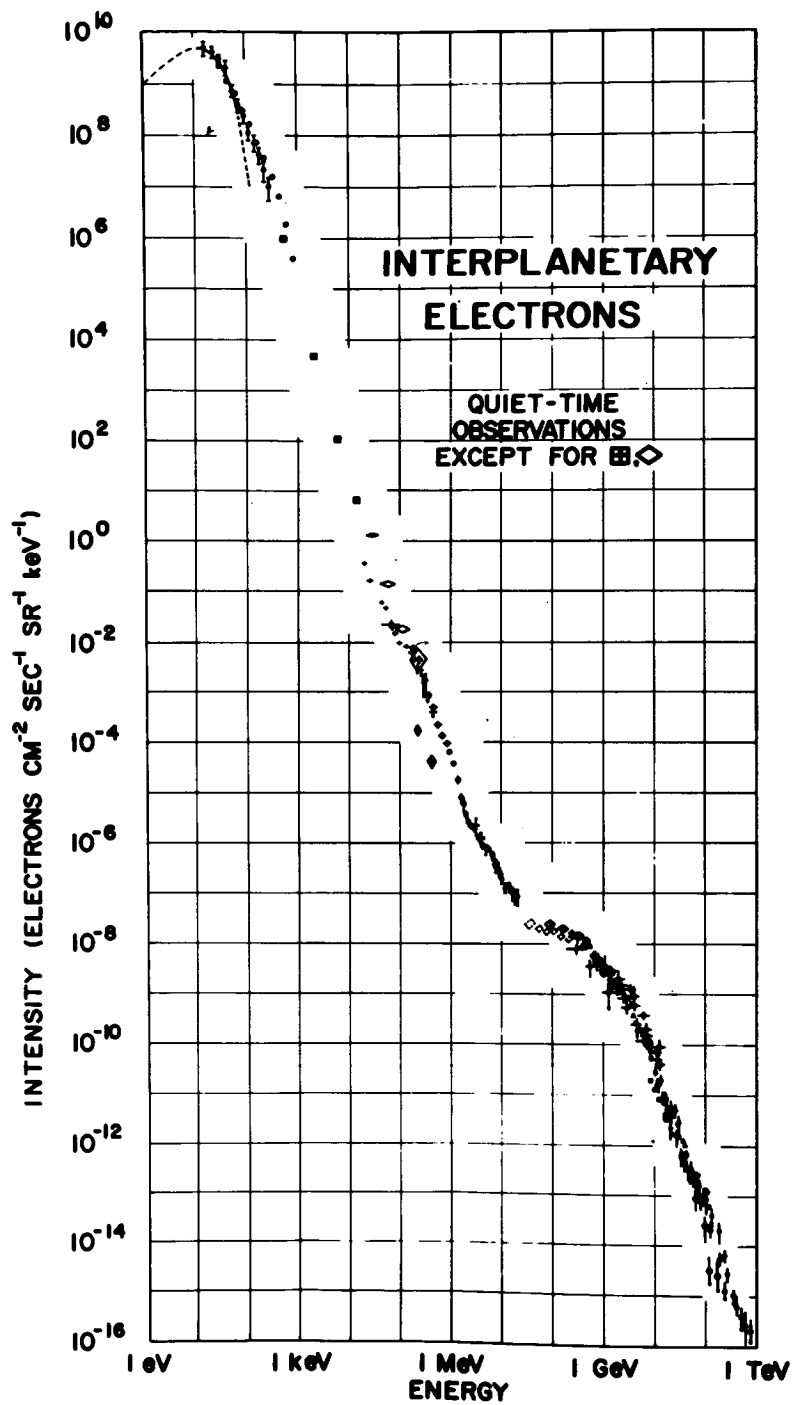
Figure 3. A compilation of all quiet-time interplanetary electron
observations, from solar-wind to cosmic-ray energies.

The basic question is, of course, where do the solar wind electrons end and the cosmic rays begin? One might be tempted to assume that the break occurs at about 20 MeV, where the greatest change in slope takes place. However, this is taken as a modulation effect, for several independent reasons. Cosmic ray electrons are then assumed instead to merge with the solar component at a lower energy, at or below a few MeV. On the one hand, the IMP-6 electron spectrum in the range of 0.3 to 2 MeV fits a power law with negative index 3.2, substantially different from the negative index of 1.75 measured for electrons from 2 to 20 MeV, possibly suggesting a noncosmic-ray origin for the few-hundred keV region. On the other hand, the lack of short-time variations in the 0.3 to 2 MeV intensity during 1971 is more consistent with the behavior of the higher energy >2 MeV cosmic-ray electrons. Only a thorough and detailed study of the time variations of both regions over a protracted period will verify whether or not all the nuances of temporal behavior above 300 keV are like those of cosmic-ray electrons.

Similarly, the presence of marked temporal variations in the electron fluxes between 18 and 100 keV indicate that these electrons are most likely of solar origin. They may represent a high-energy extension of the solar wind, or they may be a separate component related to solar active regions and storms. Thus, further studies of the time variations of the entire 5 to 100 keV electron component will also be needed to clarify its origin.

Finally, the spectral bump at about 200 keV could be interpreted, in a manner consistent with the demarkation just described, as a rather abrupt cutoff between two power law regions of solar and of cosmic-ray nature, giving a picture in which only those electrons of energy greater than about 300 keV enter the solar system from the nearby galactic medium. Theoretical studies of interplanetary propagation by Ramaty and Fisk show this to be quite plausible interpretation.

MODULATION OF LOW-ENERGY GALACTIC COSMIC RAYS
OVER THE PRESENT SOLAR CYCLE

Michele A. Van Hollebeke

An important question concerning the modulation of galactic cosmic rays is whether there
is any change near the solar maximum and the solar minimum in the modulated cosmic
ray spectrum. For the first time, observations made with the Goddard Space Flight Center
experiments on IMP-3, IMP-4, and IMP-5 cover the entire period of the solar cycle and it
has been possible to answer this question.

Figure 1 shows the variation of the intensity of the galactic cosmic rays at two different
energies. The upper plot is the ~ 10GV galactic proton intensity as represented by the
Deep River Neutron Monitor rate. The vertical bar indicates the upper and the lower ampli-
tude during the time interval of the low-energy intensity measurement. On the lower part
of the figure are the 60 MeV per nucleon proton and alpha intensities. As can be seen, the
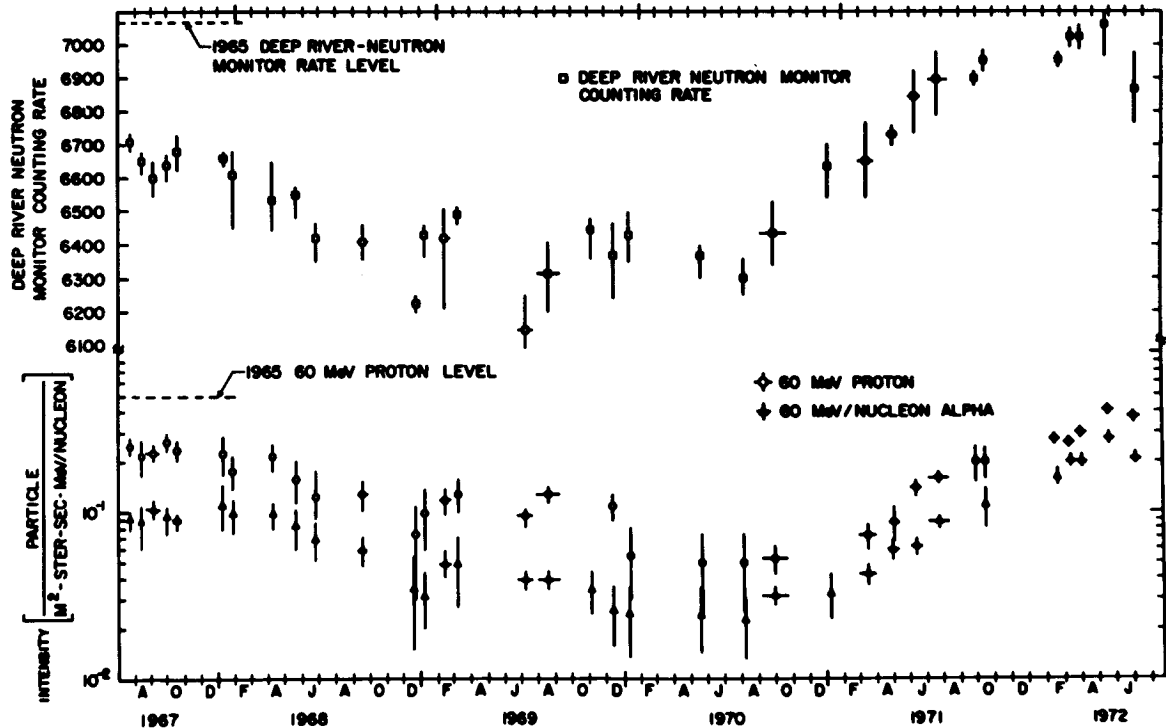

Figure 1. Variation of the intensity of the galactic cosmic rays at two different levels.

34

higher energy intensity is decreasing as the solar activity increases from 1965 to 1969, and increasing after the maximum of the solar activity until the beginning of 1972. The 60 MeV Proton and Alpha follow the same trend; but while Deep River — on the upper part of the plot — had reached the 1967 level by early 1971, the 60 MeV/Nucleon (or lower energy component), had just begun a significant increase at that point in time.

What does the variation of this intensity and the different behavior at different rigidity mean? One of the current explanations of the propagation of particles in the interplanetary medium is described in Figure 2. Starting on the left is the Fokker-Planck equation which allows for the effects of convection, energy loss, and diffusion. The intensity of galactic cosmic rays observed, for example, near the earth, depends essentially on these three basic effects illustrated in the simplified picture on the right. First, the radial outward streaming, due to convection of particles in the solar wind, depends on V. Second, the size and the frequency of the irregularities of the magnetic field by which the particles are scattered as they proceed along the interplanetary magnetic field lines is described by the parameter κ. Finally, as those particles are scattered among the magnetic irregularities moving outward with the expanding solar wind, they lose part of their energy as described in the equation. Using a numerical solution accounted by Fisk to this equation, we find among possible forms two different ways to reproduce the observed change in the proton and alpha modulated spectrum, indicated here as Case I and Case II.

CONVECTION

$$\frac{1}{r^2}\frac{\partial}{\partial r}(r^2 VU) -$$

ENERGY LOSS

$$\frac{1}{3}\left[\frac{1}{r^2}\frac{\partial}{\partial r}(r^2 V)\frac{\partial}{\partial T}(\alpha T U)\right] =$$

DIFFUSION

$$\frac{1}{r^2}\frac{\partial}{\partial r}(r^2 \kappa \frac{\partial U}{\partial r})$$

HELIOSPHERE

B_0 SUN

CASE I:
CHANGE IN RIGIDITY
DEPENDENCE OF κ

CASE II:
CHANGE IN THE EFFECTIVE
SIZE OF THE MODULATION
REGION
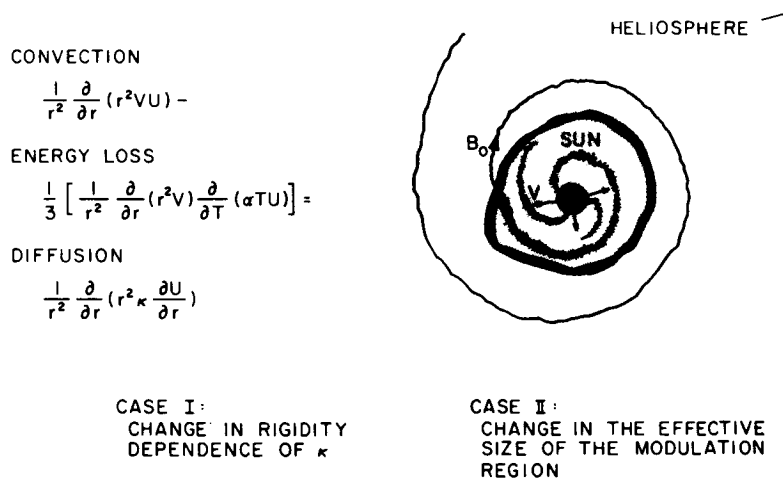
Figure 2. Explanation of the propagation of particles in the interplanetary medium.

Case I is a change in κ, dependent of the rigidity and time; Case II is a change in the effective size of the modulating region with time. These two cases give the same result concerning the fit indicated in Figure 3 by the dashed line. Figure 3 shows the well-defined
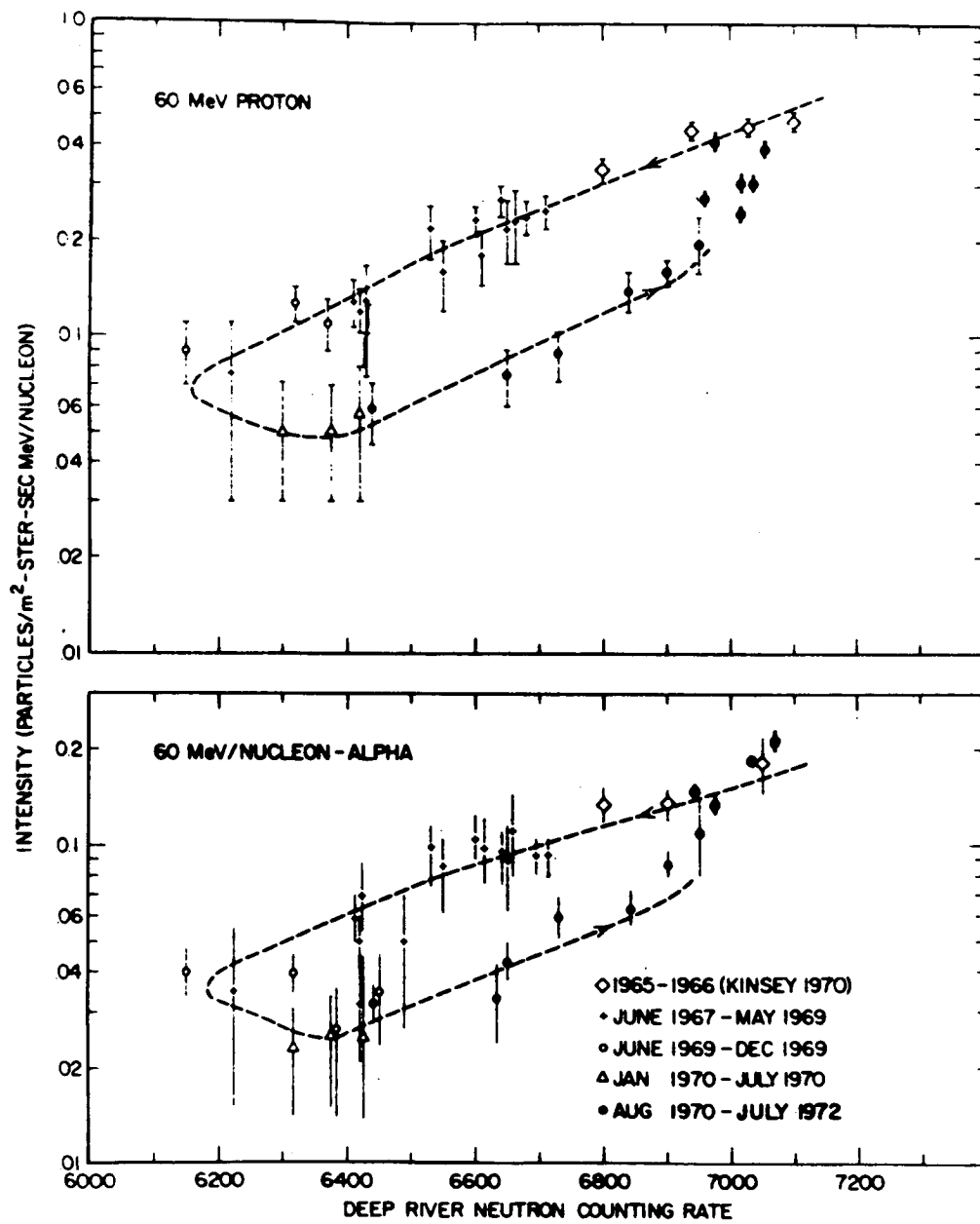
Figure 3. High energy component of Figure 1 plotted versus the low energy component.

hysteresis effect. The high-energy component shown on Figure 1 is plotted on a semilog graph versus the low-energy component. The upper curve is the 60 MeV proton intensity; the lower plot is alpha particle intensity at the same energy and twice the proton rigidity. The different symbols in both curves correspond to different periods as indicated at the bottom. The theoretical fit is essentially two parallel lines during the increasing and decreasing periods of solar activity, the variation of the lower rigidity being essentially proportional to the variation of the higher rigidity. In between is one of the transition periods during which the higher rigidity leads the lower one. The 1972 points are on the right edge of the plot with the March-July points closing the loop at the same level as in the previous solar minimum in 1965. As we said above, we have reproduced this effect by adjusting parameters. The same result has been obtained by changing κ, in a function of the rigidity; or by changing the size of the modulating region with time.

How do these changes appear regarding what happens physically? The magnetic field irregularities (reflected by κ) are affected by the hydromagnetic instabilities. The condition for which those occur depends strongly on the plasma density. In the plasma density data available, we found a positive correlation with the variation of the cosmic ray intensity, which breaks during the transition period. The absence of data during the recovery period does not allow us to comment on the reality of this effect, which was however, sufficiently interesting to mention.

In conclusion, please note that the suggestion that the alpha particles lead the proton particles during these two transition periods, making the lag time shorter for high rigidity, seems to favor a model depending on the size of the modulating region.

37

OBSERVATIONS OF SOLAR COSMIC RAYS AT 2 AU

James H. Trainor

The Pioneer-10 spacecraft was launched on March 3, 1972, on a direct flight to Jupiter. The spacecraft includes an experiment designed and built by a group here at Goddard Space Flight Center, working with Professor Webber from the University of New Hampshire. The primary purpose of this experiment is to carry out investigations in the energy spectra, charge composition, and flow patterns of both solar and galactic cosmic rays from 1 AU outward.

Additionally, the very lowest energy telescope in this system has been designed to be a very good detector system for electrons and protons in the Jovian radiation belts. In this paper, I will discuss the detector complement and data just now available of a series of solar proton events which occurred in early August. The events were the very largest of the current solar cycle. In a subsequent paper, Dr. Teegarden will discuss the radial gradient measurements with the same experiment.

The first figure shows a cross-section of the three detector telescopes within this experiment, a high-energy telescope and two low-energy telescopes. The drawing is not to scale in that the low-energy telescope II has a small geometry factor to allow the detector to measure large fluxes of very low energy particles. The detector area is ~ 50 mm^2 for LET-II as opposed to 10 cm^2 for HET.

To demonstrate the operation of these detector systems, I'll discuss the LET-I telescope first. Each silicon solid-state detector is a circular disk with thicknesses varying from 50 microns to a few millimeters. The figure is obviously shown in cross section. There are four individual detectors, which we call D_1, D_2, E, and F. F is an anticoincidence detector at the rear. We derive quite a large number of count rates from this telescope: a D_1 singles rate; a $D_1 D_2 \bar{E}$ coincidence rate; $D_1 D_2 E \bar{F}$; and so on. There are varying thresholds on many of these rates. Additionally, there are many rates which are sectored with respect to spin.

In addition to rate information, the double and triple coincidence events are processed through a pulse-height analysis system, whereby the energy deposited in each detector is digitized to 10 bits accuracy and put into telemetry, together with auxiliary bits which identify the sector of spin in which the data was taken, the state of a priority matrix, and other auxiliary bits of information. The priority system is a rolling set of four conditions, whereby if a higher priority condition is satisfied before the readout time has come around, then we dump the event ready for telemetry and replace it with the higher priority event. This technique emphasizes rare events in the data. Thus, in addition to the large

number of logical rates (more than 100 in this experiment), we obtain a rate of energy loss and total energy for each event. In effect, we are able to generate what we call a dE/dX versus E matrix, whereby one can readily separate elements and isotopes.

The high-energy telescope on the left of the diagram operates in a very similar fashion. The detectors are larger, and therefore a larger geometrical factor results. The detectors are thicker, and the stackup is larger, so we can process higher-energy events. Two operating modes are available with HET. We can look at stopping particles, in which case we get two dE/dx measurements from A and B, and a total E measurement in C. In addition, we get range for the event, and thus we have redundant information which is useful for eliminating background events. We also can look at penetrating particles coming from either side of the stack, in which case we get three dE/dx measurements.

The low-energy telescope II on the far right is a very small geometry telescope for looking at low-energy particles in the 50 keV to the few MeV region, where we are bothered by interference from the gamma rays originating in the spacecraft radioisotope power supplies. For that reason, there is a substantial lead and aluminum shield around the detector. Shields have adverse effects also in that Compton electrons result from the interactions in the
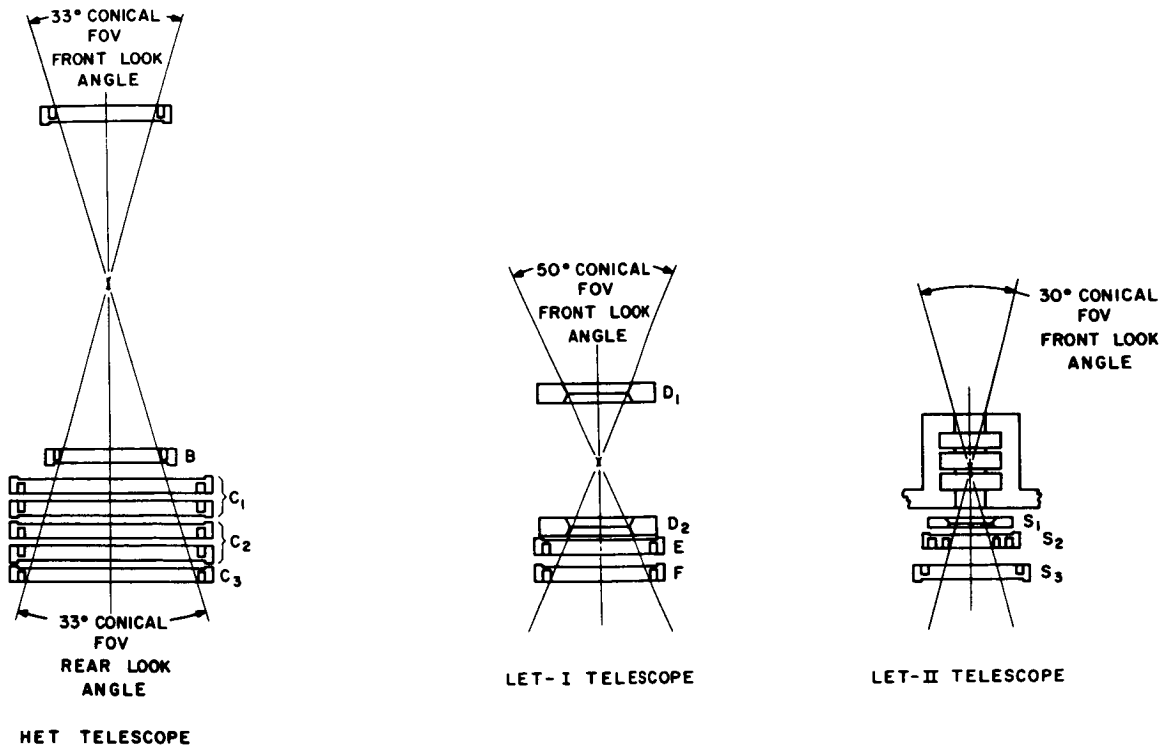

Figure 1. Pioneer-F and -G detector complement for cosmic ray energy spectra.

shield. Detector S_2 has an annular, integral anticoincidence ring around the central active detector itself, in order to reduce the effects of the Compton events. From first encounter with the Jovian magnetosphere, at perhaps 40 to 50 Jupiter radii, to perhaps as close as 10 Jupiter radii, this detector may in fact be the optimum detector on board the spacecraft.

I won't discuss the instrumentation further; the electronics and the mechanical systems will be discussed in another paper. I'll note that we cover the following energy regions: for electrons, from 50 kilovolts to about 5 MeV; protons, 50 kilovolts to about 800 MeV; alphas to 600 MeV per nucleon; and the light elements up through neon, to 200 MeV per nucleon for the complete dE/dx lines.

These detector systems are really a major advance in the design of successful high-energy particle detector systems. They are all solid-state; they're very light, very low power, and very long life. There are no photomultiplier tubes or crystals or the problems associated with them. They are high-resolution devices, and particularly clean in operation, as you'll see now.

In the next figure, data is shown both from IMP-5 and Pioneer-10 for the period in August when Pioneer-10 was at about 2.2 AU. In late July and early August, there were a series of complex events on the sun, leading to probably three large injections of particles from the sun, noted by the circled 1, 2, and 3 at the top of the figure. Figure 2 shows hourly differential flux (or count rate) from IMP-5 in the top series of curves; differential flux reported by Pioneer-10 is plotted on the bottom series of curves. Both were plotted as hourly averages for the period from August 1 through August 16. These were selected from the more than one hundred rates we have available as convenient and comparable rates suitable for a quick look.

There are several quick points to make:

- In shape, in amplitude, and in timing, the character of an event at 1 AU is much different than at 2.2 AU. At 1 AU the velocity dispersion is as you would expect. The higher energy protons arrive first, followed by the lower energy or slower protons.

- For event 3, at 2.2 AU, the low-energy, slower protons arrive first by many hours. The complete set of data from ~ 50 keV to ~ 100 MeV bears this out. Explanations for this phenomenon are presently being developed.

- In the period August 9 to 11, if one looks at the decay rate as a function of energy, the higher energy particles are falling off more rapidly. We also have Pioneer-9 at 0.77 AU on a radial line with Pioneer-10 at the same time, and IMP-5 at 1 AU from the earth. Looking at the time rate of falloff in the particles versus energy distance can then lead one to a measurement of the size of the modulation region, and this is now ongoing.

40
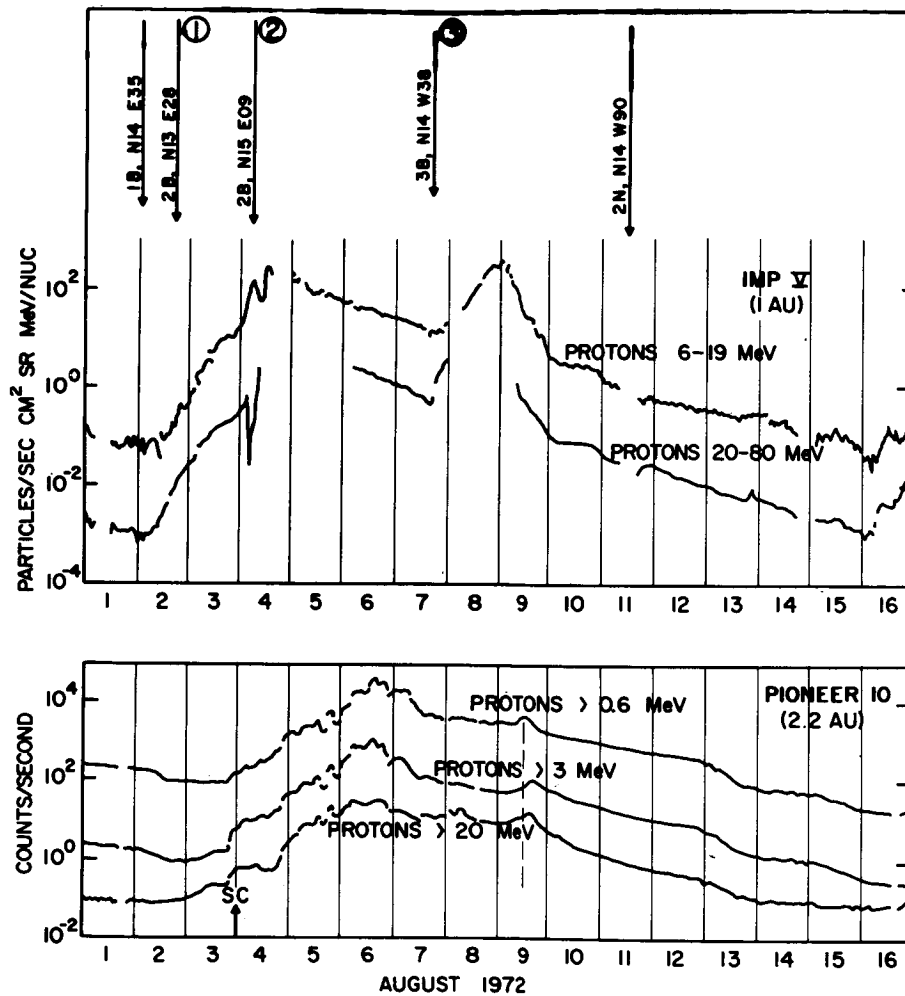
Figure 2. Hourly differential flux measured from IMP-5 and Pioneer-10.

Figure 3 is a plot that I referred to earlier, where we plot dE/dx versus E to display the separation of the elements and isotopes that are involved here. This is from the LET-I telescope. We're plotting more than 1000 channels in each direction, and the calibration lines for the various elements are labeled. In looking at the data for carbon in detail, we can resolve the isotopes of carbon for the first time. One expects, on such a plot, to see that carbon and oxygen are predominant, as you do see. Another feature of interest here is the almost total absence of many of the very light elements in this event. Also note the absence of any fluorine in this event.

I pointed out earler that our range was up to neon. Actually, we're doing quite a bit better than that. One can clearly see the lines above neon. The interesting thing here is that these are the first measurements ever of the solar particle lines for sodium and aluminum. These are the odd elements which are discriminated against in the nuclear building processes.

The relative abundancies are comparable to the abundancies found in the galactic cosmic rays, and are quite different from those abundancies derived from optical observations of the sun.

The performance of the instrument so far has been superb. At the moment, we're about 3 AU from the sun, and should fly by Jupiter on December 4, 1973.
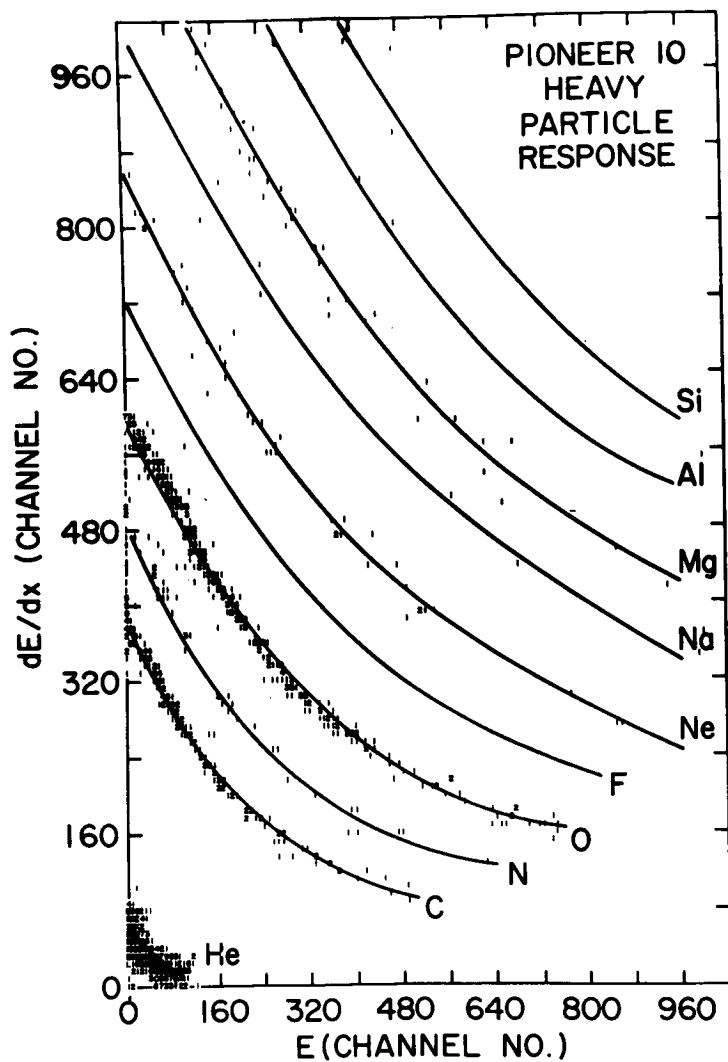
Figure 3. Pioneer-10 heavy particle response.

DR. NAUGLE:

Could you say a word about the explanation of why the solar particles get there?

DR. TRAINOR:

The question had to do with how the lower energy particles get to 2.2 AU first for the August 3, 1972, event. One of the possible explanations has to do with the scale of the irregularities that might exist in the magnetic field structure between here and there. Look at low-energy particles and think of them in terms of their radius of gyration about the field. If their radius of gyration is smaller than the scale of these irregularities in the field, they will tend to follow the field lines. If the spacecraft is at the right location, the particles will follow more-or-less direct paths to the spacecraft.

On the other hand, if the higher energy particles have radii of gyration comparable to or larger than the scale of the irregularities, they will tend to scatter. Those particles will have to diffuse across field lines in order to get to the spacecraft. This is at least one way to explain the data at 2.2 AU on August 9, 1972.

MEMBER OF AUDIENCE:

But nobody predicted it beforehand.

DR. TRAINOR:

The explanation I've just summarized was stated as a possibility by Dr. Len Fisk and others prior to the occurrence.

DR. RASOOL:

You said you can resolve Carbon-12 and isotopes?

DR. TRAINOR:

Carbon-12 and -13.

DR. RASOOL:

Yes, what is the abundance?

DR. TRAINOR:

It hasn't been calculated yet. Dr. Teegarden is agreeing with me. We've had the raw data only a week and one has to look very carefully at each event, the selection criteria, and so on.

DR. PIEPER:

You can sort of count the events on the curve. There were three to five carbon-13's, and the rest were I don't know how many carbon-12's.

MEMBER OF AUDIENCE:

How many?

DR. PIEPER:

I don't know, but I counted at least three -13's.

.

RADIAL GRADIENTS OF GALACTIC COSMIC RAY PROTONS AND HELIUM NUCLEI

Bonnard J. Teegarden

The galactic cosmic ray spectrum that we measure at the earth's orbit is severely distorted at low energies by the screening effect of the sun's magnetic field. Irregularities in the field are carried outward radially by the solar wind, and act to sweep low-energy cosmic rays out of the solar system. In addition, because of the outward expansion of the solar wind, cosmic rays reaching the earth are effectively cooled by their interaction with the wind through its coupling with the sun's magnetic field.

The Pioneer-10 deep-space mission offers the first real opportunity to make a direct measurement of the undistorted spectrum of interstellar cosmic rays. The question is, how large is the region about the sun where the interstellar cosmic ray spectrum is significantly modulated? Most recent estimates place the boundary of this region well within 10 astronomical units (AU), with some estimates as nearby as 2 to 3 AU. Pioneer-10, if all goes well, will return data from distances as great as 16 AU.

The variation of the cosmic ray intensity as a function of distance away from the sun and its derivative, the radial gradient, is a fundamental quantity whose measurement will serve as an indication of the extent of the modulation region and as an important parameter in understanding the equations governing modulation.

The Goddard/University of New Hampshire experiment, a similar experiment from the University of Chicago, and the Pioneer-10, are important achievements in that high-resolution, low-background instruments have been carried to significant distances outside the earth's orbit.

Transient changes in the interplanetary cosmic ray intensity, such as Forbush decreases occur from time to time; such decreases in general represent periods when the interplanetary medium is not in equilibrium. Since we're interested in measuring an equilibrium gradient, it's important to be sure that these transient effects are not playing an important role.

The presence of these effects can be determined by looking at sea-level neutron monitor data as shown in Figure 1; the Forbush decreases are marked with F's. The times of launch, 1.5 AU, and 2 AU are also indicated. There are four distinct decreases present during the critical period when Pioneer-10 was traveling between 1.5 and 2 AU, culminating in the largest decrease of the present solar cycle, associated with the solar events of early August 1972. Also shown in Figure 1 are the periods of data thus far available to us, and the periods when solar activity was present on IMP-5 at low energies (> 6 MeV). It is clear then that during this dynamic period the gradient determination is a nontrivial problem.
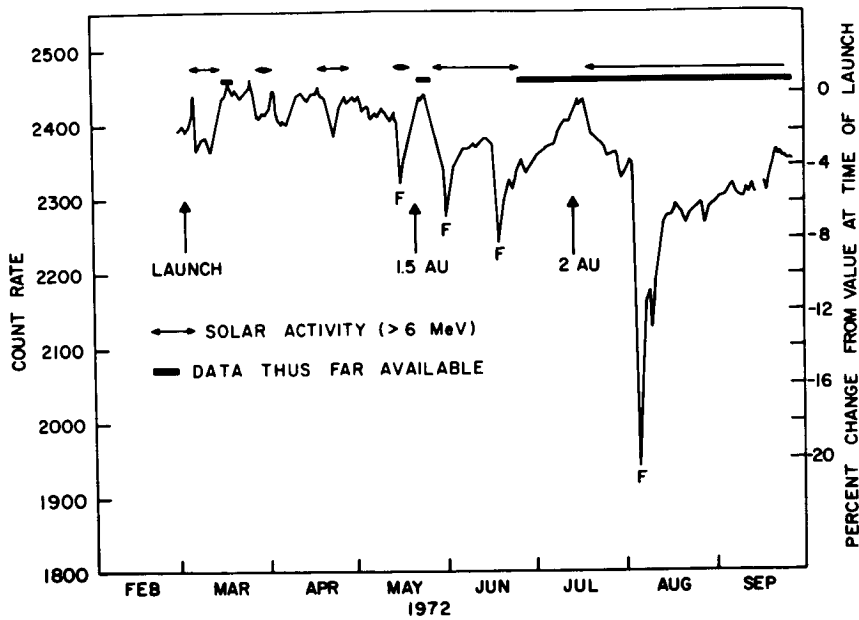
Figure 1. Mt. Washington neutron monitor rate.

The gradient determination is further complicated by the so-called hysteresis effect in the time-variation of galactic cosmic rays. This effect is illustrated in Figure 2 where the 40 to 80 MeV proton intensity as measured on IMP-5 (at 1 AU) is plotted against the Mt. Washington neutron monitor counting rate. The hysteresis or double-valued effect is quite pronounced at these energies. The data shown here encompass the better part of a solar cycle, beginning at the least solar minimum in 1965 and continuing up through the present. The lower and upper legs are quite distinctly separated and differ in intensity by approximately a factor of 3. It is also very interesting that the loop has apparently closed itself by early 1972. This is approximately 4 years earlier than expected, based on the usual 11-year periodicity of the solar cycle. The points on the loop when Pioneer-10 was at 1.0, 1.5, and 2.0 AU are also indicated. During the critical period when Pioneer-10 was between 1.0 and 1.5 AU, the low-energy intensity at 1 AU was in the process of transferring between the lower and upper legs of the loop. This illustrates the fallacy of using the neutron monitor as a reference to correct for time variations. If, for example, we were to compare Pioneer-10 at launch to Pioneer-10 at 1.5 AU, the neutron monitor would indicate that the time-variation correction was negligible. Because of the double-valued nature of the hysteresis curve, however, a significant correction must, in fact, be made.

We have established that the comparison must be made at the same energy, but the question remains: Should it be made for identical times? The question could be alternatively stated:

46

Is there a lag or phase difference between the time variations at different radial distances? In an attempt to answer this question and also to derive the gradient itself we have plotted
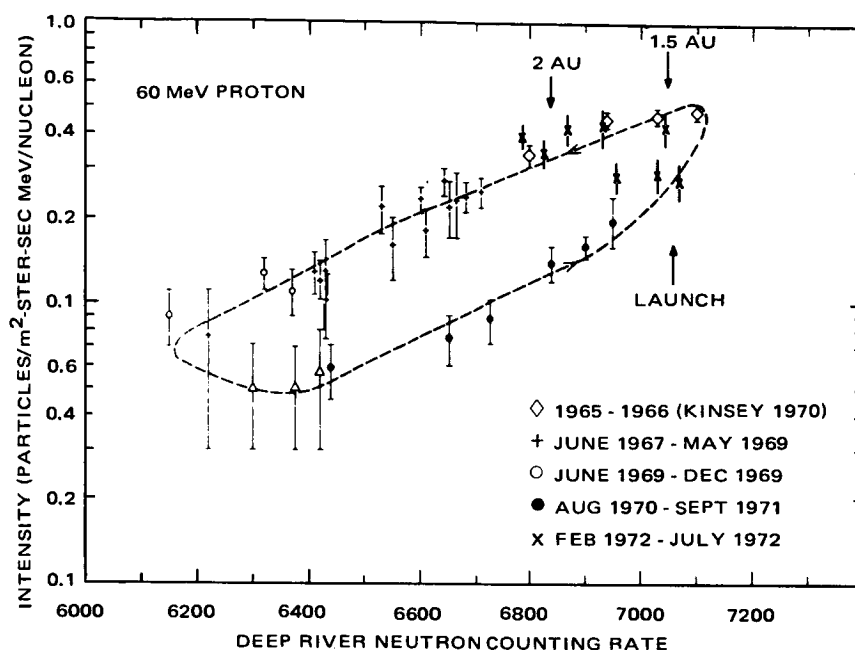
Figure 2. IMP-5 versus Mt. Washington neutron monitor.

in Figure 3 an integral rate > 56 MeV/nuc from Pioneer-10 versus an integral rate > 80 MeV/nuc from IMP-6. Data are shown for two time intervals, near 1 and 2 AU, respectively. The first important feature to note is that the 2 AU data points are consistent with a single regression line. The time period covered by the data taken at 2 AU included periods when the IMP-6 rate was both rising and falling. If a significant time lag were present between 1 and 2 AU, then data from the period where the intensity was rising should lie on a different regression line than data where the intensity was falling. The fact that the data are consistent with a single regression line argues that we can neglect any possible phase lag effects.

The second important point is that, at least to the first order, the data at 1 and 2 AU are both consistent with the same regression curve. This, of course, implies the absence of a radial gradient. We have drawn two straight lines, each passing through the origin, as reasonable limits on the spread of the data points. These lines differ in slope by 4 percent. We therefore can place an upper limit on the integral gradient (> 56 MeV/nuc) of 4 percent/ AU. Van Allen has recently reported a gradient measurement from another detector also onboard the Pioneer-10 spacecraft. He obtains an upper limit for the integral gradient > 80 MeV/nuc of 3 percent/AU, which is certainly consistent with our value.

These data, along with more recent data near 2 AU show that the solar modulation cavity extends well beyond 2 AU. In view of this, it becomes increasingly important to extend
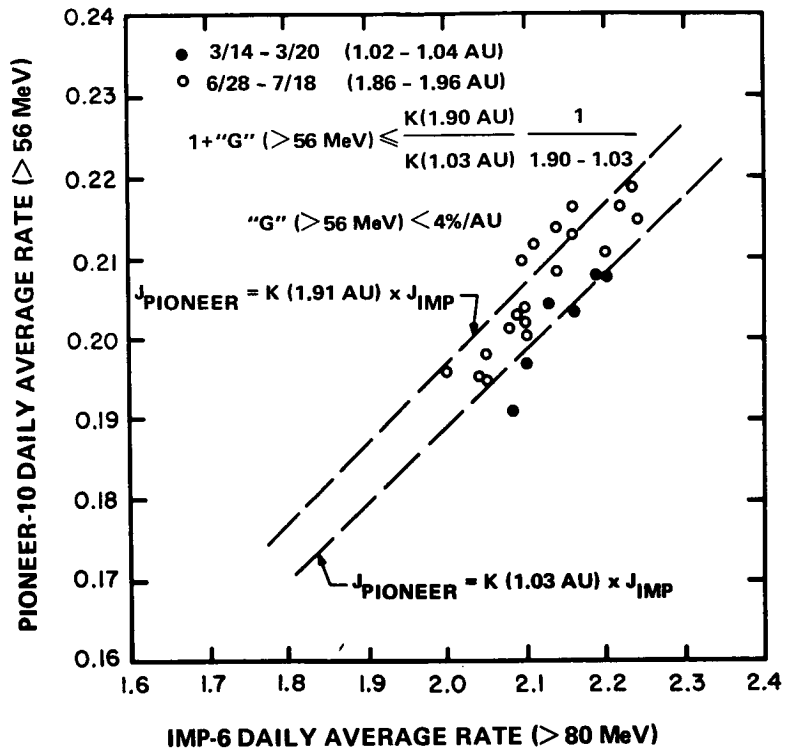
47

Figure 3. An integral rate > 56 MeV/nuc from Pioneer-10 plotted
versus an integral rate > 80 MeV/nuc from IMP-6.

cosmic ray measurements to large distances from the sun.

In closing, then, I'd like to take this opportunity to put in my own recommendation for the MJS mission as an ideal platform to continue these studies.

SOLAR FLARE PRODUCED PULSATIONS IN METER
AND X-RAY WAVELENGTHS

Kenneth J. Frost

Recently, several cases of very regular modulation of synchrotron radiation in the meter wave range, from a solar flare, have been observed. A specific example of such an observation made at 140 MHz from Culgoora, Australia, is contained in Figure 1, for a flare on November 5, 1970. These data are compared with those of 160 MHz observation from Nobeyama, Japan, which also show the modulation.

The proposed explanation for the modulation[1] is based on the interaction of a flare-generated shock front with a magnetic flux tube extending out into the corona over the flare. Figure 2 is from the paper by D. J. McLean, et al., in which the mechanism is described. According to McLean, as the shock wave propagates out through the flux tube, Alfven waves are set up in each let. The Alfven waves travelling up the tube toward each other accelerate electrons and protons by the fermi mechanism, in a fashion somewhat analogous to a "colliding magnetic mirror" scheme. This concept is illustrated in Figure 2a. The top of the flux tube thus becomes filled with energetic electrons which produce the initial rise in synchrotron radiation evident in Figure 1 just before the oscillations begin. As the shock front becomes parallel to the magnetic field direction, as shown in Figure 2b, radial oscillations are set up in the flux tube. As the tube oscillates, the magnetic field contained within it alternately increases and decreases. The intensity of the synchrotron radiation, being proportional to the magnetic field, is consequently modulated by the flux tube oscillations. As the shock wave moves on, the oscillations cease and the continuum decays (Figure 2b). Wild and Smerd[2] have suggested that this mechanism could also occur lower in the solar atmosphere at a height where the X-ray and microwave radiation is generated.

An instrument aboard OSO-5 detected a hard X-ray burst associated with the flare that produced the modulated radio emission we have just considered. The X-ray burst was detected in the 14 to 250 keV range and is displayed in Figure 3. The encircled part of the X-ray burst contains what appears to be an oscillation in the X-ray emission. At least five cycles are identifiable by eye. Figure 4 presents a power spectrum analysis of the encircled feature. The oscillations seem to be superimposed on a broad hump in the X-ray emission. Using a parabolic fit, this hump was subtracted from the data and the power spectrum analysis was performed on the residue. A prominent peak was found in the analysis at a period of 26.9 seconds.

[1] D. J. McLean et al. *Nature,* **234** (1971). p. 140.
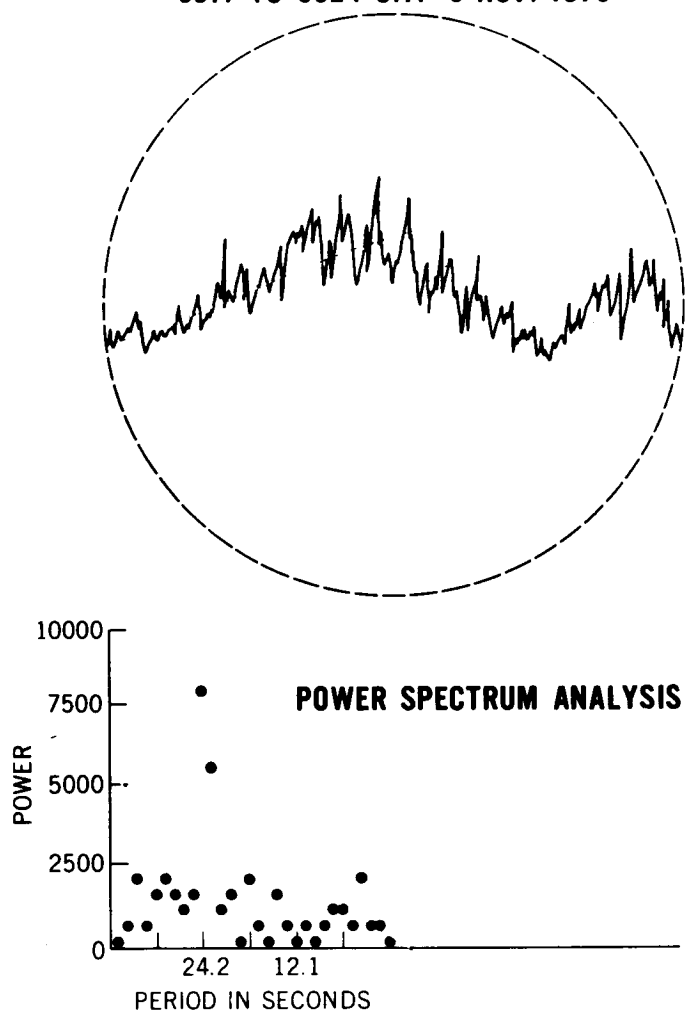[2] J. P. Wild and S. F. Smerd. *Ann. Rev. of Astron. and Astrophys,* **10** (1972). p. 159.

Figure 1. Oscillating feature and power spectrum.

A word of caution is necessary concerning the 26.9-second period, due to the manner in which the experiment measures solar X-ray bursts. The measurements are collected from the rotating wheel of the OSO spacecraft by sampling the solar burst for 0.19 seconds during every period of revolution of 1.91 seconds. It is therefore possible that the 26.9-second period is a beat period between a shorter period and the sampling period of 1.91 seconds. If this is the case, then the shorter period could be 2.0 or 1.8 seconds. The period of the radio oscillations is 1.8 seconds. That the radio and X-ray periods are so close is disturbing in that one would not intuitively expect the lower-lying flux tube responsible for the X-ray modulation to oscillate with nearly the same period as a flux tube in the corona.

The mechanism responsible for the modulation of the X-ray burst in different in one respect from that presented for the radio modulation. Since the X-radiation is produced by bremsstrahlung it is most likely the increase and decrease in density which takes place within the oscillating flux tube that accounts for the X-ray modulation and not the magnetic field variations.

The X-ray pulsations occur about 15 minutes earlier than the 140 MHz pulsations. We assume that this delay is the travel time of the shock front from the level of X-ray flux tube to that of the radio. With the additional assumption that the X-ray and radio flux tubes are at 1 and 1.5 solar radii, respectively, then the velocity of the shock front calculates to be 580 km/sec. This value is well within the range of the distribution of shock front velocities.

We have no satisfactory explanation for why the X-ray pulsations appear distinctly only in the highest energy channel.
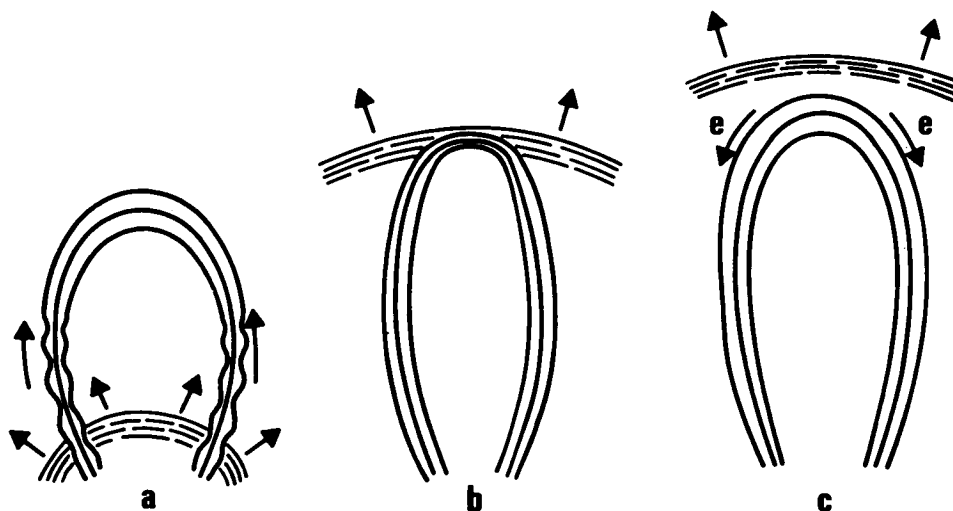
Figure 2. The three diagrams represent successive stages of the upward expansion of a shock wave and its interaction with a discrete magnetic flux tube (after D. J. McLean et al.).
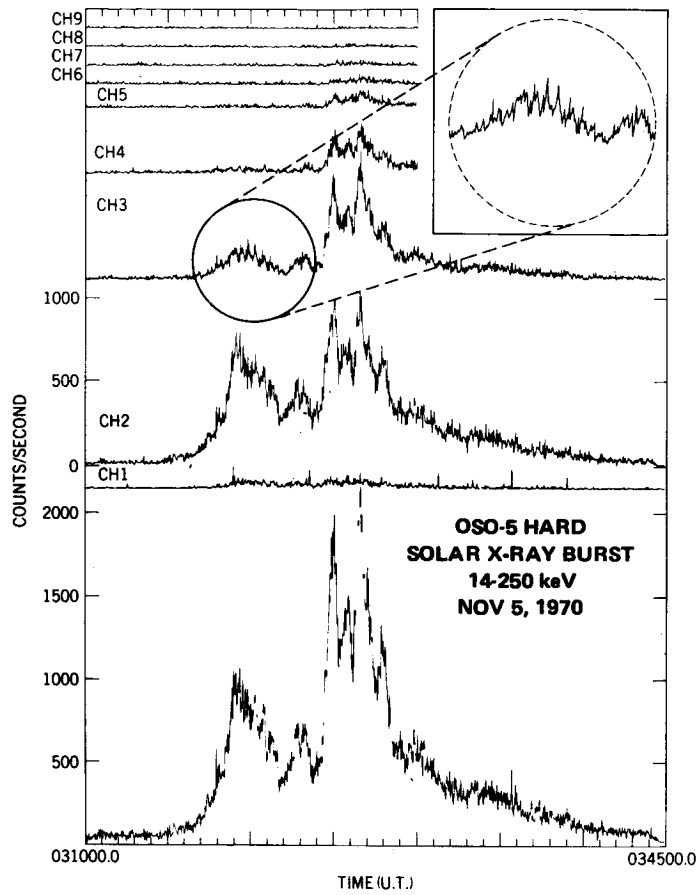
Figure 3. OSO-5 hard solar X-ray burst, 14-250 keV,
November 5, 1970.

52

CULGOORA , AUSTRALIA   140 MHz

03ʰ 35ᵐ   03ʰ 40ᵐ
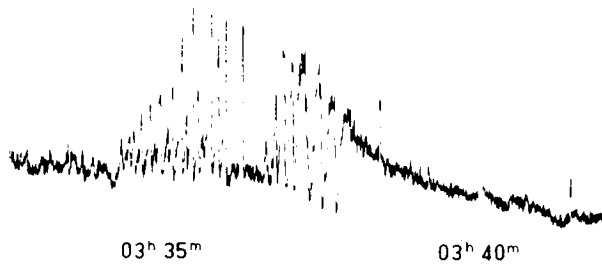
NOBEYAMA , JAPAN   160 MHz

03ʰ 35ᵐ   03ʰ 40ᵐ   03ʰ 45ᵐ
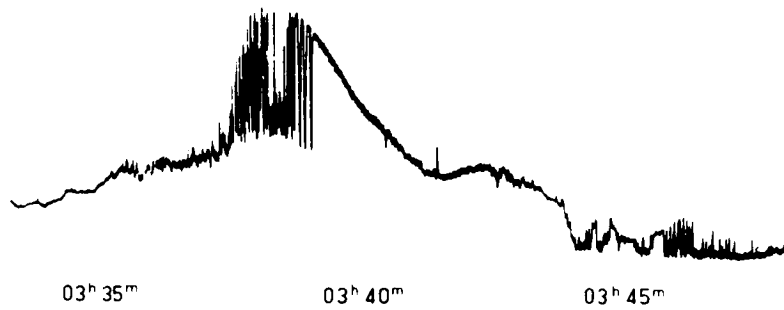
Courtesy Paul Wild

Figure 4. Power spectrum analysis.

53

SPATIAL STRUCTURE OF A TWO-PHASE SOLAR FLARE
OBSERVED IN THE EUV BY OSO-7

Roger J. Thomas

The Goddard experiment on OSO-7 is a very versatile instrument with a number of observing modes available for study of different solar problems. For the flare study I'll describe today, we were in the small-raster mode of operation with a spatial resolution of 13 by 20 arc seconds.

Figure 1 is an Hα photo of the sun made at the Goddard optical site some time before the launch of OSO-7, but we have superimposed a box to indicate the size of the EUV maps that I'll discuss later. The maps are five arc minutes on a side, corresponding to about 218,000 km on the sun. It takes one minute to make a complete small-raster map, but we
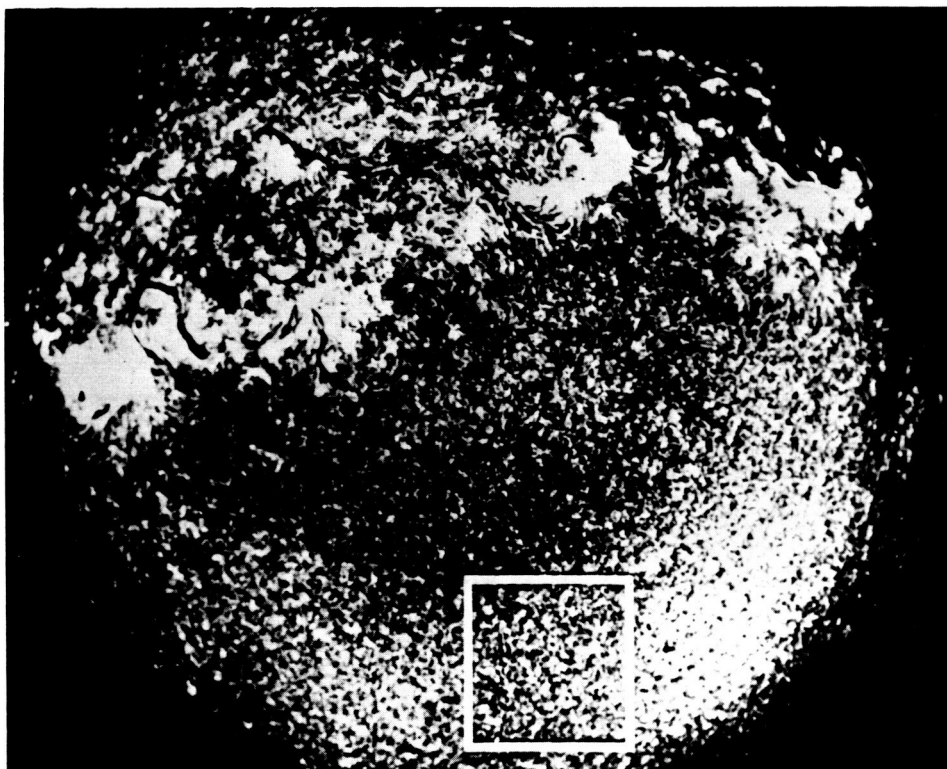
Figure 1. Hα photo of the sun. The boxed area shows the size of the EUV maps acquired by OSO-7.

have four data channels, so that we get four maps simultaneously at four different wave-lengths each minute; and these sets of maps continue to be produced at one-minute intervals throughout the observing run.

To trace the time history of the flare studied here, we have picked off the peak intensity measured on each map and plotted these versus time, as shown in Figure 2. We can monitor a great variety of wavelengths, but at the time of this flare on February 13, 1972, we were measuring Hα and the two soft X-ray bands seen in the top three curves. These curves show the typical flare behavior — a rapid rise to maximum and a more gradual exponential decay, with good time correlation between the soft X-rays and Hα.

The fourth channel was measuring the EUV emission of Fe XI at 180Å and shows a much different time history. Seen at this wavelength, there are two distinct phases in the event, an initial rapid burst (the impulsive phase) and a more gradual component (the so-called quasi-thermal phase). These two phases are common features of hard X-ray bursts as seen by Ken Frost among others; and they have also been inferred for EUV bursts from ground-based measurements of disturbances in the earth's ionosphere. Unfortunately, such ground-based measurements can only say that this EUV emission is somewhere between ten and 1000 Ångstroms.

Our OSO-7 observations can identify the emission at a single wavelength caused by a single ionic species, Fe XI in this case. But the most powerful aspect of our instrument is that we can see where on the sun the flare emission is produced and how the emitting regions evolve with time.

As examples, I have selected three of the EUV maps in this sequence; the maps in Figure 3 were made at the start of the impulsive phase (0828 hours UT), the peak of the impulsive phase (0829 hours UT), and the peak of the gradual phase (0850 hours UT).

These are contour maps, each tone representing a certain intensity range, with the brighter areas shown by lighter tones. As the impulsive burst begins, the emission is coming from this point, but one minute later the emission site is significantly different. One possible interpretation is that we are actually seeing two different bursts during the impulsive phase, each rising and decaying more rapidly than our one-minute time resolution. We hope that some ground-based observations with higher time resolution will show whether or not there were multiple bursts at this time. The other interpretation is that there was an actual physical motion of the exciter source. If this were the case, it moved 20,000 km in one minute, corresponding to a velocity of ~ 300 km/sec. This is just the order of plasma shock velocities in the solar atmosphere mentioned by Ken Frost in the previous talk.

One problem with such an interpretation, however, is that after this initial apparent motion, the emission source remained nearly stationary at this location throughout the rest of the event, as can be seen in the map made at the maximum of the quasi-thermal phase (map at lower right in Figure 3). This has some important implications for solar flare models. Frost has shown that there must be two distinct particle acceleration mechanisms responsible for
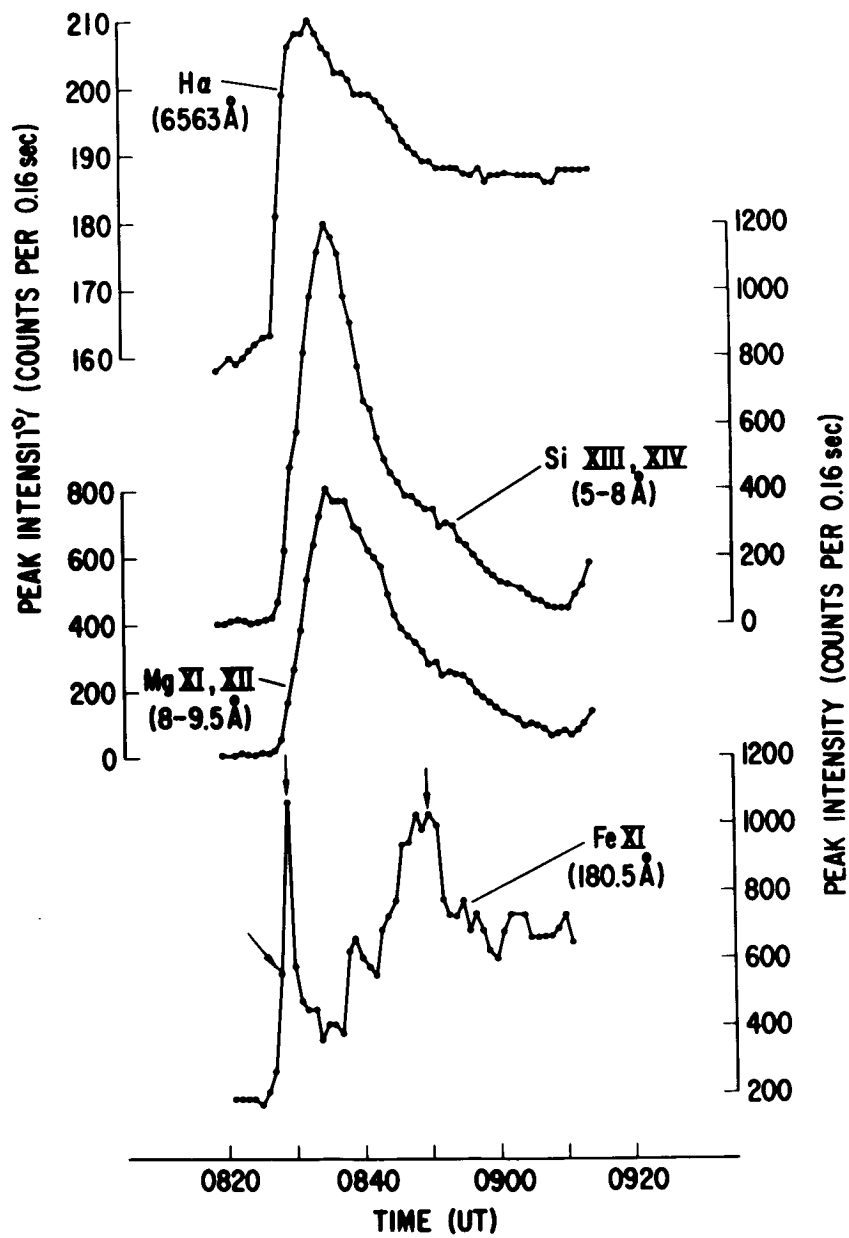
Figure 2. OSO-7 flare observations of February 13, 1972.

these two phases, yet our observations show they occur at the same location. This suggests that the same volume in the solar flare must be capable of producing both types of accelerations. That will be a very stringent requirement for future solar flare models to satisfy.
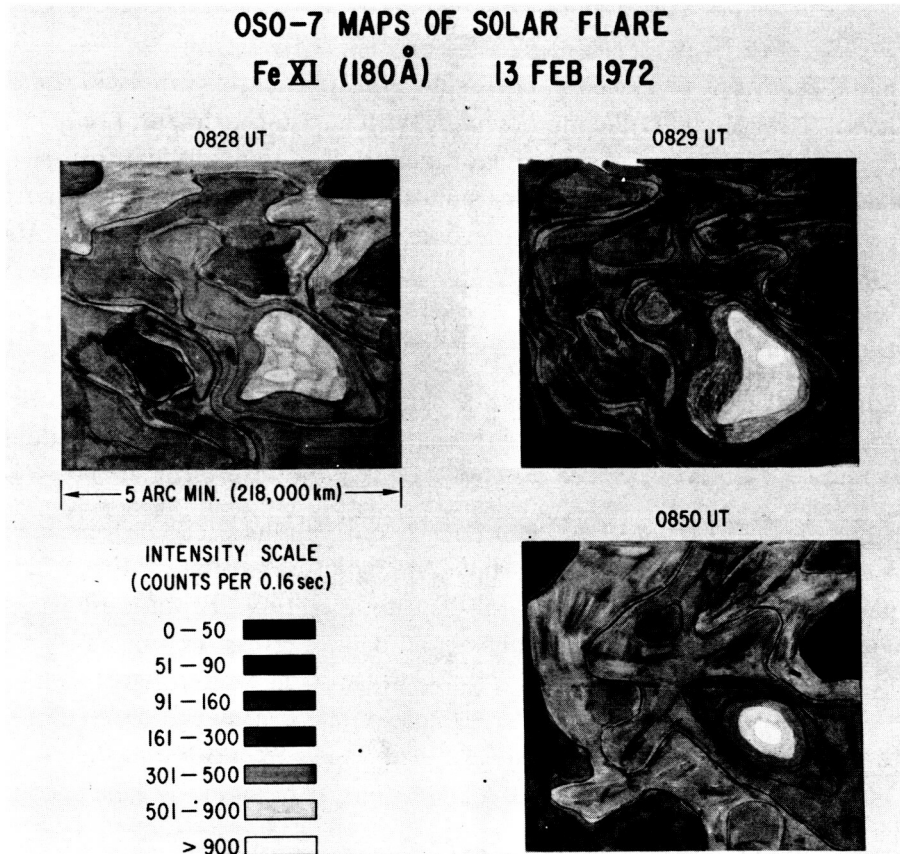

Figure 3. OSO-7 maps of solar flare activity of February 13, 1972. The sensor was measuring EUV emission of Fe XI at 180Å·

GROUND-BASED FLARE STUDIES AT SACRAMENTO PEAK

Stephen P. Maran

For more than a year now, we have operated a novel instrumental system on Sacramento Peak, at Sunspot, New Mexico. We are observing with a 35.6-centimeter (14 in) vacuum solar telescope and a multichannel spectrophotometer. The two key features are the ability to make photoelectric measurements simultaneously at up to 40 wavelengths and the high time resolution, which is 200 milliseconds for the complete system, or 100 milliseconds when up to 20 channels are recorded. The spatial resolution is adjustable and can be as fine as 1 arc second. The wavelengths covered range from 3200 to 10,830 Angstroms, with resolutions from 0.02 to 0.25 of an Angstrom.

We are conducting a variety of observational programs. This past week, for example, we observed an active region in conjunction with related measurements by the Goddard OSO-7 experiment and by a Goddard team at the Green Bank radio interferometer.

Our chief interest is in flares, and I will concentrate on them here. Some years ago, Svestka gave an interesting argument for small-scale structures in flares. From flare spectra, he derived parameters such as electron density and temperature. From these parameters, he calculated the intensity of the continuum at the Balmer limit. This intensity was sufficient, so that the continuum should be detectable in emission even in flares seen against the solar disk. But to quote Svestka, "No . . . emission has ever been observed in the Balmer continuum in the flares on the disk, although the spectra of more than 60 such flares were photographed at Ondrejov, and many others were taken by flare spectrographs at other solar observatories."

He concluded that flare emission actually comes from small knots or filaments, finer than the available spatial resolution, so that the radiating volume is smaller than assumed, and thus the Balmer continuum emission is lower than calculated.

Many lines of evidence now support the concept of small-scale structures in flares, including the so-called "flare points." We have observed an isolated flare point; it possesses in miniature the characteristics of a true flare event.

Figure 1 shows the flare point data, recorded on October 22, 1971, by Gabriel Epstein. At first, we dismissed this as a 30-second instrumental glitch. But correspondence with three other groups established its reality:

- Lockheed Hα patrol photos for the time of our event show a tiny bright spot at the projected solar location of our spectrograph entrance slit. The bright spot lasted less than 30 seconds.
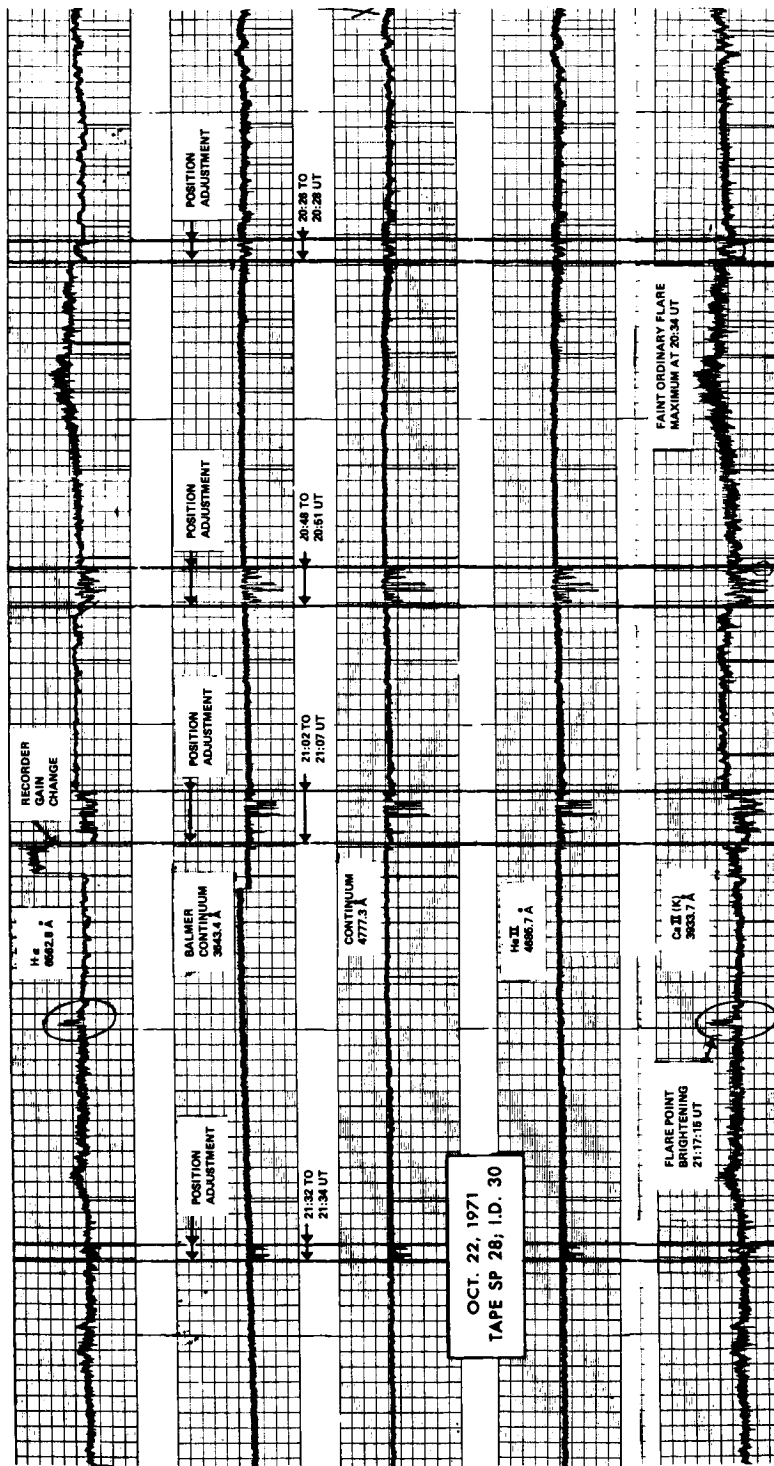
Figure 1. Solar flare-point data recorded on October 22, 1971.

- Colorado radio data show a Type-III solar burst, coincident to within 1 second with the onset of our flare point.

- State University of Iowa Explorer-35 measurements show a soft X-ray burst peaking at the time of this event.

If this is a true flare-like process, it can't be explained by electromagnetic models. For example, the calculated ohmic dissipation times are of order tens of minutes for flares of size only tens of kilometers.

Figure 2 shows our slit-jaw photos of the great flare of August 7, 1972. Figure 3 shows some of our data on this flare. We recognize some unique phenomena. First, two impulsive events, visible in many wavelengths, each lasting only some five seconds, occurred around 1521 hours UT. Second, at 1519 hours UT, there is a considerable increase in the red wing of the Ca II K-line, with no corresponding increase in Hα. The emission at 1521 hours UT, at wavelength 3645 Angstroms in the Balmer continuum, has been shown by H. P. Jones of Goddard to be attributable to line radiation, primarily by neutral iron.

60
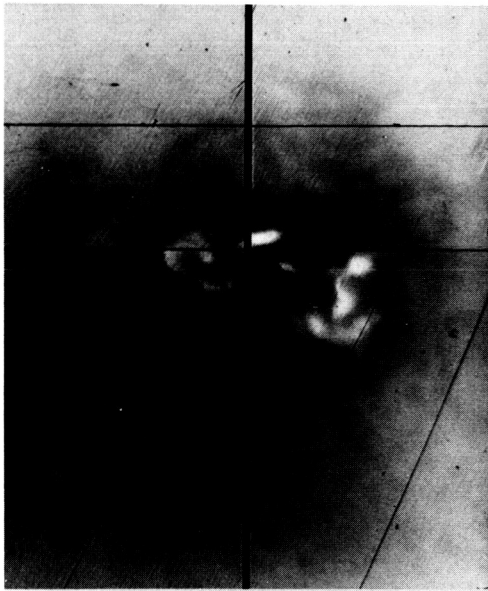
Approx. 15:12:00 UT
Beginning of Flare
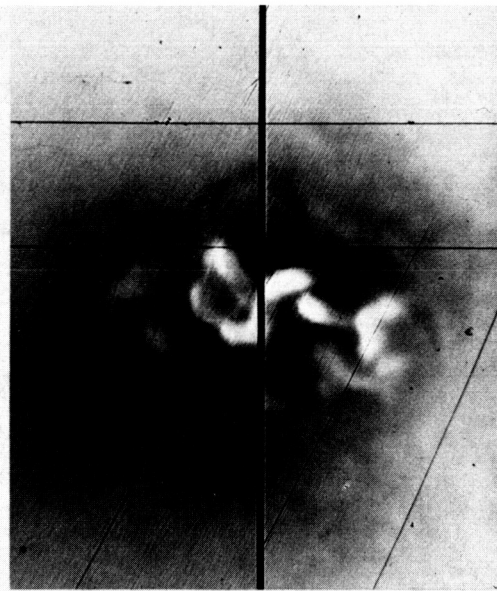
15:17:00 UT
Moved to Flare Region

15:19:00 UT
Peak in CaⅡ K

15:28:00 UT
Flare Maximum

Figure 2. Solar flare of August 7, 1972.

λ3645.2 Fel, Col, ScII

λ3679.8 Fel

λ4778.6 CONTIN.

λ5877.1

λ3934.9 CAII-K+1.2Å

λ6564.6 H-ALPHA+1.8Å

TIME

15 14 58   10 sec   15 22 57
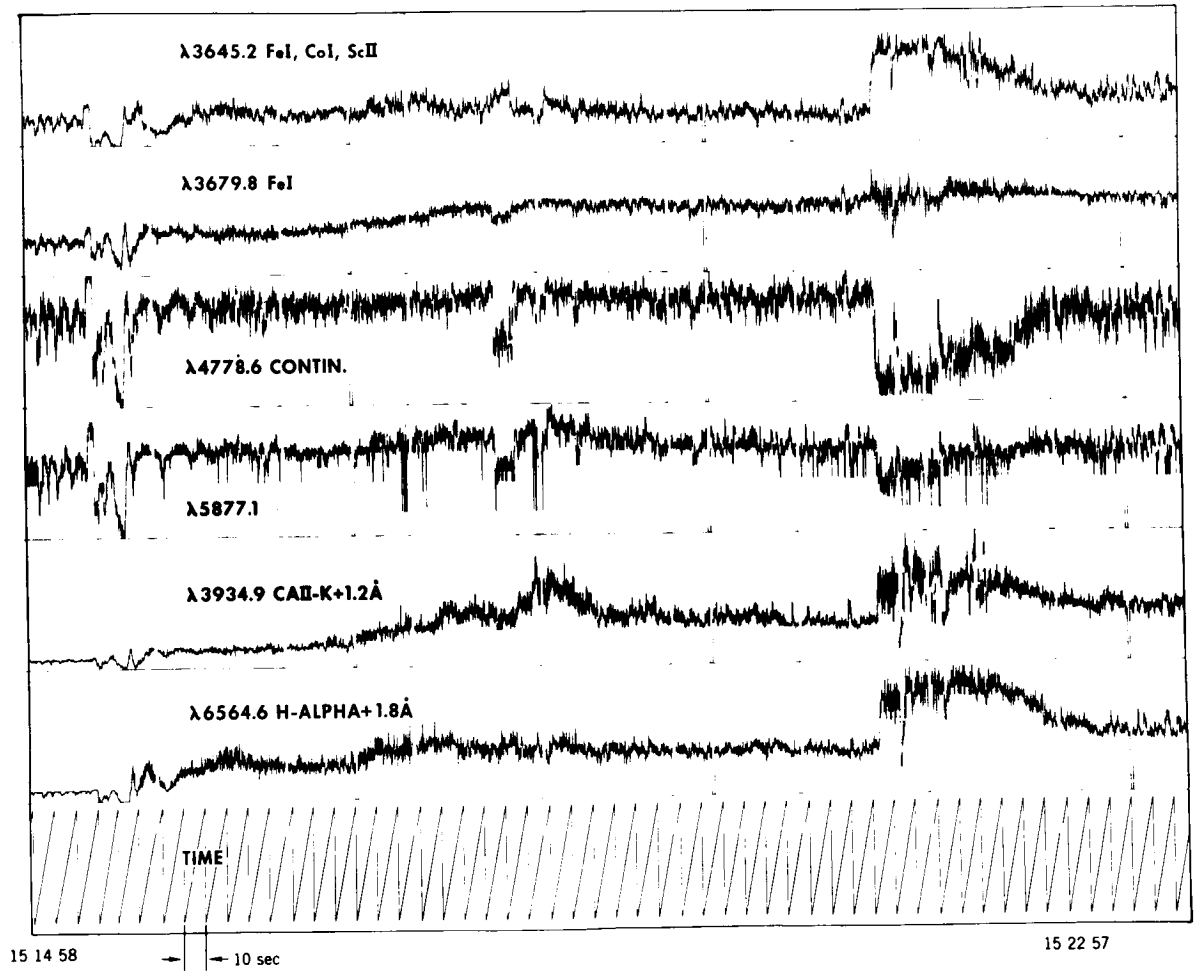
Figure 3. Data for the flare in Figure 2.

62

THE STUDY OF SOLAR FLARES
DURING THE NEXT SUNSPOT MAXIMUM

John C. Brandt

In the last three papers, you've heard some results of recent Goddard Space Flight Center sun studies. Now we'd like to give you some idea of what lies ahead for the Goddard solar program.

Solar flares are an excellent example of high-energy processes, and their origin is one of the three outstanding problems in solar physics. The other two are the heating of the sun's outer atmosphere; and the structure of the solar interior, with emphasis on the rate of neutrino production (and possible rapid rotation of an inner core).

Observations of neutrinos are not amenable to satellite treatment. The problem of the heating of the sun's outer atmosphere is a long-range problem. However, the problem of the origin and energetics of solar flares appears to be within our reach for a concentrated effort at the next solar maximum, which is estimated to be in 1979.

We need three things to tackle the comprehensive study of flare energetics and origin: First, a dedicated ground-based observatory. Second, we need access to radio telescopes such as the NRAO interferometer at Green Bank, West Virginia. We've already carried out some observations, and we can get a resolution of two or three sec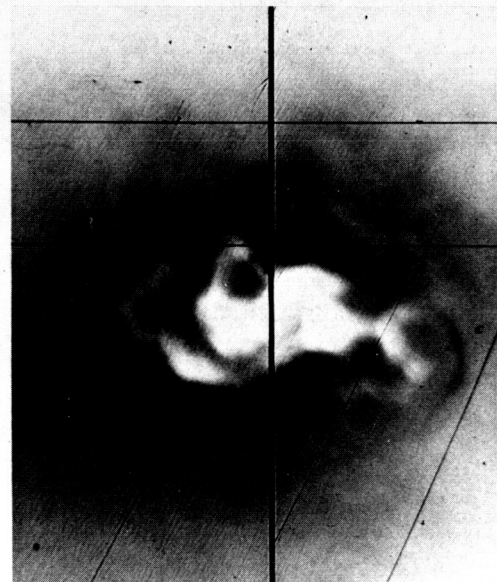onds of arc on the sun at wavelengths of two or three centimeters. This matches the kind of resolution that we can get from the ground, and the kind we can expect to get from a spacecraft such as an OSO. Finally, the point of this presentation, we need to have an OSO-K or its equivalent.

There is a problem with the schedule. Informed guesses place the next solar maximum in 1979. We would like to be up a year before maximum, and that requires a 1978 launch. If I understand the current schedules for the Shuttle correctly, we cannot utilize the capabilities of the Shuttle to study solar flares at the next maximum. If we miss the next maximum, we must wait until approximately 1990.

In Figure 1, we've summarized some of the things that we would like to do in the study of solar flares. We'd like to focus on the hot component of the flare. Nearly everyone believes that there is a primary energetic event. It's nature is unknown, but it determines or produces a small volume of energetic plasma, which then interacts with the rest of the solar atmosphere to produce effects that reach all the way out to the earth. We would like to know how the solar atmosphere evolves in response to flares. We would like to know the structure or topology of the energetic plasma along with the energy and anisotropy of the nonthermal electron and protron streams.

```
                    SCIENTIFIC GOALS FOR OSO-K

A)   Prime Objective - Investigate the cause and nature of solar flares

     Emphasize the hot component of the flare

          -determine the physical state (temperature, density, velocities, etc.) as a
           function of time and space

          -determine the structure, energy, and anisotropy of the non-thermal electron
           and proton streams

     Check the solar magnetic field as a flare energy source

          -determine the chromospheric and coronal magnetic fields from OSO-K

          -determine the photospheric magnetic field from ground-based observations


B)   Secondary Objective - Investigate solar flare effects

     Heating of the chromosphere

     Solar-terrestrial relationships
```

Figure 1. Scientific goals for OSO-K.

```
            OSO-K/SOLAR FLARE MISSION STUDY GROUP


     Harold V. Argo, Los Alamos Scientific Laboratories

     Jacques M. Beckers, Sacramento Peak Observatory

     John C. Brandt, Goddard Space Flight Center (Chairman)

     Elmo C. Bruner, University of Colorado

     Kenneth J. Frost, Goddard Space Flight Center

     Gordon Garmire, California Institute of Technology

     Fred T. Haddock, University of Michigan

     Charles L. Hyder, Goddard Space Flight Center

     John T. Jefferies, University of Hawaii

     Robert Liefeld, New Mexico State University

     A. Keith Pierce, Kitt Peak National Observatory

     Peter A. Sturrock, Stanford University

     Einar Tandberg-Hanssen, High Altitude Observatory

     Arthur B. C. Walker, The Aerospace Corporation
```

Figure 2. Members of the OSO-K Solar Flare
Mission Study Group.

The solar magnetic field has been blamed as the energy source of solar flares for quite some time, but I don't believe that really convincing evidence exists. Certainly it could be the source, and one of the ways to try to disprove or prove this hypothesis would be to measure the magnetic fields directly in the chromosphere and corona. If we can measure them simultaneously in the photosphere, and if the magnetic field is responsible for solar flares, we should be able to obtain observational proof.

An instrument that will attack the major problems listed here will certainly have enough structural resolution to tackle other problems such as the heating of the chromosphere.

A group called the OSO-K Solar Flare Mission Study Group was formed and the people involved are listed in Figure 2. I believe that we have a wide representation throughout the scientific community. We met four times: in April, here at Goddard; in May, at the University of New Mexico, in Albuquerque; in July, at Los Alamos, New Mexico; and in September, in Stanford, California. These four meetings were used to iterate what we wanted to do, and the kind of instrument that would do it—one that would fly on the spacecraft but not cost 10 percent of the Gross National Product. All these meetings were attended by John Donnelly of the OSO Project, so that we would not suggest something that was never going to be. The resulting instrument package is shown in Figures 3 and 4.

In Figure 3 we give a descriptive name for the instrument, the spectral range, the energy or wavelength resolution, and the spatial resolution. We also describe the field of view (if it is not exactly the same as the spatial resolution), and the time required to make a significant measurement.

We need a flare finder on the spacecraft to make decisions concerning the flare locations on the sun. There is no way you can relay information down to the ground to make the decision. The rise times of hard X-rays are on the order of one second or less. There is no way around that, and so we need a simple imaging device. It can even be a pinhole camera that works in the wavelength range from 1 to 15 Angstroms and provides an image of the sun. The instrument locates the flare, generates error signals, and drives the pointed section to the flare location.

The low-energy polarimeter is intended to look for impact polarization. The instrument observes a group of lines simultaneously and the observations give us the energy and anisotropy of the exciting stream of electrons. The medium-energy polarimeter is intended to measure the total polarization in this energy range. The X-ray spectrometer is intended to do line profiles, and we believe that we can do them quite well. The ultraviolet magnetometer-spectrometer utilizes several lines of multiply-ionized iron in this wavelength range to determine the coronal magnetic field. The chromospheric magnetic field can be determined from lines of nitrogen. The instrument would be similar to the ultraviolet spectrometer that The University of Colorado has on OSO-I, but with a magnesium fluoride quarterwave plate. Now, this instrument can also operate as a spectrometer and produce excellent line profiles in this wavelength range.

The EUV spectrometer covers the wavelength range that contains the iron lines; it can also do profiles of the helium lines and various kinds of coronal diagnostics. The H-alpha photometer must be included on the spacecraft so that we are absolutely sure of our location on the sun. It is, in essence, a spatial template. The hard X-ray imaging experiment is a device that will give us the topology of the flare emission directly—in the hard wavelengths themselves. The UV spectrometer covers the wavelength range of 500 to 1500 Angstroms. This range provides all the information that a theorist would need to calculate the properties of the solar atmosphere based on the diagnostics of the hydrogen atom; of course, there are a lot of other possibilities in that wavelength range.

All of these instruments, believe it or not, will fit in the pointed section of an Orbiting Space Observatory.

Figure 4 shows the instruments that do not require precise pointing, and so may be located on the OSO sail. We would like to put on the sail a hard X-ray spectrometer, which will provide us with continual polarization measurements. Next, we have a cooled solid-state detector. This instrument observes the entire sun and produces continuum measurements. The energy range overlaps the medium energy polarimeter, but with high time resolution.

Two other experiments can be placed in the wheel of OSO. One is a gamma-ray instrument. When we began this study, solar gamma rays were something that existed in theoretical papers and nowhere else. But since that time, gamma ray lines have been detected in the flares of the first week of August 1972. Now we have some observations on which the experiment can be based.

Finally, if we can commit two compartments on the satellite, it will be possible to include a neutron detector that will be more sensitive by a factor of 100 than any neutron detector that has flown to date. Hopefully, one might detect neutrons. There's no time resolution for that—you either detect neutrons or you don't.

To run this package one has to have an onboard computer to process the data from the flare finder and generate the command signals for the spacecraft. Of course, we anticipate many other uses for the computer, such as data compression. We actually have a specific computer in mind. This is the CDC-469, which we understand is being qualified for flight hardware, and should be available long before we need it.

In summary, we have generated an instrument package which has rather high time resolution in almost all of the individual instruments and runs almost the entire gamut of the types of measurements that one would like to make. The one exception is a white light coronagraph, which would require the deletion of four or five other experiments. In our judgment, a coronagraph would not contribute efficiently and directly to the study of hot plasma part of the flare, or to answering the basic questions of flare energetics.

One of the political aspects of any kind of study of this nature concerns the mode of operation of such a facility. Our consensus is that it should be operated essentially as a national facility or national observatory—sort of a solar Kitt Peak in the sky. Perhaps one

Instrument	Range	E/δE or λ/δλ	Resolution	Field	δt
Flare Finder	1-15Å	3-5	10"	Full Sun	0.1 sec. (for 5' x 5')
Low Energy Polarimeter	1-20Å	$\sim 10^3$	10-30"	-	3 sec.
Med. Energy Polarimeter	10-50 keV	5-10	-	-	10 sec.
X-Ray Spectrometer	1-25Å	$3 \times 10^3 - 3 \times 10^4$	5-20"	-	0.1 sec.
UV Magnetometer-Spectrometer	1100-2200Å	$3 \times 10^4 - 10^5$	2-15"	-	1 sec. (for 300 gauss)
EUV Spectrometer	20-700Å	$3 \times 10^3 - 3 \times 10^4$	2"	-	0.5 sec. (for 1 line profile)
H-α Photometer	6563Å	10^4	2"	5' x 5'	0.1 sec.
Hard X-Ray Imaging	10-80 keV	10	4"	Full Sun	30 sec.
UV Spectrometer	500-1500Å	$3 \times 10^3 - 10^4$	2"	-	10 sec. (for 100Å)

Figure 3. Pointed instruments for the OSO-K solar flare instrument package.

Instrument	Range	E/δE or λ/δλ	Resolution	Field	δt
Hard X-Ray Spectrometer	10-500 keV	2-5	-	-	0.1 sec.
Passively Cooled Solid-State Detector	1-20 keV	5-50	-	-	0.3 sec.
WHEEL INSTRUMENTS					
Instrument	Range	E/δE or λ/δλ	Resolution	Field	δt
"Gamma Ray" Instrument	300 keV - 10 Mev	7-20	-	-	1 min (continuum) 10 min (lines)
Neutron Detector	10-100 Mev	5	-	-	-
Computer					

Figure 4. Sail and wheel instruments for the OSO-K solar flare instrument package.

could also adopt the Kitt Peak formula of 60 percent of the observing time for guest investigators and 40 percent for the groups that built the facility.

Specifically, we will recommend in our report that a substantial guest investigator program be set up, and that guest investigators be funded. The mode of operation would involve a guest investigator coming to the control center, presumably here at Goddard, and at that time, the person would have the entire spacecraft at his disposal to carry out his observing program. If the observer desires, we envision that supporting observations at Sacramento Peak (with the spectrometer) and at suitable radio observatories would be available at the same time. About a week of such observing, with a little bit of luck, would keep a solar group busy reducing and interpreting the data for quite some time.

We are working quite hard on the report of this study group, but progress has been much slower than I had anticipated. Our goal is to stimulate an AFO, essentially along the lines that we have outlined, and we cannot avoid the issue of cost. I cannot give you a dollar value today, but we have put considerable thought into the problem. We believe that the solar flare mission can be done at a reasonable cost, if we make cost a prime consideration.

SECTION II

OPTICAL AND UV ASTRONOMY

OVERVIEW

Anne B. Underhill

Optical Astronomy, what is it? It is a study of stars and other astronomical objects by means of the radiation emitted in the range of 1000 to 10,000 Angstroms. This range is limited by available techniques. It is a homogeneous range so far as physics is concerned.

Figure 1 shows the three types of work carried out by optical astronomers. You can sort objects into classes of similar properties — spectrum classification; you can use the energy stream from the object to deduce the physical properties of the object — astrophysical studies; or you can put together information about the distribution in space and the physical properties of individual objects, to develop a grand view of the formation and evolution of the universe.

1. SPECTRAL CLASSIFICATION

2. ASTROPHYSICAL STUDIES

3. EVOLUTION OF THE UNIVERSE

Figure 1. Optical astronomy — the types of work.

The plan of attack we use is four-pronged, as shown in Figure 2. Instruments are developed to collect starlight at all wavelengths in the optical band and, by using appropriate dispersing and detecting devices, to record the spectral intensity distribution for typical stars. We develop methods of data processing so that the information in the recorded signal can be extracted.

Secondly, we must select characteristic stars for unraveling key problems, and we must observe significant parts of their spectrum. Two areas are important: the recognition of key problems in the physics of stars, and the recognition of which are the key parts of the spectrum for the solution of any particular problem.

The third part of our attack is to study the distribution of the various star classes in our galaxy and other galaxies in order to obtain an understanding of the universe.

And fourthly, we study the composition and physical state of interstellar material. Such study is fundamental, for interstellar material is a fluid from which stars are made and to which stars gradually return.

INSTRUMENTATION AND DATA ANALYSIS

KEY PROBLEMS IN STARS

GALACTIC STRUCTURE

INTER-STELLAR MATERIAL

Figure 2. The optical astronomer's plan of attack.

Figure 3 shows the Goddard program which is to study the physics of the stars and other astronomical objects. We record in detail the spectra from these objects over as much of the optical range as possible. We do this by using 91- and 150-centimeter (36- and 60-in) ground-based telescopes, with spectrographs and spectrum scanners equipped with the newest of detectors to record from 3300 to 10,000 Angstroms. We do it by building rocket payloads to obtain high and moderate resolution spectra of stars from 1000 to 3000

USE GROUND-BASED TELESCOPES

BUILD AND USE ROCKET PAYLOADS

DESIGN AND USE SATELLITES

DEVELOP THEORY OF STELLAR SPECTRA

Figure 3. The GSFC optical astronomy program.

Angstroms; by designing satellites which carry telescopes and various analytic instruments; and by developing theory to explain stellar spectra.

The Goddard Astronomical Satellite Program includes the GEP, which is a 94-centimeter telescope and scanning spectrometer, the prototype of which is now in storage, awaiting a suitable carrier satellite, perhaps the Space Shuttle in a sortie mode.

Plans for new instruments include the International Ultraviolet Explorer (IUE), which is a 45-centimeter telescope, followed by high and low resolution spectrographs; and the Large Space Telescope (LST) which is a 3-meter telescope that feeds diffraction-limited cameras and spectrographs.

At present, observations of stellar spectra are being actively made with ground-based equipment, rocket payloads, and the Orbiting Astrophysical Observatory (OAO-2). You will hear some of the results.

In addition, theoretical studies are being pursued to determine what a stellar spectrum means. At the same time, an active part is being taken in the design of suitable astronomical instruments for the IUE and for LST. These will be reviewed later.

Thus the work of understanding stars is going forward on all fronts. Stars are central to our studies, for they create most of the optical radiation in the universe. Radiant energy is created from mass in the centers of stars. This energy then works its way out through the condensed gas which forms a stellar interior until it can come to us as the light from a star.

This light forms a spectrum composed chiefly of absorption lines on a continuous background, with a few emission lines. The modulation pattern impressed on the light carries information about the outer layers of the stars and of the interstellar material through which the light has passed.

Optical astronomy is concerned with observing this pattern over the optical wavelength band, and with deducing what stars are like, what they are doing either singly, in binary systems, or in groups.

One can also deduce information about the interstellar medium. In one sense, the interstellar medium is the basic material of the universe, and the stars can be considered merely devices for processing interstellar material. Such a view is, however, extreme.

Stars are very diverse in their characteristics, and just because of this, they are fascinating objects to study. Their interaction with the interstellar medium is one of our areas of research.

Now let us look at a stellar spectrum (Figure 4). This shows a typical stellar spectrum from 1150Å to 6000Å with the flux received at the surface of the earth plotted against wavelength. The flux is in units of ten to the minus-ten ergs per square centimeter per second.
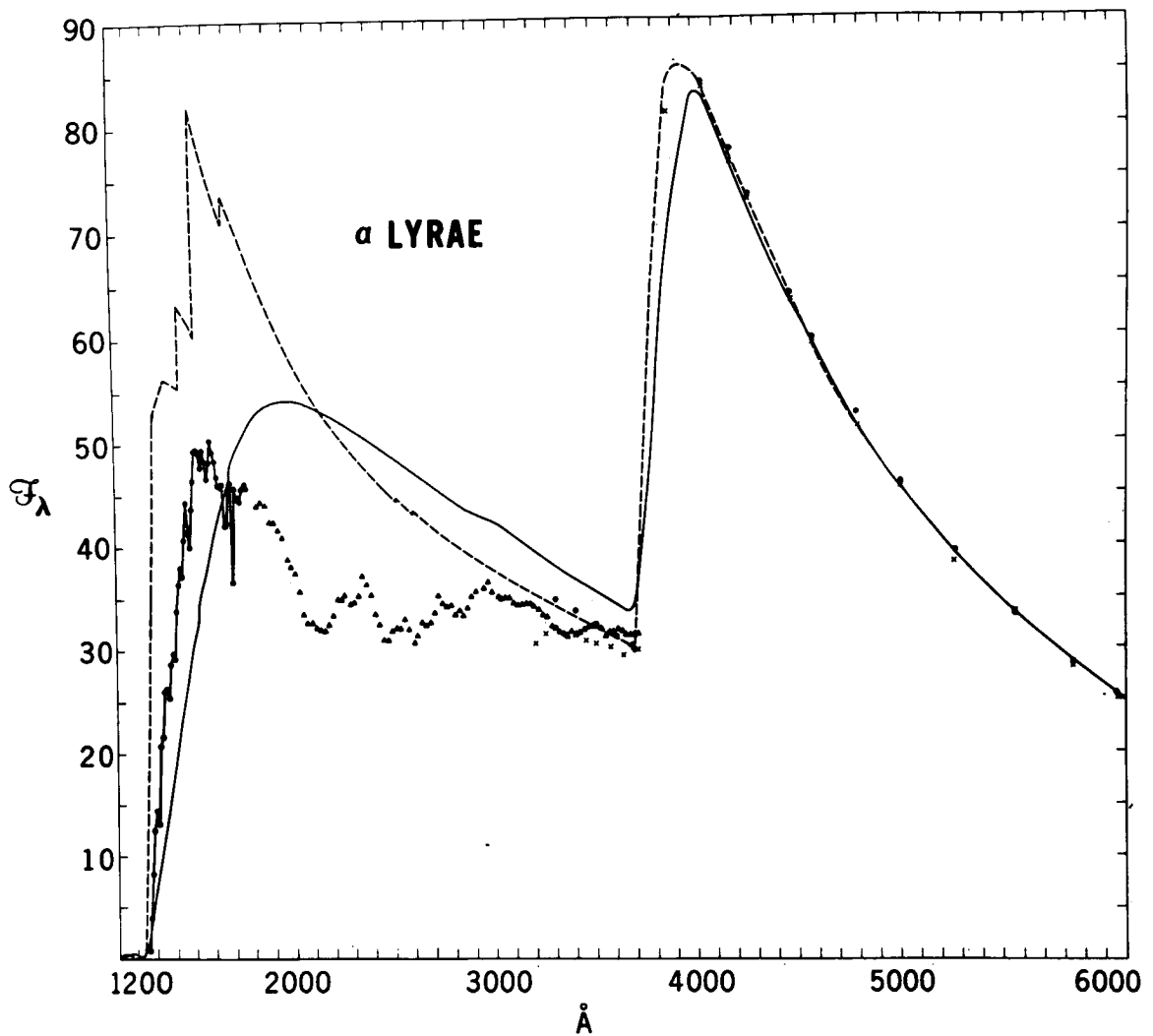
Figure 4. A stellar spectrum.

The observations from 1150 to 3600 Angstroms are made from OAO-2 spectrum scans which have been put on an absolute energy scale by comparison with absolute energy scans made by Dennis Evans, using a calibrated spectrum scanner, launched as part of the Goddard Rocket Program.

The visible spectrum range is from published spectrum scans of Oke and Schild. The observed spectrum envelope in the ultraviolet shows many blended absorption features, which at the resolution of the OAO-2 cannot be resolved further.

Future high-resolution work such as we have planned will resolve these blends and permit more detailed study. They are due to many absorption lines, all blended together.

There are two predicted flux envelopes shown in this diagram, each of which fits the ground-based observations well, but neither of which fits the ultraviolet observations. This is an interesting point. In fact, that they are not the same is also an interesting point.

The solid line in Figure 4 is from a hydrogen line-blanketed model atmosphere by Klinglesmith. The broken line is from a fully line-blanketed model by Schild, Peterson, and Oke. It is evident that the observed ultraviolet flux distribution is not like either of these predicted flux distributions.

This discrepancy is serious, for it means that there is a systematic error in the effective temperatures, because effective temperatures, which are equivalent to the area under the curve, are generally found by fitting the visible radiation to a theoretical curve, and then integrating the theoretical curve.

As it is, the theoretical integral is 25 percent larger than the actual integral for a star such as Alpha Lyrae, which results in a 6-percent systematic error in the effective temperature.

The difference between the two theoretical flux distributions is interesting. It shows that the theoretical treatment of line blanketing poses problems. Dr. Fischel is leading a group which will study this question further. Already, a fully line-blanketed model atmosphere for Sirius has been developed which gives a flux distribution much closer to what is observed.

One final point of interest is the far ultraviolet brightness of Vega with respect to, for example, the Klinglesmith model. This seems to be a real deviation from the reference model but it is not shown by other A0 stars. It may be an indication that Vega is really a double star. This suggestion has been made before to account for the peculiarities of Vega, but it has not yet been conclusively proved.

Figure 4 gives you an idea of what the total optical spectrum of a star looks like. The detail in the far ultraviolet is what we have not yet resolved and what our future work is largely aimed towards interpreting.

ULTRAVIOLET OBSERVATIONS OF PECULIAR
B AND A STARS FROM OAO-2

David S. Leckrone

The peculiar B and A stars differ from normal stars in a number of ways. Their spectra contain greatly enhanced absorption lines of such elements as silicon, strontium, chromium, mercury, manganese, and the rare earths. Many such stars are known to possess strong magnetic fields. Frequently they are found to be too blue in color for their spectral classes, as compared to normal stars, and this latter property is one I would like to emphasize.

The effective temperature of a Si star estimated from its UBV colors, from its "blueness," may be as hot as 17,000°K. The temperature of the same star estimated from its spectral class would typically be 10- to 11,000°K. This is a huge discrepancy. The universal view is that the colors of a peculiar star correctly describe its physical properties, such as its temperature. Its spectral class—and the cooler temperature estimated therefrom—is considered to be the spurious result of an atmospheric deficiency of helium, lines of which serve as the indicators of spectral class. This idea is cause for concern because it is not at all clear how one gets rid of all that helium in the atmosphere of a presumably young, unevolved star.

The work I'm going to summarize represents the first comprehensive ultraviolet photometric survey of A_p and B_p stars. My principal aim is to determine whether the close similarity between these peculiar stars and normal B stars of like UBV colors, as observed from the ground, is maintained at wavelengths short of 3000 Angstroms, as observed from space. I've observed 24 A_p and B_p stars and 31 normal comparison stars at seven wavelengths ranging from 1430 to 4250 Angstroms, with the Wisconsin Experiment Package photometers on OAO-2. The data I'm presenting are in the form of absolute fluxes normalized to unity flux at 3320 Angstroms.

In Figure 1 are plotted photometric data in two far-ultraviolet bandpasses at 1550 and 1430 Angstroms for both normal and peculiar stars. Normalized absolute flux, in magnitude units, is plotted as a function of color index, U-V, measured from the ground. The brighter a star is in the far UV, the farther up it appears on the ordinate axis. The bluer it is in its UBV colors, the farther left it appears on the abscissa. The hotter stars fall to the left and above the cooler ones.

Normal stars are filled circles, the other symbols are various classes of peculiar B and A stars. Clearly all the peculiar stars are deficient in the ultraviolet, on this normalized flux scale, as compared to normal stars of similar UBV colors. This is directly translated into an absolute ultraviolet flux deficiency when you take into account well-known information about the absolute visual magnitudes and radii of the peculiar stars.
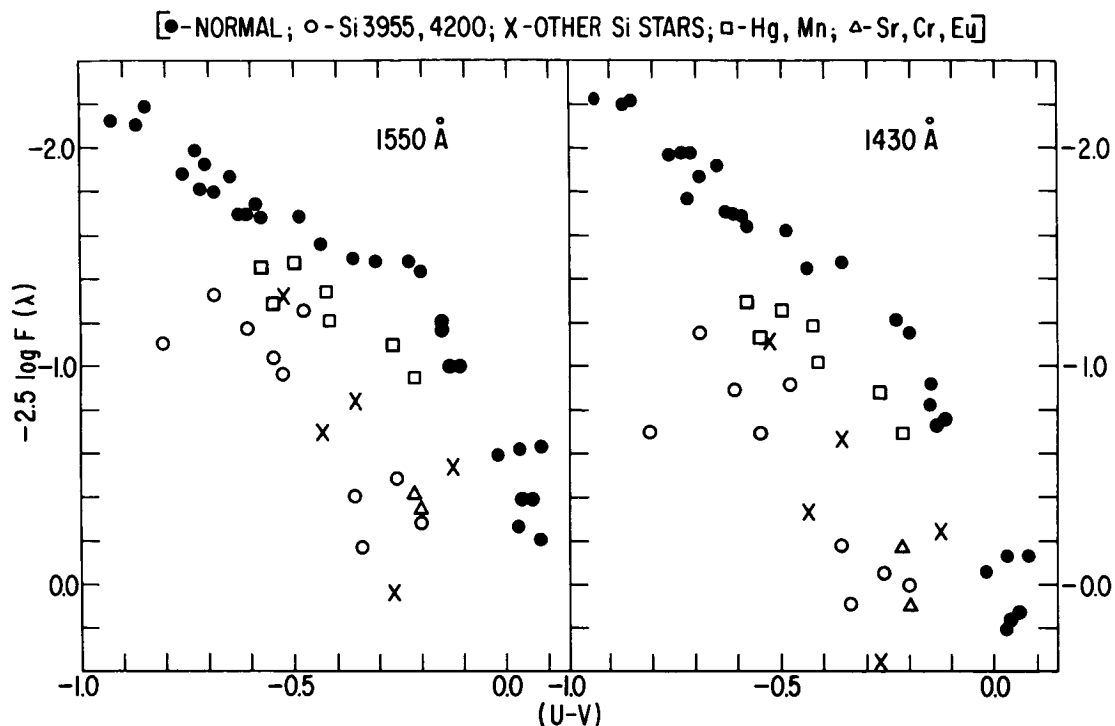
76

Figure 1. Far-UV data for both normal and peculiar stars.

In Figure 2 I've compared the gross ultraviolet flux distribution of a typical individual A_p star, 49 Cnc, with comparable data for two normal stars. Here I've plotted normalized, ized, absolute fluxes in magnitude units versus wavelength, with the normalization point shown at 3320 Angstroms. Note that in the ultraviolet the peculiar star 49 Cnc, denoted by dash-dot lines, resembles very closely the normal star γ Cnc, denoted by solid lines, and looks nothing at all like β CMi, shown by dashed lines. As you can see from the table, 49 Cnc has nearly the same UBV colors as β CMi and it has the same spectral class as γ Cnc.

In summary, the ultraviolet flux distribution of an A_p or B_p star is consistent with its spectral class, and is notably inconsistent with its UBV colors. This is exactly the opposite of what one would have expected from ground-based work prior to these observations.

In my view, the spectral classes of the peculiar B and A stars can no longer be regarded as the accidental result of an atmospheric deficiency of helium. Another mechanism must be found for suppressing the strengths of the helium lines. This may be related to an abnormal atmospheric structure in the peculiar stars, resulting perhaps from the presence of strong magnetic fields.
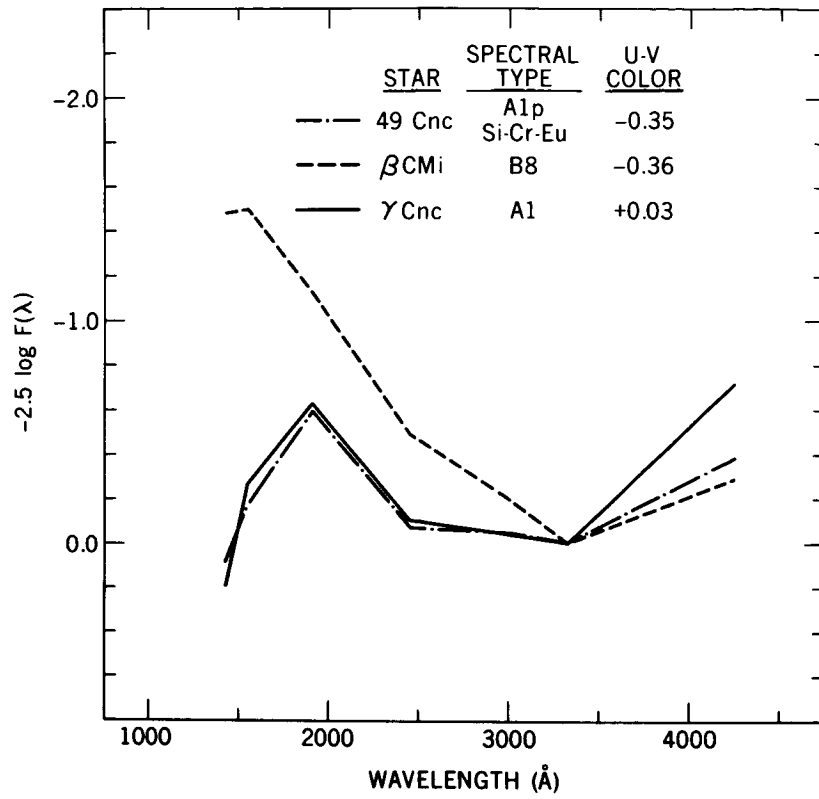
77

Figure 2. Observed stellar UV flux distributions.

UV PHOTOMETRY OF ECLIPSING VARIABLES

Stanley Sobieski

Although the study of eclipsing variables extends back into antiquity, we are currently in a period of intensive observational and theoretical activity. This has been prompted in part by the recent discovery of X-ray emitting binaries and the possibility that either neutron stars or black holes may be members of close binary systems.

By way of introduction to this discipline, let us consider a typical eclipsing variable named Rā's Al Ghūl, "changing spirit." As its name indicates, astronomers of the ancient Middle East recognized Rā's Al Ghūl as a variable object (as did the ancient Chinese).

It was John Goodricke, an 18th century deaf astronomer, who not only chronicled its variability but also conjectured that the periodic dimming of its light every 2.8 days could be caused by the interpositioning of a dark body into our line of sight, or, in a word, by eclipses. This brilliant suggestion remained a hypothesis, much ridiculed, until Vogel, a hundred years later in 1889, confirmed the orbital motion this hypothesis required by observing the doppler variations of the star's spectral lines. And this, with the star now known as Algol, began the modern-day study of eclipsing variables.

Now I will report on observations of eclipsing variables made with the most advanced instrumentation, the Wisconsin experiment aboard OAO-2. In mid-April of 1971 29 orbits were used to do photometry of the eclipsing variable CW Cephei, a binary consisting of two hot, massive stars. It was hoped that this apparently uncomplicated binary could become a touchstone for much basic stellar information. As will be seen, the ultraviolet observations revealed CW Cephei to be a system in an active stage of evolution, with evidence for stellar mass loss or mass exchange.

Figure 1 shows representative light curves. Brightness decreases downwards and the observations have been folded onto a phase scale. Primary eclipse of the hotter star occurs at phase = 0. The first indication of something unusual arose when a conventional anaylsis for an orbital solution failed when using data from both the primary and secondary eclipses. Furthermore, although not readily apparent to the eye, the shape of the secondary eclipse changes with wavelength. I have interpreted these observations to mean that mass is being lost from at least one component, and that the smaller star (the eclipsing star at primary) is surrounded by an optically thin shell of gas which emits an observable Balmer continuum.

To confirm this interpretation, spectra were obtained with the Goddard 91-centimeter (36-in) telescope, and indeed the Balmer α-line of hydrogen was observed in emission. The α-line varied in strength with the periodicity of the binary. This is positive proof for an extended gaseous envelope. As further evidence for the anomalous nature of CW Cephei,
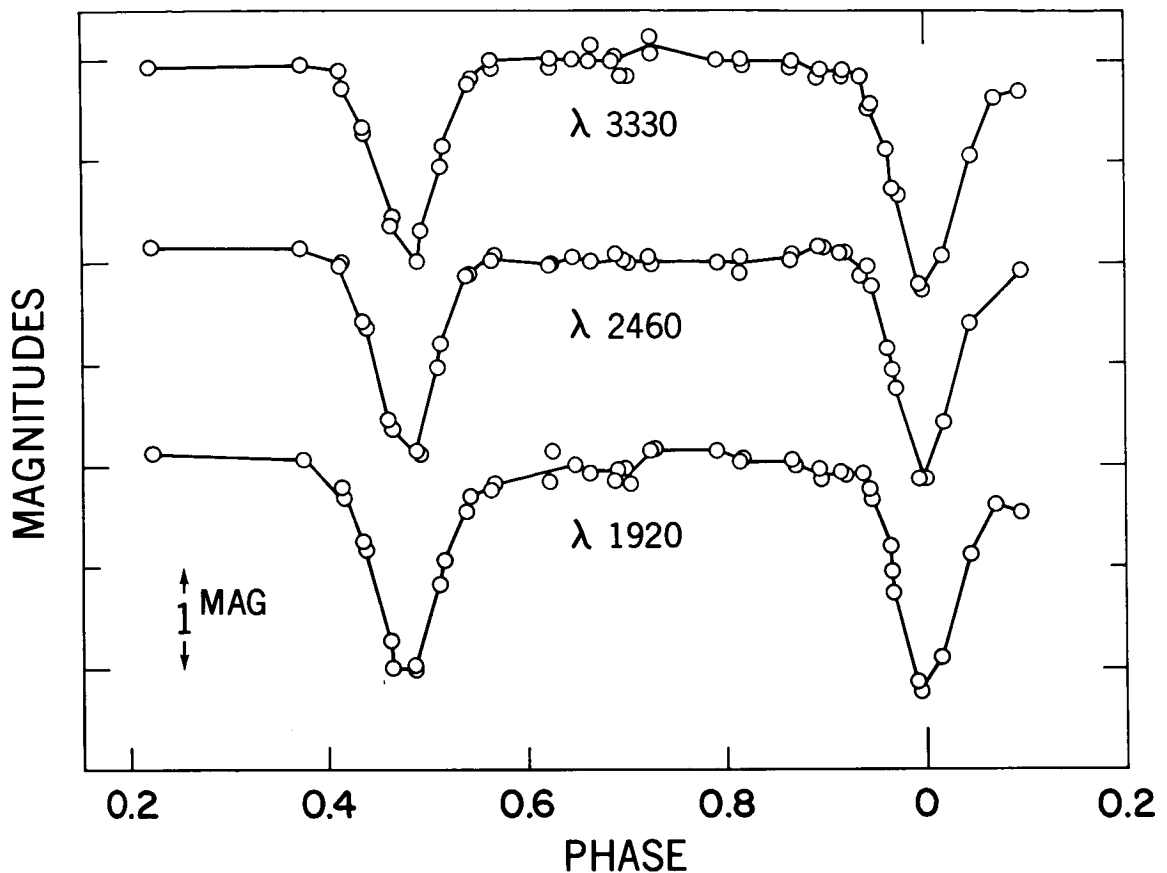
Figure 1. UV light curves plotted for CW Cephei.

the ultraviolet extinction derived from the photometry lacks the now familiar hump at 4.7 μ^{-1}. The differential extinction is quite similar to that found for θ Orionis, another young binary system, by Bless and Savage. This interesting binary is sure to be a primary target for future observations.

More recently, Dr. Heap directed the OAO-2 satellite to observe an O7 f star which had been proposed as the likely optical counterpart for an X-ray eclipsing binary found in Scorpius. This binary has been observed with the Uhuru satellite to be variable with a periodicity of approximately 3.4 days.

Figure 2 shows the data obtained with the Wisconsin photometer set at a wavelength of 1910Å. In Figure 2, photometer counts are plotted as a function of time of observation. Clearly, variability is present — the bars merely indicate the uncertainty in the background correction for scattered moonlight. Variability occurs with a minima every $1^d.9$, which is not commensurate with the X-ray period. Since no O f star is known to be intrinsically

variable, these observations of optical variability strengthen the case for identifying Uhuru X-ray source with the O f star. They also raise interesting problems concerning the nature of the object.
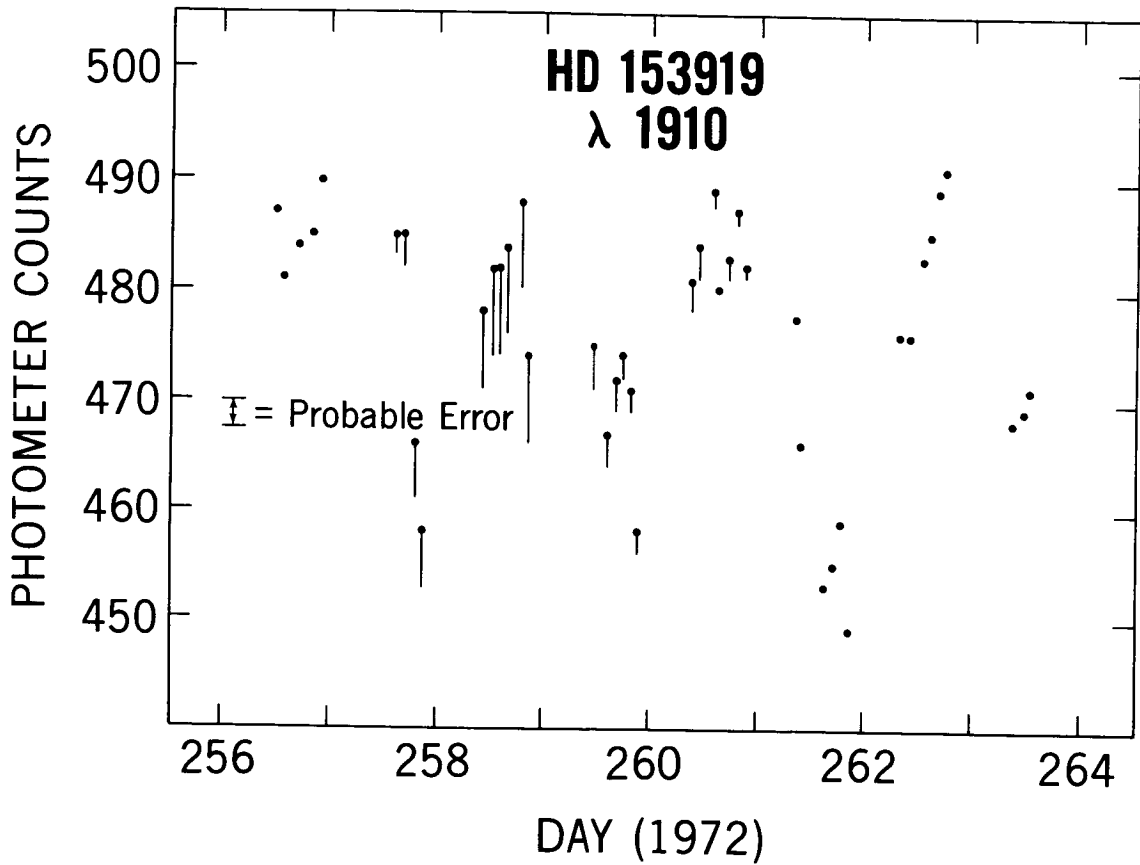

Figure 2. Data obtained from the Wisconsin photometer set at a wavelength of 1910 Å.

THE FORMATION OF PLANETARY NEBULAE

Warren M. Sparks

There are certain stars in the sky that have ejected a large fraction of their mass with low velocities to form thin gaseous spheres (Figure 1). In the early days of astronomy, viewed through small telescopes, these spheres looked like planets and were called *planetary nebulae*. This name has stuck, although these nebulae have nothing whatever to do with planets. Observations indicate that a planetary nebula is composed of hydrogen-rich material, while the remaining remnant of the star is of helium or heavier material.

The objective of my research is to find out what causes this ejection, to produce a hydro-dynamic model of the ejection, and to find out in which mass range of stars the ejection occurs. Various authors have suggested that this ejection is the result of a large luminosity causing the radiation pressure gradient to exceed the force of gravity. In order to study this mechanism we consider a model of a star consisting of a helium shell and a hydrogen-rich shell overlying a hard core. Using a time-dependent implicit hydrodynamic computer code, the luminosity from the core is slowly increased. At the lower luminosities the hydrogen-rich envelope pulsates in its fundamental mode. The pulsation period, luminosity, and effective temperature of our theoretical models agree with the observational data of long-period variable stars.

At a higher luminosity, the hydrogen-rich envelope is ejected. We define this point as time = 0. In Figure 2, the average rates of gain or loss of the various energies are plotted as functions of time. PH is the gradient of the photon flux; I is the time derivative of the internal energy, which includes ionization and excitation energies; G is the time derivative of gravitational energy; KIN is the time derivative of kinetic energy; and M is the gradient of mechanical flux.

The solid lines represent energy sources and the dashed lines energy sinks. Now although this graph appears complicated, it contains in a nutshell the rather complex behavior of planetary nebula ejection. For example, since the time derivative of the gravitational energy is always negative, we see that the envelope is always expanding. Also by looking at the dominant energy sources we can tell what causes the ejection. For example, at 10^7 seconds photon flux is the dominate energy source, with most of the energy going into internal energy. A critical event occurs at 1.4×10^7 seconds when the internal energy ceases to be a sink of energy and soon becomes the dominate energy source. Most of this internal energy is from the electron recombination of hydrogen due to the expansion and cooling of the envelope. At 1.9×10^7 seconds the photon flux gradient changes from a source to a sink of energy, that is, more radiation is flowing out of the envelope than into it. From this time on, as the envelope becomes thinner, most of the internal energy is lost from the envelope by the photon flux. As the gas decouples from the photon field,

82

the kinetic energy must become the main source for the gravitational energy. At 3.6×10^7 seconds the hydrogen-rich shell has reached escape velocity and drifts outward from the star to form a planetary nebulae like the one shown in Figure 1. The helium shell remains upon the star because of its lower opacity.

We conclude that the ejection is initiated by the photon pressure gradient, with the electron recombination of hydrogen playing an important role later on. Furthermore, planetary nebulae ejection is preceded by long-period variability.

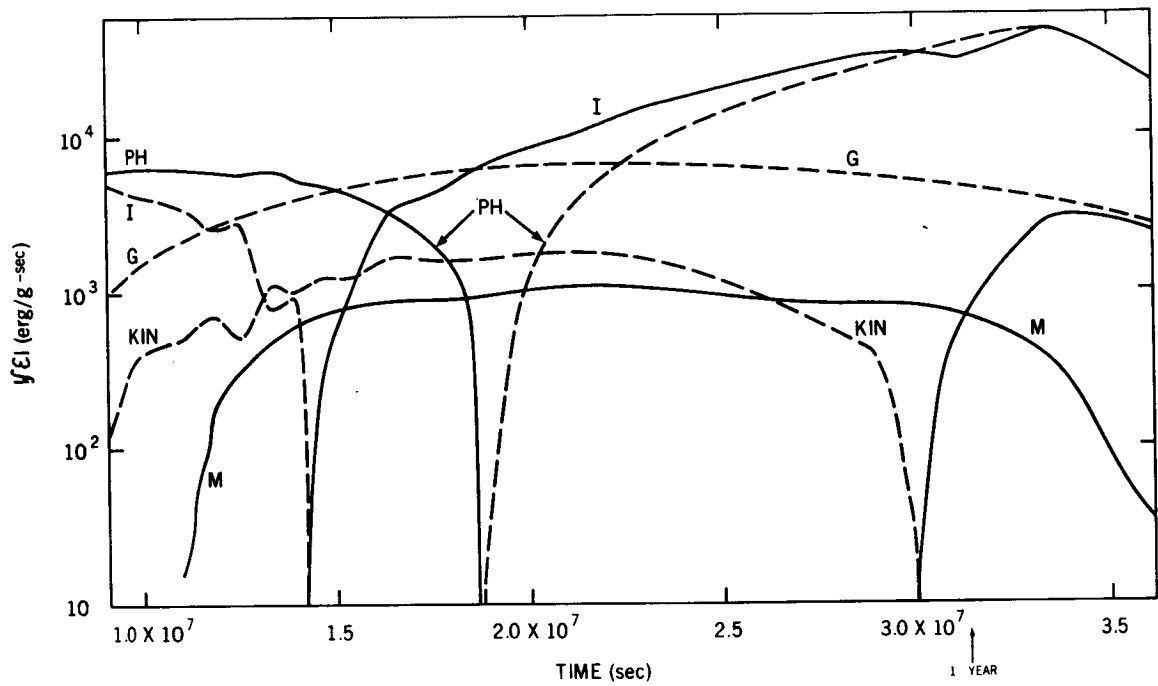
Figure 1. A typical planetary nebula

Figure 2. Graphic summation of planetary nebula ejection.

INTERSTELLAR MOLECULAR HYDROGEN OBSERVED IN
THE ULTRAVIOLET SPECTRUM OF DELTA SCORPII

Andrew M. Smith

In the recent past considerable work has been expended on the subject of interstellar molecular hydrogen. If found to be generally present in interstellar clouds, the molecule could play an important role in star formation and perhaps comprise a significant portion of the "missing dynamic moss." In addition, the molecular spectrum would reflect sensitively the temperature of the gas which included the molecules through the population of the lowest rotational levels of the ground state.

Unfortunately, the only spectral regions where there is a strong possibility of finding molecular hydrogen signatures are well away from visible wavelengths in the infrared and vacuum ultraviolet. Only one positive detection of interstellar molecular hydrogen has been reported, namely that of Carruthers.[1] In this study, a rather large (0.38) abundance ratio of atoms in molecular form to all atoms was found.

However, on June 8, 1972, using rocket techniques, an ultraviolet spectrogram of δ Sco was obtained. It exhibited ten bands of the Tyman system ($\beta\ ^1\Sigma_u^t \leftarrow X\ ^1\Sigma_g^t$) and one band of the Werner system ($C\ ^1\Pi_u^t \leftarrow X\ ^1\Sigma_g^t$) arising, presumably, in one or two clouds along the line of sight.

The results of this observation have been plotted in Figure 1 as the measured relative flux as a function of wavelength in an interval extending from 984 to 1114 Angstroms. The vertical lines show the positions of laboratory-measured lines in the Lyman and Werner bands of the hydrogen molecule. I wish to emphasize the good correlation which exists between the observed strong absorption features and the laboratory-measured line positions. I also want to point out that in general each observed band is composed of two features: The first is a blend of transitions arising from the lowest rotational level (J=0) and the first excited rotational level (J=1) of the ground state; the second is a single transition arising from the J=1 level of the ground state only. This circumstance permits one not only to determine the column density of H_2 molecules, but the cloud temperature as well.

Thus, using curve of growth techniques, and averaging the results obtained from the data associated with the Lyman bands where v' = 2, 3, 4, 7 and 8, I found an average hydrogen molecule column density of $3.5(+2.2, -0.9) \times 10^{19}\ cm^{-2}$, and an average temperature of

---

[1] G. R. Carruthers. 1970. *Ap. J. Letters,* **161**.
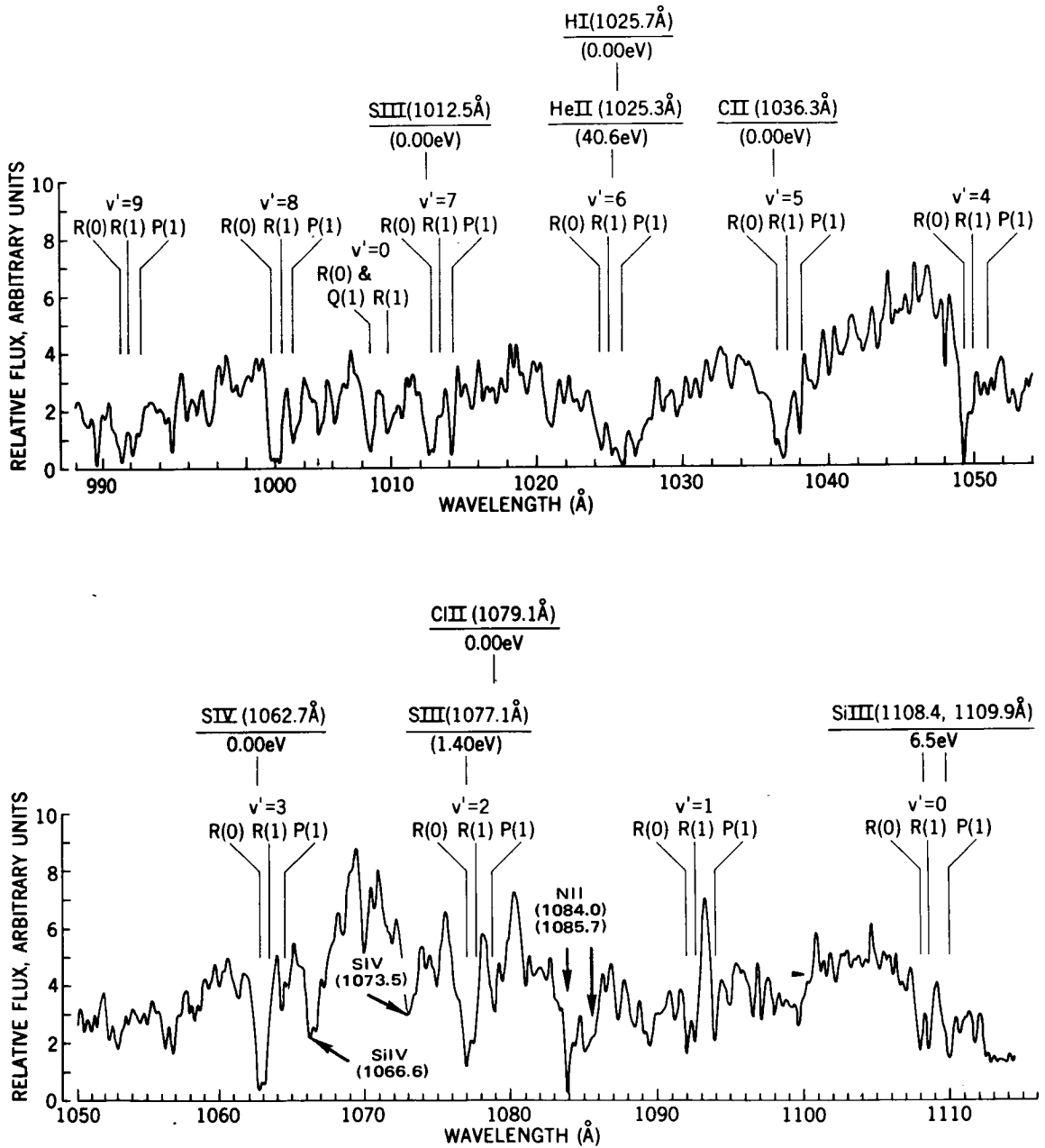
Figure 1. Ultraviolet spectrogram of δ Sco.

47 K. The uncertainties in the measurement may be used to indicate a minimum temperature of 25 K. The fact that no transitions arising from the second excited rotational level (J=2) of the ground state are observed, implies a maximum cloud temperature of 98 K.

The column density of hydrogen atoms, as determined from the observed Lα line, is $(1.5 \pm 0.5) \times 10^{21}$ cm^{-2}, which is in good agreement with previously determined values. Considering the atomic and molecular column densities together, it is apparent that 4.4(+7.0, −1.8) percent of all of the line-of-sight hydrogen atoms are in the form of molecules.

A current theory of Hollenbach, Werner, and Salpeter,[2] in which the molecule formation rate on grain surfaces is balanced against the Stecher-Williams photodestruction rate, predicts an abundance of molecular hydrogen about five times that derived here. The reason for the discrepancy may well lie in our ignorance of the geometry involved in the observation, and I think, therefore, that the observations promote confidence in the theory rather than doubt.

[2] D. J. Hollenbach, M. W. Werner, and E. E. Salpeter. 1971. *Ap. J. Letters* **163**, 165.

LOW-INTENSITY OPTICAL EMISSIONS FROM
THE INTERSTELLAR MEDIUM

Ronald J. Reynolds

Various models of the interstellar medium have been proposed to explain the high degree of ionization of interstellar hydrogen indicated by pulsar dispersion measures and the absorption of low frequency galactic radio emissions. One way to study the ionization state of the interstellar medium, and perhaps to determine the mechanism of ionization is to study the faint optical emission lines that must be emitted by interstellar gas. Such a study is presently being conducted, using a large-diameter, two-etalon, high-resolution, Fabry-Perot spectrometer at the Coudé focus of Goddard's 91-centimeter (36-in) telescope. This work is being done in collaboration with Dr. Scherb, an NAS fellow on leave from the University of Wisconsin, Dr. Roesler from the University of Wisconsin, and Dr. Boldt at Goddard.

Figure 1 illustrates typical scans of the faint, spatially diffuse Hα and [NII] λ6584 emissions in the direction of the galactic equator, at a galactic longitude of 104 degrees. The photomultiplier counting rate is plotted versus the radial velocity with respect to the
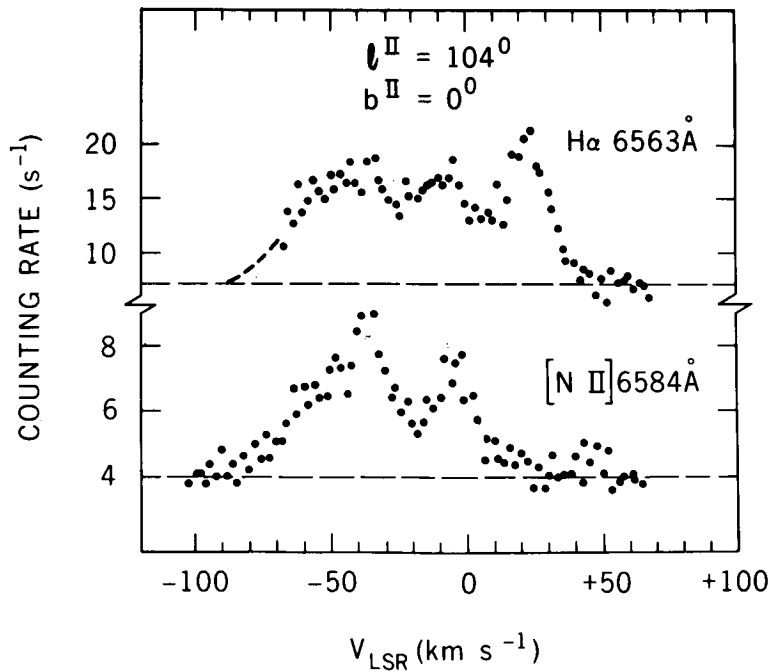

Figure 1. Typical scans of Hα and [NII] λ6584 emissions.

velocity of the local galactic medium near the sun in kilometers per second. The spectrometer's high spectral resolution has made it possible to use radial velocities to distinguish between various sources of faint emissions lying along the line of sight. In the Hα scan, three separate lines are clearly resolved: the ever-present Hα line from the earth's geocorona at plus 26 kilometers per second; and two galactic lines at minus five kilometers per second and minus 45 kilometers per second. The galactic line at minus five kilometers per second is presumably originating in the local Orion arm of the galaxy, while the line at minus 45 kilometers per second, greatly blue-shifted by the rotation of the galaxy, is probably associated with the more distant Perseus arm. These two galactic arms are clearly visible in the second scan, that of singly ionized nitrogen emission.

Observations of this spatially diffuse galactic Hα emission have now been made in more than 150 directions between galactic longitudes zero and 160 degrees, and forbidden lines of oxygen and nitrogen have also been observed in a limited number of directions. With the large number of observing directions, we have been able to observe systematic variations along the galactic plane in both the intensity and the radial velocity of the galactic Hα. These variations suggest that the diffuse emission is strongly associated with the three nearby galactic spiral arms.

In Figure 2, the distribution of diffuse Hα has been plotted in galactic coordinates with galactic latitude ranging from minus 40 to plus 40 degrees and galactic longitude from zero to 120 degrees. The contour values denote the counting rates above background at the peaks of the Hα lines. Observations in directions of known bright H-II regions were not

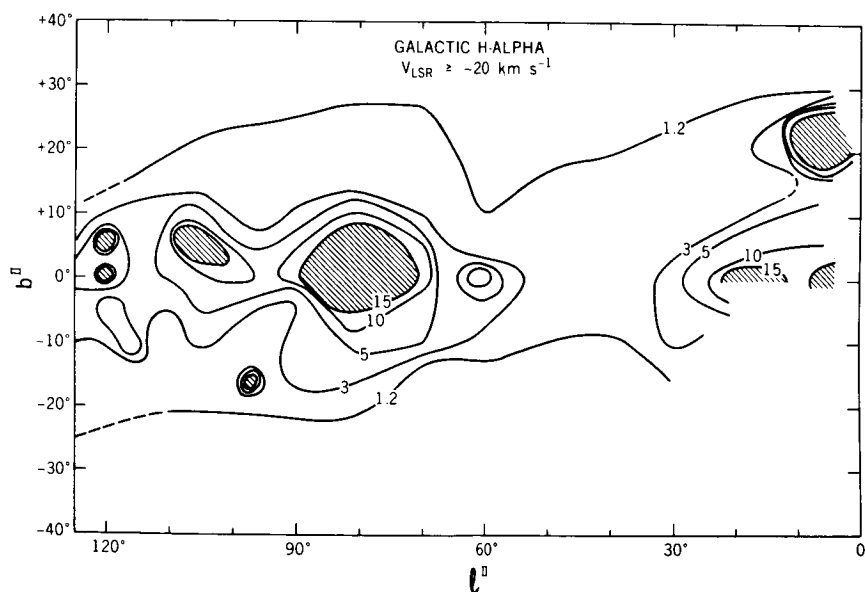Figure 2. Plot of distribution of diffuse Hα.

used in construction this map; and for the sake of clarity, emission from the Perseus arm was also not included.

The ridges of relatively high Hα intensity at galactic longitudes less than 25 degrees and greater than 68 degrees correspond to the projected optical positions of the inner Sagittarius arm and the local Orion arm respectively. The sun is located just on the inside edge of the Orion arm. The large maximum in Hα intensity centered on 78 degrees longitude is in the direction in which the Orion arm is viewed projected edge-on, while the region of minimum intensity between 35 and 50 degrees galactic longitude corresponds to the adjacent inner arm region.

Various properties of the interstellar medium can be determined from these observations, and they are listed in Figure 3.

In the anticenter direction, where galactic rotation is negligible, the observed line width places an upper limit of 6000 kelvin on the temperature of the emitting region in this direction. We soon hope to be able to use the observed difference in the line widths of Hα and [NII] λ6584 to determine the temperatures in other directions.

In directions of high galactic latitude pulsars, the Hα intensity can be combined with the pulsar dispersion measure to set the limits on the sizes and electron densities of the ionized regions in the interstellar medium. In four such directions investigated so far, the ionized regions were found to occupy at least 20 to 50 percent of the line-of-sight distance through the galactic disk, with average electron densities less than 0.2 per cubic centimeter within the regions.

The average ionization rate per hydrogen atom was also computed from the data, assuming steady state. Computed values ranged form 10^{-15} per second in some directions to more than 10^{-14} per second in other directions.

TEMPERATURE	$\leq$6000 K FROM LINE PROFILE IN ANTICENTER DIRECTION.
SIZE OF REGIONS OF IONIZATION	$\geq$20% - 50% OF LINE-OF-SIGHT DISTANCE THROUGH THE GALACTIC DISK IN DIRECTIONS OF HIGH-LATITUDE PULSARS.
ELECTRON DENSITY	$\leq$0.2 cm^{-3} IN DIRECTIONS OF HIGH-LATITUDE PULSARS.
IONIZATION RATE PER HYDROGEN ATOM	FROM 10^{-15} s^{-1} TO $>10^{-14}$ s^{-1} (ASSUMING STEADY-STATE).
IONIZATION FRACTION	$\frac{n(H^+)}{n(H)} = ?$ ($\geq$0.05 FROM PULSAR DISPERSION AND 21 cm) $\frac{n(N^+)}{n(N)} = ?$ $\frac{n(O^+)}{n(O)} = ?$ $\frac{n(O^{++})}{n(O)} = ?$

Figure 3. Properties of the emitting interstellar gas.

An important question we hope to resolve in the near future is whether the regions of ionization contain totally ionized, or only partially ionized, hydrogen. Most current theories of the ionization of the interstellar medium predict the existence of a partially ionized medium, and observations of forbidden lines of neutral and ionized oxygen and nitrogen should provide the first direct observational check on the validity of such models for the interstellar medium.

THE SULFUR DOUBLET IN GALACTIC H-II REGIONS

Curtis W. McCracken

The ultraviolet radiation from young hot stars of O and early B spectral types ionize the interstellar gas in their vicinity to form galactic H-II regions. The Orion nebula is the brightest such region visible to us. The emission line spectra of these regions commonly include not only the permitted recombination lines of neutral hydrogen and helium; but they also include forbidden lines from ions such as singly ionized sulfur and nitrogen, and both singly and doubly ionized oxygen.

The forbidden lines arise from metastable energy levels into which the ions have been excited through collisions with electrons. The relative intensities for some of these lines show almost no dependence on the electron velocity (or temperature) and depend mainly on electron density.

Typical examples are the blue forbidden doublet of singly ionized oxygen near 3727 Angstroms; and the red forbidden doublet of singly ionized sulfur near 6724 Angstroms. Measurement of the ratio of the intensities for the lines in either of these doublets provides a means of determining electron densities.

The oxygen doublet has long been used for determining electron densities in gaseous nebulae. The sulfur doublet only recently has found widespread application in this field. The introduction of image intensifying tubes with their increase in red sensitivity and their gain in speed over photographic emulsions has provided the opportunity for spectrographically observing the sulfur doublet in a large number of gaseous nebulae.

I have used the Goddard 91-centimeter (36-in) telescope in such a program. The data for 60 slit positions in four dozen galactic H-II regions are now being processed to yield electron densities based upon the sulfur doublet.

The scientific objectives are: (1) determining at least one value of electron density in each nebula, and (2) studying the variation of electron density as a function of position in the nebula for those cases where this is possible.

The second objective is illustrated in Figure 1 for one location in the Orion nebula. In the top plot, the electron density in electrons per cubic centimeter is displayed on a logarithmic scale as a function of position in the nebula. The slit was 6.6 minutes of arc long, was oriented from north to south, and was centered at a point 40 seconds of arc west of θ_1 C Orionis.

The individual points were obtained by successively scanning in the direction of dispersion across the sulfur doublet, and then stepping the analyzing slit (which was six seconds of arc long) by half of its length, until the entire length of the slit had been covered.

92
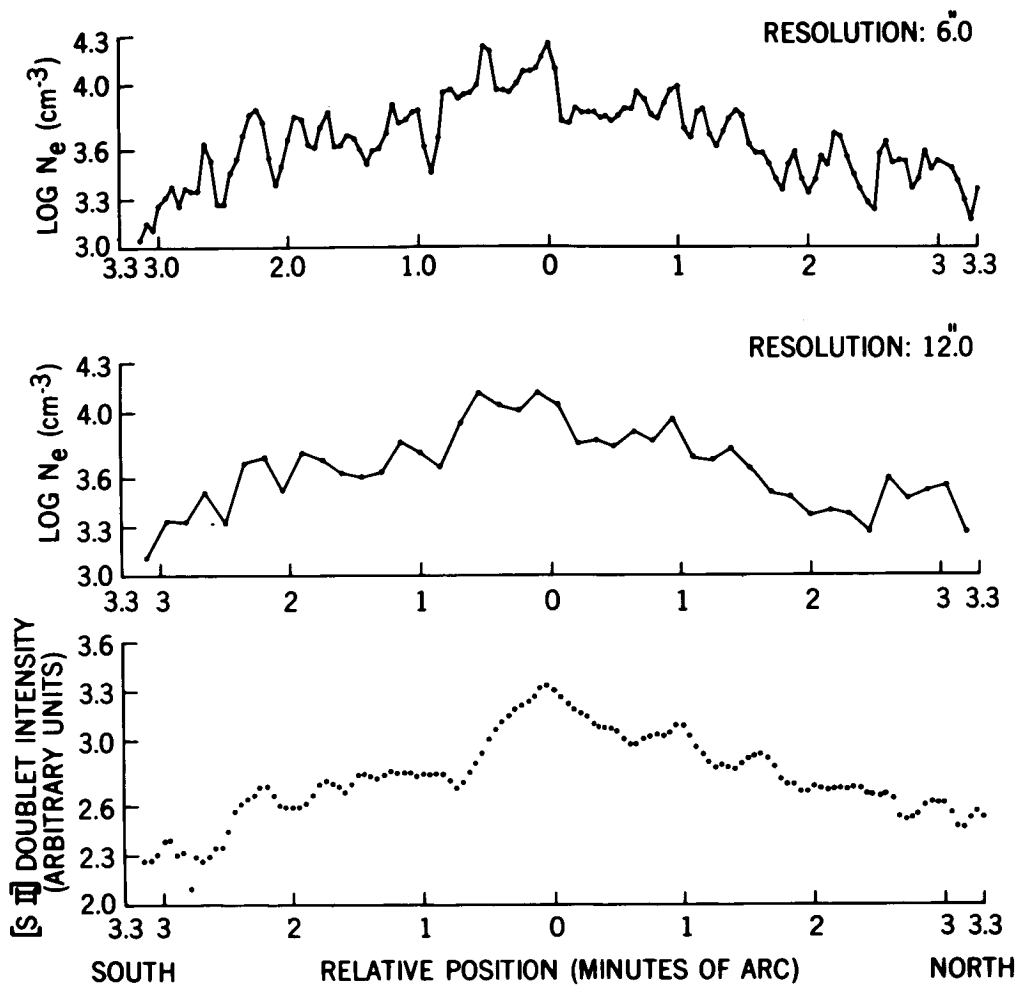
Figure 1. Data from a north-south spectrograph, slit centered 40 seconds of arc west of θ_1C Orionis.

The first thing to note in this plot is the general trend in the electron density, whereby it decreases from a value of about 15,000 down to about 1500 electrons per cubic centimeter within a few minutes of arc in both directions from the maximum.

The next thing to notice is that there appears to be small-scale structure in the electron density, with variations by a factor of two being very common. Some of the features probably are not real since they involve only a couple of points.

The middle plot again shows electron density on a logarithmic scale, but averaged over three scans at a time to get rid of some of the possibly spurious features.

There still are structures present with angular sizes of something like 20 to 30 seconds of arc. I believe that several of these features represent real variations in electron density.

The conclusion that these represent real variations in the electron density by something like a factor of two over distances of 25 seconds or so of arc is strengthened if we compare the middle plot with the plot shown at the bottom. The bottom plot shows the total intensity of the sulfur doublet; that is, the sum of the intensities of the two lines within the doublet. And if we look closely, there are some of these features which still show correlations. I believe this correlation helps to strengthen the conclusion that some features really represent variation in electron density.

The Orion nebula was included in my observing program primarily to serve as a check against results previously obtained by other investigators.

Figure 2 shows the electron densities derived from line ratios of the oxygen doublet in the second column at six of the twelve positions observed by Osterbrock. These positions in the nebula are shown in the first column.

The third column lists the electron densities which I have derived from my studies of the blue oxygen doublet; and the last column lists those derived from the red sulfur doublet.

Comparison of the oxygen doublet results of mine with Osterbrock's shows that at slit position V there is very good agreement. The agreement is a factor of 2.2 at the position A and at the other four points; my values are approximately 1.4 higher than those of Osterbrock.

Comparison of my oxygen and sulfur results shows that the sulfur doublet always gives higher electron densities than the oxygen doublet. The factors range between 1.9 and 3.1 for these six positions.

SLIT POSITION	OSTERBROCK [O II]	McCRACKEN	
		[O II]	[S II]
A	$3000 \ cm^{-3}$	$6500 \ cm^{-3}$	$15500 \ cm^{-3}$
B	1950	2800	5200
V	1275	1300	3600
W	2100	3050	9500
X	1750	2600	6000
Y	830	1150	2350

Figure 2. Electron densities in the Orion nebula.

The fact that the sulfur doublet gives results higher than the oxygen doublet is commonly attributed to the fact that sulfur, with its slightly lower first ionization potential, generally should be concentrated more towards the high-density concentrations.

The agreement between my results for oxygen and Osterbrock's for oxygen, as well as the agreement between my results for sulfur and for oxygen seem to be, in my opinion, quite satisfactory.

The conclusions to be drawn, then, are: (1) The variations in electron density as a function of position show that the small-scale condensations for regions of higher electron density exist; and (2) There is satisfactory agreement between my results for electron densities derived from the oxygen doublet and the earlier ones by Osterbrock, as well as between my results for the electron densities as derived from oxygen and sulfur doublets.

MEMBER OF AUDIENCE:

What is the characteristic size of these condensations?

MR. McCRACKEN:

Twenty-five seconds of arc corresponds to 10,000 astronomical units in the Orion nebula.

INTERSTELLAR POLARIZATION IN THE ULTRAVIOLET

Theodore P. Stecher

Astronomers measure the intensity of starlight as a function of wavelength as well as they possibly can and usually ignore the additional physical information one might be able to get if the polarization were also measured. This is partly because polarization is difficult to measure, and partly because it is also difficult to interpret.

In the interstellar case, though, polarization actually presents more information about the grains than the extinction does, that is, intensity versus wavelength. This is because the interstellar grains are lined by the magnetic field; as the starlight comes through and is attenuated, it is attenuated more at one position angle than at a second angle 90 degrees from the first, depending on how the grains are aligned.

I have tried to measure this in the direction of Zed Ophiuchi, the ideal star because it is bright but still has enough extinction to have sufficient numbers of grains to make the measurement possible.

Figure 1 shows my instrument, which incidentally is an old instrument. I used it to do spectrophotometry on stars and to measure the extinction curve. It is a 33-centimeter (13-in) telescope with a three-channel scanning spectrophotometer behind it. I opened up the spectrophotometer slits as wide as possible, which was about 50 Angstroms, and put polarizing elements behind them.

A rocket sometimes has greater degrees of freedom than we need, so the instrument is very easily adaptable as a rotating telescope. We fired the rocket up, pointed it at the star, and rotated it to the position angle of the maximum electrical vector as determined from the ground. Then we scanned through the spectrum and back, rotated the instrument 90 degrees, and scanned through the spectrum and back again. Thus we measured the extinction curves 90 degrees apart, and the difference measured is the polarization.

The spectrophotometer was calibrated in the laboratory beforehand by putting it in a beam of polarized light; Figure 2 shows the results. I have plotted the percent polarization, one, two, three, and so on, against inverse wavelength in microns. The polarization is running around 1.5 percent for this star, which is consistent with the visible observation. One can probably fit a fairly straight line through this.

As seen in Figure 3, one tries to push data of this kind as far as possible. This is a freehand drawing. The individual statistics on the points vary. The oscillation is at a familiar frequency, appeared on two different detectors, and those detectors had opposite signs in the experimental setup.

Figure 1. 33-centimeter (13-in) telescope with a three-channel scanning spectrophotometer behind it.

The first thing I did was to see how the ground observations agreed, as they are the only narrow band of observations which are available.

The OAO extinction curve for this star is a feature which I first found seven years ago in the ultraviolet, and which has since been confirmed. I plotted it this way to compare this feature. It looks like the polarization goes to zero. This is subject to a number of interpretations, but for a pure absorber you wouldn't get any polarization in two different directions.

Curves of this kind appear in the Mic-scattering for materials as a result of interference between the diffracted ray and the transmitted ray of a grain, but all the particles must be of the same size for this to occur.

If the grains come in crystals, why that might be possible, or at this point, it is pure speculation as to what I actually have here. I hope by next year I can give you a rather definitive answer.

MEMBER OF THE AUDIENCE:

What was the magnitude of your instrumental polarization, and how did you compensate for it?
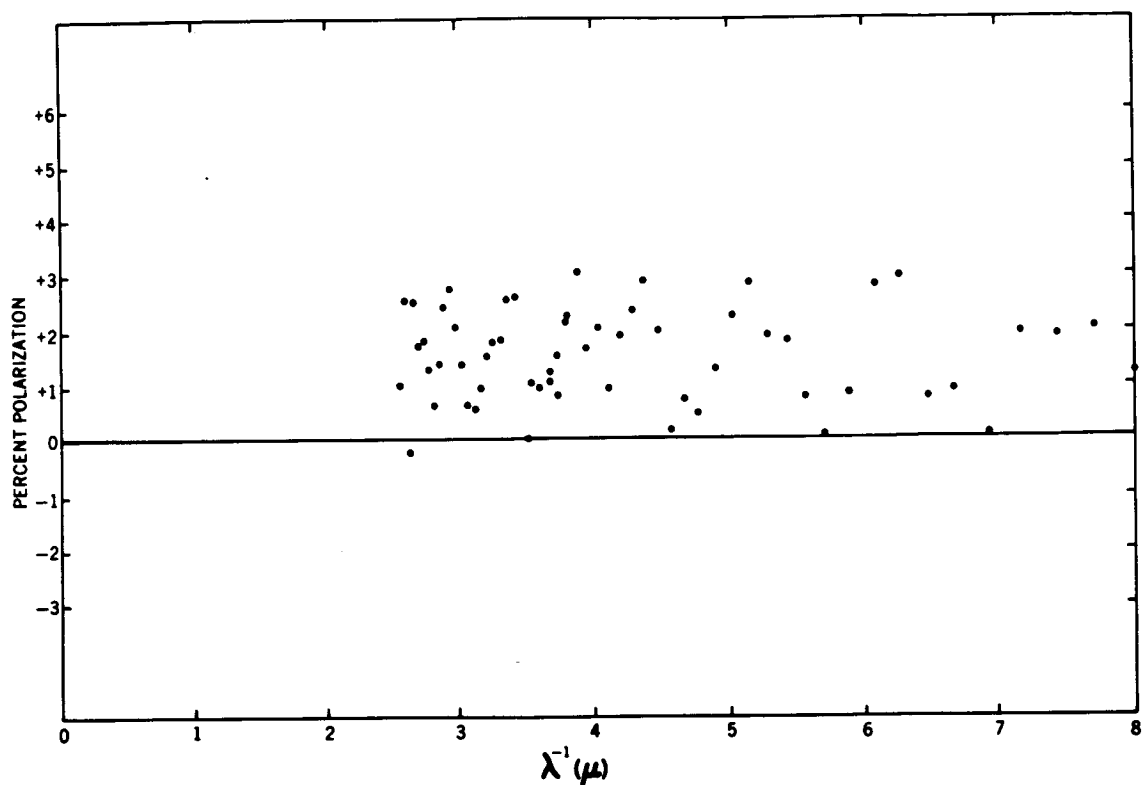
Figure 2. Calibration of spectrophotometer shown in Figure 1.

MR. STECHER:

Well, in the longer wavelengths I was able to have something like 90 percent polarization in one axis with the filters that I was using, an organic film on quartz. At the shorter wavelengths, I was only able to obtain 50 percent polarization of the instrument. In order to get some transmission, I used a stack of lithium floride plates with a Brewster angle.

Now, to calibrate it you pick up the rocket payload, put it in a tank of parallel light, and so measure it at right angles to each other. It is a rotating telescope, which is also the best way to measure it on the ground.

DR. ROMAN:

Here are two curves, one with the oscillating pattern, the other with a straight line, which have very different accuracies as part of your observations; so different that I would think you might be able to predict which was more likely. Which is?

MR. STECHER:

The real point here is that nobody has done this on the ground, and it can be measured on the ground. I have several people who are going to do this, but the people on the ground measuring polarization got interested in mapping the magnetic fields of the galaxy, and used broadband photometry in order to get good signals.

98
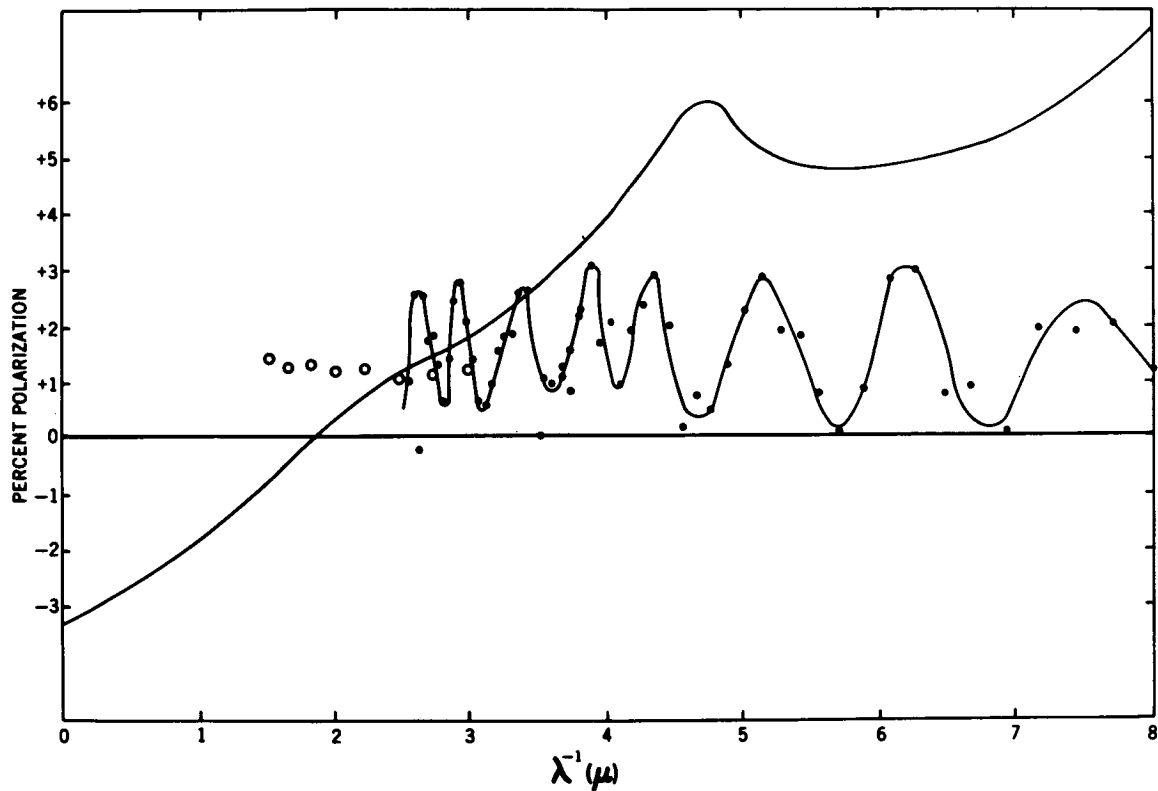
Figure 3. Freehand curve of data shown in Figure 2.

DR. ROMAN:

That doesn't answer my question. What accuracy did you predict from your photon statistics, and the accuracy with which you could make the measurements in the laboratory, and so forth; and what scatter do you expect?

MR. STECHER:

The individual point, uncertain by about a percent, maximum. The straight line set would certainly be acceptable and I always try to push for a little bit more.

100-MICRON OBSERVATIONS OF GALACTIC AND EXTRAGALACTIC SOUTHERN HEMISPHERE OBJECTS

William F. Hoffmann

This paper concerns far-infrared observations of the interstellar medium. Last winter, the Goddard far infrared balloon-borne telescope was flown twice from Paraná, Argentina. With a 30-centimeter (12-in) telescope operating at a wavelength of 100 microns, approximately forty new sources were observed in the galactic plane and in the Large Magellanic Cloud. Patterns and some degree of understanding are beginning to emerge from the observations of objects in the far infrared.

Figure 1 shows a contour map at 1400 megacycles in the radio region of the spectrum. Superimposed on it are circles at the positions of the 15 brightest sources observed from the Southern Hemisphere. Sources were found at the edge of the Coal Sack Nebula, the Eta Carina Region, and the Vela Region.
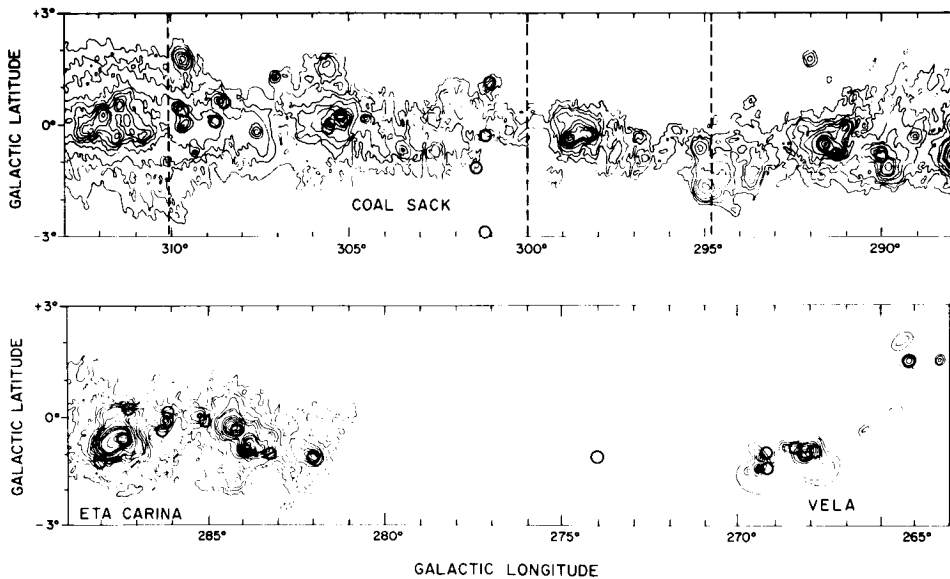

Figure 1. Contour map at 1400 megacycles in the radio region of the spectrum. Superimposed on it are circles at the positions of the 15 brightest sources observed from the Southern Hemisphere.

100

The remarkable thing about this figure is the coincidence between the peaks in the radio map and the circles we have shown, even of the detailed structure of multiple sources. The coincidence is remarkable because it is not possible for the same mechanism to be producing both the radio and the infrared emission. The radio emission is produced by free-free transitions from ionized hydrogen at a temperature of 10,000 degrees or so. An extrapolation of that free-free emission to the infrared region falls three orders of magnitude too faint to explain the infrared observations. On the other hand, the infrared, it appears, can be explained as thermal emission from interstellar dust, at low temperatures of about 50 degrees kelvin. An extrapolation of the thermal dust emission into the radio region cannot account for the radio intensity and spectrum. Not only is it not obvious that the radio continuum and infrared flux should go together, but on the contrary, it is surprising that they should. In fact, a priori, one does not expect dust to thrive in the destructive environment of a hot plasma. More strikingly, these regions where we observe infrared radiation are also regions where molecules are found in some abundance.

We conclude from the coincidence of infrared and radio continuum radiation that the dust must be made from a refractory material; that the dust and gas densities appear to go together; and that the dust is heated mainly by young, hot, stars.

One method for understanding these conclusions is to look at the data more quantitatively. In Figure 2, we plot the radio continuum flux versus the 100 micron infrared flux. There clearly is a trend providing a quantitative relationship. The solid circles are from the Southern Hemisphere flight, the open circles from previous Northern Hemisphere flights. The brighter objects in the radio frequency are brighter in the infrared. The scatter relative to a linear fit is about a factor of four. The lower line represents the fit with the radio flux 1/1000th of the infrared; the upper, 1/250th of the infrared.

In order to further understand what this apparent relationship means, one has now to study a few of these objects in detail to decide what aspect of them provides the mechanism to insure that the dust and the ionized gas survive together, or must be together.

Another method for getting at the question of why these things go together is to examine the phenomena in other galaxies. The nearest galaxy is the Large Magellanic Cloud at 50 kiloparsecs distance. Figure 3 shows some of the characteristics of the galactic center and the Large Magellanic Cloud. The left-hand column gives the appearance the center of the Milky Way Galaxy would have at a distance of 50 kiloparsecs. The radio flux at 1410 megahertz is forty flux units, the radio size is about two arc minutes, and the mass derived from the radio data is about 2.5×10^5 solar masses.

Correspondingly, radio flux from the 30 Doradus region, which is the most intense radio region of the Large Magellanic Cloud, is again about 40 flux units, the size is about four arc minutes, and the mass derived from the radio data is about 3×10^5 solar masses.

Radio astronomers find this fairly compelling evidence for the conclusion that the 30
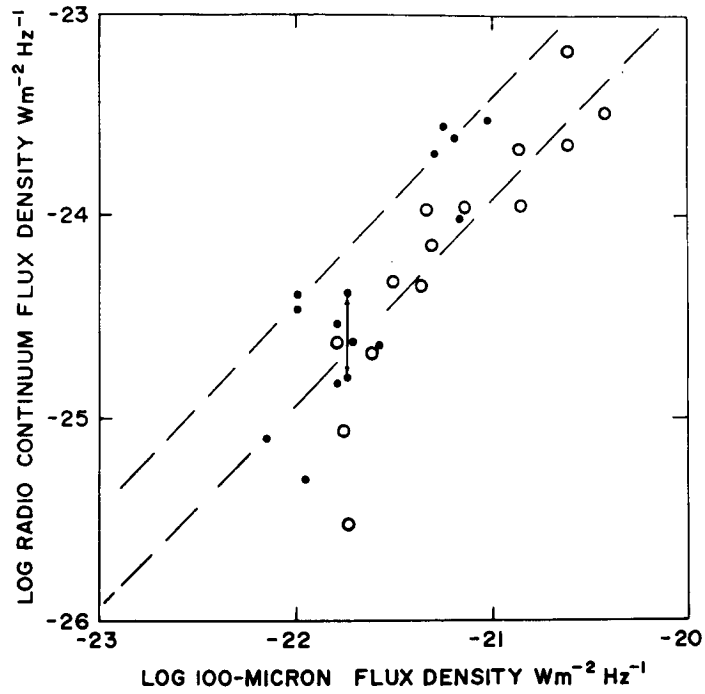
Figure 2. Radio continuum flux versus the 100-micron
infrared flux.

	GALACTIC CENTER (AT 50 KPC)	LARGE MAGELLANIC CLOUD
RADIO FLUX (1410 MHZ)	40 FLUX UNITS	40 FLUX UNITS
RADIO FLUX (THERMAL CORE)	2'	4'
MASS (FROM RADIO)	$2.5 \times 10^5 \, M_\odot$	$3 \times 10^5 \, M_\odot$
INFRARED FLUX (100 MICRON)	6×10^4 FLUX UNITS	1×10^4 FLUX UNITS

Figure 3. Comparative characteristics of the galactic center
and the Large Magellanic Cloud.

102

Doradus region of the Large Magellanic Cloud has many similarities to the Milky Way Galaxy and is most likely the nucleus of the Large Magellanic Cloud. In the same way, we can extrapolate the infrared flux from our own galactic center to the distance of 30 Doradus. This turns out to be 6×10^4 flux units, an easily detectable intensity.

We surveyed the Large Magellanic Cloud and appeared to find a faint source at the position of 30 Doradus with a flux of 10^4 flux units. From this, we conclude that in the far infrared, the center of the Large Magellanic Cloud is similar to, but fainter than, the center of our own galaxy. Recalling Figure 2, the upper linear relationship for a collection of galactic infrared sources had a ratio of about 250, the same ratio that is exhibited for the 30 Doradus region for the Large Magellanic Cloud.

So it appears that while the infrared is weaker relative to the galactic center, it does fit fairly well the general picture of galactic H-II regions. It also provides evidence for the abundance of dust in the 30 Doradus region similar to the abundance of dust relative to gas in the H-II regions in the Milky Way Galaxy.

MEMBER OF AUDIENCE:

Is there any explanation for the linear relationship between the flux density in the infrared and the flux density in the radio?

DR. HOFFMANN:

A number of people have done calculations, but there is no complete model. The basic argument is that the radio flux gives a measure of both the gas density and the ionizing radiation. These are the same two factors which control the infrared emission, if you assume the dust density goes with gas density, and the main heating mechanism is the ultraviolet radiation from the ionizing star.

SECTION III

PLANETARY, LUNAR, AND COMETARY STUDIES

OVERVIEW

Norman F. Ness

For some time, one of the main themes of NASA's scientific program has been to solve the problem of the origin of the solar system, and in a sense, that's what this series of talks will address, although not directly.

There has been a lot of activity, satellite-wise, in the area of lunar and planetary studies. In the first figure, I'd just like to review briefly for you those satellite missions which have been conducted during the past year, about which you'll be hearing some results. On the top left you see the two Apollo launches which have taken place in the last year, Apollo-15 and -16, plus the subsatellite. We're going to be hearing about results not only from Apollo -15, but from earlier Apollo missions, in a talk on the chemistry of the lunar material.

There was a time, before Apollo, when it was thought that all we had to do was to get to the moon and obtain a sample of the moon, and that would be, essentially, a Rosetta Stone of solar system physics. It would be a replication of the entire history of formation of the solar system without the contaminating effects associated with such geological features as erosion by wind and water and other chemical processes related to the presence of a large amount of water.

Well, of course, as most of you know, this has certainly not been the case. We sometimes seem to see our goals reduced to very simplistic objectives, and the return of one or two or any small number of samples from the moon has in fact shown the moon to be highly differentiated at some time in its history, probably very, very long ago.

APOLLO 15	**26 July - 7 August 1971**	**Mariner 9**	**30 May 1971 - 13 November 1971**
APOLLO 16	**16 - 27 April 1972**		
(+ Subsatellite)	**(24 April - 30 May)**		
LUNA 18	**2 September 1972**	**MARS 2**	**19 May 1971 - December 1971**
LUNA 20	**14 - 25 February 1972**	**MARS 3**	**28 May 1971 - December 1971**
		VENERA 8	**27 March 1972 - 22 July 1972**

Figure 1. Recent lunar- and planetary-oriented satellite missions.

The processes which led to that differentiation and the processes which affect the moon's present structure are of importance. Satellites and the manned missions which return information from the moon are contributing bits of data that help answer these important questions.

In the case of the Soviet activities, they, of course, have gone at the problem a little bit differently: They've sent unmanned vehicles in relatively large number to the moon and have successfully returned lunar samples from the moon with these unmanned devices. Within laboratories here at Goddard, samples of such material have been analyzed along with material returned from the Apollo program itself.

Well, the moon has been very exciting. There've been lots of interesting results from a geological viewpoint. Let me turn now to the planets.

Mariner-9, although it was launched in May of '71, was not injected into Mars orbit until November 13, 1971. It has returned remarkable photographs, not only of the planetary surface, but also of Mars' satellites, Phobos and Deimos. Serendipity certainly held: A dust storm arose, and was initially thought to be a very adverse condition, but in fact it turned out to be an extremely fortuitous transient event. Combined with the unexpectedly long lifetime of the Mariner spacecraft, the storm provided valuable, unanticipated data which have aided us in studying how the winds act on the surface of Mars, and how material is transported.

We'll also be hearing today in much more detail about one of the very significant experiments on Mariner-9 from Dr. Hanel, principal investigator for the IRIS experiment. This complex device returns information in a classical, remote-sensing context in which the emission at various levels in the atmosphere and from the planetary surface give an integrated result which must be deconvolved, or separated. Attempts must be made to uniquely identify the sources of the various emissions with respect to temperatures of the surface, composition of the atmosphere, and of course the surface material itself.

In the case of the other nations engaged in Martian spacecraft activities, the U.S.S.R. Mars-2 and -3 spacecraft launched in the same launch window achieved orbit slightly after the Mariner-9 spacecraft in December 1971, and returned very interesting scientific data. I will be returning to that topic shortly.

The Russians have also developed a continuing, vigorous program of Venus probes. The latest probe landed on the day side, and reported temperatures and chemical compositions which, when folded together with results obtained previously, yield a somewhat different result than anticipated. The uniformity of temperature, the same on both the day side and the night side, is a little bit surprising.

As time has gone on, and as our studies of the solar system have proceeded, we have become aware of the relative importance of matter that is not in a condensed, solid state. In fact, for a long time, it's been known that the majority of the solar system is made up

108

of ionized material particles stripped of outer shell electrons. So we're concerned mainly with a fourth state of matter, and here at Goddard we've actively carried out a great many in situ measurements of magnetic fields, plasmas, and energetic particles in the earth's environment, and in the sun's environment in heliocentric space.

In the case of a comet, which is of course a primitive space probe—it samples from the outer limits of the solar system to within a very short distance of the sun—there are those who believe that comets represent the most primitive state of material in the solar system that is presently available to us. So there is interest in the possibility of examining the chemical and physical characteristics of comets in interplanetary space.

In the talks today, you'll hear about chemical equilibria in interstellar space, as well as about chemical composition of cometary atmospheres. You'll also hear a very interesting talk discussing the possibility that we already have samples of cometary composition, obtained from rocket observations in the earth's atmosphere. It's undoubtedly certain that some of the dust particles and other nonvolatile components which survive entry into the earth's atmosphere must represent a cometary origin.

In the line of meteoritic research there is a fair consensus that condritic meteorites themselves probably represent burned-out comets, burned out by repeated passages past the sun, in the course of which all the volatiles have been evaporated, so that only very lightweight, fragile material remains.

It's a very comprehensive area, and I don't intend to review all of the various theories of solar system origin. But I'd like to take this opportunity to add a very short talk on the Mars-2 and -3 probes, based upon some recent results sent to me by the Russians, which I think are sufficiently important to merit our consideration.

The manuscript arrived in Russian, and I will subsequently make available a translated version. The essence of the results is that the Russians believe that they have detected a planetary magnetic field on Mars, and they think they've detected it well enough that they're submitting the manuscript for publication in an American journal, *The Journal of Geophysical Research.*

You'll recall that some years ago we were engaged in a controversy with the Soviets on the investigation of the magnetic field of the Moon—their Luna-10 results had been interpreted in terms of an intrinsic lunar magnetic field. This was subsequently shown to be false by Lunar Explorer-35. And although the Moon does appear to have very weak magnetic signatures associated with surface and subsurface variations in chemical composition, by no means does it have a very large-scale magnetic field as we are speaking of in terms of the planet Mars.

Figure 2 shows data obtained from Mars-3, which shows three components of the magnetic field. Unfortunately I've had to clip the scale which shows the values. The quantization step size for the three components X, Y, and Z, is one gamma; the maximum amplitude
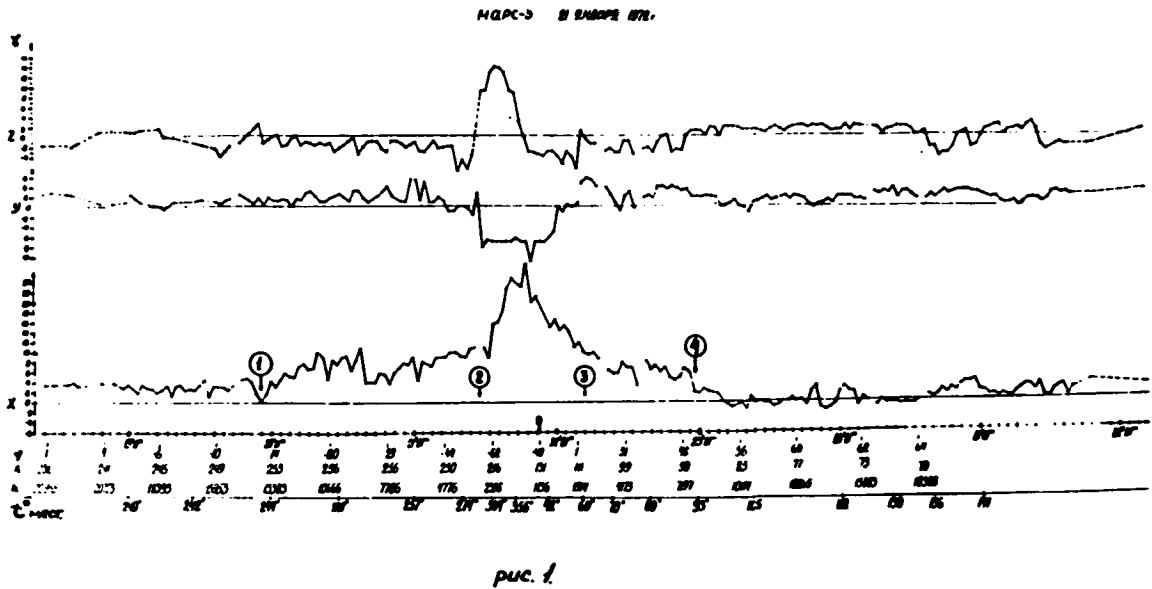
Figure 2. Mars' magnetic field data from the U.S.S.R. Mars probe, Mars-3.

here is about 27 gammas. Along the bottom are plotted the typical parameters describing coordinates of the spacecraft as aereocentric coordinates.

Points 1, 2, 3, and 4 are characteristic boundaries between regions of space which we're familiar with through the interaction of the solar wind with the Earth. Point 1 corresponds to a bow shock wave. Between Points 1 and 2 is the transition region. At Point 2, the abrupt change in the direction and large increase in magnitude in the three components, corresponds to magnetopause traversal. Point 3 is magnetopause exit, and Point 4 is shock exit back into interplanetary space. The results, placed in a coordinate system amenable to physical viewing, are shown in Figure 3. The Sun is to the left in this plot; the night side of the planet Mars is shown here. The units are planetary radii. The solid lines shown here with the attached points 1, 2, 3, and 4 correspond to trajectory plots, projected in a plane which is kept fixed with the Mars-Sun line; but the plane then rotates with the space-craft as the spacecraft goes around the planet, a typical format in these types of investiga-tions. There are additional trajectory plots which are shown here; the data was taken mainly in January and February 1972. When I was at COSPAR in May, I asked the Russians why they hadn't reported any results, and they told me that they weren't certain that they could believe the results they'd obtained in January. They were at that time undergoing an evaluation of more recently obtained data, which was from April 6 and April 18. Periapsis, which was originally 1100 kilometers from the surface of the planet, had by then moved up to some 2350 kilometers. Well, the Russians have very convincing evidence for a planetary magnetic field, and based upon my experience in the field, I don't think they're really that far wrong.
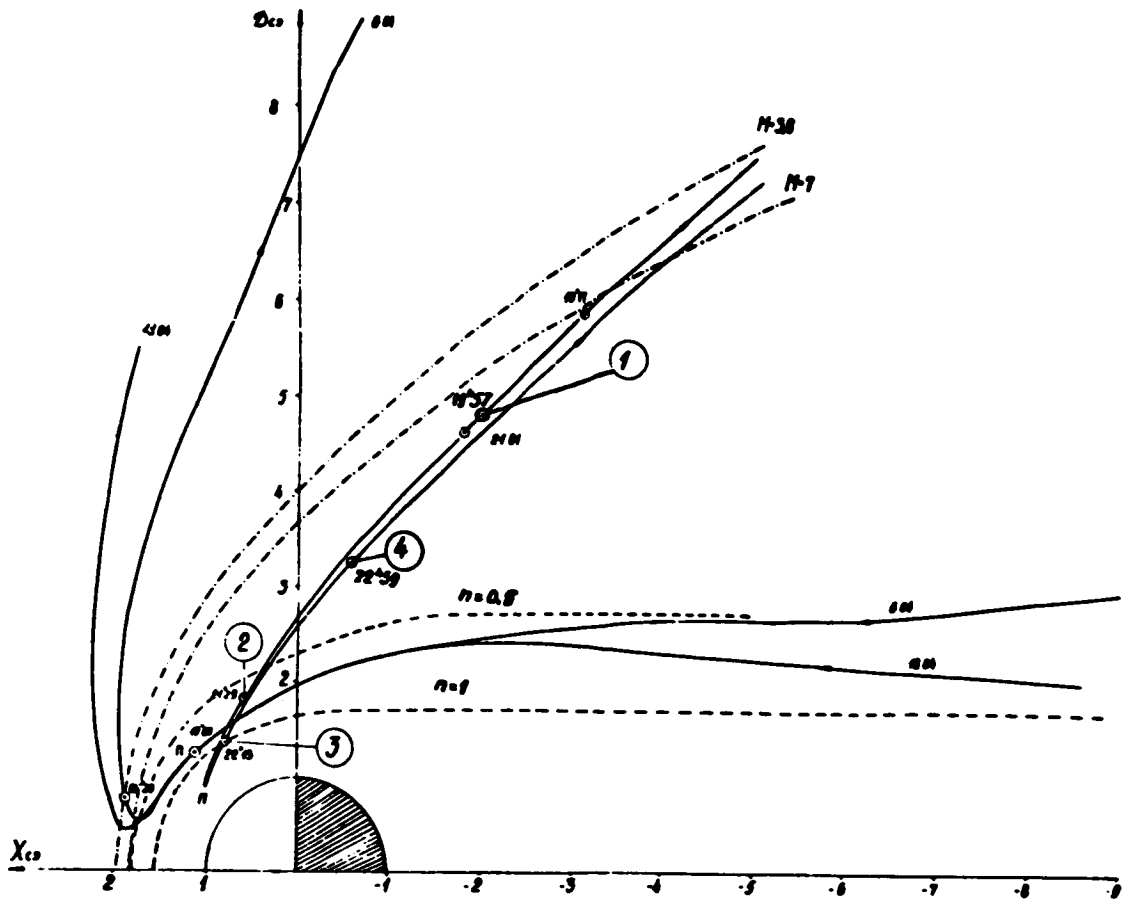
110

Figure 3. Trajectories of Mars 2-3 with superposed magnetopause (dashed) and shock wave positions (dot-dashed) for Mach numbers 3.8 and 7.

The result is tantalizing for the following reasons: It means that Mars, which is one of the terrestrial planets, and which rotates at approximately the same rate as the Earth, today has a dynamo which is weak, providing a surface field at the equator of some 67 gamma, or a magnetic moment of Mars which is 2.4×10^{22} Gauss·cm^3 whereas the Earth is 8×10^{25} Gauss·cm^3.

It means the solar wind does not impact the planetary atmosphere. It means it is not the ionosphere of the planet which stands off the solar wind, but in fact, it is the planetary magnetic field. The chemical composition and the evolution of the atmosphere may then be independent of solar wind input, quite unlike the situation in the case of the Moon. In that case, the atmosphere is completely dominated by the solar influx, and we believe the same situation is also true in the case of Venus.

Well, how do these results fit in with the only U. S. results that we have to date, and the only U. S. results we can expect to be available for the next ten years? There was a signature in the data and the interpretation of the position of the shock wave was then extrapolated to an ionopause down at the subsolar point of Mars. The Russians have shown that the measurements were not wrong for Mariner-5, but that the interpretation was wrong. It isn't the ionopause, but a legitimate magnetopause, and an intrinsic planetary magnetic field of Mars itself. Well, that's the kind of surprise we're in for in lunar-planetary-cometary studies. In keeping with our attempt to provide an evolutionary program for our continuing study of the origin of the solar system, the last speaker will address himself to the question of an evolutionary program in cometary missions.

MARS: ITS ATMOSPHERE AND SURFACE

Rudolph A. Hanel

About a year ago Mariner-9 arrived at Mars. At that time, we expected to find a planet almost like the moon, extrapolating from the Mariner-4 and -5 data, but much to our surprise, we found quite a different planet, one which is still in a state of evolution.

The last data from Mariner-9 showed an almost clear atmosphere. We have also recently obtained spectra of ice clouds. But I think I'm getting ahead of my story.

To introduce this subject, we plotted in Figure 1 the spectral radiance as a function of wave number from 200 to 100,000 wave numbers, or from one-tenth of a micron to 50 microns. The solid curve represents the spectral distribution of solar energy available at the distance of Mars. Most of that energy is being absorbed by the planet and its atmosphere. Part of it is reflected, and that portion of the solar energy provides the signal for the television and ultraviolet spectrometer which, along with the infrared interferometer spectrometer (IRIS), is part of the instrumentation aboard the Mariner-9 spacecraft. The absorbed energy is used to heat up the planet. The planet is, we think, in equilibrium with solar radiation, and this energy eventually is being re-emitted in the infrared as thermal emission. You see in the illustration a typical spectrum of that emission, with water vapor, carbon dioxide, and silicon oxide features. The spectral
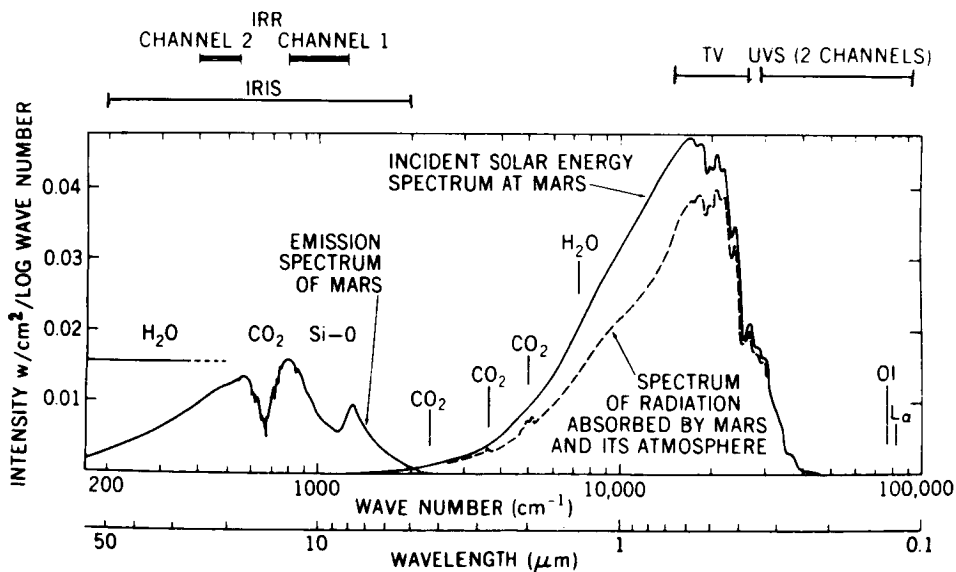

Figure 1. Spectral experiments on Mars Orbiter and typical energy distribution of electromagnetic radiation.

113

range of the infrared interferometer spectrometer was chosen to cover the range from 200 to 2000 wave numbers, so it covers the major part of thermal emission.

The infrared radiometer on Mariner-9 had two channels in these spectral intervals. But while those channels gave essentially single data points, the IRIS spectrum is broken up into approximately 750 individual spectral intervals.

What are we measuring in the emission spectrum? We measure the specific intensity as a function of wave number, and this expression is the assembly of many individual parameters which all enter into the solution of the equation of radiative transfer (Figure 2). We have the task of recovering the individual parameters out of each spectrum.

The problem has been compared to unscrambling scrambled eggs and reassembling the eggs, and that's essentially the problem of remote sensing under such circumstances.

It is clear that one has to measure the spectra with the necessary precision to be able to recover the individual parameters. We display again the radiance as a function of wave number, but this time on a linear scale. The top spectrum has been taken over the north polar area which was the winter pole on Mars at that time.

The majority of the radiances follow very closely the radiance from a black body of about 145 degrees kelvin, which indicates to us that we are looking at a frozen CO_2 surface, since 145K is the equilibrium temperature for CO_2 frost, at a pressure appropriate for Mars. In this spectral interval, where the emission comes from CO_2 gas, we see higher brightness temperatures — the equivalent blackbody temperatures are given here by the dashed curves — and they indicate a warmer atmosphere above that level.

The south polar region has a very different appearance. First of all, we see somewhat higher radiances, then we see deviations from the blackbody curve. These are due to the

$$I(\nu) = \epsilon_s(\nu) B(\nu, T_s) \tau_s(\nu) - \int_{\log P_t}^{\log P_s} B[\nu, T(\log P)] \frac{\partial \tau(\nu, \log P)}{\partial \log P} d \log P$$

$\epsilon_s(\nu)$ ———— SURFACE COMPOSITION

T_s ———— SURFACE TEMPERATURE

$T(P)$ ———— VERTICAL TEMPERATURE PROFILE

P_s ———— SURFACE PRESSURE

τ_s ———— ATMOSPHERIC CONSTITUENTS

$\tau(P)$ ———— VERTICAL DISTRIBUTION OF CONSTITUENTS

Figure 2. The equation of radiative transfer.

fact that the emission within the field of view of the instrument comes not only from a single surface, but from frozen CO_2, and another, warmer part. The warmer areas are the outcrops of the cap, which are dark and have a high equilibrium temperature. You also see water vapor lines in emission, which you will see later on in more detail.

The appearance of the CO_2 band here is much more complex; the most absorbing part, the center of the band, gets cold again, which indicates a temperature inversion in the atmosphere. We also see the emission of atmospheric dust, which we'll discuss later.

One can also display the spectra in terms of the brightness temperature, as shown in Figure 3. In Figure 4 we have the same mid-latitude and south pole spectrum displayed in terms of brightness temperature. The water vapor rotational lines show up in absorption here and emission there, which is consistent with a colder atmosphere overlaying a warmer surface at mid-latitudes, and just the opposite in the case of the south pole region.

Most of those features are due to CO_2, and some are not fully identified yet. We have here the Q branch of $C^{12}O_2^{16}$; and here $C^{12}O^{16}O^{18}$. So we see several signatures due to isotopic components. Preliminary inspection shows that the isotopic ratios are not greatly different from those found on earth.

The most important things I want to show you in Figure 3 are the large smooth bump here and the corresponding absorption feature here, which are due to silicate dust in the atmosphere. From the position of the maximum and minimum as well as from the
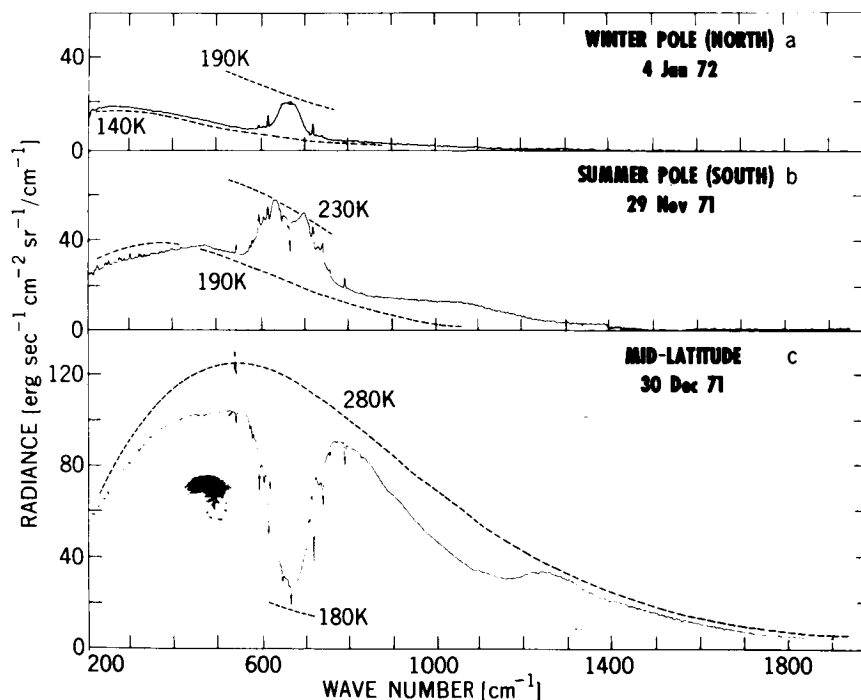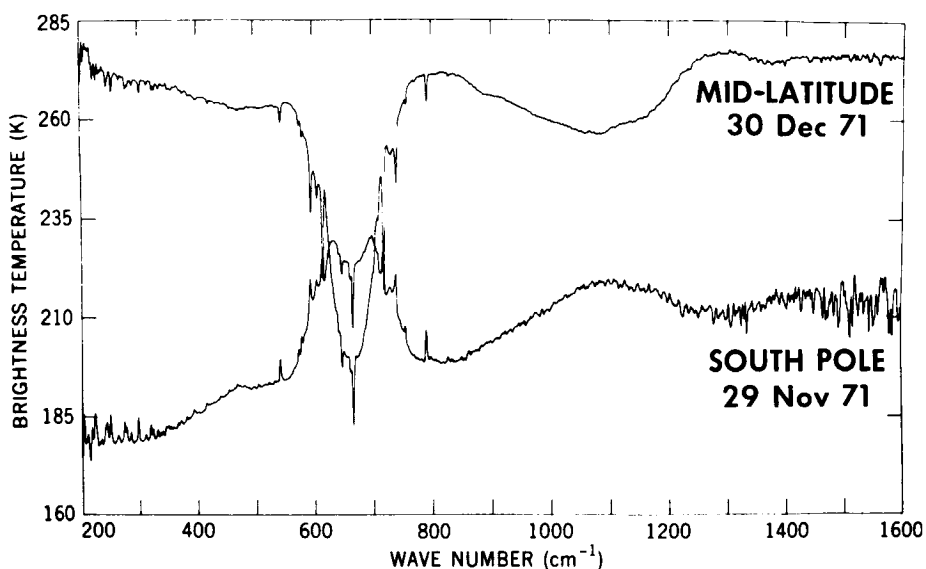

Figure 3. Brightness temperature.

Figure 4. Brightness temperature.

position of the most transparent part, one can derive, just by comparison with laboratory data, the silicon oxide content of that material, which appears to be relatively acidic — rich in silicon oxide. The preliminary analysis shows a silicon oxide content of about 60 percent. This is an indication of a relatively high degree of geochemical differentiation of the planet. This high degree of differentiation was already found in the early part of the mission. Later on, as the dust cleared and television pictures became available, this conclusion was quite consistent with the appearance of large volcanic features, such as the one seen in Figure 5.

Figure 5 is a picture of South Spot, which has been detected by the Mariner-9 television team. It's a caldera, a huge volcanic feature, which has a dimension of approximately 125 kilometers in diameter. It's much larger than calderas on earth, such as in the Hawaiian Islands.

We were able to get one spectrum right into the caldera, and from that spectrum it was determined that the CO_2 pressure was approximately 1.7 millibars. From that, one can determine the relative height to an arbitrary reference level. We have taken the triple point of water vapor, 6.1 millibars, as the reference level, and calculated the height of this caldera at about 14 kilometers.

From the surface pressure one can derive the topography, and Figure 6 is a map of the Tharsis region, in which lies the South Spot (the circular area in the center; the figure "14" indicates the height of the mountain). The base of the mountain is at an elevation of approximately 8 kilometers. The volcano has a height of 6 kilometers. Those are huge mountains; but the diameter of the structure is a couple hundred
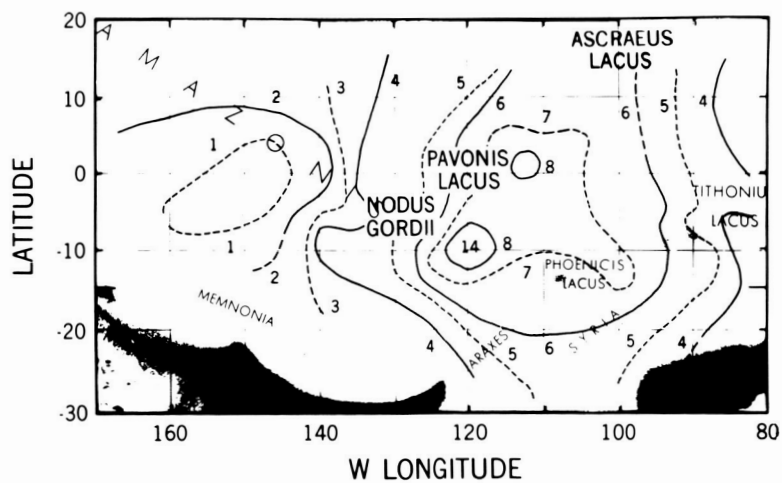
Figure 5. Mariner-9 photo of South Spot.

Figure 6. Topography of the Tharsis region of Mars. South Spot is
centered at 10°S, 120°W. (Above 6.1-mb pressure surface.)

117

kilometers, so the mean slope is only about three degrees. This is quite consistent with a very fluid lava with a relatively high silicon oxide content.

Here is Middle Spot and North Spot is here. These are the three major volcanoes, and Nix Olympica, the tallest of them, is just off here. We are presently preparing a global topography map of Mars.

Another parameter one may derive from the CO_2 spectrum is the temperature profile (Figure 7). We see here the temperatures in degrees kelvin, displayed as a function of pressure, or better, the log of pressure, which is approximately proportional to height in a linear scale. Typical profiles taken from the early revolutions show a much flatter characteristic than later profiles. Later on, the atmospheric lapse rate increased. The surface temperatures on the other hand, were lower first, then higher. The dashed curve indicates some uncertainty due to the large amount of dust in the atmosphere in the beginning. One can take temperature data at a certain level, for example, at 2 millibars, and plot planet-wide maps which are shown in Figure 8.

On this map isotherms are plotted in latitude versus local time. The goal here was to study the diurnal behavior of the atmosphere. Much to our surprise, we found the maximum temperatures on the early revolutions of Mariner-9. This was at the time when the atmosphere was heavily dust-laden. We found the maximum temperatures towards evening and at relatively low latitudes, around 60° south.

At that time, the south pole region of Mars was tilted towards the sun and the maximum integral value of solar heating is at about 60°. The late maximum is consistent with an atmosphere of large thermal inertia which responds to the total integral of the
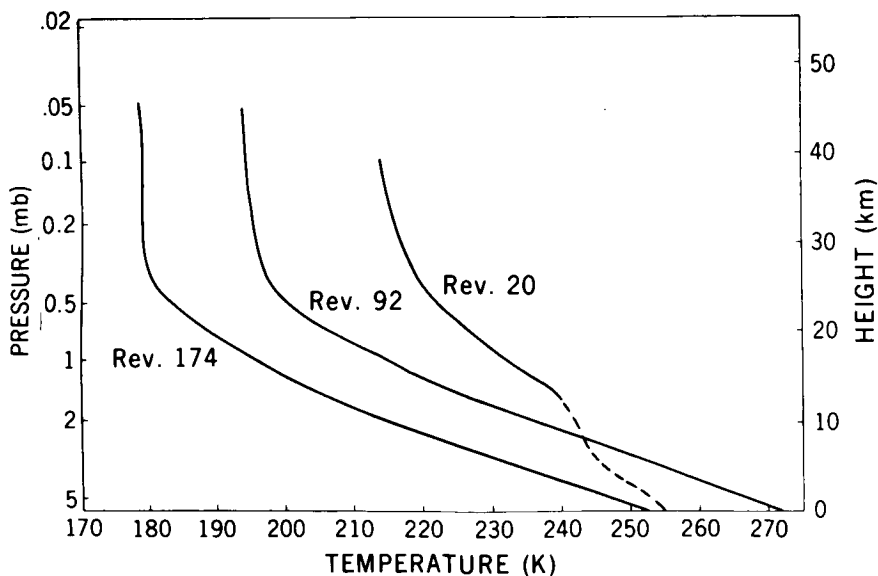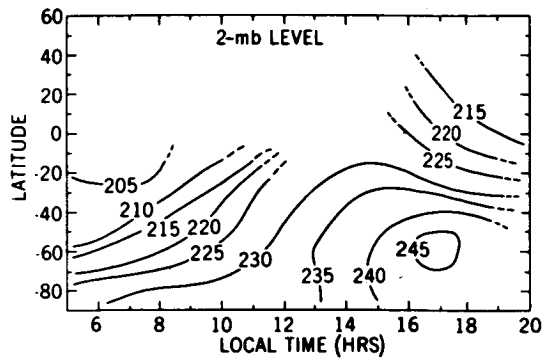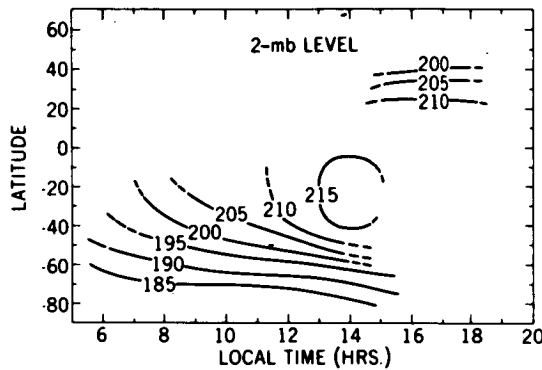

Figure 7. Mariner-9 IRIS atmospheric temperature profiles.

118

Figure 8. Atmospheric temperature (K) at 2-mb level.

solar radiation, rather than to the instantaneous value. Later on in the mission, after partial clearing, this maximum moved from late afternoon and 60° south towards the subsolar point, as one might expect with a clear atmosphere.

In contrast to the atmosphere, the surface temperatures, which were derived from spectral intervals where the atmosphere is more transparent, did not change between the early part of the mission and later (Figure 9). During the so-called dusty part, the maximum surface temperature was always very close to the subsolar point.

From the behavior of the surface temperature with respect to local time, one may derive the thermal inertia of the soil, which is consistent with a very loose powder.

From the temperature profile, one can go to the equations of conservation of momentum, mass, and energy, and derive a wind field. Figure 10 shows the winds near the surface. In general, you see a windspeed on the order of about 10 to 20 meters per second. At some latitudes, the wind direction follows very closely the diurnal cycle. We have displayed winds in the south polar area. On the south pole itself, the wind is always blowing from the night into the day side, so if you stand on the south pole and look towards the sun, the wind is always coming from behind.
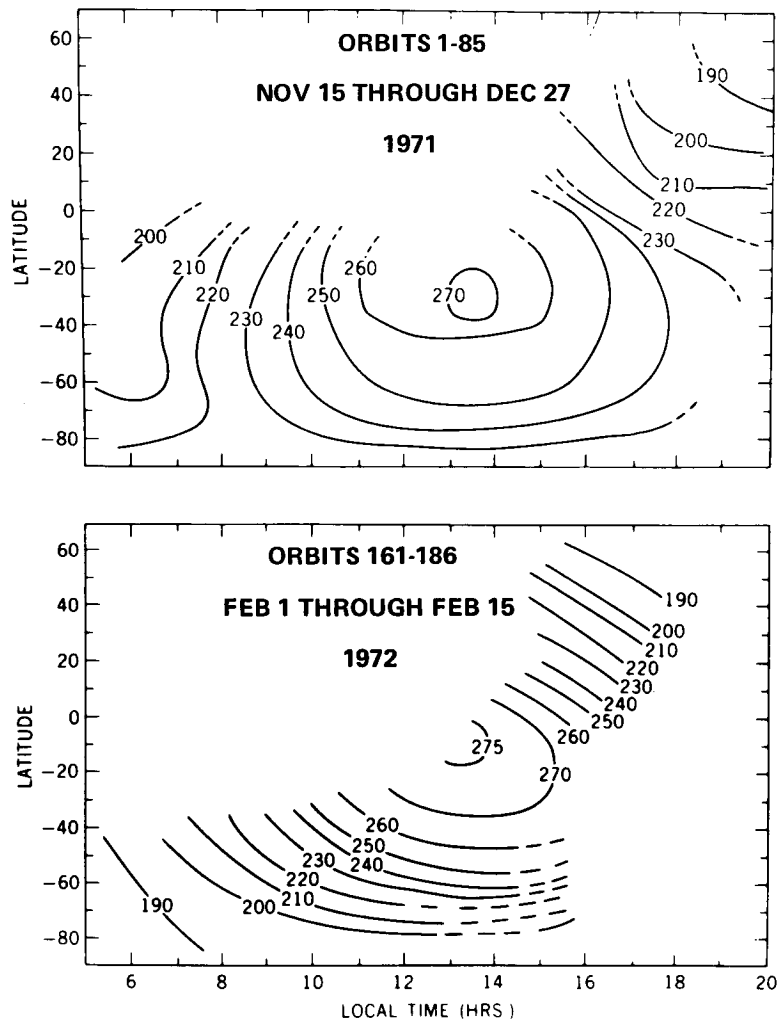
Figure 9. Surface temperatures (K).

Figure 11 shows quite recent data. We have been able to sum, or average, about 2500 spectra taken over the whole period of the mission. In doing so, one diminishes greatly the random noise in individual spectra. The measured spectrum has been compared here to a synthetic spectrum which we have computed using a mean temperature profile and about ten precipitable microns of water vapor.

The point here is not so much to study the amount of water vapor in the atmosphere, but to identify all those spectral features which show up in the spectrum, and to search for unknown constituents. The features marked with vertical bars are all of the CO_2 molecule. Most of those also show up in the artificial spectrum, like those although some are not yet in it.
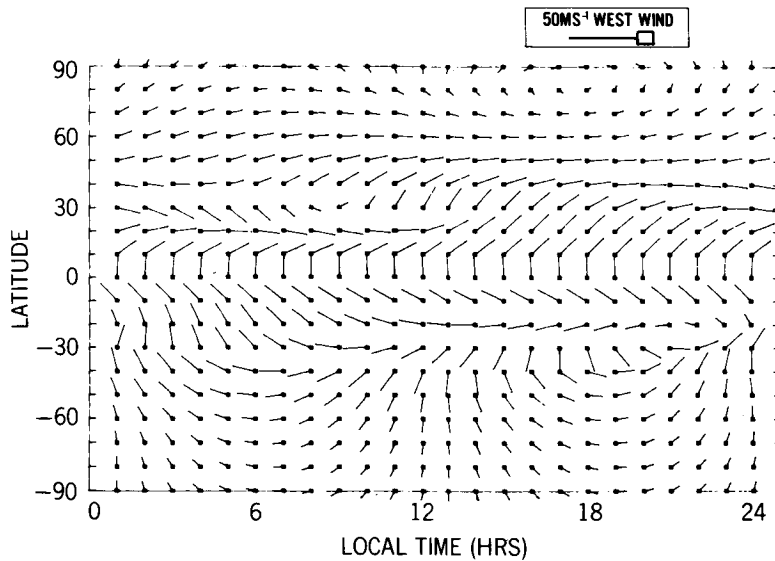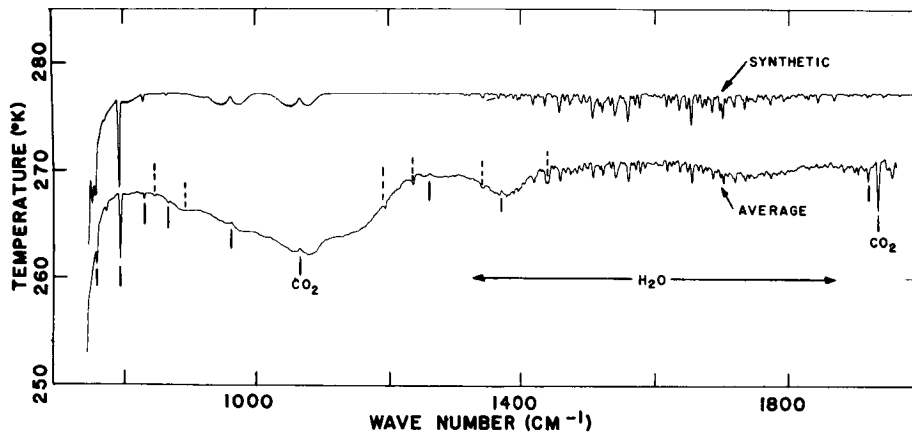
Figure 10. Near-surface tidal wind.

Figure 11. Mariner-9 IRIS spectra.

We also have not included in the artificial spectrum the CO_2 lines that show up at the upper limit of our spectral range. Most of the other lines visible are due to water vapor, the so-called 6.3-micron band of water vapor. Several features are apparently not water vapor, but features which have so far escaped identification. We have seen this average spectrum only for about a week now.

In summary, I should say that we found Mars quite interesting; the atmosphere has been much more dynamic than we expected it to be. We have also demonstrated that Fourier spectroscopy, and particularly infrared emission spectroscopy, is a very useful tool in studying Mars.

121

DR. ROMAN:

What were those sort of large waves in the last spectrum you showed? Your synthetic spectrum was pretty level.

DR. HANEL:

The larger features are due to the silica dust.

MEMBER OF THE AUDIENCE:

Can you give me any information about the height of the silica dust in the atmosphere?

DR. HANEL:

I think most of the dust is in the first scale height.

DR. DUBIN:

Typical winds are under 50 meters per second. That seems to be much lower than the amounts required to lift the dust up, is that correct?

DR. HANEL:

This is quite right. The wind speeds we see seem to be somewhat higher than the average winds in the earth atmosphere, but at that time, they could not lift dust on a large scale. We think that at the beginning of the storm there was a large temperature gradient between atmosphere and surface, which led to an instability of the atmosphere. This turned over the dust, and then it worked like a hurricane on earth, except the heat comes not from the latent heat of water, but from solar absorption by the dust.

In time, the dust storm spreads, but by the time it engulfs the whole planet, the upper atmosphere has already warmed. We have a very stable situation then. The winds are much below the level where you would expect them to carry dust up on a large scale. By the time Mariner-9 arrived, I think the dust storm was over.

RETURNED LUNAR SAMPLE ANALYSIS

John A. Philpotts

For the past three years, a group of us at Goddard has been studying returned lunar samples with particular emphasis upon certain trace elements, including the rare earths. The immediate goal of this research is to work out the origin of the various lunar rocks.

I'm going to try to bring you up to date on this aspect of lunar science. At present, three families of lunar rock are recognized, and two basic models have been put forward to explain the relationships between these three families. The early missions, Apollo-11, Apollo-12, and Luna-16 visited mare areas (Figure 1), and the local rock is mare basalt. Basalt is a type of cooled lava. However, it became apparent from studies of the soils at these mare sites that at least two other types of rock existed elsewhere on the moon.
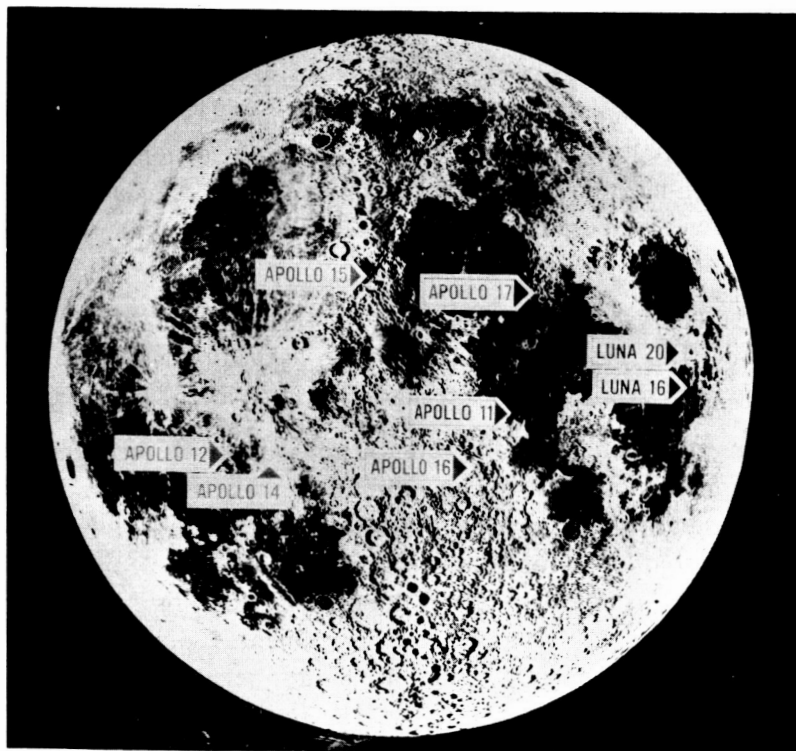

Figure 1. Lunar mission landing sites.

Samples returned from the Fra Mauro Hills on the very next mission, Apollo-14, consisted predominantly of one of these other rock types. This has become known as KREEP basalt— K potassium; REE, rare earth elements; P, phosphorous. In addition to being high in these trace elements, KREEP is also high in aluminum, whereas the mare basalts are high in iron.

The third type of material, anorthosite, was first returned from the Apennine Mountains on Apollo-15. Anorthosite is a rock consisting mostly of the mineral plagioclase. Anorthosite is presumably formed by accumulation of plagioclase, crystallizing from a silicate liquid.

Those are the three types of materials: the iron-rich basalts that fill the mare basins, KREEP basalt, and anorthosite. Our studies of soils from all these various sites, excluding Apollo-17, show that the KREEP component increases in a westward direction. The Fra Mauro Hills are largely KREEP, and the orbital gamma-ray experiment shows that KREEP-like material is highest in concentration in Mare Imbrium and in regions within Oceanus Procellarum.

The soil studies also show that the anorthosite component increases towards the highlands, and highlands material returned from Apollo-15, Apollo-16, and Luna-20 are rich in anorthosite. This is in agreement with the very informative data returned by the orbital x-ray experiment.

It's not possible, by any simple mechanism, to relate the KREEP basalt and the mare basalt. It appears that these basalts result from fusion of two quite different source materials. For this reason, a number of investigators, perhaps most notably Gast in Houston and Ringwood in Canberra, have proposed an initially layered moon model, also called a heterogeneous accretion model.

They assume that there was once an outer shell on the moon of more refractory, aluminous material; that the KREEP basalt results from fusion in the outer shell; and that the younger mare basalts come from deeper within the moon, from fusion of less refractory material.

This heterogeneous accretion model, however, is not without its problems, and one of these relates to the europium anomalies which are found in essentially all lunar materials. Figure 2 shows what a europium anomaly is. The various trace elements that we analyzed are lithium, potassium, rubidium, strontium, barium, the rare earth elements, and zirconium and hafnium. Europium is in the middle of the rare earths. This is merely an abundance diagram, but the abundances of each one of these elements is normalized to its concentration in chondritic meteorites, merely to produce a more regular plot.

In Figure 2, 12013 Dark and the 14 soils are representative of KREEP basalts; 15555 is a mare basalt; and 15415 is an anorthosite analyzed by Gast. Now, all mare basalts returned to date have shown a depletion in europium. This is a negative europium anomaly, and the best place to put this missing europium is in the highland anorthosites, which obviously
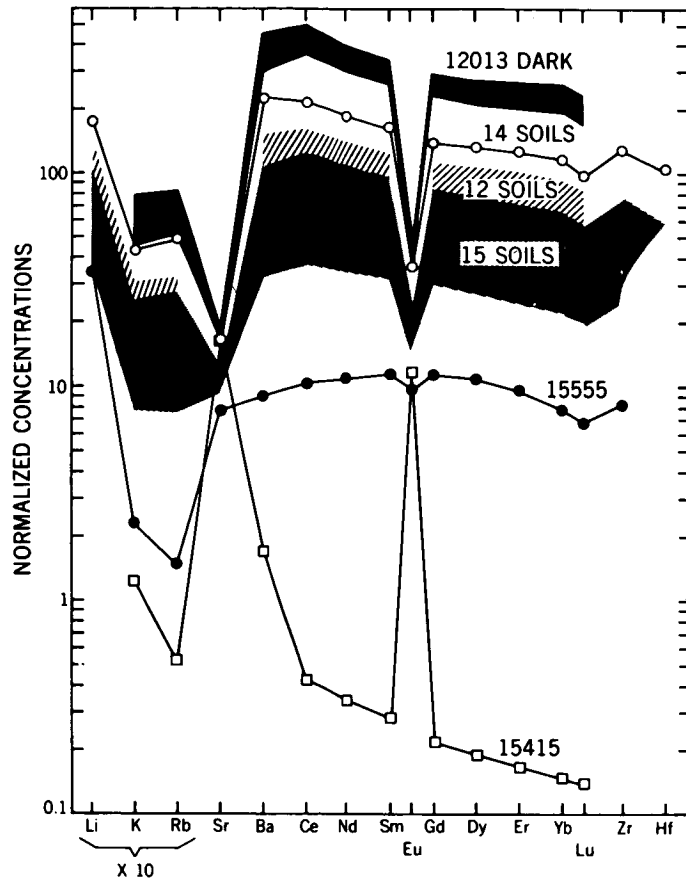
Figure 2. Chondrite-normalized trace-element
abundances in selected lunar materials.

have very large positive europium anomaly. In the heterogeneous accretion model, how-ever, there would be no connection between the old highland anorthosites and the younger mare basalts coming from the interior of the moon.

A stronger argument against the heterogeneous accretion model is that many ratios of volatile to involatile elements are quite constant in all lunar materials. This is shown for the potassium-barium pair in Figure 3. All the samples that we have looked at here at Goddard are plotted, and you can see that the ratio of potassium to barium is quite con-stant within a factor of two. This may be compared with a range for potassium/barium for natural solar system materials of over three orders of magnitude.

Potassium is a volatile element; barium is relatively refractory. So the constancy in this ratio might not be expected if heterogeneous accretion had taken place, at least, simple temperature-dependent heterogeneous accretion. So we have proposed another model, starting with a homogeneous moon, rendered heterogeneous by igneous processes; that
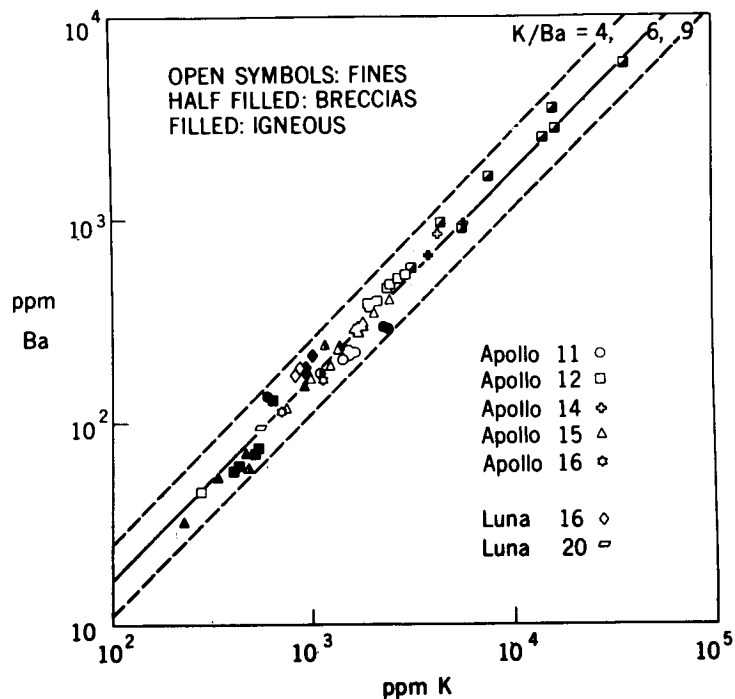
Figure 3. K versus Ba for lunar samples

is, by processes of melting and crystallization. In this model, the mare basalts would result from fusion of iron-rich source material that was produced by accumulation of iron-rich crystals during a previous igneous event. The anorthosites would be formed by cumulation of plagioclase crystals during this previous igneous event.

So, that's the picture as it stands at present. Essentially three types of rock: the iron-rich basalts filling the mare basins; the KREEP basalts in Mare Imbrium and Oceanus Procellarum; the anorthositic suite of the highlands; and the two models, the heterogeneous accretion model and the igneous differentiation model.

I think we have enough material in hand at present to work out the origin of these various rocks, and from that, the evolution of the moon and its relation to other solar system materials. The next few years are going to produce the major payoffs in lunar science.

126

APOLLO ORBITAL GEOCHEMISTRY: X-RAYS

Isidore Adler

John Philpotts has established the need for the orbital experiments which I'll describe here. He has pointed out that there's strong evidence for feldspar lost in the mare basalts, quite likely to the lunar highlands. And he's also pointed out the significance of the three major rock types found in the various Apollo missions in understanding the evolution of the moon.

I think it's fairly obvious that the information we have about these rocks comes from very carefully selected areas—the particular areas at which the various landings took place (see Philpotts, Figure 1 above). So I think it is reasonably evident that a knowledge of the large-scale distribution of these various rock types is very important in understanding the moon's evolution.

The experiments which I will describe here have actually enabled us to learn a great deal about the global distribution of these rocks and about the nature of the lunar crust. Let me briefly describe the experiments which flew on Apollo-15 and -16 as part of the lunar orbital science program, and then I'll show you some of the results.

In Figure 1 we see the science instrument module and the experiments which are the subject of this talk. At the base of the module is an X-ray fluorescence device, and in the same envelope is a series of detectors for looking at alpha particles, presumably from processes involving radon and thoron diffusion. The gamma-ray experiment is located on a retractible boom, also found at the base of the spacecraft.

I'll discuss the X-ray experiment, and then Jack Trombka will tell you about the gamma-ray experiment. The X-ray experiment was based on the simple fact that the sun bathes the moon in very large fluxes of soft X-rays, capable of producing characteristic X-rays from the lunar surface of some of the elements in the lunar surface. The nature of the solar flux is such, however, that it can only produce characteristic radiation from a few elements, including magnesium, aluminum, and silicon. Fortunately, in respect to this study, nature's been kind, because these are important signature elements for the types of rocks that Dr. Philpotts has mentioned.

The experiments functioned very well on both missions. In the X-ray case, we obtained over 100 hours of data during the Apollo-15 mission, and at present we have about 60 hours of useful data from Apollo-16.

Figure 2 points out the sort of aerial coverage of the X-ray experiment. Keep in mind here that we only looked at those areas which were illuminated by the sun. Aluminum-silicon ratios and magnesium-silicon ratios are plotted here. I want to point out that we covered
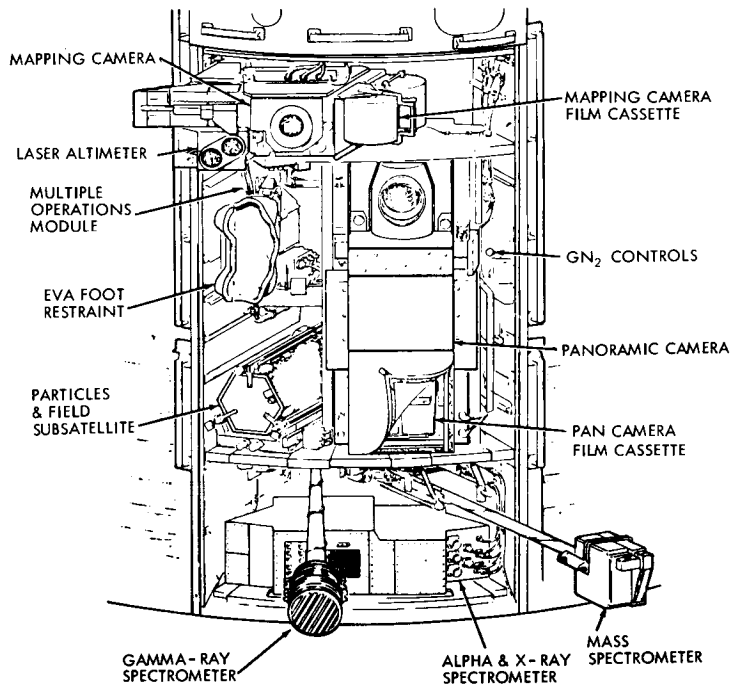
Figure 1. The science instrument module.
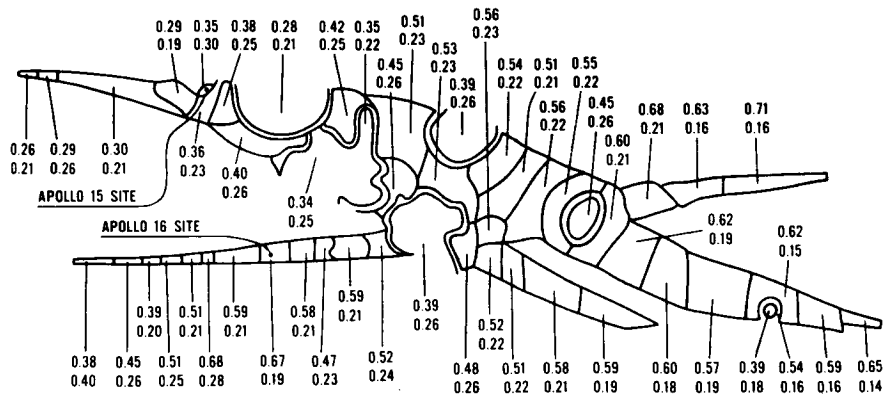
Figure 2. Al/Si and Mg/Si concentration ratios along the Apollo-15 and -16 groundtracks. The upper values are Al/Si and the lower values are Mg/Si.

an area ranging from the backside of the moon, the eastern highlands, clear over into the Mare Imbrium Basin. We had a substantial area of overlap between 15 and 16 and got very good agreement between them; in fact, agreement on the order of about 10 percent.

Figure 3 shows the results from Apollo-15—we have similar results from Apollo-16. We've actually been able to identify a number of features on the moon, and have also identified

Figure 3. Al/Si intensity concentration ratios versus longitude.

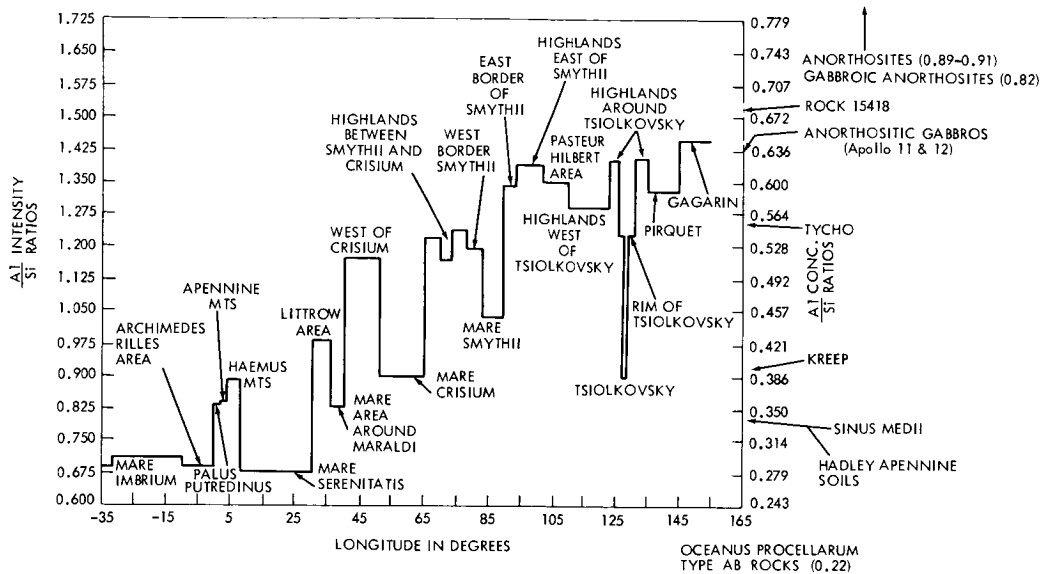the aluminum-silicon intensity ratios and magnesium-silicon intensity ratios for these various features. What we've plotted here for reference purposes are a series of analyzed materials—materials which were either brought back by the Apollo missions, or were analyzed by the Turkevich-backscatter experiments, or were analyzed by the Soviets.

We observed that the highlands, particularly the Eastern Limb highlands, are very rich in aluminum, which is what one would have predicted if in fact anorthosites come from the highland areas. We also find, looking at the aluminum-silicon intensity ratios, that when going from east to west they drop very markedly as one approaches the eastern mare areas; in fact, there's an enormous difference, like a factor of two.

There are some other very interesting things to be observed: As one flies over relatively smaller features and looks at the aluminum-silicon ratios, one sees very distinct contrasts between the small mare basins and the surrounding highlands. This has considerable significance with respect to the horizontal transport of materials. For example, I might mention that one of the points of view expressed about horizontal transport is that it is due to electrostatic charging. In fact it has been pointed out that the mares are filled by material which has drifted down from the highlands. If one keeps in mind that this X-ray experiment is entirely a surficial one—it doesn't see down below a fraction of a millimeter—then it is obvious that this puts a distinct limit on horizontal transport of this sort.

If this were a very active mechanism then we would see no contrast between the mare and the highlands. I think a very spectacular example of this is the crater Tsiolkovsky,

which is a relatively small feature. It's one of the few craters on the backside that actually shows a dark fill, and we're able to say now that the fill is basalt, like the other mare basalts. The observation that it's a small feature and yet we see such excellent contrasts does in fact put this distinct limit on horizontal transport.

An on-going debate has been whether there's some relationship between the measured optical albedo values and chemical composition. In fact, it has been suggested by Dr. Paul Gast that we make a study of the correlation between optical albedo and the chemistry represented by the aluminum-silicon values in Figure 4. We find that the aluminum-silicon values and the optical albedo values follow each other very nicely for the most part, except that on occasion one sees an anomaly.
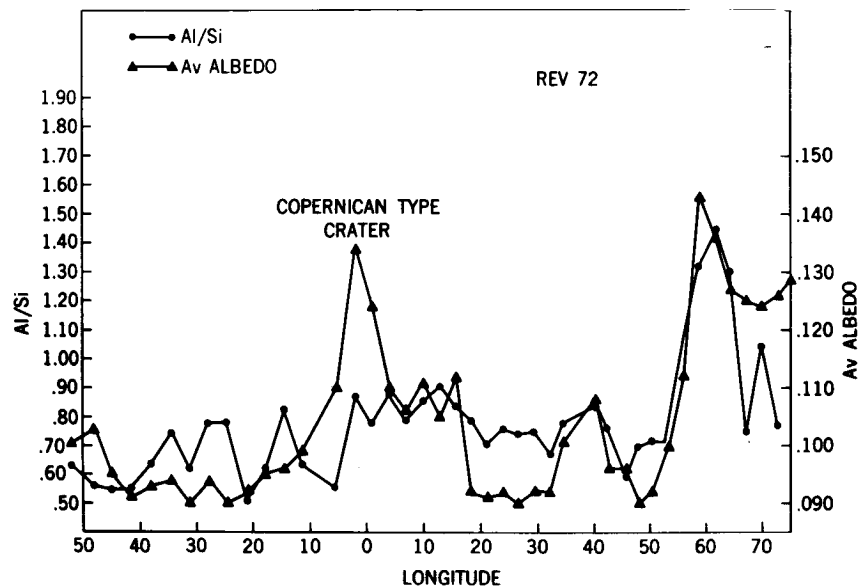

Figure 4. Al/Si intensity values versus optical albedo for an
Apollo-15 groundtrack.

Where the mare basalts are very dark and the optical albedo is low, the aluminum-silicon intensities are low. In the highlands, which are bright, the aluminum-silicon intensities are high. Now and then one discovers an anomaly such as we see in Figure 4, which observation proves to be a Copernican-type crater. It's a small crater which is quite bright. Thus we do occasionally see a change in albedo which is not accompanied by a chemical change. I think, therefore, that for the most part the optical albedo is a good clue to the chemistry, but always with the reservation that there may be terrain-related phenomena which can give anomalous results.

Perhaps the only other reservation is that a small feature can give you a large effect in the optical albedo, on a scale much finer than we can actually see with the X-rays.

Nevertheless, it seems to be a very good clue to compositional changes.

Let me conclude by telling you what the X-ray experiments have told us. We have now essentially a global look at the lunar surface. We have a fair notion of the scale at which we can expect to see these various types of rocks.

The X-ray experiment shows that the moon is well differentiated; it tells us that the mare basalts actually cover very large areas; it tells us how representative are the lunar samples of the large area from which they were collected; and it shows us something about the limitations of horizontal transport, namely, that the highlands are very rich in feldspar. They're not pure anorthosites as had been proposed, but they certainly are rich in anorthositic type material. This experiment, together with the gamma ray experiment which is described in the next presentation, do go a long way towards tying the various observations from the lunar samples into a more comprehensive picture of lunar evolution.

APOLLO ORBITAL GEOCHEMISTRY: GAMMA RAYS

Jacob I. Trombka

Gamma-ray spectra were obtained during Apollo-15 and -16, using an omnidirectional detector. We had no collimation thus our view extended from horizon to horizon. If one looks at the resolution in terms of line features, we did have the capability of being able to resolve features of approximately two and a half degrees in terms of the lunar surface, roughly 100 to 200 kilometers wide.

The spectrum shown in Figure 1 was obtained on Apollo-16. This was one of the best of either mission. The spectrometer on Apollo-16 was improved from that flown on Apollo-15; our energy resolution was much improved. The data plotted in Figure 1 is the sum of seven hours of data and therefore represents an average total lunar orbit spectrum.
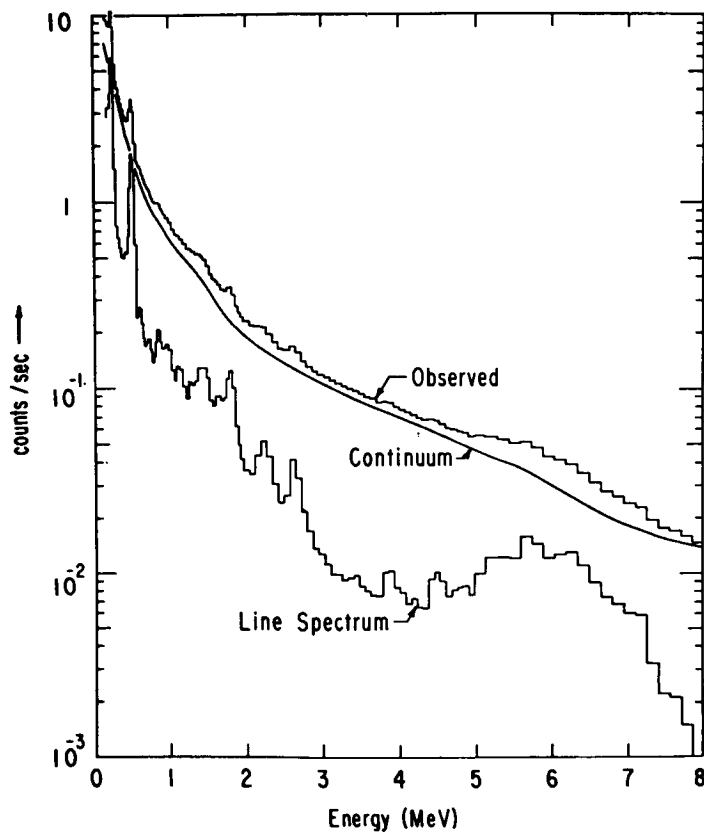

Figure 1. Lunar gamma-ray spectrum.

132

There are two components of the observed spectrum: The first is a continuum, which we believe contains no information which can be used for geochemical interpretation and which must be subtracted before one can start seeing the detailed structure of the surface chemistry. The second component of the spectrum is due to discrete energies representing interpretable geochemical information.

This background curve is our best estimate of the magnitude of this effect. It is approximately 85 percent of the total measured spectrum. Once this is subtracted, the discrete line structure can be seen. Again, there are two components of the discrete line spectrum: one, the natural radioactivity due to potassium, thorium and uranium; and the other, due to the cosmic-ray-induced activity in the lunar surface. Because of the lack of hydrogen, the major contribution to the induced spectrum is due to high energetic neutron interactions produced by (p,n) reaction in the lunar surface. We see very few if any, thermal neutron interactions, so, the major induced interactions can be attributed to neutron inelastic scattering. Starting at the highest energy position of Figure 1, we see the triplet line of oxygen at about 5.1, 5.6, and 6.1 MeV. We then come to the 2.6 line, which is characteristic of uranium, a natural gamma-ray emitter. The next line you see here is about 2.2; we suspect this is partially due to hydrogen in the spacecraft rather than in the lunar surface. There are some lines of silicon in this same region.

As we look at the lower energies, we come to the 1.78 line of silicon, which is an (n,n') reaction. The next two major lines are the 1.47 MeV line of potassium and the 1.37 line of magnesium. There are a number of lines of uranium and thorium in the intermediate energy region. Finally we come to the 0.84 MeV line of iron due to an (n,n') interaction. Below this line there are again a number of lines due to uranium and thorium.

The major line at 0.51 MeV can be due to a myriad of interactions, and so in terms of our interpretations, it will be ignored. Rather than performing a detailed unfolding of the spectrum, we have studied the integrated spectrum in the region from 0.58 MeV to 3 MeV. In this region 90 percent of the emission lines are due to radioactivity; the rest are due to the inelastic scattering reaction mentioned above; and if one assumes that silicon and oxygen are relatively constant, the variation in the photon intensity in this region is almost directly proportional to the variation in radioactivity.

Figure 2 summarizes the results obtained on Apollo-15 and Apollo-16 for the distribution of radioactivity. The empty areas do not indicate a depletion of radioactivity; but regions not overflown. The cross-hatched areas are the only areas where data were obtained.

The intensity or closeness of cross-hatching is proportional to the activity. The radioactivity is at a low in the highlands on the backside of the moon. This corresponds to a half part per million (ppm) to three-quarters of a ppm of thorium in this region as compared to about 10 ppm in the Oceanis Procellarum/Mare Imbrium area on the front side of the moon.
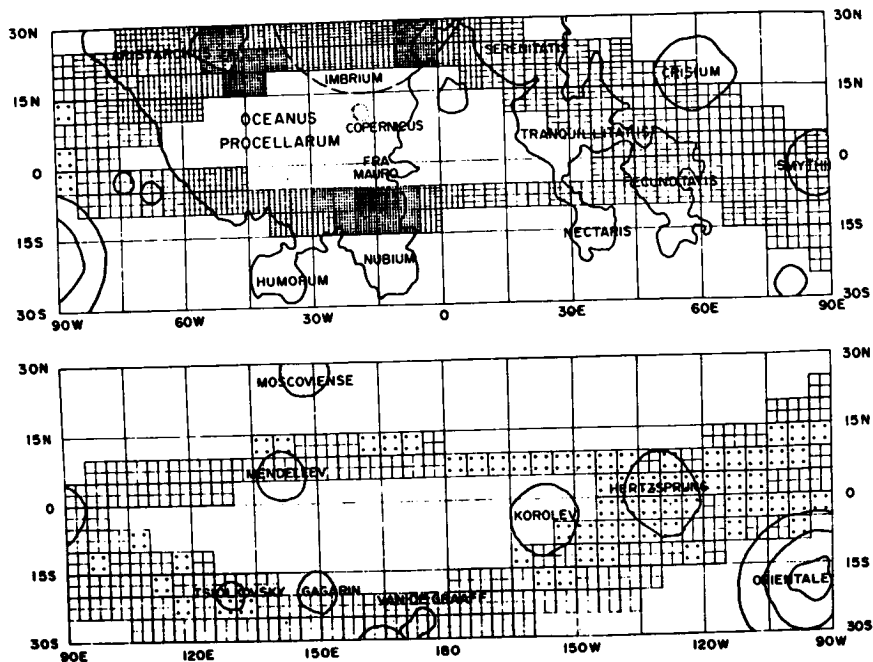
Figure 2. Distribution of lunar radioactivity.

What becomes very obvious is that most of the radioactivity is confined to this Oceanus Procellarum/Mare Imbrium region. And the very interesting characteristic of this region is that there is very definite structure within this region. In fact, there are three radioactivity peaks; one south of Archimedes, the second around Aristarchus, and the third south of Fra Mauro. Since Apollo did not overfly Fra Mauro, it is hard to see how far this peak radioactivity extends. The amount of radioactivity tends to decrease in all directions away from these peaks.

Also in the highlands, surrounding the maria area, one sees a much higher radioactive content than in any of the other highlands. Thus there seems to be quite a bit of lateral mixing around the basin area itself.

Further, as you go towards the eastern maria area, there is a decrease of radioactivity in the Serenitatis basin. One does not see much contrast between the mare area and the highlands around it. This lack of contrast may be due to lateral mixing from the Imbrium area.

When you look at Mare Smythii, for instance, you see quite a significant contrast between the mare area and the highland area around it, a maximum corresponding to the basin and lowering as you go up into the highlands. As we move to the backside of the moon, what we consider the western highlands area, we find less activity than in the eastern highlands area.

Another very interesting feature occurs around the Van de Graff area: We see another peak of radioactivity. This is the only spot on the backside where we have seen such an increase. This peak occurs in the same region where a magnetic anomaly has been observed.

134

Again, how does one describe these distributions? I think one sees two types of radioactive distribution on the lower surface. The peak areas could be explained by assuming emplacement by an impacting body. I find this a little hard to believe, in terms of the placement and extent of the radioactivity.

One could also say that these peaks are due to ejecta, and possibly to the release of the materials from far beneath the lunar surface. One could also consider this as a sort of heterogeneity in the lunar surface itself. The latter explanation, or possibly a combination of the last two or three explanations, seems to explain the distribution more reasonably.

The second component of the radioactive distribution shows a very interesting correlation with lunar topography. Let us consider Figure 3.
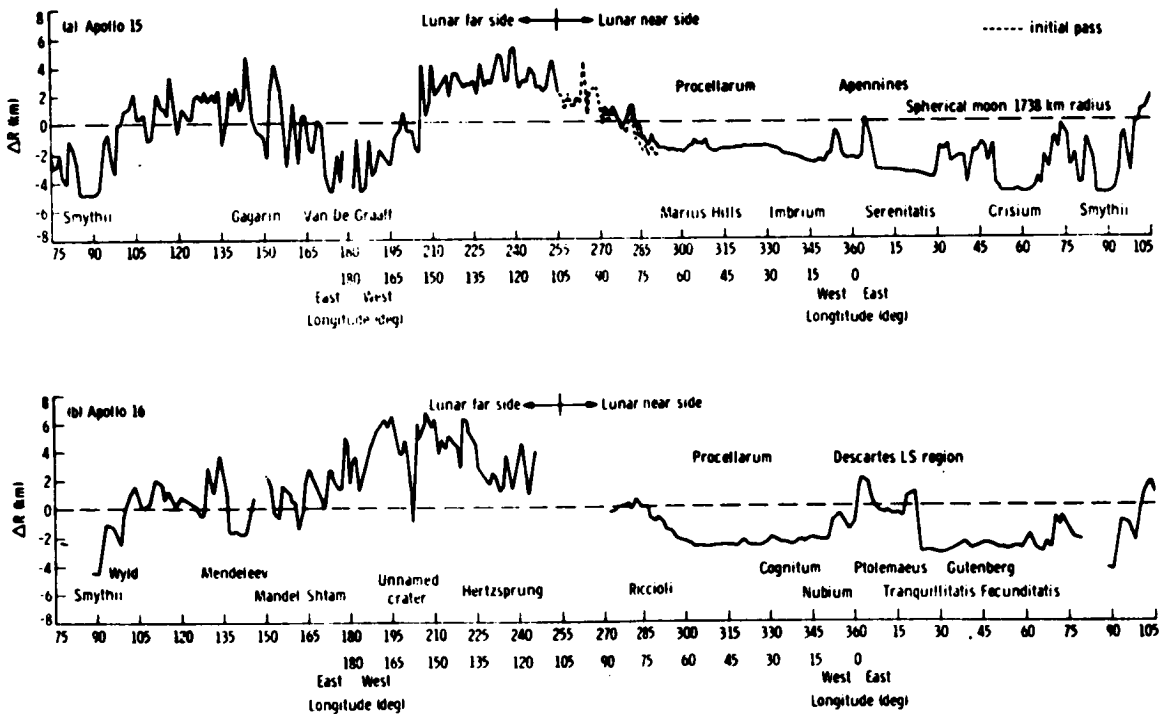
Figure 3. Lunar topography.

These lunar topography data were obtained with the Apollo-15 laser altimeter. If you correlate the radioactivity with this plot, you find a significant anticorrelation. That is, if you ignore the peak areas described above, radioactivity increases with decreasing height. Thus the Van de Graff area, a major depression on the backside, corresponds to the maximum of activity. This correlation appears to hold for the entire lunar surface except around the peaks in the Imbrium area.

CHEMICAL EVOLUTION OF COSMIC CLOUDS

Bertram D. Donn

In this report I will attempt to relate several recent observational results on the inter-stellar medium and some associated chemical problems. These phenomena deal with the early evolutionary stages of star formation. There is evidence suggesting that these facets of galactic research may be brought much closer, spatially and temporally, by the comets which Dr. Jackson will talk about in a later presentation.

One of the unexpected and exciting developments in astronomy in the last few years was the discovery of a complex array of polyatomic molecules in heavily obscured clouds. This is shown in Figure 1, which has a horizontal scale indicating time and a vertical scale show-ing the rate of discovery of molecules. It started with diatomic species, then added ammo-nia and water, and now runs up to molecules like methyl acetylene with seven atoms. Notice the prevalence of organic molecules in this figure. This is not unexpected in view of the exceptional ability of carbon to form such a wide variety of molecules.
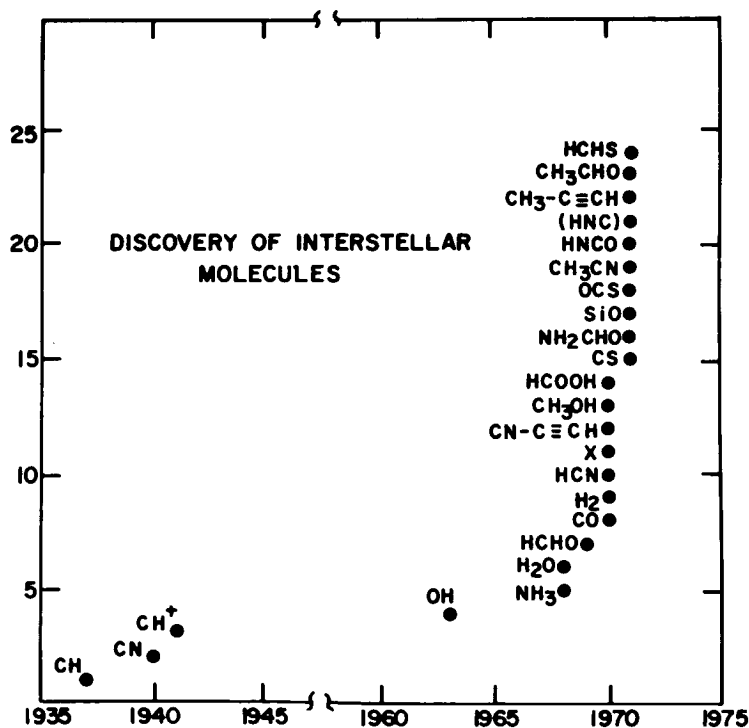

Figure 1. Discovery of interstellar molecules.

One of the characteristics of interstellar chemistry is the fact that it differs in some very significant ways from the terrestrial chemistry to which we are accustomed. Because of the comparatively low densities in interstellar clouds, thermodynamic equilibrium is not generally attained. Therefore, the nature and rates of chemical reactions will tend to be different in these clouds from similar reactions in the laboratory. The application of terrestrial data to interstellar conditions must be done with great care. A second factor that must be taken into account is the relative time scales for chemical reactions compared to those for changes in the astronomical system. Again, if conditions change faster than the reaction proceeds, equilibrium will not be reached.

Figure 2 shows one of the best delineated of the dense, dark clouds – this is the Coal Sack in the southern hemisphere. It's a very dark cloud, quite isolated against the background of the Milky Way. I think it represents the type of structure characteristic of regions where polyatomic molecules are found, such as Sagittarius B2 and the Orion Nebula source. These regions, however, are so overlaid with both bright and dark material that their structure cannot be seen.

Recent work by Bok and his students has shown that the Coal Sack is not a uniform cloud; you can see some indication of this in the figure. There are regions where stars shine through and some regions that are very dark. Bok proposes a conglomerate of many clouds, some large and some small. The dimension across the Coal Sack is about 2 million astronomical units (AU). Some of the subclouds that he has found are about 30,000 AU across.

Radio astronomers have found that in one of the regions where Bok observes a dense subcloud there is a localized concentration of formaldehyde. Quite generally, there seems to be an association of molecular clouds with regions of radio emission and infrared sources. The two latter regions are localized zones of higher temperatures and densities.

Thus, we come to a scheme in which the clouds where the molecules are found are really an array of what probably represent collapsing regions, where densities and temperature are going up. These are precursors to primordial stellar nebulae, where in time, stars will form, and in some cases, solar systems.

What we want to do is study the nature of the molecular processes of these clouds and to be able to say something about the chemistry that is going on. What molecules may we expect and how may they be related to various problems? How are these molecules related to other classes of astronomical molecules, molecules in the less dense clouds, and molecules present on primitive planets or planetary surfaces and atmospheres? Cometary molecules are particularly interesting. As Dr. Ness pointed out in his introduction, in comets we are probably seeing the most primitive material of the solar system. Cometary flybys and more advanced missions will enable us to study them much better. Finally, these complex organic molecules suggest a transition from chemical to biological evolution and raise the question of exobiology and the origin of life.
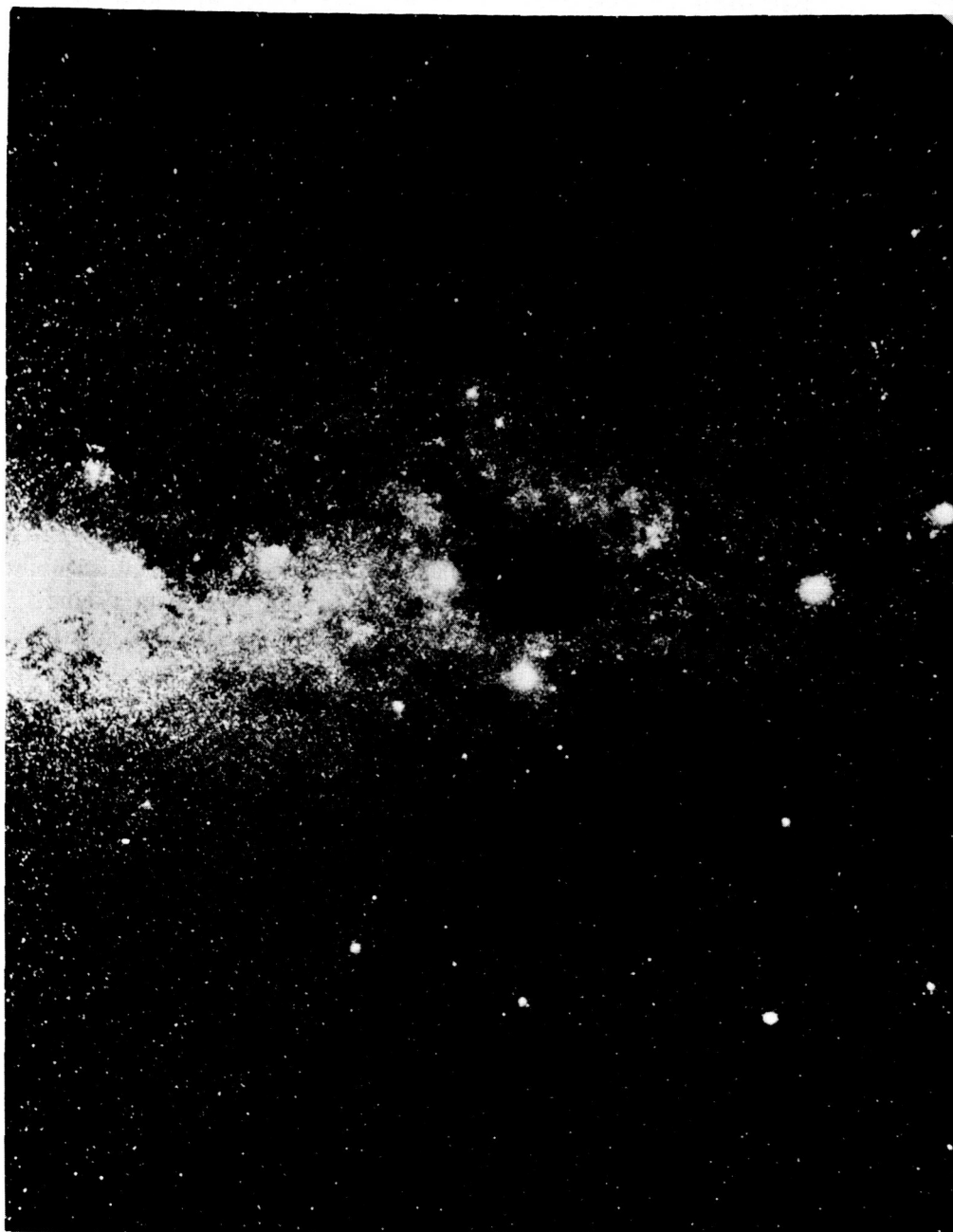
Figure 2. The Coal Sack.

In regard to these molecules, I pointed out that one cannot safely assume thermodynamic equilibrium, make thermodynamic calculations, or take laboratory data out of handbooks. We have to be careful for three main reasons; two were given earlier but may be worth repeating. One is that we have to look at the time scales. If the chemical processes take

place within a time scale that is comparable to, or even less than the astronomical time scale, that is, the rate at which temperatures and pressures are changing in the astronomical system, equilibrium will not be attained. Second, the calculation of thermodynamic equilibrium does not predict what molecules will form. One has to assume the molecules and put them into the calculations. If we make a wrong guess, or leave out some molecule, a numerical result will come out, but it will be for the wrong array. Lastly, recent work in the laboratory has shown that the chemical reactions and mechanisms are very sensitive to the detailed energy distribution of the molecules. In ordinary laboratory work under thermodynamic equilibrium there is a Boltzmann distribution among internal energy states, and the resultant mechanisms and reaction rates depend on that. At the low interstellar densities, we do not have statistical equilibrium, as astronomers have known for a long time. There is not a distribution of excited molecular states, but only of the very lowest-lying state. Therefore, the reaction rates characteristic of interstellar matter can differ by orders of magnitude, and in some cases will, from what one would expect based on a laboratory result.

In order to follow up how these molecules may react as the cloud collapses and the chemical system heats up and cools down, we have done some experiments to get an idea of time scales and products. For this, we have settled on a fairly simple system, the reaction of hydrogen cyanide and molecular hydrogen at about 1000 K. Hydrogen cyanide is one of the fairly abundant interstellar molecules and it is also a very significant molecule in terms of chemical evolution and life processes. Therefore it seemed interesting to study this reaction. We have done these experiments at an HCN to H_2 ratio of 1 to 100 to simulate the large excess of cosmic hydrogen. We measured the amount of hydrogen cyanide that was remaining in our system as a function of time. The equilibrium calculations say that there would be very little hydrogen cyanide left at equilibrium; and that nitrogen, ammonia, and methane should be the main products.

Figure 3 shows what we observed. We found that HCN decays with a half-life of about 20 hours. One complication is shown by the cross in Figure 3, corresponding to a much faster rate when we increased the surface of our vessel by a factor of about ten. This indicates a large surface contribution to the reaction. We are in the process of doing some experiments to elucidate just what this effect is, and how to take the effect into account.

Measurements of the HCN half life at different temperatures are shown in Figure 4. Most of the experiments are done at 1093 K, yielding an 18-hour half-life. If we go about 100 degrees higher, the half-life decreases to about nine hours, and at about 100 degrees lower, the rate increases to 53 hours. These rates correspond to an activation energy of about 80 kilojoules (kJ) (20 kilocalories) per mole, just under one electron volt. This seems low for this type of reaction with stable molecules and is probably affected by the surface reaction.

The significance of these experiments to astronomical problems can be shown by considering Cameron's latest model of the primordial solar nebula. He obtained the following
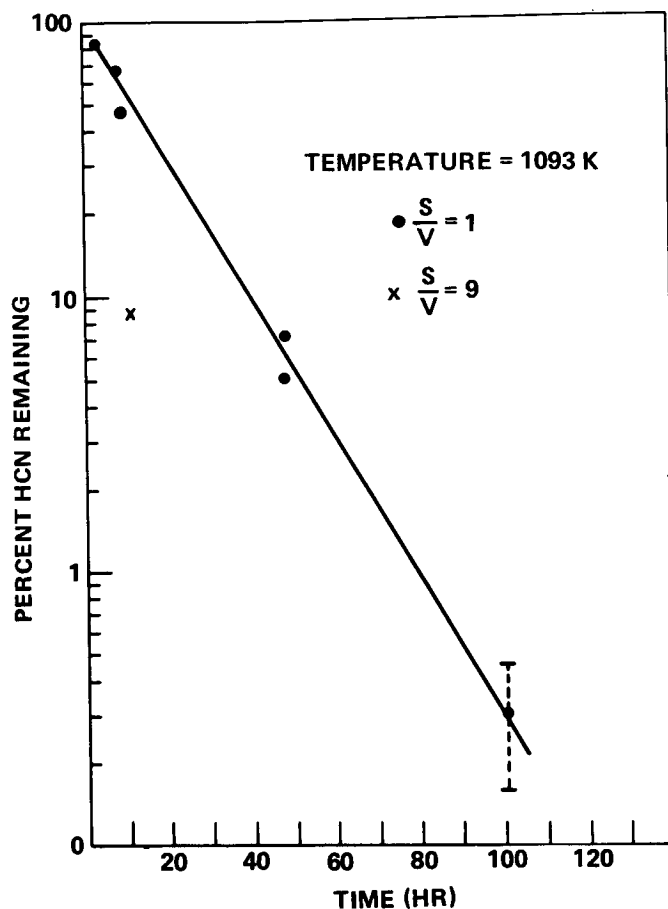
Figure 3. HCN decay rate.

T (K)	$\tau(e^{-1})$ (HR)
1170	9
1093	18
980	53

Figure 4. Half-life of HCN-H_2 reaction (measured).

results for the temperature and cooling times of the nebula. Within one AU the temperature was about 2000 K and cooled with a time scale of one to ten years. Between one and ten AU, the temperature drops from 2000 K to 200 K and the cooling time scale is

140

about ten years. Beyond ten AU, the temperature becomes lower yet and chemical processes will be frozen.

Figure 5 displays the chemical half-life as a function of temperature for the experimental activation energy of 80 kJ (20 kcal) per mole and for a value of 200 kJ (50 kcal) per mole, probably more appropriate to a pure gas phase reaction. With an activation energy of 80 kJ (20 kcal) per mole, the reaction time becomes several days at 800 K, and a year just below 700 K. At 500 K it is 270 years. For Cameron's nebula these reactions would effectively freeze out near 700 K between the positions of the Earth and Saturn. At the higher activation energy for the same nebular region, chemical and astronomical time scales become comparable at temperatures between 800 K and 900 K. At 700 K, reaction times are on the order of 10^4 years. Reaction rates may be considerably increased by energetic processes that produce free radicals and ions. The final composition for such reaction mechanisms again would deviate from equilibrium calculations.

T(K)	E	
	80 kJ/mole	200 kJ/mole
2000	0.27 hrs	2 sec
1500	1.48 hrs	140 sec
1000	40 hrs	147 hrs
900	120 hrs	101 hrs
800	20 days	94 days
700	123 days	7.2×10^3 yrs
500	270 yrs	1×10^9 yrs

Figure 5. Half-life of HCN-H_2 reaction (theory).

What this means is that if one is going to study and predict what sort of molecules may form in one of these clouds, and then try to relate this to the observed interstellar molecular clouds, to the preplanetary nebulae when the plants and comets formed, or to the composition of early planetary atmospheres, we need to take into account nonequilibrium effects. This involves the effects mentioned previously; the time scale, which we discussed here; the density-internal energy problem; and the role of ions or radicals. The experiments and theoretical analysis need to be continued in order to be able to estimate molecular compositions of interstellar clouds. This is the direction in which we are working.

COMET ENCKE: METEOR METALLIC ION IDENTIFICATION
BY MASS SPECTROMETER

Richard A. Goldberg

Arthur C. Aikin

Positive metallic ions have been measured in the Earth's atmosphere between 85 and 120 km, during the period of the β Taurids meteor shower, which is associated with Comet Encke. The ions originate during and following ablation of extraterrestrial debris by the Earth's atmosphere.

The existence of metallic ions in the upper atmosphere has been known for some time. Many elements have been discovered with the aid of rocket-borne ion mass spectrometers. In most cases, the major components are Mg^+ and Fe^+ with lesser quantities of Na^+, Al^+, K^+, Ca^+, Cr^+, Si^+, and other metals (1,2,3,4). Normally a layer of these constituents is observed near 95 km with a 3-5 km half width. Since metallic ions are atomic, they have long lifetimes and can be acted on by external forces such as those generated by wind shears in the presence of the terrestrial magnetic field (5). At mid-latitudes, this can result in additional layers of enhanced metal ions having extremely narrow half width (1/2 to 2 km) and located between 105 and 130 km at the wind shear levels. When these layers are observed by ground based ionosondes, they are termed sporadic E (E_s).

The enhancement of metal ion density during meteor showers is primary evidence for their extraterrestrial origin (1, 3). In addition, Junge et al. (6) have argued that constituents such as sodium could not diffuse from the Earth's lower atmosphere to 100 km in a reasonable time. Comparisons of metal ion relative abundances with neutral species in Earth crust samples and chondrites have shown closer agreement with chondritic relative abundances even though such comparisons disregarded ion and neutral transport processes and ion-neutral chemistry in the atmosphere (7).

The present results were obtained from a rocket-borne ion mass spectrometer, similar to that discussed previously (4,8). The instrument was flown on July 3, 1972, at 7:43 LMT (solar zenith angle = 57.1°) from El Arenosillo, Spain (37.1° N, 6.7° W) and reached an apogee of 122.8 km. The launch occurred during a growing enhancement of E_s, observed just prior and during the rocket flight by a ground based ionosonde.

Figure 1 illustrates the measured currents for the observed metallic ion distribution (major isotope for each constituent) from 85 to 120 km. Metal ions (24^+, Mg^+; 40^+, Ca^+; 56^+, Fe^+; 58^+, Ni^+) were first detected at 85 km. Near 90 km the ions 23^+ (Na^+) and

28^+ (Si^+) also appeared. The density of ions continued to increase to 100 km where other constituents emerged. Above 100 km, the distribution remained nearly constant to 112 km. At this height, the density increased approximately 30 times to form a well-defined metallic ion peak, which terminated abruptly at 115 km. The vertical arrows indicate the maximum observed value for each constituent within the peak.
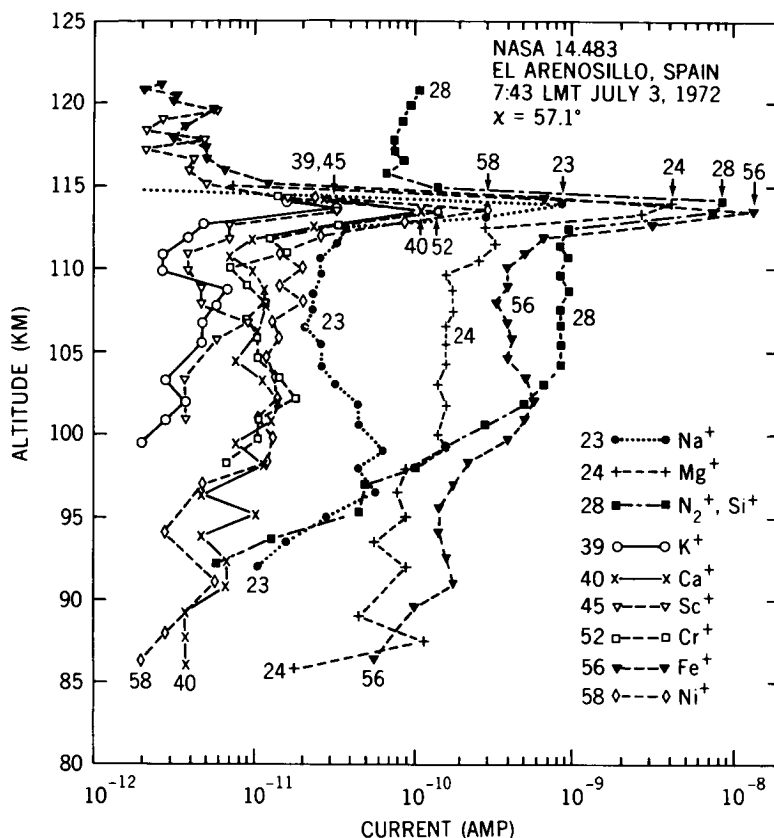

Figure 1. Vertical height profile of positive metallic ion composition observed during the upleg flight of 14.483. Arrows mark the observed peak value for each metallic constituent within the E_S layer.

The total metal ion density comprises 15 percent of the total ion density within the layer at 114 km, and is less at other altitudes. Narcisi (3) has shown that during the Leonid meteor shower, metal ions may comprise as much as 40 percent of the total ion density. The β Taurids shower normally extends over a few weeks' duration (9) with typical flux increases of only a few percent, possibly accounting for the reduced enhancement of metal ions observed during the β Taurids shower. Comparison of local ionograms for the time period of the rocket flight on days prior and during the day of the flight show an abnormal enhancement of foE_s to 10 MHz from the more nominal 5-MHz values observed on preceding days. This enhancement occurred within the 10-minute period prior to launch and

disappeared 45 minutes after launch. The possibility does exist that enhanced meteor activity before launch could have contributed to this observed phenomenon.

Figure 2 illustrates four upleg spectra obtained during transit through the E_s layer. The altitude scale is shown on the abscissa. The spectra ordinate in volts is approximately logarithmic in current. The region between each spectrum reflects the period during which the spectrometer operated in a high-pass filter mode, the data of which are not pertinent to this discussion.
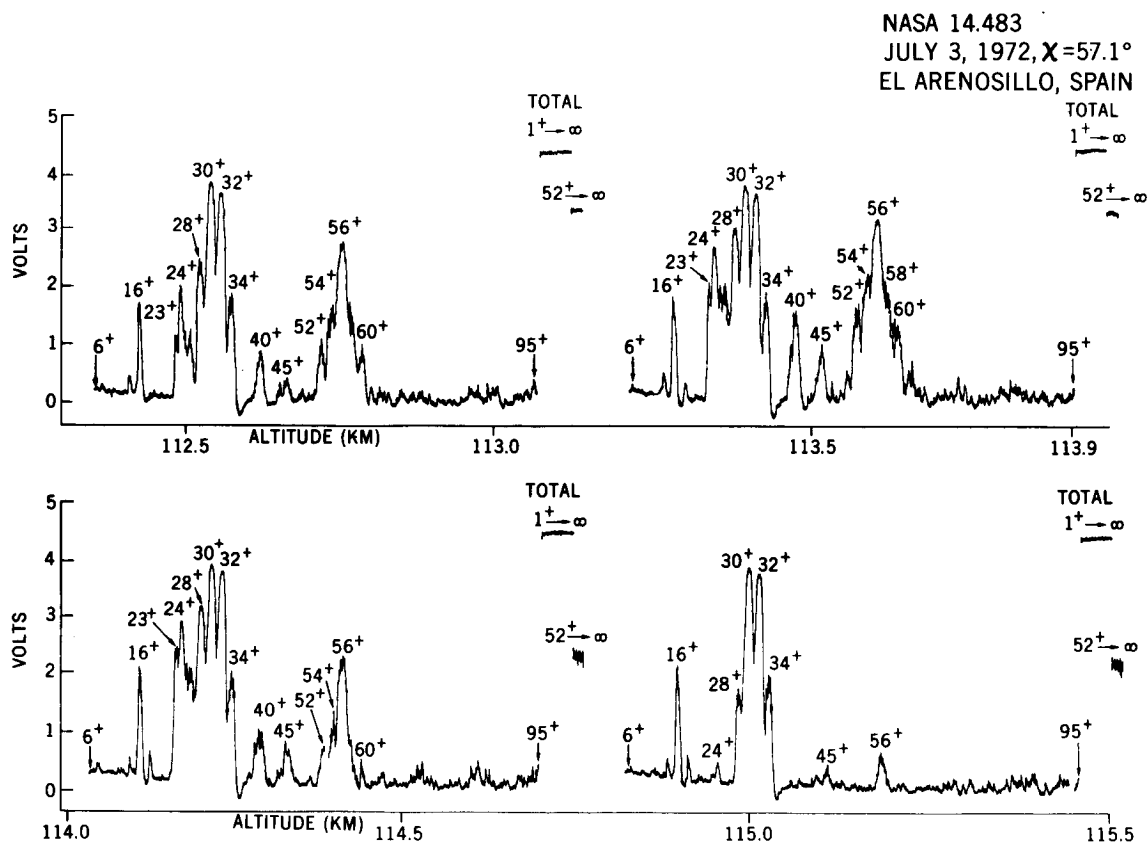

Figure 2. Raw spectra depicting ion composition during transit through E_s layer on uplet of 14.483. The voltage display is approximately logarithmic in current and thereby, in relative composition among species.

Assuming the ions to be singly ionized, metallic constituents with their principal isotopes in the layer are identified as $23^+(Na^+)$; 24^+, 25^+, $26^+(Mg^+)$; $28^+(Si^+)$; $39^+(K^+)$; $40^+(Ca^+)$; $45^+(Sc^+)$; $52^+(Cr^+)$; 54^+, $56^+(Fe^+)$; 58^+ and $60^+(Ni^+)$. Other isotopes and constituents, e.g. $27^+(Al^+)$ and $55^+(Mn^+)$, may have been present, but instrument resolution did not permit accurate identification of such constituents during the flight. The ions $16^+(O^+)$; $30^+(NO^+)$; 32^+, $34^+(O_2^+)$ as well as a certain fraction of $28^+(N_2^+)$

are gaseous ions normally present at these altitudes. They result from ionization of the different neutral constituents in the Earth's atmosphere together with ion-neutral chemistry.

Figure 3 provides the observed relative abundance of each metallic ion species normalized to Si^+, near 101 km and 114 km. Values of major constituents are believed accurate to ± 20 percent; of minor constituents, to ± 100 percent. Each result contains contributions from all isotopes using the measured value for the principal isotope and the known isotopic abundance ratios to more accurately evaluate minor isotopic concentrations. Since the height resolution near 114 km is 0.8 km, the narrowness of the ledge required comparison of the observed rather than exact maximum value for each constituent within the ledge. Between 101 and 114 km, most constituents maintained a constant relative abundance, with the exception of 28^+, which became dominant between 102 and 112 km. This effect was caused in part by a contribution from N_2^+, estimated to be not greater than 10 percent at 114 km and unknown at 101 km. The ratios are therefore lower limits and subject to a uniform increase due to N_2^+. However, the similarity of the abundances at both heights would tend to suggest a negligible or equivalent contribution of N_2^+ to 28^+ at either height. For comparison, the chondritic and Earth crustal abundances of the neutral metals (10) are also included. Due to low Si^+ concentrations below 100 km, ratios based on Si^+ are usually not possible except within the E_s structure. This may reflect a low proportion of Si in the normal daily meteor influx, a higher altitude for Si^+ ablation, or a unique atmospheric behavior of Si^+ for sufficient periods of time to permit ion-neutral reactions to oxidize Si^+ and enhance recombination, at least below 100 km.

	ION ABUNDANCES NASA 14.483		NEUTRAL ABUNDANCES (AHRENS, 1965)	
ELEMENT	101 km	114 km	CHONDRITES	CRUST
Na	12	9.1	3.8	8.5
Mg	49	57	80.9	6.9
Si	100	100	100	100
K	0.81	0.38	0.51	7.4
Ca	3.6	1.2	7.9	14.9
Sc	1.0	0.35	0.005	0.008
Cr	3.4	1.77	1.7	0.0085
Fe	149	158	141	19.9
Ni	4.2	4.7	7.6	0.027

Figure 3. Relative abundances of ions (rocket data) and neutral elements (chondritic and crustal) normalized to SI^+, SI = 100.

The table demonstrates the similarity of the relative atmospheric ion abundances to neutral metal abundances in chondrites. In particular, the species Mg, Cr, Fe, and Ni most clearly illustrate the extraterrestrial origin of the ion composition. We also note the apparent overabundance of Na^+, an enhancement that has also been observed during other metal ion samplings (7). The origin of the large sodium ion densities is not understood.

One intriguing aspect of this data is the relatively high abundance of 45^+, identified as Sc^+. This is the first reported observation of m/e = 45 at metallic ion heights. Sc^+ is not a comfortable identification because of the apparent difficulty in producing a source so rich in this constituent. The suggestion that it might be the molecule NH_2HCO, which is believed to be a stable precursor in cometary material, appears unlikely, as ablation processes would probably dissociate this molecule prior to ionization. Doubly ionized constituents seem to be ruled out because of the rapid recombination rates required for such ions and because there are no observed ions at m/e = 90. This constituent also exhibits peak concentration in the E_s layer (Figure 1) implying a high probability that it is atomic in structure. Instrumental contaminants and irregularities do not appear likely since 45^+ reappears at the same altitude in the downleg data. The above indicate an ion enhancement of order 10^2 times the normal relative abundance of Sc seen either in chondrites or in the Earth's crust. This may be a property of the cometary debris.

The measurement of upper atmospheric metallic ions during the β Taurids meteor-shower period suggests that extraterrestrial debris can contain enriched abundances of trace constituents not predictable from cosmic abundance arguments. The enhanced densities of such constituents are still quite small and probably below the threshold of detection by other techniques such as ground-based optical sensing. Hence, in situ ion composition measurements during and following significant atmospheric entry of extraterrestrial debris offers a unique opportunity to analyze and study such a material.

REFERENCES

1. V. G. Istomin. *Space Research,* 3 (1963). 209.

2. J. M. Young, C. Y. Johnson, and J. C. Holmes. *J. Geophys. Res.,* 72 (1967). 1473.

3. R. S. Narcisi. *Space Research,* 8 (1968). 360.

4. A. C. Aikin and R. A. Goldberg. *J. Geophys. Res.,* 78 (1973). 734.

5. G. Chimonas and I. W. Axford. *J. Geophys. Res.,* 73 (1968). 111.
   J. D. Whitehead. *Radio Science,* 7 (1972). 381.

6. C. E. Junge, O. Oldenberg, and J. T. Wasson. *J. Geophys. Res.,* 67 (1962). 1027.

7. D. Krankowsky, F. Arnold, H. Wieder, and J. Kissel. *Int. J. Mass Spectrom. Ion Phys.* 8 (1972). 379.

8. R. A. Goldberg and A. C. Aikin. *J. Geophys. Res.,* 75 (1971). 8352.

9. P. M. Millman and D. W. R. McKinley. *The Moon, Meteorites, and Comets,* B. M. Middlehurst and G. P. Kuiper, ed. 1963. p 715, Table 9.

10. L. H. Ahrens. *Distribution of the Elements in Our Planet,* 1965. Appendix A, p 97.

COMETARY SPECTRAL ISOPHOTES

William M. Jackson

Today I would like to talk to you about our observations of two recent bright comets, Comet Bennett and Comet Tago-Sato-Kosaka. Comet Bennett is an example of the dust comet; Comet Tago-Sato-Kosaka is an example of a bright comet that shows no dust. The observations were made by Mr. Curtis McCracken here at Goddard on our 91-centimeter (36-inch) telescope, using the image intensifier; and the reductions were done by Dr. Jurgen Rahe from the Technical Institute in Berlin.

Figure 1 is intended to get us oriented on what we are talking about and shows schematically the various regions of the comet. We are not going to discuss the tail, but we are interested in the region of the coma within 10^4 to 10^5 kilometers of the nucleus.
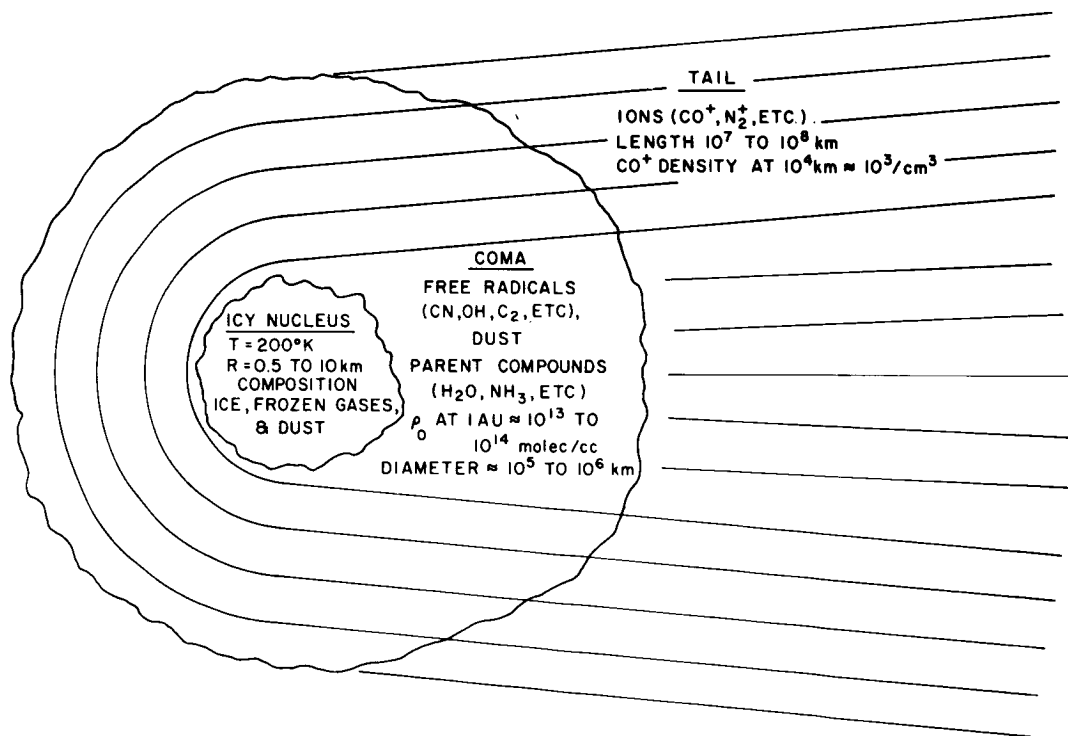

Figure 1. Schematic drawing of a typical comet.

This figure, of course is not done to scale. By way of comparison, the OAO result of Code on the Lyman α halo extends to a distance of 10^7 kilometers from the nucleus. The inner region of coma we are concerned with is not resolved by the OAO results.

Spectral analysis of the light from this region in the coma shows molecular emission lines superimposed upon a continuum. By isolating these molecular emission lines, we can obtain a picture of a comet in one of the unstable species, for example, CN, C_2 or CO^+.

In Figure 2, I have tried to show you what kind of scientific results might be expected from these monochromatic isophotes. The monochromatic isophotes of comets give us the spatial distribution of radicals, ions, and dust in comets. Theories of comets predict spatial distribution of these species and we can test the theories by comparing the predicted with the observed spatial distributions.

The theories tell us how the radicals and ions are formed, and also tell us something about the hydrodynamics of the inner coma. This in turn gives us information on the origin of comets and their interaction with the interplanetary medium.
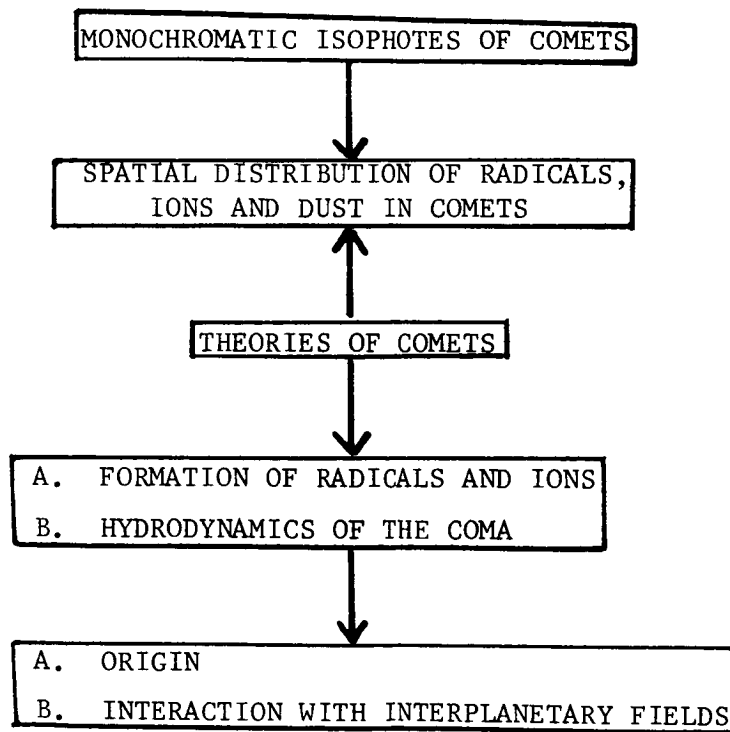

Figure 2. Results of monochromatic isophotes.

149

Figure 3 shows monochromatic isophotes of CO⁺. We are beginning to see at distances of 5×10^4 kilometers from the nucleus, the formation of the ion tail. At distances within one to two thousand kilometers of the nucleus, the isophotes are fairly circular.

An alternate explanation of this kind of behaivor is that we could be seeing the formation of the superimposed dust tail. However, these features are rather narrow and one would expect the dust tail features to be much broader.
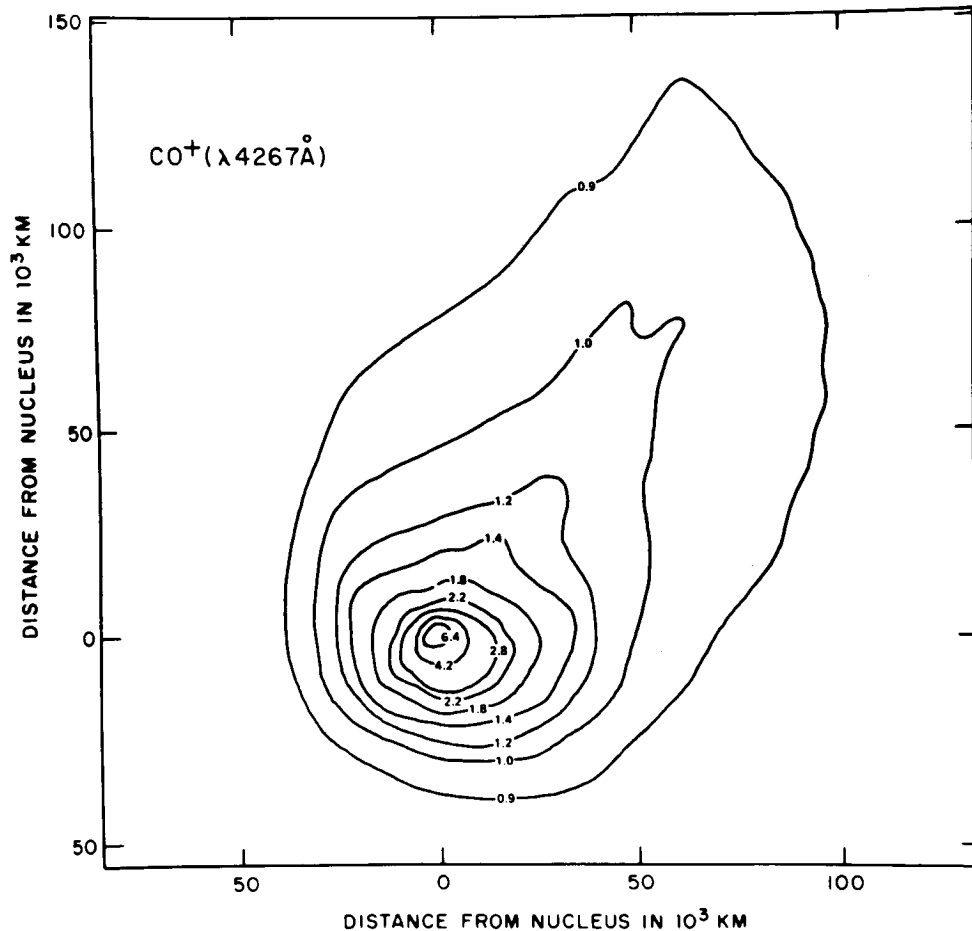

Figure 3. Monochromatic isophotes of CO⁺.

In Figure 4, we have a picture of the C_2 isophotes in Comet Bennett. In the inner region we also have circular isophotes. At large distances, we get a pronounced asymmetry. This asymmetry, we feel, is somehow related to the dust in Comet Bennett. Now, there are two possible explanations. One is that we just haven't isolated the dust component with our monochromatic filter; the other is that we have an extended source of gas along the path of the orbit of the comet.
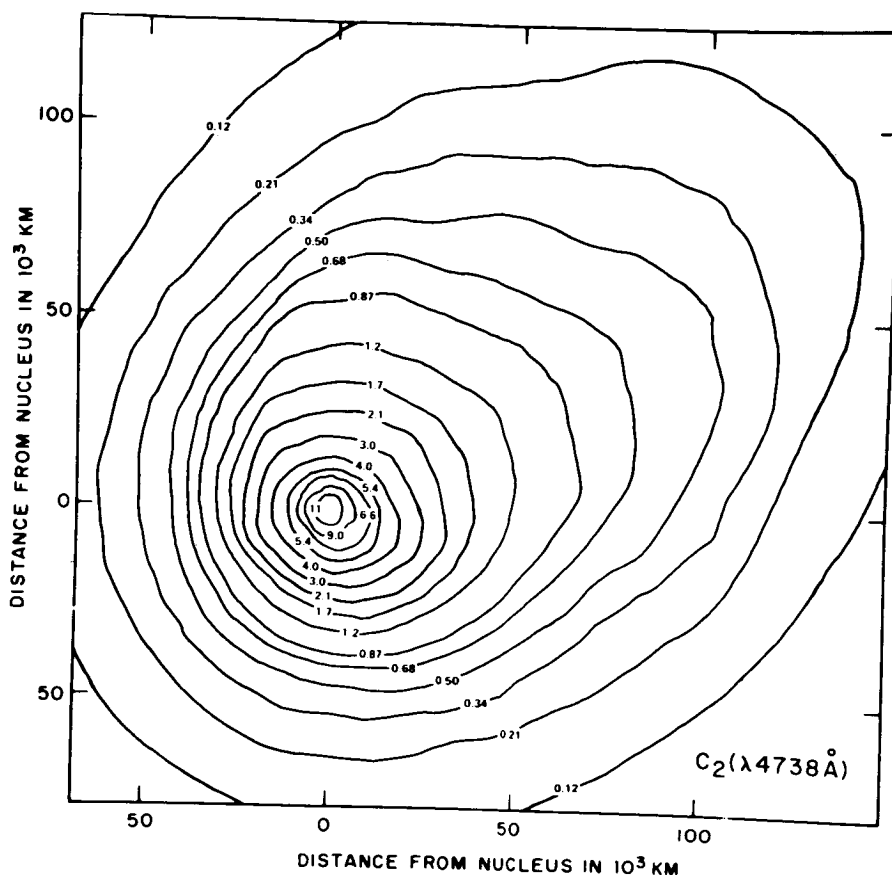
Figure 4. The C_2 isophotes in Comet Bennett.

Now, one could envision that as the comet comes near the sun it releases dust. Some of this dust is still volatile, heats up further, and evaporates, forming more parents of the C_2 molecules. This would then explain this nonuniform distribution.

In Figure 5 — by way of comparison with the previous figures, we have the C_2 isophotes from Comet Tago-Sata-Kosaka, which does not show an appreciable amount of dust. You see that these isophotes are much more uniform. There is still some asymmetry, and Freeman Miller has ascribed it to nonuniform evaporation of gas.

In summary, we have obtained a wealth of valuable information whose continuing analysis should throw a great deal of light on the chemical and physical mechanisms that occur in comets. I have shown only three pictures of isophotes, and we have something like 75, so there is a lot of data to be analyzed.
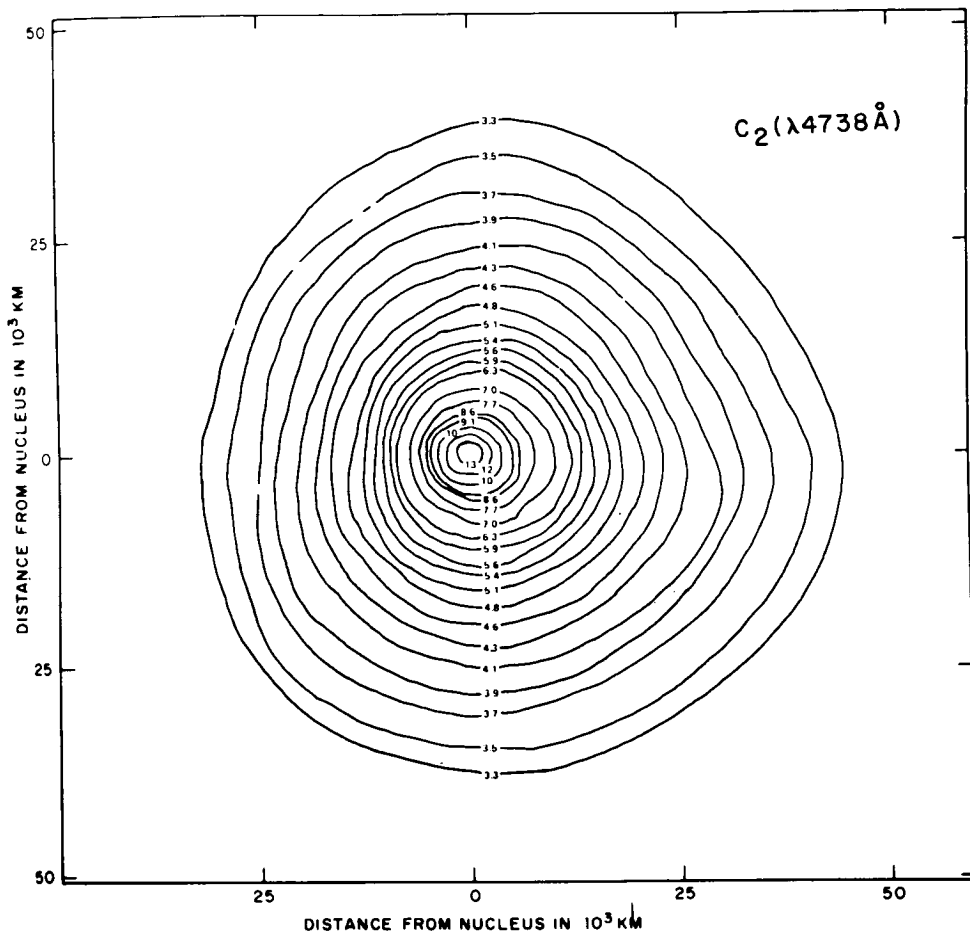
Figure 5. The C_2 isophotes from Comet
Tago-Sata-Kosata.

Member of Audience:

Where is the sun?

Dr. Jackson:

The sun in all these photos is opposite the direction of the extended isophotal lines.

152

MISSIONS TO COMETS

Robert W. Farquhar

We have heard some of the reasons why we might want to send a space probe to a comet. Now, I am going to address the question of how this could be accomplished. In doing so, I shall outline a sequence of missions to comets that could form the basis of a new program in this area.

The two most important guidelines that were used in formulating this mission set are listed in Figure 1. The first one is scientific. It specifies that the early missions will be limited to simple flythroughs of the coma, or head, of the comet. Although this type of mission will not have quite as much scientific yield as a rendezvous mission, it would be much easier to execute. A flythrough of the coma would give us some valuable information about the composition of the ionized and neutral particles that make up the cometary atmosphere. It would also tell us something about the nature of the solar-wind interaction with the comet, answering such questions as: Does a bow shock exist, and if so, how far is it located from the nucleus? If the targeting accuracy is good enough, some imaging of the nucleus might also be possible.

GUIDELINES

SCIENTIFIC — COMA FLYTHROUGH

$\left\{ \begin{array}{l} \text{COMPOSITION OF COMETARY ATMOSPHERE} \\ \text{NATURE OF SOLAR — WIND INTERACTION} \end{array} \right.$

TECHNOLOGY — USE EXISTING CAPABILITY

MISSION SEQUENCE

1977	GRIGG — SKJELLERUP
1980	ENCKE
1985 – 86	HALLEY

Figure 1. Missions to comets.

The second guideline states that we should use existing capability as much as possible. This means present-day launch vehicles and state-of-the-art spacecraft systems and subsystems.

Following these guidelines, I have devised an evolutionary sequence of cometary missions that is listed in Figure 1. The first mission, a flythrough of the comet Grigg-Skjellerup, would take place in 1977. Grigg-Skjellerup is a typical short-period comet that is very faint and can only be seen with a fairly large telescope even when it is relatively close to the earth. It does not seem to possess a tail. The second mission in the sequence would be targeted to the comet Encke, which is the brightest of the short-period comets. When it comes close to perihelion at times of maximum solar activity, it generally forms a short tail. These two missions, then, would be precursors to the comet mission of the century, which is the mission to Halley in 1985-86. Halley comes around only once every 76 years and it is the brightest periodic comet. To make the most of this rare opportunity, it is important to carry out the precursor missions early enough to permit experiment-design feedback.

The nominal mission profile for Grigg-Skjellerup in 1977 is given in Figure 2. The main reason that this comet is such an attractive target in 1977 is its extremely favorable orbital geometry at this apparition. To minimize launch-energy requirements, it is planned to intercept the comet as it crosses the ecliptic plane, which just happens to be very close to the comet's perihelion. Notice that the intercept point is only 0.20 astronomical units (AU) from the earth. Other noteworthy features of this mission are:

GRIGG – SKJELLERUP'S ORBIT

PERIHELION DISTANCE	0.99 AU
INCLINATION TO ECLIPTIC	21.10°
PERIOD	5.10 YEARS

NOMINAL MISSION PARAMETERS

INTERCEPT NEAR COMET'S PERIHELION

RELATIVE VELOCITY	15.2 KM/S
EARTH DISTANCE	0.20 AU
TRANSFER TIME	159 DAYS
LAUNCH VEHICLE	DELTA-2914

EXPLORER SPACECRAFT

SPIN-STABLIZED

| TOTAL WEIGHT | 430 KG |
| EXPERIMENTS | 68 KG |

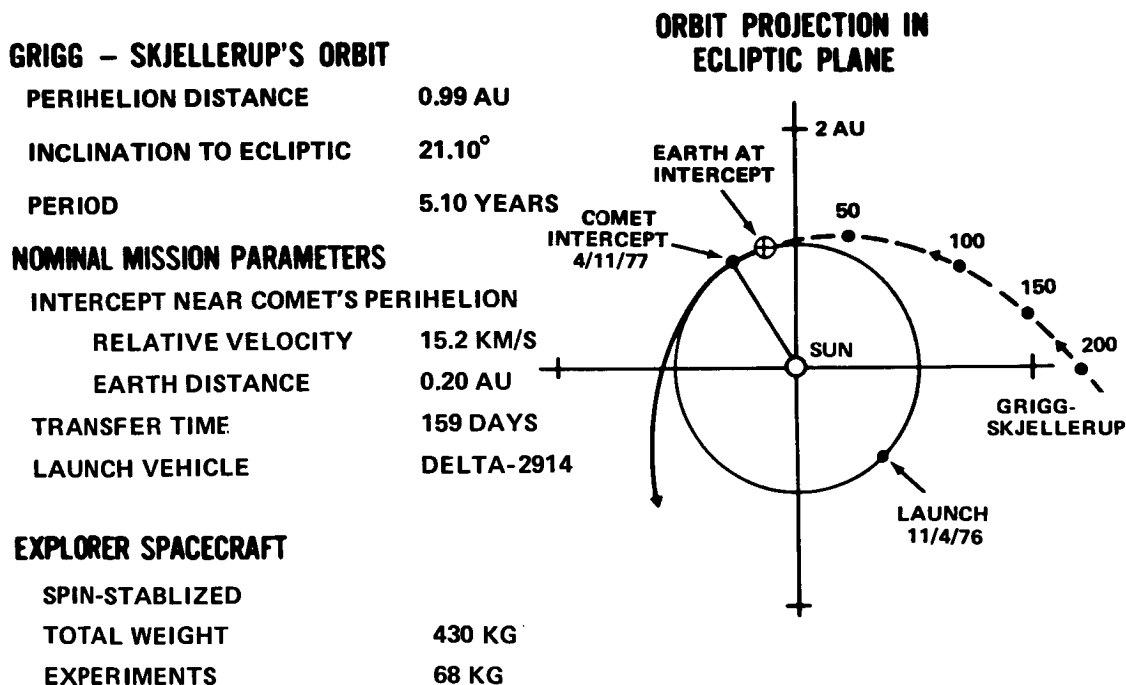### ORBIT PROJECTION IN ECLIPTIC PLANE

Figure 2. Cometary Explorer to Grigg-Skjellerup, 1977.

154

- Good earth-based sighting conditions will exist for comet orbit updates prior to intercept. This is important for spacecraft guidance and navigation, and it will enable the spacecraft to fly closer to the comet's nucleus than would be possible otherwise.

- The relative velocity between the spacecraft and the comet at intercept is only 15.2 km/s, which is quite satisfactory for comet flythrough missions.

A recently completed study has shown that this mission could be carried out with a slightly modified version of an IMP-H type spacecraft. The principal modifications would be the addition of a hydrazine propulsion system for midcourse corrections, and a high-gain antenna. Because of the small launch-energy requirements, the comparatively inexpensive Delta-2914 launch vehicle could be used to boost the 430-kilogram (950 lb) payload.

The proposed mission to Encke in 1980 is outlined in Figure 3. It should be noted that, out of all the short-period comets, Encke comes closest to the sun, about 1/3 of an AU; and its period is the shortest, about 3.3 years. The inclination of its orbit is only 12 degrees.

ENCKE'S ORBIT

PERIHELION DISTANCE	0.34 AU
INCLINATION TO ECLIPTIC	11.95°
PERIOD	3.30 YEARS

NOMINAL MISSION PARAMETERS

INTERCEPT NEAR ENCKE'S PERIHELION

RELATIVE VELOCITY	7.13 KM/S
EARTH DISTANCE	1.03 AU
TRANSFER TIME	102 DAYS
LAUNCH VEHICLE	TITAN-3D/CENTAUR

HELIOS SPACECRAFT

SPIN-STABILIZED	
TOTAL WEIGHT	430 KG
EXPERIMENTS	68 KG

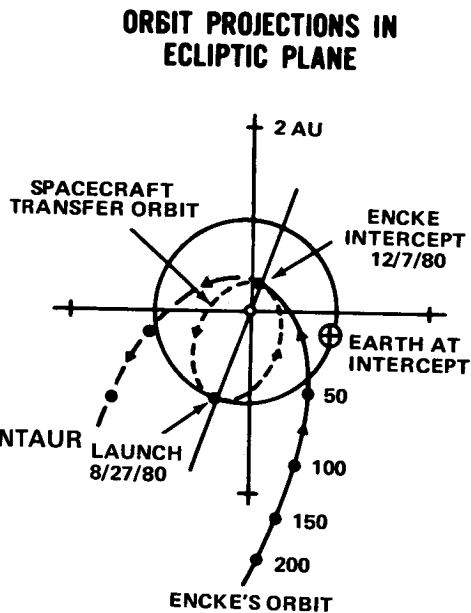## ORBIT PROJECTIONS IN ECLIPTIC PLANE

Figure 3. HELIOS mission to Encke, 1980.

Just as in the case for Grigg-Skjellerup in 1977, the orbital geometry for an intercept of Encke in 1980 is almost perfect. By specifying an intercept near the comet's perihelion, when it is very active, it is possible to use a Hohmann-type transfer orbit which minimizes the launch-energy requirements. But what is even more important is that the line of nodes

of the spacecraft transfer orbit are nearly aligned with the line of nodes of Encke's orbit, permitting a transfer in Encke's orbital plane, which reduces the relative velocity at encounter to only 7.13 kilometers per second.

Because the intercept would take place relatively close to the sun at 0.34 AU, the spacecraft must have the proper thermal characteristics to operate in this regime. A Helios spacecraft which is designed to approach the sun as close as 0.25 AU would be more than adequate for the Encke mission. The only major spacecraft modification that would be needed for the Encke mission would be to add a hydrazine propulsion system.

One other aspect of this mission which I should mention is that the period of the transfer orbit is almost exactly 0.55 years. Therefore, a second encounter with Encke would be possible after the spacecraft goes through six orbital revolutions, because Encke's period is 3.30 years. This extended-mission strategy should receive serious consideration during the preflight planning phase.

Now we come to the Halley mission, which is shown in Figure 4. The mission plan shown here is somewhat less ambitious than many of the complicated and expensive rendezvous
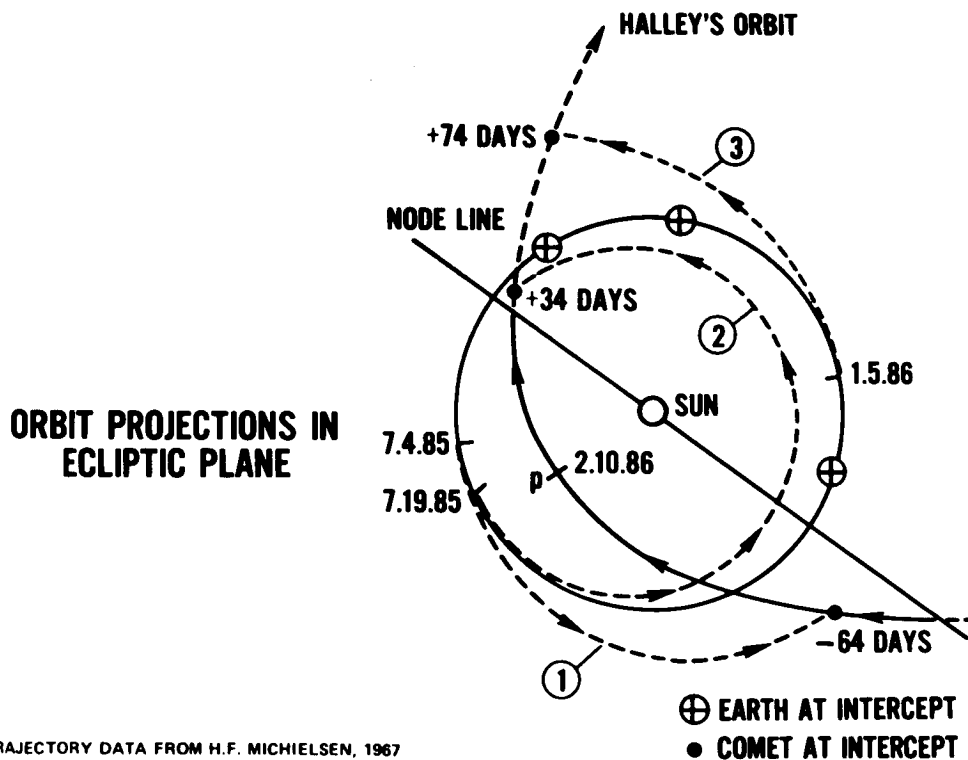

Figure 4. Multiple launch to Halley, 1985-1986.

156

missions (using nuclear-powered electric-propulsion stages) that have been proposed elsewhere. Because of Halley's retrograde motion, a rendezvous mission would be extremely difficult to achieve. I feel that many of the scientific advantages of the rendezvous mission could be realized in a much simpler way. That is, to have three separate launches (spacecraft trajectories numbered 1, 2, and 3 in Figure 4) that would intercept Halley at three different points in its orbit, 64 days before perihelion, 34 days afterward, and 74 days afterward.

The flyby speeds for each of these encounters are rather high (55, 67, and 46 kilometers per second, respectively), but long residence times within Halley's coma will still be possible because the coma is quite large.

Finally, I would like to say again that it will be extremely important to obtain scientific feedback from the earlier comet missions to take full advantage of the Halley opportunity.

MEMBER OF AUDIENCE:

You didn't describe the spacecraft that would be used for the Halley mission.

DR. FARQUHAR:

That is correct. Because the Halley mission is about 14 years away, it is not clear to me just what types of spacecraft we will have at that time.

DR. NAUGLE:

Are all of the spacecraft trajectories based on chemical propulsion?

DR. FARQUHAR:

Yes.

MR. DUBIN:

What is the accuracy of the intercept position relative to the nucleus?

DR. FARQUHAR:

They are all a little bit different. For Grigg-Skjellerup, we figure that we can come within 1000 kilometers of the nucleus. It may even be somewhat less than this. For Encke, I think that we could get almost as close as we would like. That is because Encke's orbit is very well known. The accuracy for the Halley intercept has not been calculated.

SECTION IV

EARTH OBSERVATIONS

OVERVIEW

William Nordberg
Presented by William R. Bandeen

When Dr. Nordberg indicated several days ago that he was going to the hospital for about a week he asked me if I would give the paper that he had prepared. I said I would. I would like to point out that I am no longer a member of the Laboratory for Meteorology and Earth Sciences, having been transferred recently to the Lead Center Meteorology Program Office; but most of the research that Bill discusses in his paper was carried out during the past year, when I was a member of his laboratory. To the many present who know Bill Nordberg, it will come as no surprise that even in absentia he will utilize the full twenty minutes allotted for his talk. I will in essence read his manuscript, so that, indeed, it is Bill talking to you today.

This will be a very brief overview of the Center's activity in the earth observations program. It is intended to highlight — within the framework of the various programmatic elements — some significant milestones which we have reached during the past year as well as some of the shortcomings in the program. Specific significant accomplishments in certain topics of the earth observations program will be presented in greater detail by individual investigators following this overview.

Figure 1 relates in matrix form the Center's activities in the earth observations program; both the various missions and projects shown on the right and the five classical milestones which should be inherent in each earth observations program activity shown on the left. Ideally, each of the missions and projects listed on the right should follow the logical sequence of program elements on the left. As can be seen, the thrust of our activities tends to run horizontally across all of the missions and projects, although they are strongly concentrated on the development and demonstration of observing techniques. In fact, except for ITOS, GARP, and the Earth Resources Survey SRT program, we are conducting observing technique developments in each of the earth observations missions and projects. ITOS is an exception because this is an operational program for which we have only the total system implementation responsibility; and GARP does not call for any observational components.

A good example of our ongoing activity in developing and demonstrating a new observation technique on Nimbus is shown in Figure 2. This technique deals with the measurement of infrared radiation emitted by the surface of the earth in two adjacent spectral bands at wavelengths between 8 and 12 micrometers. This development has resulted in the surface composition mapping radiometer, SCMR, to be flown on Nimbus-5 next month. It is

PROGRAM ELEMENTS	MISSIONS & PROJECTS													SRT		
	ITOS	NIMBUS	ERTS	ERAP	SKYLAB	SMS	ATS	GARP	TIROS-N	EOS	SEOS	TOS IMPR.	AAFE	TECHN.	ERS	MET.
OBSERVING CONCEPTS/ USER REQUIREMENTS		P								A	F					A
OBSERVING TECHN. DEVELOPMENT	A	A	A	A	A	A			A	F	F	P	A	A		A
OBSERVING SYSTEMS IMPLEMENTATION	A	A	A		A											
EXTRACTION OF MEASURABLE PARAMETERS	A	A					A						A			A
APPLICATION TO ENVIRONMENTAL SURVEY & RESOURCE MANAGEMENT		A					A								A	A

A = ONGOING ACTIVITIES   P = PAST ACTIVITIES   F = FUTURE ACTIVITIES

Figure 1. Earth observations activity matrix.

expected that with this technique surface temperatures can be measured with greater precision than from previous meteorological satellites and that also, by comparing the two spectral bands, the surface composition will be determined.

In Figure 2, you are traveling in an airplane flying south (from bottom to top). The Atlantic Ocean is on your left, the state of Virginia and Assateague Island are on your right. You are looking in two spectral intervals, one at 8.8 micrometers and one at 10.7 micrometers. This technique has to do with the fact that an acidic material is one which has a large fraction of silicon dioxide in it, and with a feature known as reststrahlen, wherein emissivity at 8.8 micrometers becomes lower than at 10.7 when looking at acidic material. Here we are plotting the difference between the temperature at 10.7 and the temperature at 8.8 micrometers. Where we see positive values, the reststrahlen is effective at 8.8, indicating that we are looking at acidic material; and, indeed, where we have the very high positive differences, deep red, we are looking at the sandy reaches of Assateague Island which consists almost entirely of silicon dioxide. The ocean water is essentially black. If we were to see negative differences we would be looking at so-called basic materials, such as serpentine, where the silicon dioxide contents are lower. There is no serpentine in the vicinity of Assateague Island; hence, we see no negative values here.
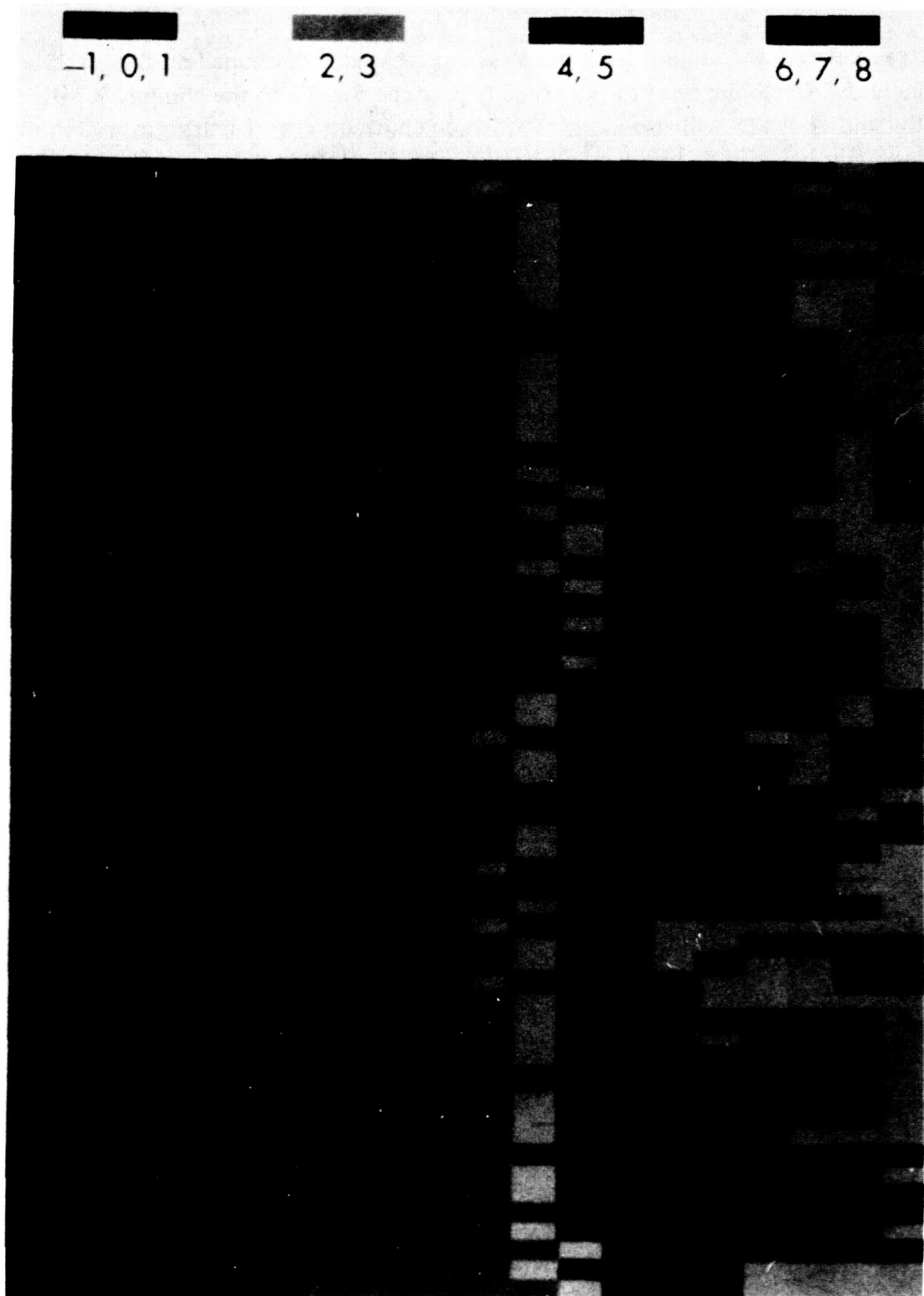
162

Figure 2. Reststrahlen effects sensed by a two-channel radiometer
flying over Assateague Island, Virginia.

This experiment on Nimbus leads us to the last technique developed on the ERTS series, namely the development of the so-called fifth band. Similar to the Nimbus SCMR, the fifth band on ERTS will also measure radiation emitted by the earth's surface in the 10 micrometer band, with, however, a spatial resolution of 200 meters compared to about 600 meters on the SCMR. On the other hand, ERTS will map radiation in only one spectral interval of this band so that interferences with regard to surface composition – acidic or basic – can be made only on the basis of temperature patterns rather than emissivity differences between two spectral intervals.

Returning to Figure 1, we will look at the earth resources aircraft program. And then we will track the observing techniques development across. We have flown an in-house laboratory model of the ERTS MSS on the U-2 aircraft to demonstrate and simulate the observations which were obtained later with ERTS. Much useful information was gained from this simulation for the interpretation of spectral signatures from ERTS. On Skylab, Mr. Shenk of the Laboratory for Meteorology and Earth Sciences is conducting an experiment to demonstrate the observation and tracking of intensive tropical and extratropical weather systems from a manned platform with very high spatial resolution. The experiment is especially geared for the identification of overshooting cloud tops and their relationship to severe storms.

And now moving across to SMS: On the Synchronous Meteorological Satellite we are attempting to advance substantially our meteorological observation capability by demonstrating the feasibility of sounding the vertical structure of the temperature and water vapor distribution in the atmosphere from a geostationary platform. This development is carried out largely under contract with Professor Suomi at the University of Wisconsin and it has progressed to the point where we are confident that such an experiment can be flown on a future synchronous meteorological satellite. Such soundings can provide a much better insight into dynamic atmospheric processes in the tropics and might also relax the present stringent requirements for wind measurements for prediction purposes. Of course, the techniques for high resolution imaging of cloud formations with the SMS 40.6-cm (16 in) scanning telescope have been under development for a considerable time now. This instrument was discussed by Mr. Phenix yesterday. This imaging system will operate in both the visible spectrum, providing a resolution of about one kilometer, and in the infrared, with a spatial resolution of about nine kilometers.

We are also developing the only earth observations sensor for the ATS-F spacecraft. The objective of the ATS-F radiometer is to map clouds, particularly cloud height in infrared emission, with greater radiometric accuracy than the SMS instrument permits. Cloud top temperatures are expected to be mapped with an accuracy of better than one degree Celsius. To achieve such high radiometric accuracy a spatial resolution of about eleven kilometers is required, somewhat poorer than on SMS.

164

Going on to TIROS-N, sensors which are now under development have grown entirely out of earlier Nimbus sensor activities. These sensors are concentrated on three major objectives. One, vertical soundings of temperature and water vapor in the TIROS sounder is based on the first sounders flown in Nimbus-3 and -4. Two, mapping of clouds — including cloud top temperatures — and of sea surface temperatures. Three, tracking of balloons and buoys and relay of data from these platforms. The platform tracking and data relay technique will be based on our experience on Nimbus-3 and -4 IRLS experiment, the TWERLE experiment to be flown on Nimbus-F, and the French cooperative EOLE experiment.

Under the AAFE and technology SRT programs, we have achieved a number of developments which have importance to future meteorological satellites as well as to earth resources survey systems.

Most noteworthy among these are development of multispectral scanners which will provide greater spatial resolution than the scanner on ERTS and will observe several more spectral bands, especially in both the reflected infrared solar radiation and the emitted terrestrial radiation. We will propose to utilize the two windows at 1.7 micrometers and 2.1 micrometers, for example. Such a scanner will have more flexibility than the ERTS scanner and will include a pointing control for limited target selection. Under the technology SRT program, more advanced component developments for very high resolution earth resources survey imaging devices, containing large arrays of photodetectors, and techniques for storing and transmitting data at much greater bandwidths than can be presently accommodated on Nimbus and ERTS are underway.

In the meteorology SRT program, observing technique developments have been concentrated during the past year on the adaptation of the back-scatter ultraviolet (BUV) experiment, which has been flown successfully on Nimbus-4 to measure ozone profiles in the atmosphere, to aircraft flights where the instrument would be pointing at the sun. In this mode it will measure incident solar ultraviolet radiation as a function of height in order to establish a reference for studying changes involving man's activities that affect the stratosphere. This development is cosponsored and partially funded by the Department of Transportation as part of the Climatic Impact Assessment Program (CIAP). Studies of new basic concepts for observing the earth and its environment as required by the various users are being conducted at the present time only under the EOS study and Meteorology SRT programs. In the former program, developments are primarily oriented toward the measurement of surface characteristics which relate to important interaction processes between the atmosphere and the surface, or to the inventory of earth resources. In the latter program, studies concentrate on radiative transfer processes which can be related to the interpretation of ERTS images or to meteorological phenomena such as the composition of clouds. Examples of each of these two areas will be given in the following presentations by Drs. Fraser and Curran.

Examples of new concepts in remote sensing developed under the EOS study are shown in the next four figures. Several years ago, we had already observed the roughness of the sea surface, and ultimately the surface wind speed can be inferred from measurements of the thermal microwave emission at wavelengths of 1-2 cm. More recently we have determined a relationship between soil moisture and the microwave emission at various wavelengths and polarization over land surfaces.

Figure 3 depicts flights over an agricultural test area in Phoenix, Arizona. Measurements were taken of emission at 1.55-cm wavelength, showing that the brightness temperature over a wet field, 35 percent of which was moisture or water, was 220 K. And over a dry field there was a high brightness temperature, 275 K. And the sensible temperature was essentially the same over both fields.
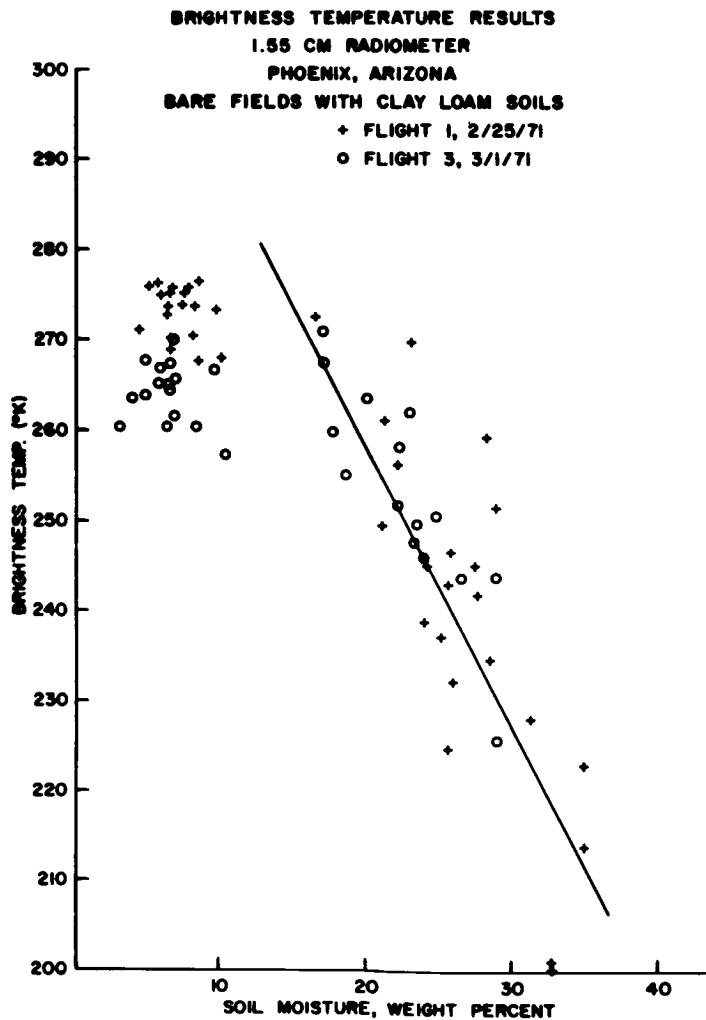

Figure 3. Microwave brightness temperature versus soil moisture.

Figure 4 is another analysis demonstrating possibilities of sensing soil moisture in the microwave region. The ordinate shows relative brightness temperature. Soil moisture in weight by percent is shown along the abscissa. Linear curves indicate data at four microwave wavelengths, showing the decrease at all wavelengths of brightness temperature with increase in soil moisture and greater slope, the longer the wavelength. Spatial resolutions achievable from even future spacecraft will probably not be sufficient to provide soil moisture information that is useful to the farmer, but it is expected that regional surveys of soil moisture conditions useful for flood conditions, for large-scale agricultural planning, and for assessment of energy exchange between the surface and the atmosphere can be obtained with such techniques.
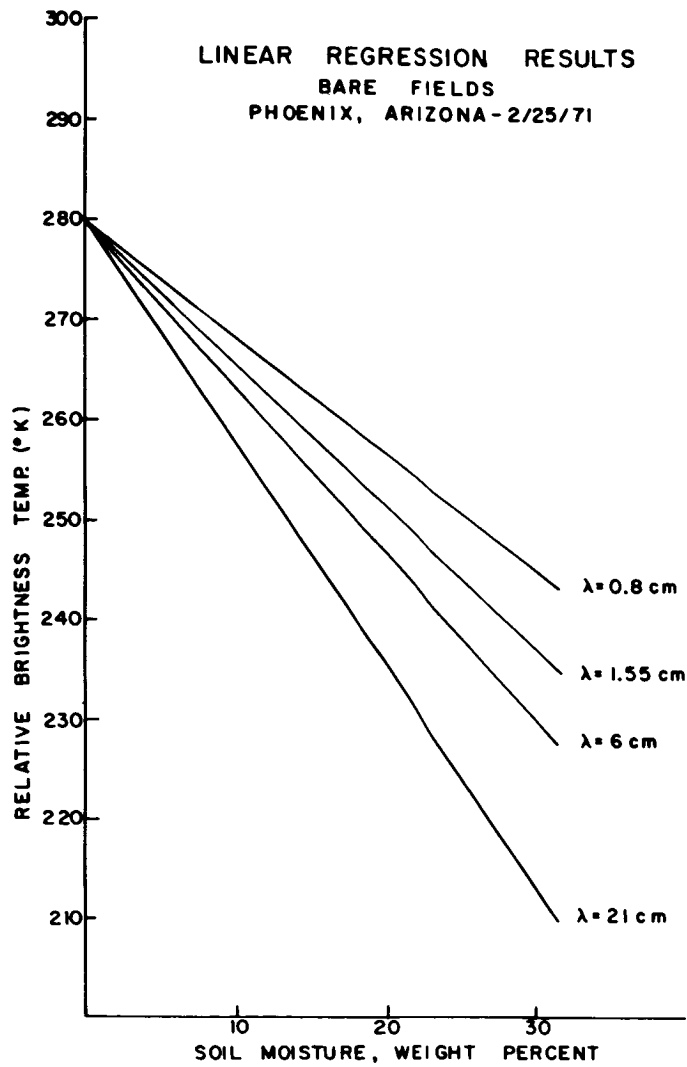

Figure 4. Relative brightness temperature versus soil moisture
for four wavelengths.

Figure 5 demonstrates both the feasibility of observing the intensity of rain clouds over the ocean and the need for correcting the effects of clouds on measurements of surface characteristics with microwaves at various wavelengths and polarizations. At the top of Figure 5 we have a storm cell over the Pacific Ocean and at the bottom we have analog presentations of brightness temperature versus arbitrary distance along a track. And quite clearly the shorter wavelengths are more severely affected by the storm than are the longer wavelengths, illustrating a point sometimes forgotten: that although microwave frequencies do penetrate and look through clouds, they do not do so completely. In future multi-spectral microwave instruments we must have a suitable mix of channels to provide not only the measurement of such parameters as the water content of clouds but to correct for cloud-shadow effects when we are attempting to infer surface properties such as temperature, roughness, surface wind, and ice mapping.

Although microwave observations of liquid water in clouds will be made to some extent on Nimbus-E and -F, we expect that they will come to fruition only in future missions on which an integrated multispectral passive microwave imaging system could be used to map simultaneously cloud liquid water content, soil moisture, sea ice conditions, and sea surface roughness. Possibly sea surface temperatures might also be inferred from such measurement to complement the infrared observing techniques now being developed for TIROS-N and EOS.

Another advanced observation concept deals with the mapping of the biological content of ocean water. This concept is largely based on detection of changes in the radiance ratio between blue and green sunlight reflected by the upper layers of the ocean. Although some information on chlorophyll content of the water over intensive upwelling areas has been derived from ERTS, as will be shown, the MSS on ERTS does not make measure-ments in the blue part of the spectrum where there is a chlorophyll absorption band and is, therefore, not well suited for biological ocean observations. The greatest difficulty in making such measurements is to correct for the strong scattering of light by the atmos-phere at the short wavelengths. Figure 6 shows that this is possible in principle. The ordinate shows energy in milliwatts per square centimeter per micrometer and the abscissa shows west longitude across the Gulf Stream. The temperature of the sea surface showed a marked rise as the aircraft passed over the west boundary of the Gulf Stream. The trace of chlorophyll content in milligrams per cubic meter shows a maximum of about two on the cold side of the Gulf Stream and a decrease as the aircraft went over warmer water crossing the boundary of the Gulf Stream. Now, the important measurements are two spectral measurements at 443 nanometers in the blue part of the visible and 550 nanometers in the green part of the visible spectrum. At low altitudes, two-tenths of a kilometer, the aircraft obtained the traces shown by the solid lines. The blue trace (443 nanometers) especially shows a distinctive rise where the chlorophyll has decreased to low values and relatively low energies where the chlorophyll is high.
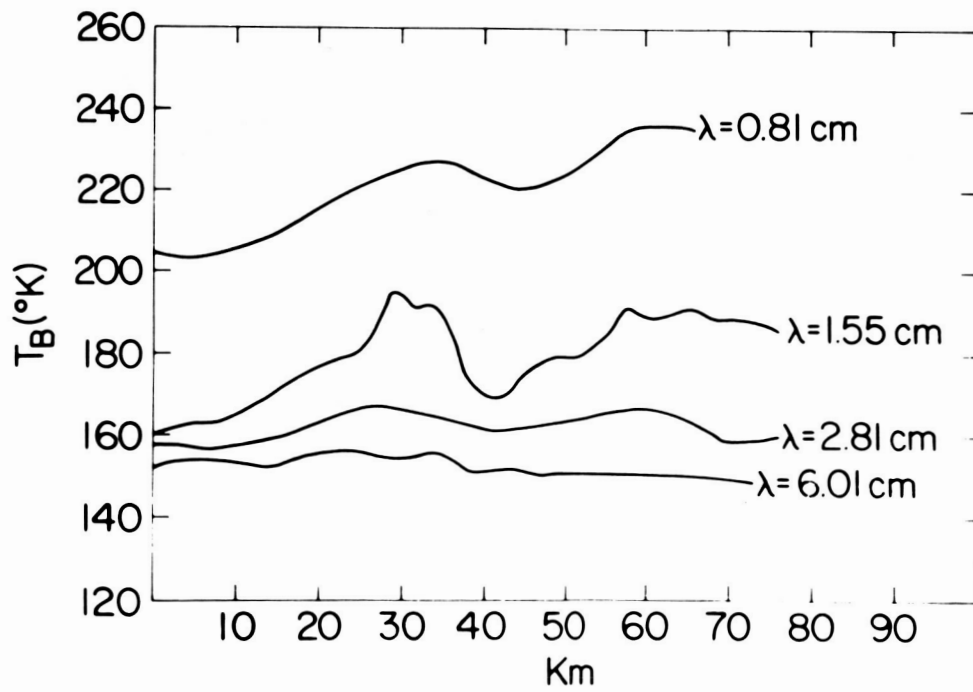
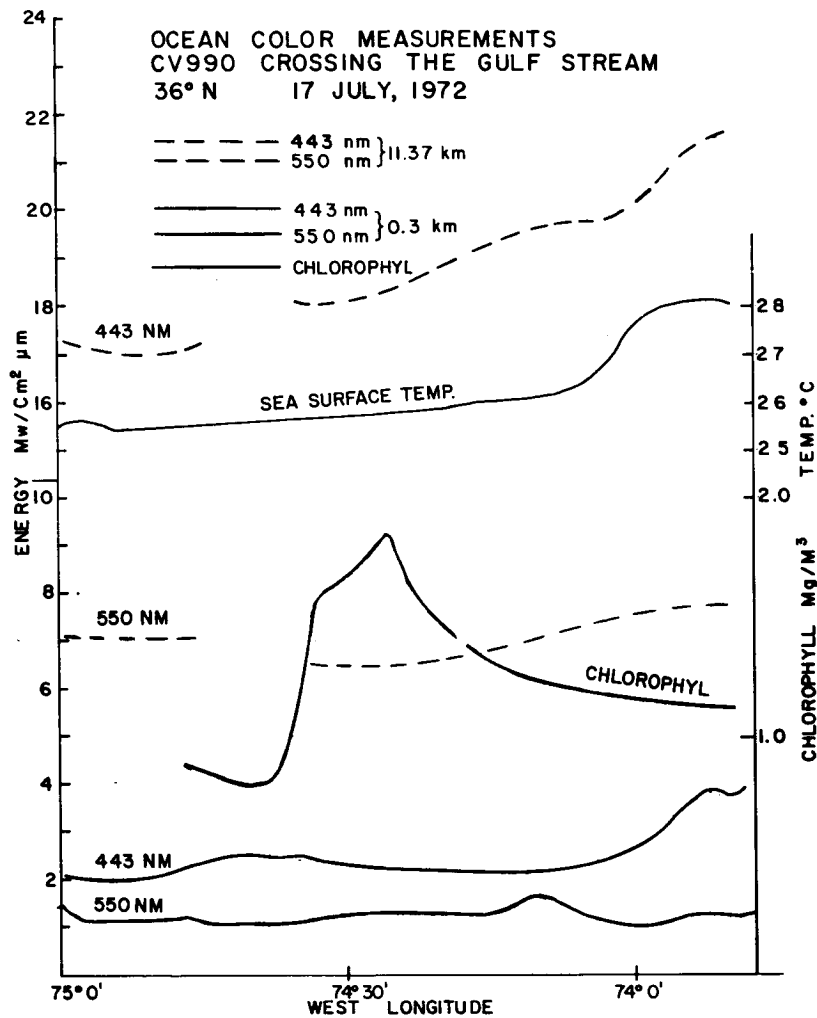Figure 5. Multichannel microwave view of a storm cell.

Figure 6. Remote sensing of ocean chlorophyll content.

On the other hand, when the aircraft flew at an altitude of 11.37 kilometers, we find that the two spectral measurements have, first of all, increased in their amplitude by a factor of about five from the quantity measured at low altitude, due entirely to scattering of visible radiation in the atmosphere. Moreover, we find that the amplitude change is generally reduced of significant features, by a factor of two, due to scattering out of the beam of the signal from the ocean and scattering into the beam of radiant skylight from all directions. Hence the contrast at altitude is down by a factor of about ten compared to the contrast at low altitudes.

So the point is that even though one can measure biological activity and chlorophyll content very well at low altitudes, there is a question — it is a much more difficult problem to make meaningful measurements at high altitudes. This analysis of data from the 990 flight does indicate that the comparison of these two channels — ratios, if you will, —

170

does contain information of the change in chlorophyll, causing a change in the two spectral quantities. Note the very strong correlations between decreasing temperature and increasing chlorophyll content, which is physically understandable, due to upwelling water from sub-surface levels. We considered the development of a system for the global mapping of both the biological and temperature parameters of the sea surface, the most important step to be taken after ERTS-B.

Little needs to be said about our activities in the implementation of observing systems; that is, the management and execution of earth observations flight missions. As can be seen from the programmatic overview slide (Figure 1), every ongoing earth observation project except the aircraft program and the Earth Resources Experiment Package (EREP) on Skylab is being conducted at Goddard. The letter A is not included in the chart under ATS even though it is conducted here at Goddard because it is not considered to be a dedicated earth observation mission.

One of the most important but very often neglected activities in the earth observation program is the very large effort required to extract observational parameters which can be related to environmental processes from the acquired satellite data. Remote sensing of these parameters, such as temperature, moisture, surface composition, vegetation, and so on, is never done directly but, rather, must be inferred from a measurement of intensity of radiation. Effort is needed to extract the appropriate parameters from the sensed signals.

A major portion of the GARP project is, therefore, focused on this extraction of meteorological parameters from the satellite measurements. Here it is planned to design a consolidated ground system which will enable us to extract efficiently the vertical profiles of temperature and water vapor from radiance measurements and to determine wind speeds from cloud picutres.

On ERTS the initial extraction process involves the conversion and registration of about ten billion bits of photometrically sensed signals into about 1000 photographic images per day. These images are then related to earth resources parameters such as land use patterns, water quality, soil or crop conditions, snow and ice cover, and so on. In the Nimbus program the extraction of observationally significant parameters is limited to the production of images from the radiances measured with contiguously scanned spectroradiometers. However, extractions involving observations such as global distributions of ozone, atmospheric temperature and water vapor profiles, and radiation fluxes relating to the energy budget of the atmosphere are performed under activities of the meteorology SRT program rather than under the Nimbus project activities. Such determinations, therefore, do not always conform to the more rigorous planning and scheduling involved in a project type activity.

Examples of such determinations made from Nimbus observations recently under the meteorology SRT program are the radiative energy budget of the globe on an annual basis.

Figure 7 shows the annual net radiation; that is, the difference between the absorbed solar radiation and the long-wave emission lost to space from the earth for one year. This is the first such annual global analysis from satellite data (Nimbus-2). The two shades of blue indicate deficit areas, where there is more energy lost to space than absorbed solar radiation; and the two tan and yellow shades indicate excess regions, where more solar radiation is absorbed. These excesses and deficits, of course, are the basic forcing functions that drive the general circulation of the atmosphere.

Another example is the determination from the MUSE experiment on Nimbus-3 and -4 of the variation of ultraviolet solar radiation which impinges on the earth and affects the structure of the stratosphere and mesosphere. Figure 8 shows work by Dr. Donald Heath analyzing the fluctuations observed by the MUSE experiments. Here Dr. Heath shows four types of enhancements observed in consonance with four types of cycles, at three different wavelengths: Lyman α, 1750, and 2900 Angstroms. In the case of Lyman α he notes enhancement (defined by the flux maximum minus the flux minimum divided by the flux minimum) of 16 percent associated with a Class 3 solar flare. In the case of the 27-day solar rotation he observes a 25 percent enhancement. He has observed one 22-month —
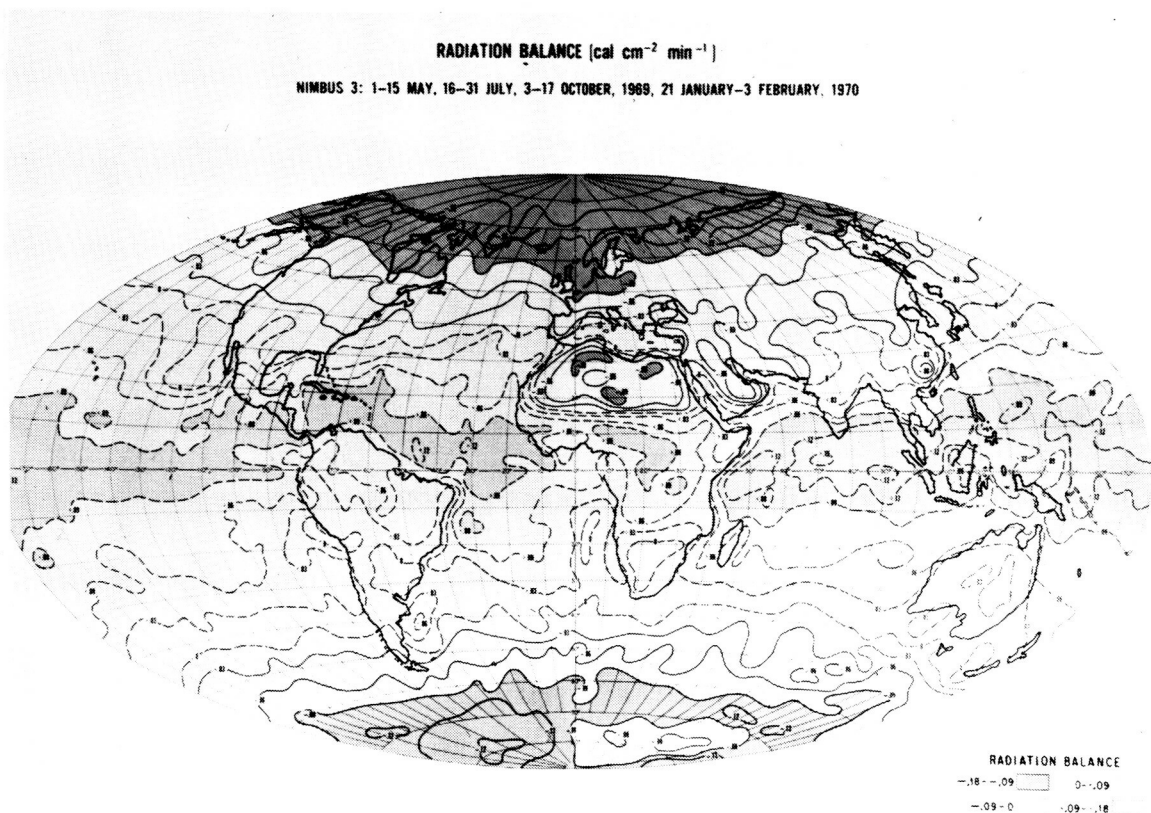
RADIATION BALANCE (cal cm^{-2} min^{-1})

NIMBUS 3: 1–15 MAY, 16–31 JULY, 3–17 OCTOBER, 1969, 21 JANUARY–3 FEBRUARY, 1970

RADIATION BALANCE

−.18 − −.09   0 − .09

−.09 − 0   .09 − .18

Figure 7. Annual radiation balance of the earth-atmosphere system.

WAVE LENGTH REGION \ PERIOD	FLARE	$\dfrac{F(max)-F(min)}{F(min)}$		$F(69) / F(66)$
		27 DAY (Rotation)[1]	22 MONTHS (?)	11 YEARS (Sunspot)
LYMAN ALPHA 1216A	$E(\%)=0.3A^{3/2}$ 16.2% class 3, OPTICAL	25%	10-30%	0.8[2]
1750A	NONE OBS.	6%	NONE OBS.	2.44
2900A	NONE OBS.	1%	NONE OBS.	1.52

[1] OBSERVED PRINCIPALLY FROM TWO ACTIVE REGIONS ABOUT 180° APART IN SOLAR LONGITUDE SINCE NIMBUS 3 LAUNCH APRIL,1969
[2] PROBABLY MASKED BY 27d VARIATION

Figure 8. Observed UV enhancements in the solar irradiance (F).

hence the question mark — cycle wherein there is a variation azimuth of from 10 to 30 percent, and over the 11-year sunspot cycle he has taken the flux in the satellite in 1969 divided by a similar flux measured by a rocket flight in 1966 near solar minimum to derive an eight-tenths factor indicative of an 11-year cycle at Lyman α. At the next wavelength, 1750 Å, he sees none during a flare, 6 percent over 27 days, none over 22 months, and 2.44 allowed to change over the 11-year cycle. At 2900 Å, we find none, 1 percent, none again, and 1.52.

Figure 9 shows global and season patterns of the vertical structure of ozone in the stratosphere from the back-scattered ultraviolet (BUV) experiment on Nimbus-4. This analysis is by Arlin Krueger and Dr. Heath of the Laboratory for Meteorology and Earth Sciences. The isolines are in terms of micrograms per gram mixing ratio of ozone. The BUV has worked extremely well and more than two years of data are now being analyzed.

This brings us finally to what we consider our most important activity in the earth observations program, the application of observations to the survey of environmental conditions and resource management.

Here our strongest activity is in the ERTS project, where we are sponsoring more than 300 principal investigators whose goal it is to demonstrate such applications in various disciplines related to earth resources, and ranging from land use, agricultural mapping, and cartography to surveys of pollution and environmental quality.

A significant application of ERTS observation, to cartography, namely the automatic and very efficient production of accurate thematic maps, is shown in Figure 10. This is the first map from space in the U.S. Geological Survey sense. The map has a very accurate
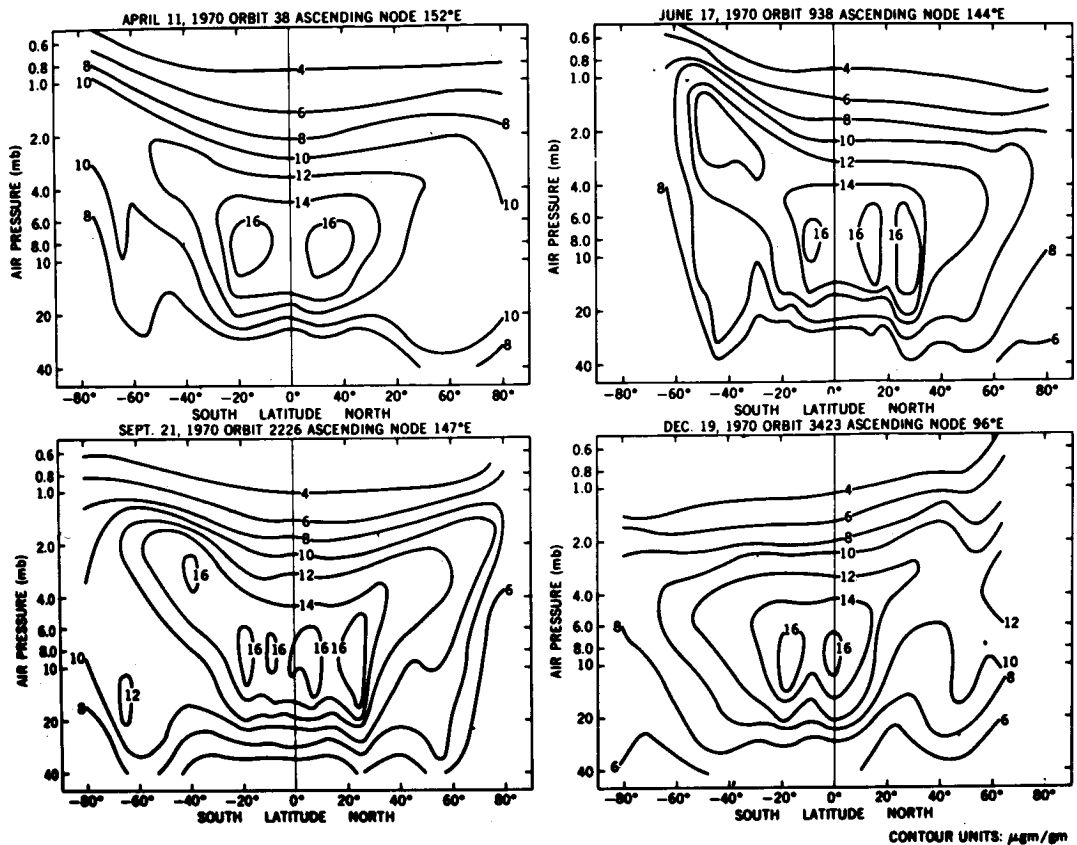
Figure 9. Seasonal changes in ozone mixing ratio; data from Nimbus-4 BUV.

reference, so one can determine very accurately distances between two points. This is a scene-corrected map at 1:1,000,000. The original product was also 1:1,000,000 from three channels of the ERTS MSS, the green, the red, and the near infrared. Lake Tahoe is the dark area and the Sierra Nevada mountains show up very red because this is a false color presentation. The chlorophyll in the foilage on the mountains absorbs radiation in the visible red, which causes the false color to come through as red in this display scheme.

Similar activities in the application of observations are also being undertaken under the GARP program, where models of atmospheric circulation are being generated at the Goddard Institute for Space Studies on the basis of actual or simulated satellite observations. Dr. Halem, who was going to talk on the numerical modeling of the general circulation at the Institute, cannot be here today. Dr. Halem would have explained the activities that are now underway, preparing for data from the vertical temperature profile radiometer on ITOS-D which is successfully operating. Soon its data will be transmitted over a link from Goddard to New York City testing the numerical forecast models that Dr. Jastrow and his group have developed in preparation for GARP.
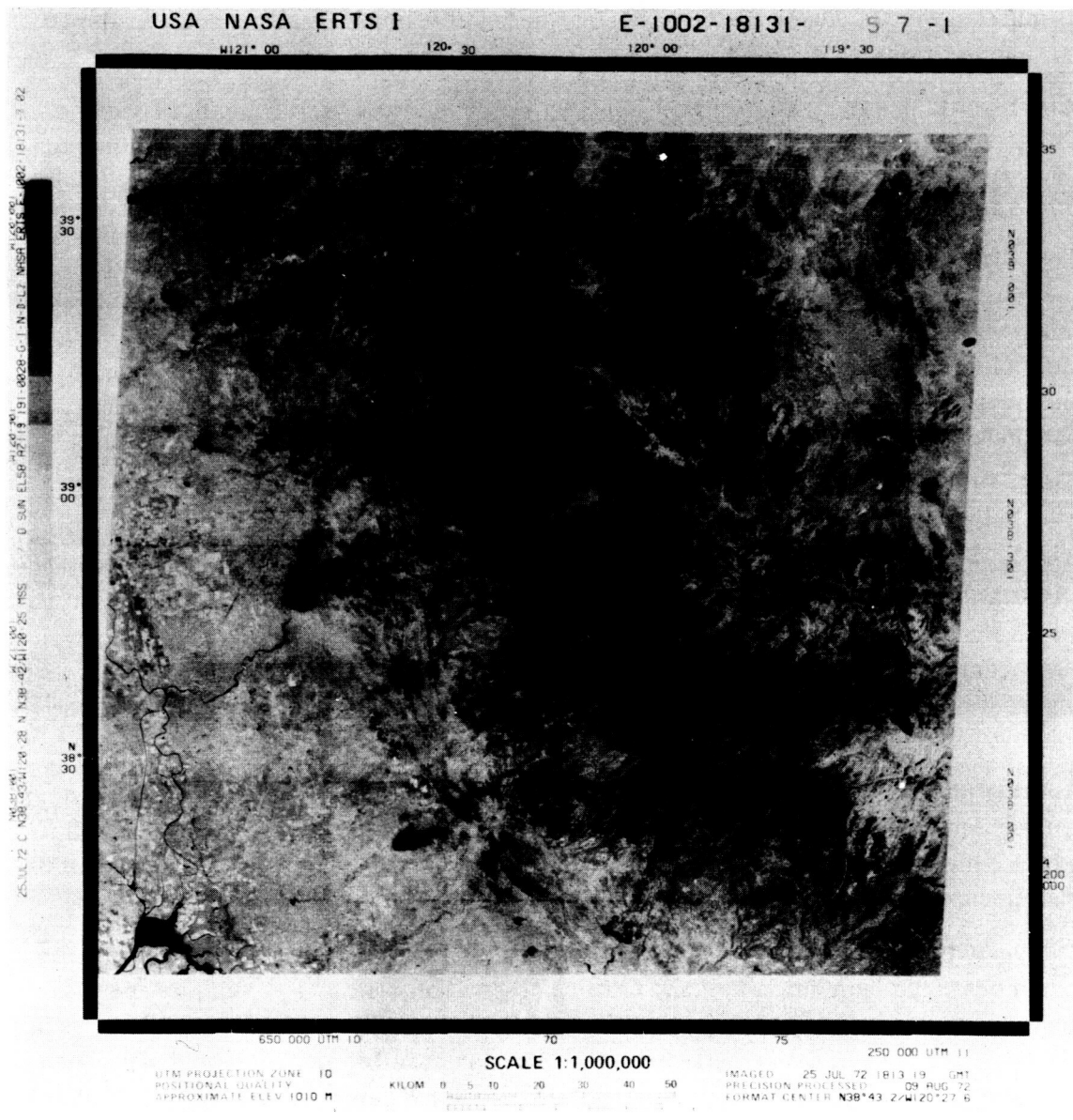
174

USA   NASA   ERTS I   E-1002-18131-   S 7 -1

H121° 00   120° 30   120° 00   119° 30

39° 30

39° 00

N 38° 30

650 000 UTM 10   70   75   250 000 UTM 11

SCALE 1:1,000,000

UTM PROJECTION ZONE 10   IMAGED   25 JUL 72 1813 19   GMT
POSITIONAL QUALITY   KILOM 0 5 10   20   30   40 50   PRECISION PROCESSED   09 AUG 72
APPROXIMATE ELEV 1010 M   FORMAT CENTER N38°43 2/W120°27 6

Figure 10. ERTS-1 MSS imagery of cartography quality (the first map from space).

175

Other applications resulting from observations with both the Nimbus satellites and the meteorological rocket observing systems have been demonstrated under the meteorology SRT program. The following presentations by Mr. Shenk on the observation of Hurricane Camille and by Mr. Theon on the analysis of tides in the upper atmosphere are examples of such applications.

Also I would like to mention that Dr. Stewart of the Institute, who could not fly down today, would have talked on models involving photochemistry, utilizing several hundred coefficients in a very involved photochemical model investigation of sources of pollutants in the atmosphere and their dispersal by the general circulation.

Looking back to Figure 1, we want to mention now some of the problems inherent in the program. As was already mentioned, our efforts in the past have been concentrated too much on the development and demonstration of observing techniques in systems. Instead, we should pursue each of the programmatic line items along the vertical columns and should concentrate more actively on the two last rows, namely the extraction of useful parameters and the application of the observations to environmental surveys and earth resources management. So far, we appear to have taken steps to achieve this goal only with ERTS and GARP. We are making an effort in the same direction with EOS.

An example of the deficiency in this area in the on-going Nimbus program is the fact that the SCMR experiment on Nimbus-5 will perform observations similar to the fifth band which was deleted from ERTS-B. However, the system will not permit us to make any significant preparations for the proper extraction or application of the information resulting from the Nimbus experiment. A similar situation exists at the present time with the microwave images which will result from Nimbus-5 and -6.

Another problem is the rapidly widening gap which has developed in the observing systems between on-going Nimbus and ERTS missions, which will be terminating by 1974, and advance missions, such as EOS and SEOS, which, by virtue of their complexity, cannot be instrumented until the late 1970s.

Parallel with the plans for EOS and SEOS activities must be initiated immediately to accommodate the more important and existing observation concepts, techniques and systems mentioned earlier on missions following ERTS-B, Nimbus-F and SMS-C. We have in the last few weeks begun activities with the Department of Interior to discuss plans for an operational earth surveying mission to follow ERTS-B. We also have plans for a Nimbus-G and an SMS with a vertical sounder.

At the other end of the time spectrum lies perhaps the most challenging and most beneficial of all earth observations space missions, continuous earth surveys with a geostationary satellite with spatial resolution similar to ERTS. We call this mission SEOS. We are planning to begin studies under the SRT program during this fiscal year. We are most concerned lest this activity, an exciting and significant concept, become a victim of the fiscal '73 cost reduction.

Finally, we believe that the budget cutback in the meteorological rocket program has resulted essentially in the termination of this program and will have brought to an end the leadership the Agency has held since its creation in the field of exploring, understanding, and monitoring the stratosphere and mesosphere environment.

POLAR MAPPING WITH ERTS-1

James R. Greaves

The list of disciplines which shall ultimately benefit from the new ERTS data is long indeed. In many cases, we shall be learning more about areas with which we are already familiar. In this presentation, I would like to focus upon some potential applications of the multispectral ERTS-1 imagery to remote, unfamiliar regions. The examples I have chosen are from the Canadian Arctic.

Figure 1 presents imagery from the 0.6 to 0.7 micrometer band of the ERTS-1 RBV sensor. This scene was recorded on July 26, only three days after launch. The area shown here is along the northeast coast of Labrador at about 57° north. This portion of Labrador is north of the tree line and is an area of open tundra. Other than a few trading posts, it is largely uninhabited.

The large bright area to the lower right represents low- to mid-level cloudiness, while a streak of cirrus may be seen extending from southwest to northeast in the upper right portion of the picture.

The most striking feature of this frame, however, is the broad area of shore-fast ice at the opening of Okak Bay at about the center of this picture. Note that a number of islands show up as isolated gray areas against the uniformly white ice background. The swirling ice patterns north and south of the pack ice can be used to define local eddys embedded in the southward flowing Labrador Current. Further offshore may be seen individual icebergs. I think you can make out a small cluster of them near the right-hand edge of the picture. Some of the other spots you see here were introduced during photographic processing. In the original imagery more than a dozen individual icebergs were observed. As will be seen in the next presentation, the day-to-day sidelap at these latitudes permits the monitoring of ice motion.

In remote regions such as this, ERTS imagery often reveals a number of mapping errors. Note the large island in Okak Bay nearly cut in two by a broad channel extending down from the north. Available maps show this as two distinct islands separated by a uniformly wide channel. While there may be a southward extension of the channel narrower than the nominal 100-meter resolution of the ERTS sensors, the designation of a uniformly broad channel is certainly erroneous.

So far we have been looking at just one spectral region. What more can we learn by comparing different spectral bands? Note in particular two lakes, the long and narrow Saputit Lake running in an east-west direction just southwest of the western extremity of Okak Bay; and the wider, rather ill-defined Umiakovik still further to the southwest.
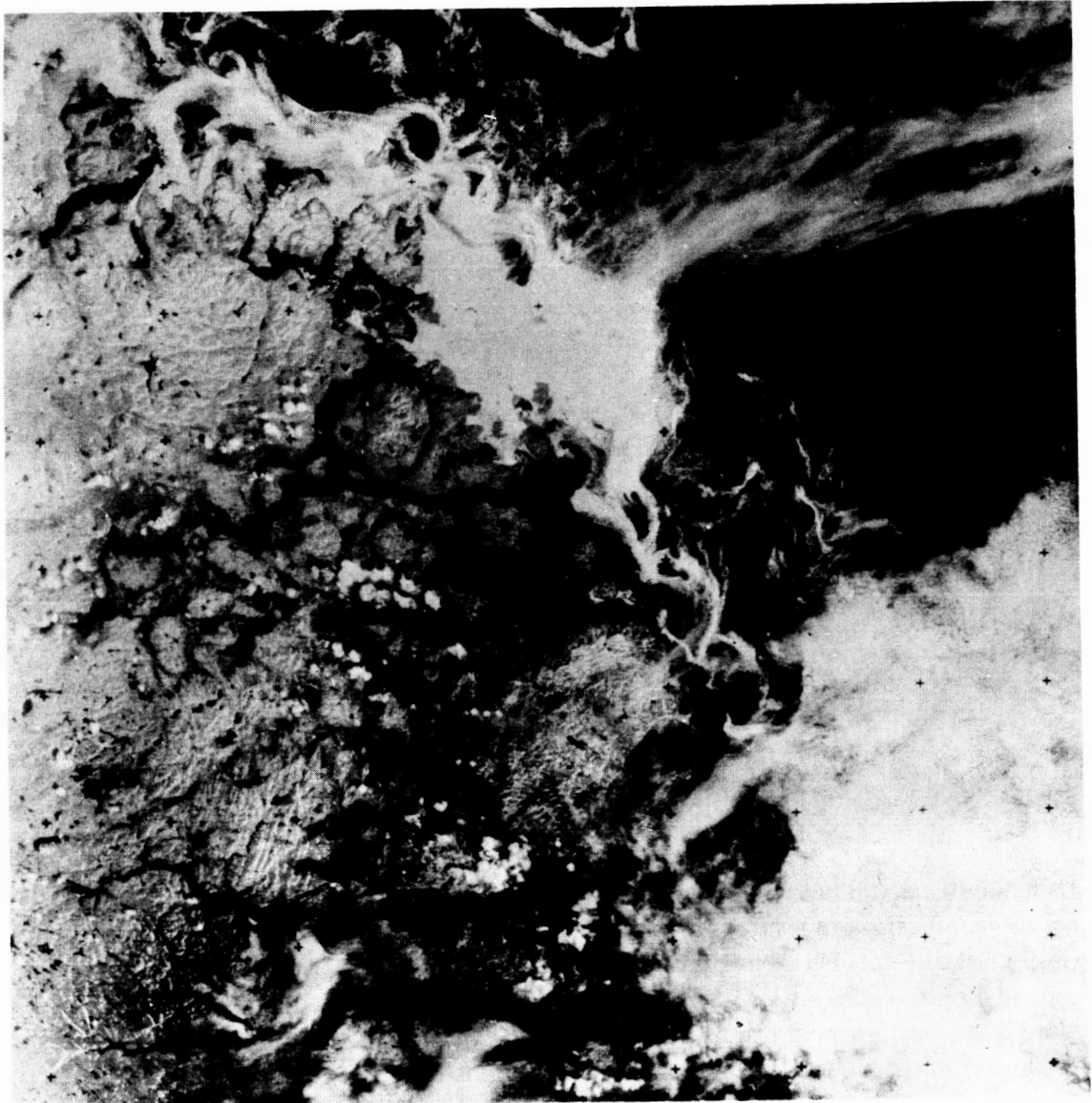
Figure 1. ERTS-1 RBV image of northeast Labrador.

In Figure 2, we see these two lakes as they appear in the three spectral bands. The outlines of both lakes are quite clear in the near-infrared band which enhances land/water boundaries. As we approach the green band, however, Umiakovik disappears! Because of the increased water penetration of the green band, this effect would be observed if Umiakovik were more sediment-laden than Saputit, or more shallow. Because of the absence of any human influence and because the environs of both lakes are nearly identical, the shallow water hypothesis is more likely.

GREEN
.48–.58 μm

RED
.58–.68 μm
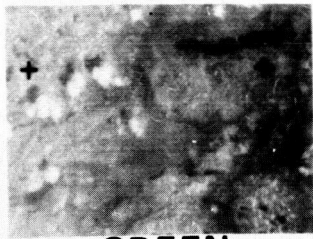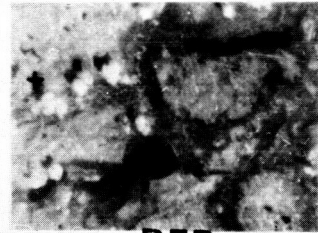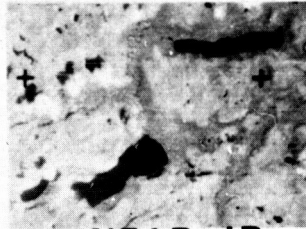
NEAR–IR
.70–.83 μm

SAPUTIT–UMIAKOVIK LAKES
ERTS–1 RBV IMAGERY

Figure 2. ERTS-1 RBV imagery of Lakes Saputit and Umiakovik.

Using multispectral imagery we can not only note the presence and extent of ice, but can get some indication of its physical condition. Figure 3 shows just a portion of the northwest coast of Coats Island in Hudson Bay. The imagery in the two frames at the top was recorded by the MSS sensor just one orbit after the RBV recorded the imagery of Labrador. Note that in the infrared band, the shore-fast ice which had displayed a generally uniform brightness in the green band, becomes darker and more patterned. This is indicative of the presence of melt water on the ice, which implies in turn that the ice is in a melting stage. This phenomenon has been previously noted in other ERTS imagery by Dr. Paul McClain of NOAA. Green-band data acquired just 36 days later (August 31) reveals an ice-free coastline and supports the melting hypothesis. Note also the small lake: On July 26, it is still frozen over, but melting; on August 31, it is completely ice free.

While these findings are of a preliminary nature, we have seen in just a few frames the potential applicability of the ERTS-1 data to ice detection, local current effects, map corrections, relative lake depth measurements, and even to estimates of ice breakup. It is clear that ERTS-1 represents a new era in earth observations.

Figure 3. ERTS-1 imagery of Coats Island.

REMOTE SENSING OF SEA ICE MOTION

Albert Rango

Jim Greaves has shown a number of applications of ERTS-1 in the polar regions, and now I would like to show some synoptic observations of dynamic changes in Arctic sea ice. A study was made on the sea ice in Hendriksen Strait, the passage between Amund Ringnes Island and Cornwall Island at about 77°45'N and 95°W (Figure 1). The distance across the strait averages 13 kilometers. To the northwest of this area is the average summertime minimum limit of polar pack ice. As will be shown here, in the six-day period from the August 23rd to the 28th, ERTS-1 provided five days of coverage. The reason for this is the orbit-to-orbit sidelap that occurs at high latitudes.

Various types of sea ice can be identified in the ERTS-1 imagery in Figure 2. Bay ice is found in Norwegian Bay; shore-fast ice in in Hendriksen Strait and in Fog Bay; ice floes are numerous throughout the strait and in the general area; and finally pack ice, which consists of many individual ice floes, is present. In general it can be observed that the pack ice drifts out of the strait over the six-day period, and some shore-fast ice was observed to break away from the land and to also leave the strait. Correlation of side-to-side movement of the pack ice as it left the strait with surface wind direction was generally found to be good. As you can see, on the 23rd and 24th the pack ice was in the middle of the strait; on the 25th it had moved to the southern shore; on the 27th it was back in the center of the channel; and on the 28th it had moved back toward the south.

In such a sequence of observations, a number of sea ice changes with time are detectable. Changes in position of individual ice floes can easily be translated to velocity. A number of ice floes were tracked over the six-day period and their velocities calculated as shown in Figure 3. The average velocity for ice floe movement was 8.5 kilometers per day, which is comparable with the figure of 4.4 kilometers per day given by Mellor* for the average drift rate of large ice islands in the Arctic.

The ice cover, or the relative amount of sea ice present in a given area, is important for shipping purposes. The ice cover in Hendriksen Strait on August 23 was approximately 7/10, decreasing to 2/10 by the 28th of August. This type of sea ice change is easily observed from ERTS and combined with possible identification of navigation routes through sea ice could be quite useful to future shipping interests.

Repeated observations of individual ice floes such as those in Hendriksen Strait will also allow calculation of the ablation of the ice mass, in this case the decrease of surface area with time. Over a four-day period individual ice floe surface areas were measured.

*M. Mellor. "Snow and Ice on the Earth's Surface. Monograph II-C 1. U.S. Army Corps of Engineers, Cold Regions Research and Engineering Laboratory. 1964.
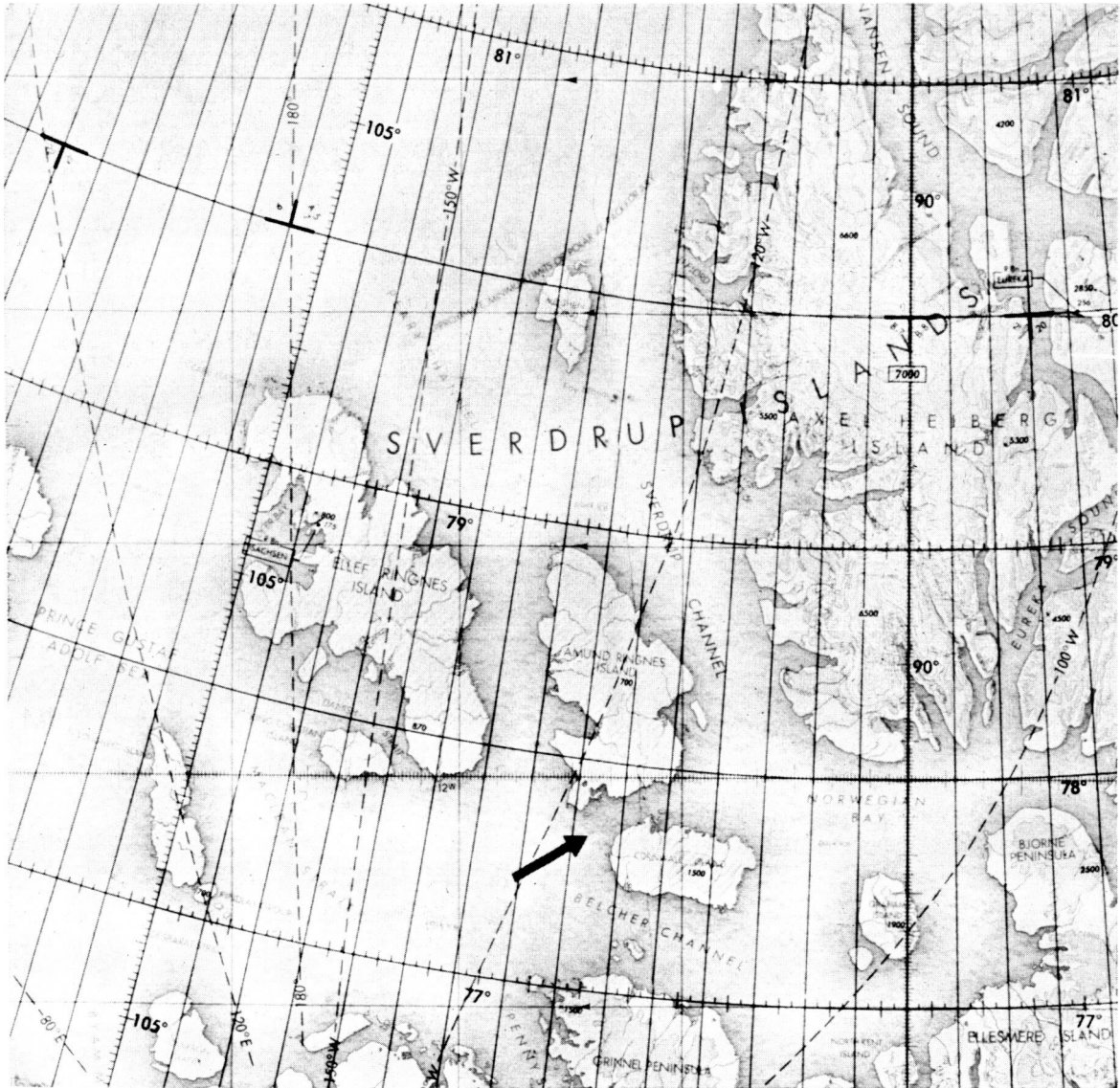
Figure 1. The arrow indicates the location of Hendriksen Strait, site of ERTS-1 sea ice studies.

The average decrease in surface area for the measured ice floes was approximately 10 percent during this time.

Although ERTS-1 provides extremely good coverage of sea ice in the polar regions, there are times when it cannot provide acceptable data, namely, during the six-month-long polar night or when clouds block the sensor's view. During these times we can use an electrically scanned microwave radiometer to measure the microwave emissivity of sea ice, and subsequently to record the identity of specific ice floes from one time period to another.

23 AUG. 1972 **24 AUG. 1972** **25 AUG. 1972**
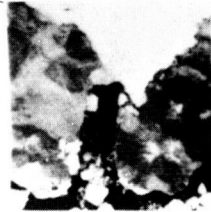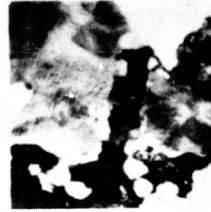
27 AUG. 1972 **28 AUG. 1972**

Figure 2. ERTS-1 observations (0.8 - 1.1 μm) of Arctic sea ice in
Hendriksen Strait, $77°45'$ N - $95°00'$ W.

**1. AVERAGE VELOCITY OF INDIVIDUAL ICE FLOES
OVER 5-DAY PERIOD
8.5 KILOMETERS/DAY**

**2. ICE COVER IN HENDRIKSEN STRAIT
23 AUGUST 1972 7/10
28 AUGUST 1972 2/10**

**3. AVERAGE ABLATION OF INDIVIDUAL ICE FLOES
OVER 4-DAY PERIOD
10% DECREASE IN SURFACE AREA**

Figure 3. Sea ice changes with time as observed from ERTS-1.

In Figure 4 we move westward from Hendriksen Strait to the north coast of Alaska in the
Harrison Bay area. This figure is a series of mosaics of false color microwave images
extending from Cape Halkett 250 kilometers north into the Arctic Ocean. Each mosaic is
formed from two flight passes by the NASA Convair 990 arranged so as to give contiguous
coverage along a 40-kilometer strip. The interval between flights was three days, except
between the second and third flight when it was five days. The flight paths were generally
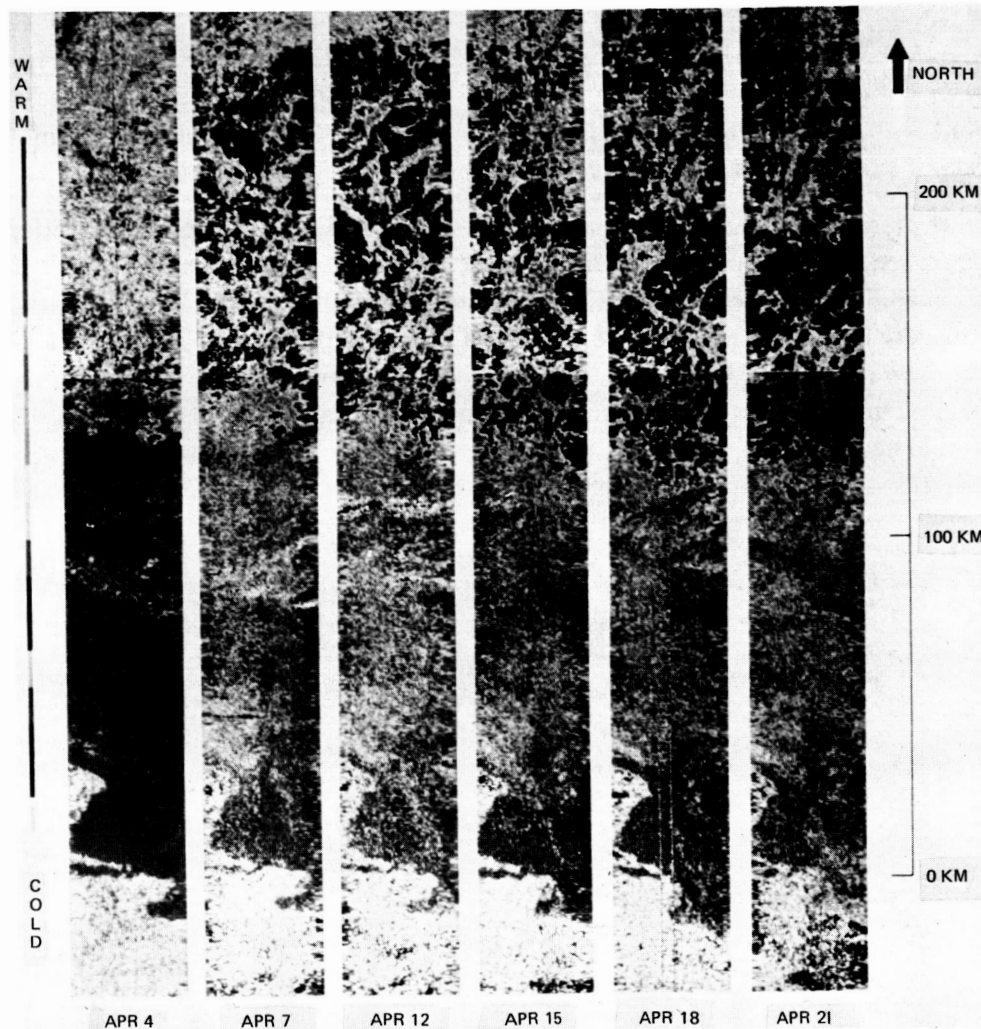along the same route for each mosaic.

Figure 4. Arctic sea ice motion (1972) photographed NASA CV-990 aircraft (λ = 1.55 CM).

Note the recurring landmarks, Cape Halkett and Saktuina Point, at the bottom of each mosaic. Since snow-covered tundra is radiometrically much colder than ice cover, we can easily distinguish these landmarks in the microwave image. Several sea ice features are visible on successive flights, and they all seem to have a westward drift. Positions of these ice features were plotted, and over three-day intervals motions ranging from as little as three kilometers to as much as 22 kilometers were observed. The average velocity of movement for these ice features was 4 kilometers per day, which is in general agreement with the 8.5 kilometers per day figure for sea ice movement in Hendriksen Strait as determined from ERTS-1, and with the 4.4 kilometers per day given by Mellor for drift rates in the Arctic Ocean.

Nimbus-E, to be launched in mid-December 1972, has an electrically scanned microwave radiometer with a minimum resolution of 25 kilometers. Because the speed of sea ice movement is about 4 kilometers per day, we should be able to measure ice dynamics on a time scale of a couple of weeks from Nimbus-E.

The results presented here indicate that for high latitudes, ERTS will provide overlapping coverage on sequential days that will allow observation of dynamic changes in the polar regions. In addition, route planning for future shipping in the Arctic should benefit from sea ice imagery of the type obtainable from ERTS-1 and Nimbus-E. Finally, ERTS and Nimbus observations of sea ice, especially amount of ice cover versus amount of open water, will be important in determining boundary conditions for future use in models of the global heat balance.

186

PASSIVE MICROWAVE IMAGES OF LAKE ICE

Per Gloersen

I would like to report here some early impressions of our first observation of the microwave emission from fresh water ice as formed in the Great Lakes this past winter. There is considerable practical interest in the Great Lakes ice from the commercial navigational point of view. The motivation is to find a feasible means of discovering early signs of the ice breakup below a persistent cloud cover, in order to permit an extension of the shipping season. To this end, we responded to a request from Lewis Research Center to fly a NASA Convair 990 mission over Lake Erie and Lake St. Clair.

Figure 1 is a photomosaic of the area to be discussed here, Lake St. Clair and its surroundings. The cities shown are Detroit and Windsor. At the top left we have the St. Clair river going to Lake Huron, and near bottom left is the Detroit River going down to Lake Erie.

Figure 1. Photomosaic of Lake St. Clair and its surroundings.

We were fortunate in having a relatively cloudless day for this mission, which allowed us to obtain photographic data for comparison with our microwave images. It is clear that there

was too much ice for commercial navigation on that day.

Before proceeding to the microwave results I would like to point out that there are many different kinds of ice formations in this scene. These can be broken down into three major components, illustrated in three enlarged portions of this mosaic shown in Figure 2.
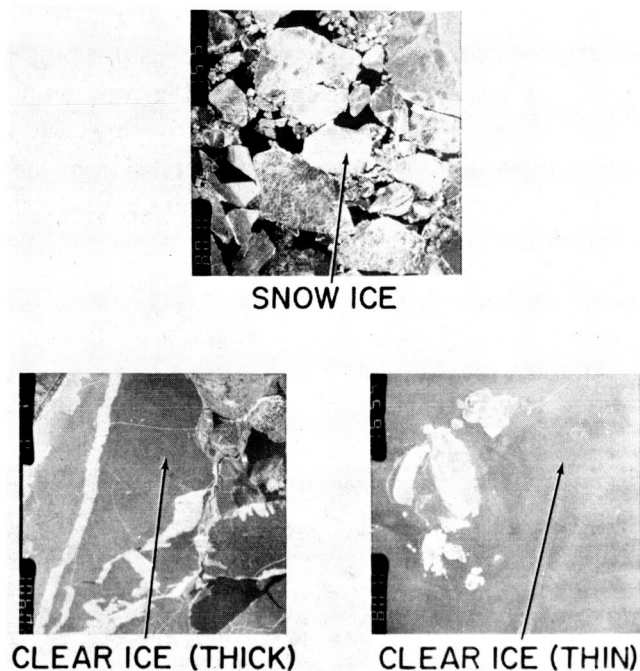

SNOW ICE

CLEAR ICE (THICK)   CLEAR ICE (THIN)

Figure 2. Three kinds of ice formation; enlarged sections
of the photomosaic of Figure 1.

At the top we have an example of snow ice, which appears white since it is full of air bubbles. Below is shown clear ice of two different thicknesses. The thin clear ice shown here is so transparent as to be almost imperceptible, but close inspection of this photograph reveals hairline cracks in areas which at first glance appear to be open water. This thin ice is estimated to be about five centimeters thick.

The thin clear ice is much more readily distinguished in Figure 3, which shows an image of the 1.55 centimeter microwave radiation emanating from the surface.

To orient you again, Detroit is at mid-left and Windsor lies in the bottom left corner.

In this scene, the snow ice appears to have the highest microwave brightness temperatures. The thick clear ice shows up some 30 degrees kelvin colder, and the thin clear ice is colder still, due to its greater transparency to the 1.55 centimeter radiation. It is only 10 to 20 degrees kelvin colder than the open water which shows up here as gray.
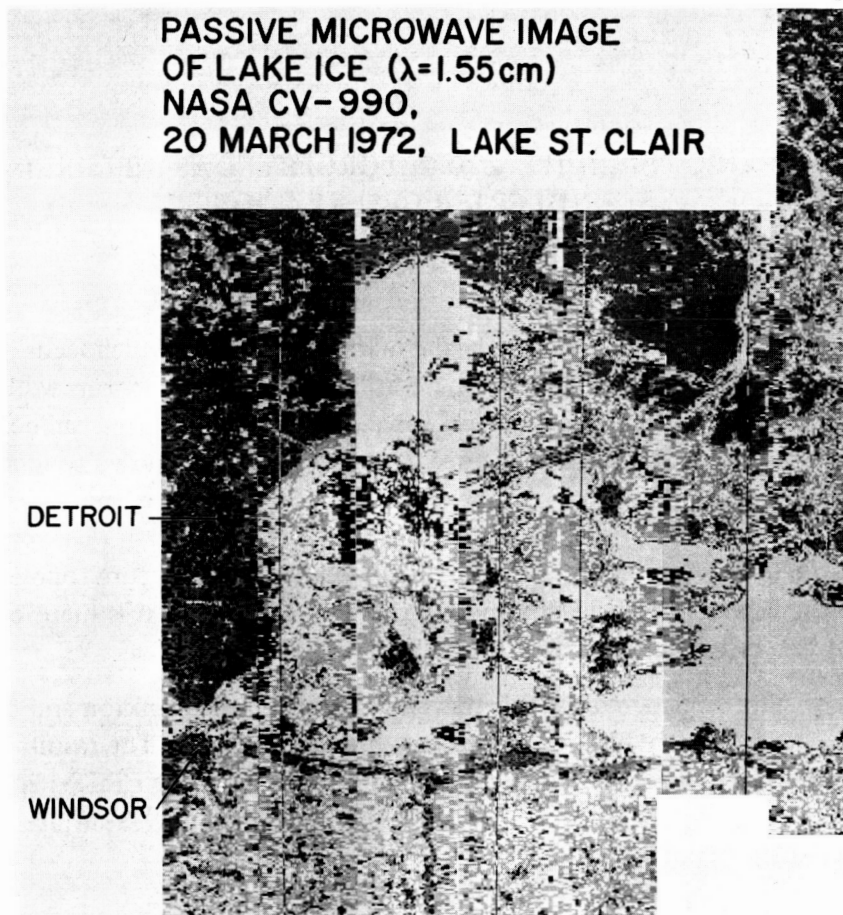
Figure 3. Passive microwave image of lake ice (λ = 1.55 cm). This image was taken from the NASA CV-990 aircraft on March 20, 1972.

What we have found here in our first attempt at obtaining a synoptic view of the microwave radiation from the Great Lakes ice is a much larger variation in the brightness temperatures than we have observed to date in sea ice from our studies of the Arctic ice canopy. Also noteworthy in this image is that the brightness temperatures of some of the nearby land areas, for example parts of Ontario, are no higher than the brightness temperatures of the thick clear ice. This condition was caused by the wetness of these agricultural areas at the time the image was acquired.

We are in the process of analyzing multifrequency microwave and infrared data obtained in this area, as well as at both ends of Lake Erie and the St. Lawrence Seaway. In the Seaway, we have also considerable surface truth information available to us through the auspices of the Canadian Department of Environment and Inland Waters. This information will assist considerably in the interpretation of these data.

OCEANIC TURBIDITY AND CHLOROPHYLL AS INFERRED
FROM ERTS-1 OBSERVATIONS

Robert J. Curran

Oceanic chlorophyll is an important link in the marine food chain which leads eventually to man. Remote monitoring of this food chain utilizing satellite platforms would be of value in managing the efficient use of this resource. Remote monitoring can be accomplished by observation of the color of the ocean surface, which is known to indicate the presence of biological organisms containing chlorophyll. Quantitative measures of ocean color have been correlated with measures of chlorophyll concentration. However, ocean color is also affected by the presence of inorganic sediments and bottom topography. To remotely sense the presence of the chlorophyll-rich phytoplankton, it is therefore necessary to discriminate against other color features.

In this study we have considered the spectral signatures of phytoplankton and other obscuring effects in order to determine how to best use satellite data. The results of this study were then used to analyze the spectral data obtained from the ERTS-1 multispectral scanner (MSS). The analyzed satellite data were finally compared with surface ship measurements of chlorophyll concentration.

The spectral signatures of the processes involved in satellite observation of ocean color may be conceptually separated into three general classes as indicated in Figure 1. The three areas are: the spectral reflectance of the atmosphere; the reflectance properties of both the water surface and beneath; and finally, the reflectance properties of chlorophyll-containing phytoplankton. The first process, the wavelength-dependence of the reflectance of the atmosphere, can be modeled quite accurately under suitable assumptions. The spectral reflectance of the ocean surface also may be separated because this quantity is wavelength-independent. The spectral properties which remain are therefore due only to the scattering and absorption properties of clear and turbid water and to the phytoplankton.

The multispectral scanner of ERTS-1 is a four-channel scanning radiometer. The wavelength intervals of the four channels are indicated by the four different colors on the original photograph. We will consider the spectral features of water and phytoplankton in relation to these four channels.

The photon mean free path indicates how far a photon may penetrate into a medium before suffering either absorption or scattering. If the absorption mean free path is longer than the scattering mean free path, an appreciable amount of backscattering can take place. If the opposite is true, then absorption will take place before the photon can be
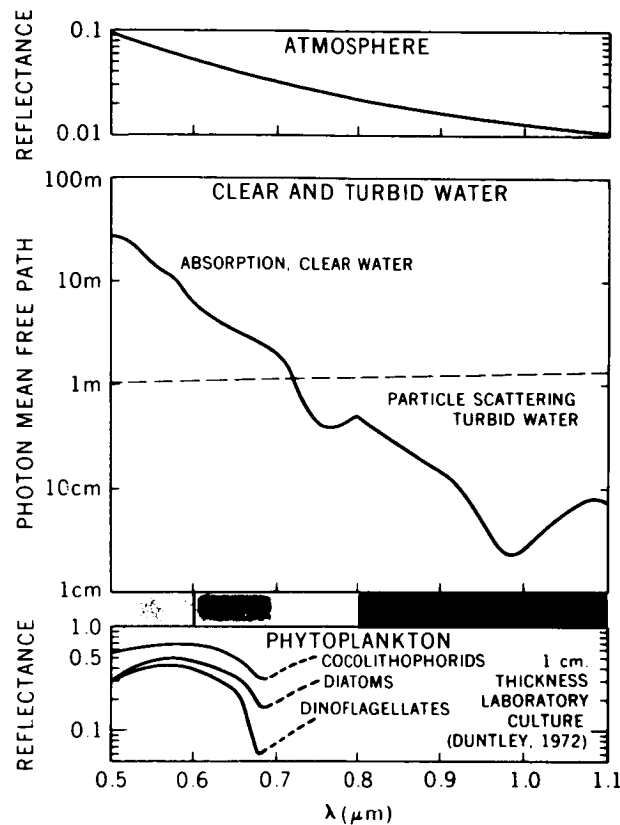
190

Figure 1. Spectral signatures for the processes which
affect satellite observations of ocean color.

scattered. For the values of scattering and absorption given in the figure, the first two MSS
channels would have appreciable reflectance, but the longer wavelength channels will appear
very black due to the strong absorption by the water. The properties of clear and turbid
water are contrasted with the reflectance properties of the phytoplankton as shown in the
bottom of this figure. Chlorophyll has a strong absorption band between 0.6 and 0.7μm,
thus making reflectance by the phytoplankton strong in the 0.5 to 0.6 μm channel and
negligible for longer wavelengths. This property of the phytoplankton makes it ideal for
emphasis by the ratio of the reflectances in the first two channels. Because the turbidity
is more broadband, this ratio will diminish the effects of turbidity. Some evidence sup-
porting this thesis was presented in the ERTS symposium of September 29. That study
concerned the very turbid St. John's River estuary of Florida. Results for a low-turbidity,
open-ocean study are presented in the next figure.

Figure 2 shows a portion of an image in the 0.5 to 0.6 μm channel of the MSS. This image
is of the northwest coast of Africa near Cape Juby. Within two days of the satellite image,
an oceanographic research vessel made measurements of the surface chlorophyll concen-
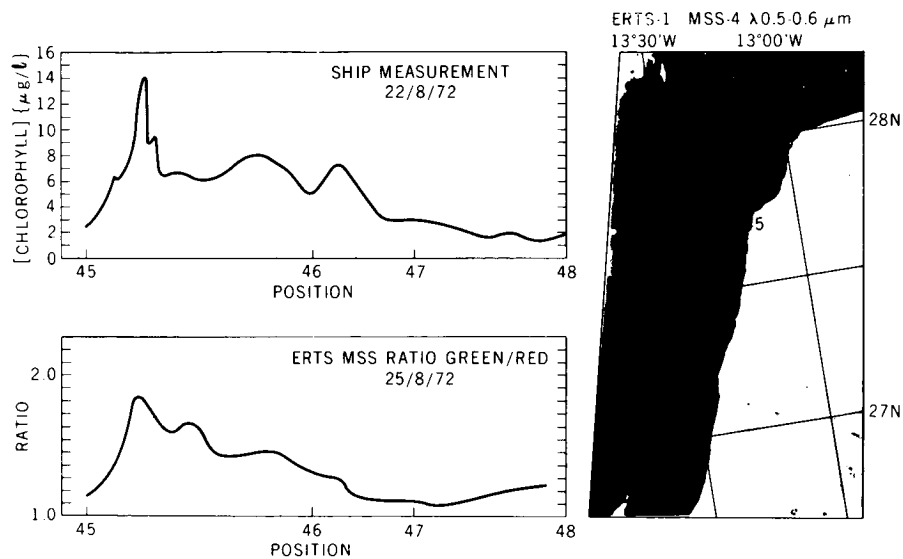tration along the rectangular path indicated. The measured chlorophyll concentrations are

Figure 2. An enlargement of a portion of an ERTS-1 MSS image (0.5-0.6 μm channel) of the northwest African coast.

indicated on the upper left-hand side of the figure. Photodensitometer measurements of the ship's path were made on the MSS image. The data obtained from the densitometer was used to determine a ratio between the 0.5 to 0.6 μm and the 0.6 to 0.7 μm channels. This ratio is plotted in the lower left-hand portion of the figure. Comparison between the ship measurement and this ratio indicates a fair degree of correlation.

In conclusion, it is asserted that the effect of phytoplankton may be enhanced by ratioing the two shortest wavelength channels. This process appears to discriminate against the effects of water turbidity.

EFFECTS OF THE ATMOSPHERE ON ERTS OBSERVATIONS

Robert S. Fraser

We have been developing atmospheric radiation models and methods of computing radiation effects that are important both in the meteorological and earth resources satellite programs. These models have a wide range of application, but today I will show you the results of using them to compute the atmospheric effects on just the ERTS observations.

The graph on the left in Figure 1 shows the sensor response for the first multispectral scanner (MSS) channel, which lies in the yellow part of the spectrum and extends from 0.5 to 0.6 micrometers. Along the bottom axis is shown the reflectivity of the ground, varying from 0 to 1.0, and on the ordinate is the voltage output in percent varying from 0 to 100 percent. The solid continuous line represents the sensor output in the absence of any atmosphere. This output reaches a maximum for a surface reflectivity of about 55 percent.
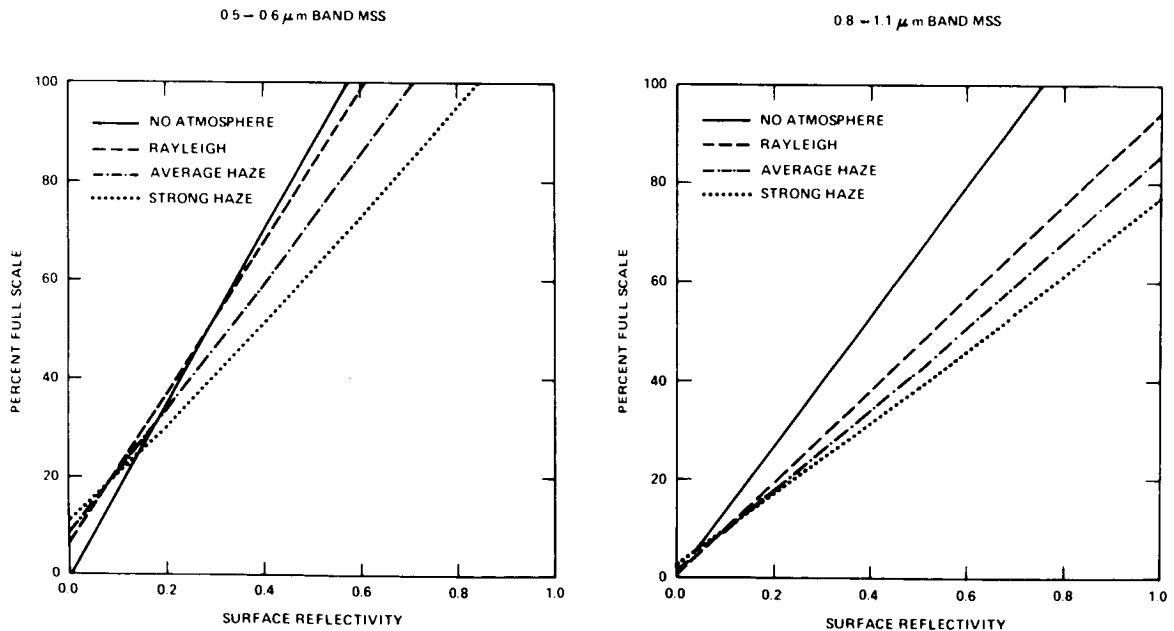
Figure 1. Sensor response of the first and fourth multispectral scanner (MSS) channels.

Each successive curve here represents what the sensor response would be in the presence of increasing atmospheric turbidity. This dashed curve is for a pure gaseous atmosphere,

the middle curve is for average haze conditions, and the bottom curve is for strong haze conditions. A slightly absorbing haze is used in this particular example. Where the surface reflectivity is low, the addition of haze to the model increases the brightness slightly; and where the surface reflectivity is rather high, addition of haze to the atmosphere decreases the brightness of the image. In many of the ERTS investigations over continental areas the reflectivity is about 20 percent. In this case, the atmosphere has a very small effect.

Eventually with the ERTS observations we will be able to establish some mean response in the presence of an atmosphere, and it probably will not be this dash-dot curve; nevertheless, this curve is the mean for this case and it indicates that when you go from an extremely clear atmosphere (dashed curve) to a very strong haze condition (dotted curve), the variations about the mean caused by the atmosphere are only about 20 percent.

The responses of the next two ERTS bands, from 0.6 to 0.7 micrometers and from 0.7 to 0.8 micrometers, are essentially the same as for this first channel.

The computed responses for the 0.8 to 1.1 micrometer band are shown on the right-hand side of the figure. The addition of haze would make the image appear darker than for the 0.5-0.6 micrometer band, not so much because of the haze, but because the presence of water vapor in the 0.8 to 1.1 micrometer band causes absorption of the energy.

One of the very important methods that is used in the ERTS investigations is to identify surface characteristics by means of their spectral signatures (as in Figure 2). In this figure I want to show you how some spectral signatures would appear when viewed from a satellite. On the left-hand side we have for the ERTS bands the sensor response over water. The bottom set of curves represents the responses to clear ocean water, and the upper set of curves are the responses to turbid coastal waters.
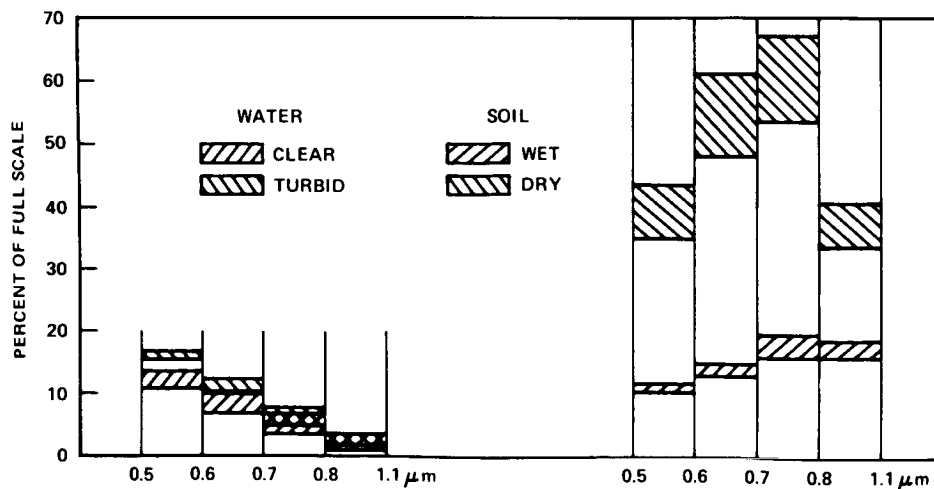

Figure 2. ERTS-1 MSS response to various surface features.

You can see what the variation caused by the atmosphere is. There is some separation between clear and turbid water in the first band, but the separation decreases with increasing wavelength. The separation disappears in the last band, where one would not be able to discriminate between the clear and turbid waters of this calculation.

The right side of the figure shows the effect of the atmosphere on the spectral signature of a higher reflecting substance, standard loam-type soils that are found in the vicinity of Goddard. The top set of curves shows the responses of the sensors over dry soil. The surface reflectivity of this dry soil varies from 25 percent in the first band to about 45 percent in the last band. The last band has a somewhat lower response than the first three bands because the instrumental gain setting is less for this last band and also because of the water vapor absorption. If the soil is saturated, it becomes darker. The surface reflectivity changes from about 10 percent in the first band to 20 percent in the last band. The MSS responses in the presence of atmospheric conditions are shown by the bottom set of curves. The separation between the dry and wet sets indicates that about five stages of wetness could be specified.

We have shown the initial computations on atmospheric effects on the ERTS measurements. We will continue investigating other types of ERTS problems under several different additional atmospheric conditions.

SATELLITE OBSERVATIONS DURING THE RAPID INTENSIFICATION OF HURRICANE CAMILLE

William E. Shenk

Tropical cyclones can intensify rapidly in a few hours. Two such instances occurred near shore in the last decade, namely Hurricane Cleo in 1964 and Hurricane Celia in 1970. In one case (Cleo) the increase came as a complete surprise to the residents of Miami, Florida. In 1964, we were fortunate to observe the rapid intensification of Harricane Camille as it moved from the north coast of Cuba into the Gulf of Mexico. These observations were made with the spin-scan camera on ATS-3 and with the Medium Resolution Infrared Radiometer (MRIR) on Nimbus-3.

Figure 1 shows a representation of the minimum central pressure profile as a function of time of Hurricane Camille. As in intensity reference, a 1000 millibar central pressure is associated with a fairly weak tropical cyclone, 960 millibars with a strong one, and 900
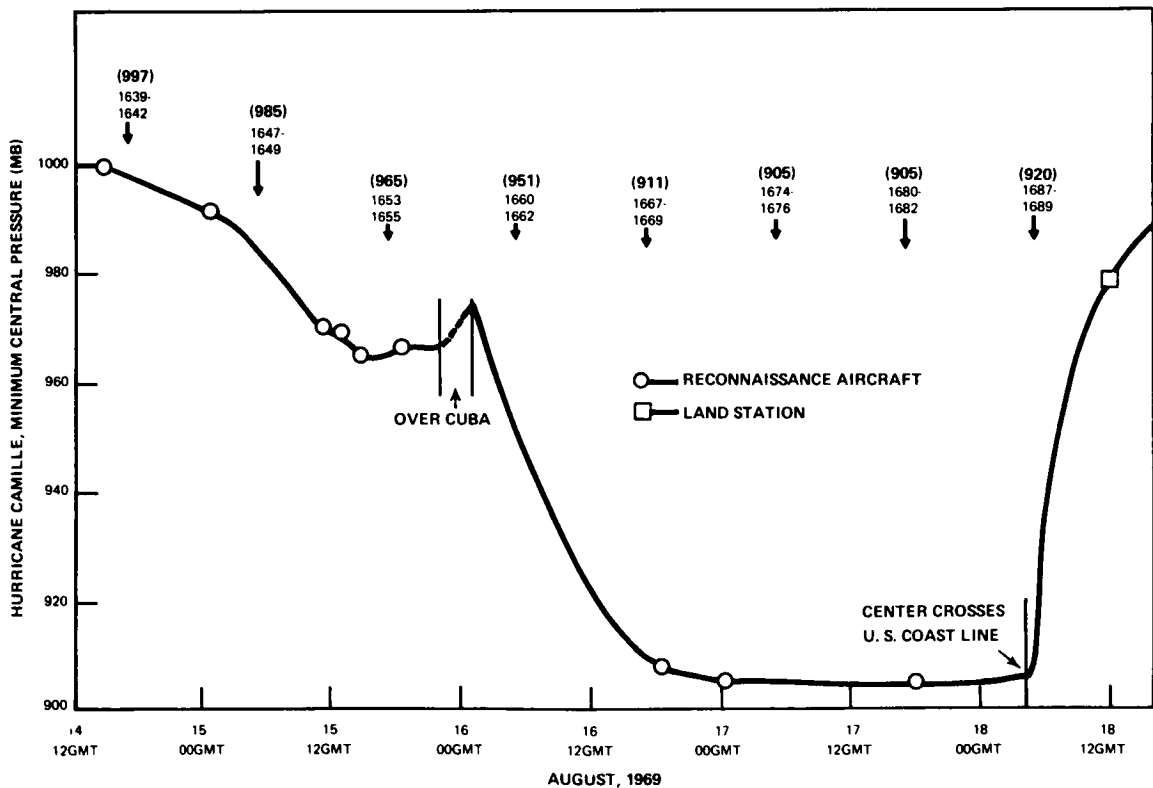
Figure 1. Minimum central pressure profile of Hurricane Camille, August 14-18, 1969. The Nimbus-3 orbit numbers used for each observation are shown above the curve and the estimated central pressure (in mb) above the orbit numbers.

196

millibars with a hurricane of extreme intensity. Hurricane Camille was the greatest Atlantic hurricane of record. According to four closely spaced reconnaisance aircraft reports, Camille initially deepened at a moderate rate and appeared to reach equilibrium while just south of Cuba. However, once moving across Cuba it deepened dramatically, about 65 millibars in 24 hours.

The rapidly deepening portion of the curve was constructed partly from satellite data, since there were no aircraft reconnaisance penetrations of the eye from the time when Camille was just south of Cuba to when it was nearly at maximum intensity over the Gulf of Mexico. The period of interest is the two satellite observations that were made by the MRIR during the maximum intensification phase. Two spectral regions were analyzed; namely, the 6.7 μm and the 11 μm regions.

A hurricane is like an inefficient heat engine — warm moist air flows in at low levels, is lifted within the interior with the release of latent heat, and then the air is ejected in the outflow layer in the upper atmosphere, moving away from the storm and subsiding. The subsidence compensates for the rising air within the interior.

It was expected that the two spectral intervals previously mentioned would indicate whether there were any dramatic changes in Camille's circulation during the period of maximum intensification. Figure 2 shows 2 measurements in the 6.7 μm region. The measurements were taken 12 hours apart. The first observation was made just after the storm moved off the north coast of Cuba and the second one when Camille was over the Gulf of Mexico and had reached maximum intensity.

The first observation indicates a band of relatively high equivalent blackbody temperatures T_{BB}'s west of the center. Other investigators have shown that regions of high T_{BB}'s are associated with areas of subsiding air.

Twelve hours later the warmer T_{BB}'s indicate that the region of subsiding air had increased dramatically and the subsidence had apparently intensified. This is evidence that increased upward vertical motion had occurred or is occurring in the interior of the cyclone, which is an indication of rapid intensification.

In addition to the MRIR measurements, Dr. Tetsuya Fujita (University of Chicago) analyzed the ATS-3 measurements and showed that west of the center there was an intense upper tropospheric convergence zone which was associated with subsidence. The convergence zone is confirmation of the inference of subsidence from the 6.5-7.0 μm measurements.

Figure 3 shows the 10-11 μm measurements for the same period. First, there is evidence from the cloud bands southeast of the center of the movement of warm moist air toward the center at low levels. This air is lifted near the center and a large fraction of the kinetic energy of the circulation is obtained from the release of latent heat.

The cloud bands first appeared at the time when Camille was just beginning the rapid intensification; therefore they were an indication of future development. Thus, if
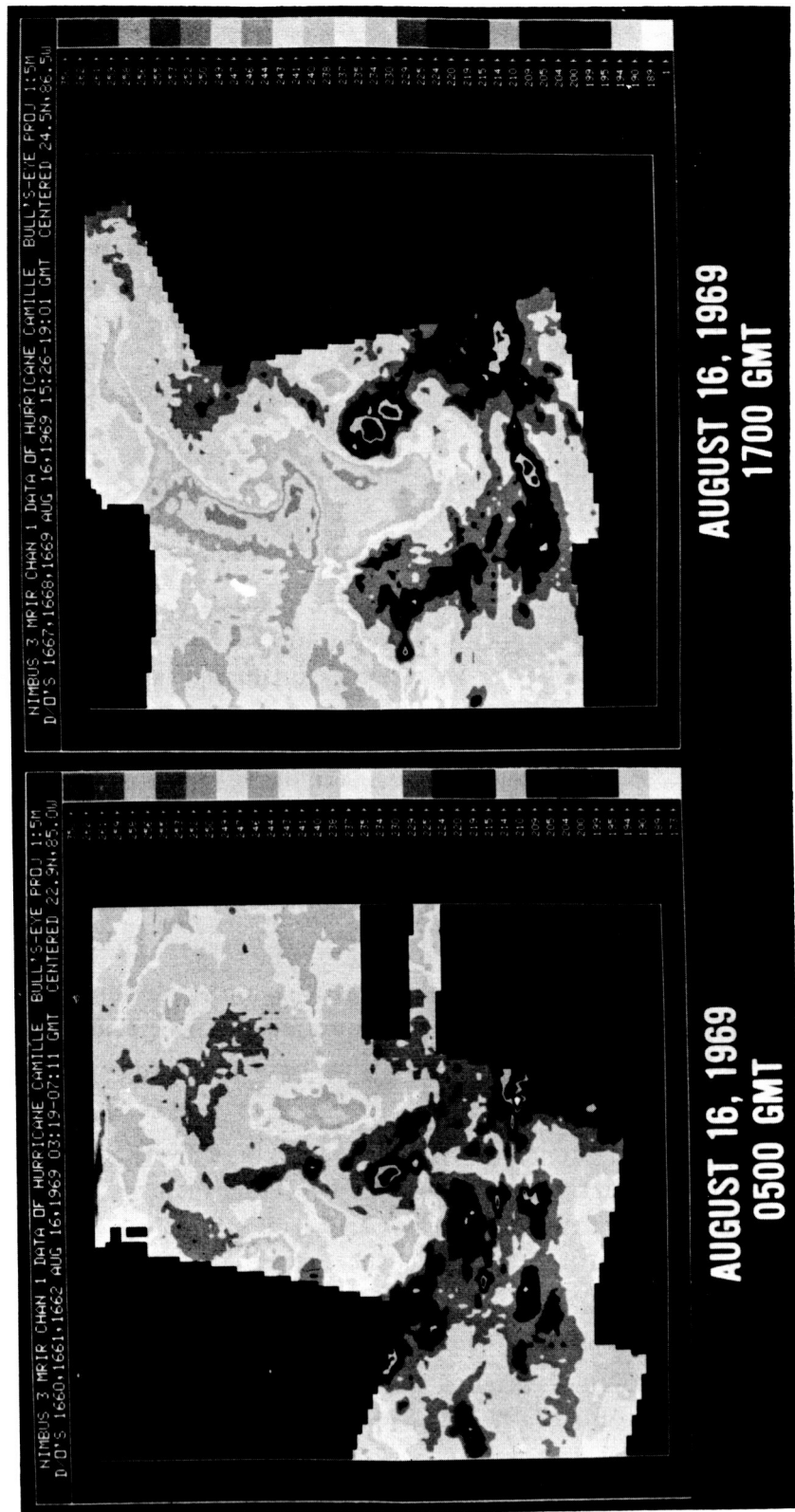
197

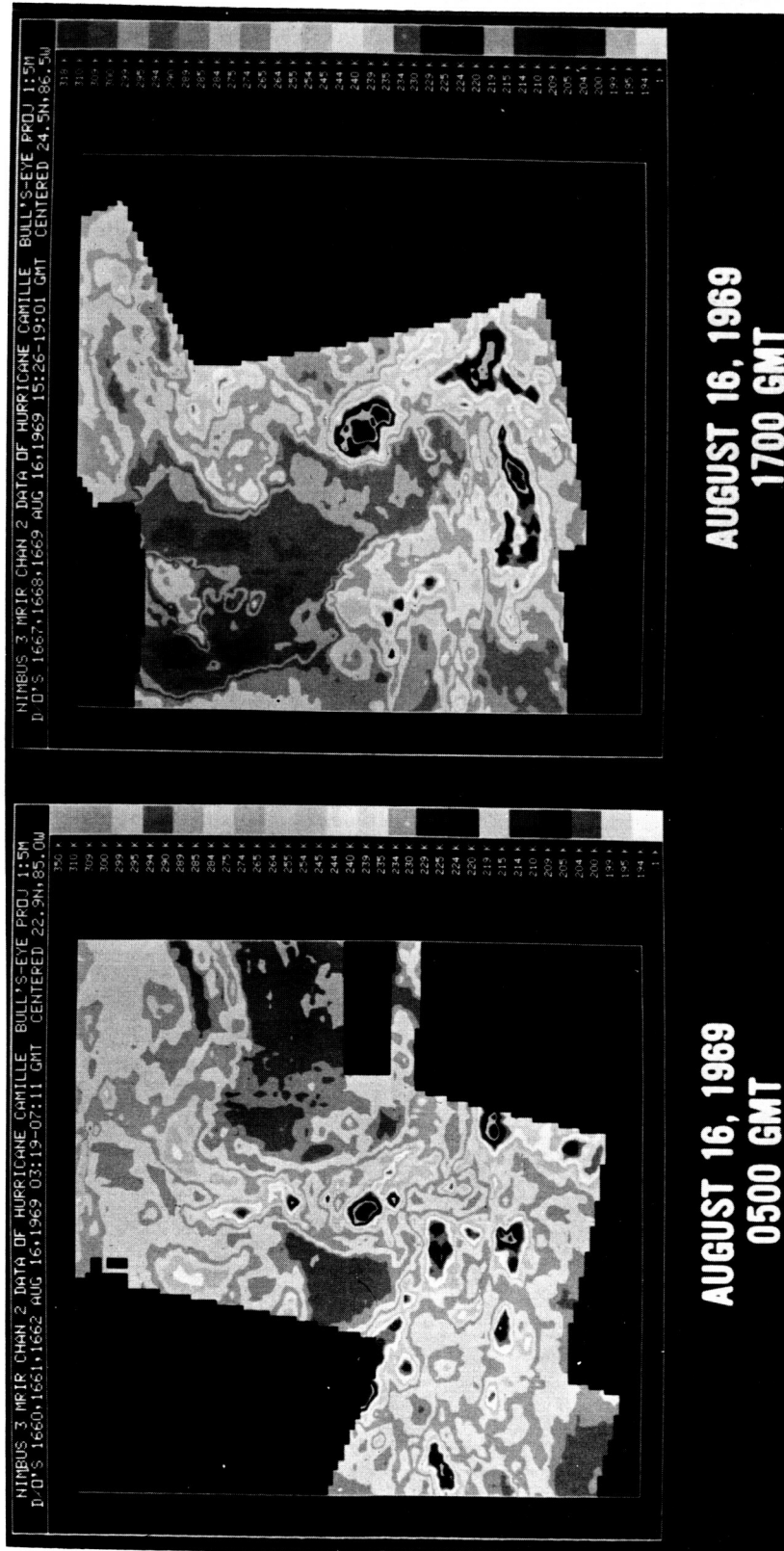Figure 2. Nimbus-3 MRIR imagery (6.5-7.0 μm) of Camille.

Figure 3. Nimbus-3 MRIR imagery (10-11 μm) of Camille.

199

measurements were available from a geosynchronous satellite every few minutes instead of every twelve hours, as was the case with these observations, we could have detected the beginning of the occurrence of these bands.

In the region of subsidence west of the center there is an area of high equivalent blackbody measurements which are close to what would be expected from the sea surface. Therefore, the subsidence was not confined to the upper troposphere but, due to the suppression of low-level cumulus over the ocean, was also occurring in the lower troposphere. The combination of the measurements from both channels gives a reasonably good three-dimensional picture of the structure of the storm.

In conclusion, if we had a geosynchronous satellite measuring in these two spectral intervals we would be able to determine much more about the circulation of tropical cyclones. This knowledge would provide some useful diagnostic and predictive information on significant changes in cyclone intensity.

CLOUD EMISSIVITY

Robert J. Curran

The infrared interferometer spectrometer on Nimbus-4 observed many peculiar broadband spectral effects which were found to be attributable to clouds. An example of the peculiar effect may be found in the spectra shown in Figure 1. Plotted here is the brightness temperature derived from the measured radiances, as a function of wave number. The wave number interval chosen covers the 8- to 12-μm window of the thermal infrared. Most plots of brightness temperature over this wave number region follow lines of constant brightness temperature. However, the three spectra presented show a brightness temperature
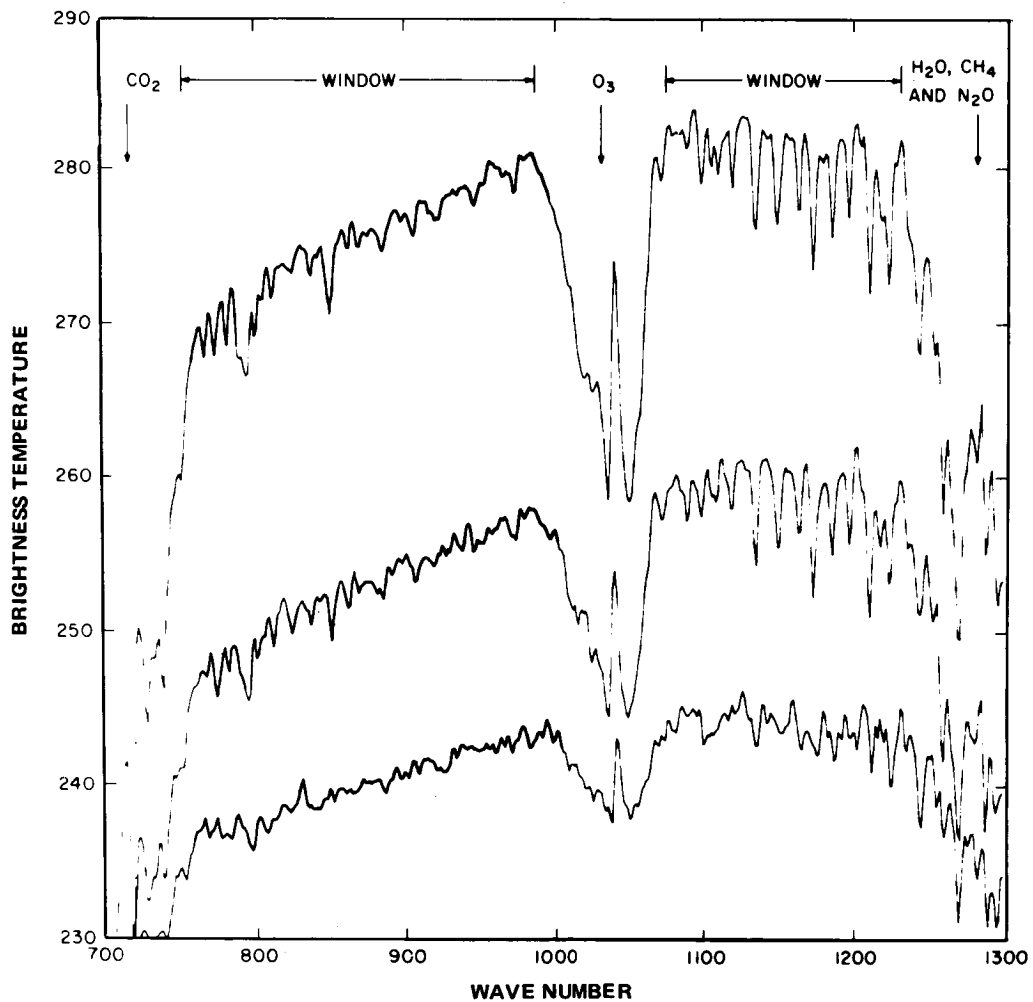
Figure 1. Nimbus-4 IRIS observations of the spectral properties
of cloud brightness temperature.

difference of 5 to 15 K over the wave number interval 750 to 950 cm^{-1}. The envelope of the temperature slope is emphasized by the shading.

For some time this spectral feature was difficult to explain yet appeared to be of importance, because this is the same spectral region used to determine cloud altitude by matching measured brightness temperatures with known altitude temperature distributions. To better understand the physical problem of the transfer of infrared radiation through ice and water clouds, models were developed to calculate their spectral properties. Some of the results of these calculations are presented in Figure 2.
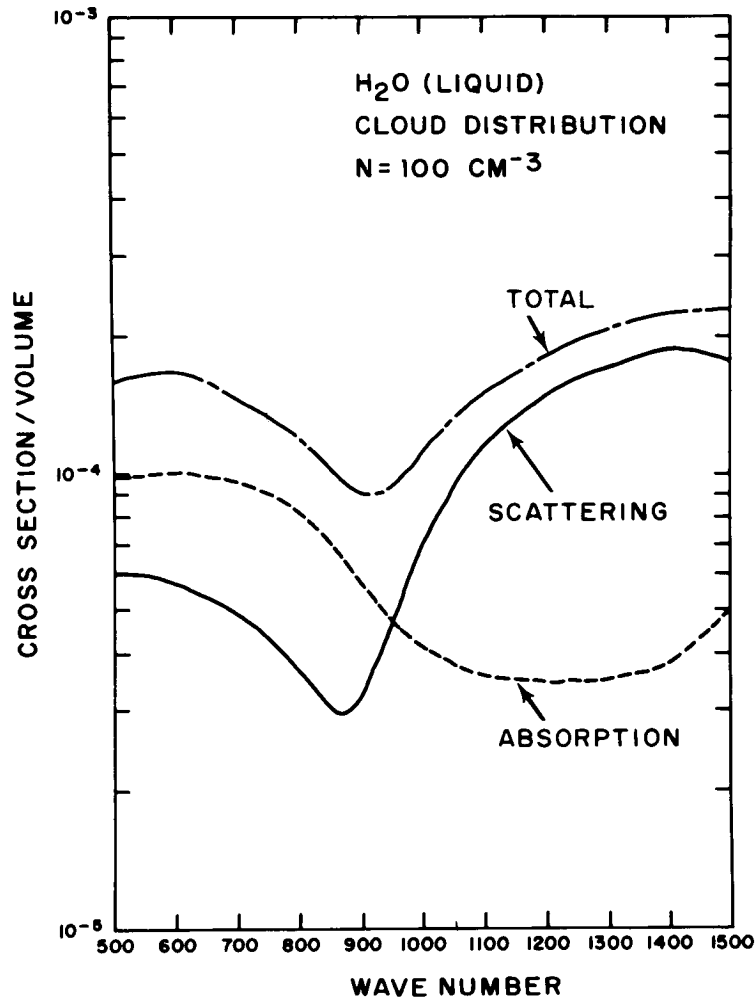
Figure 2. Calculations of the spectral absorption, scattering, and total cross section per unit volume. Calculations were made for spherical water droplets distributed in size according to a terrestrial cloud model.

We assumed we had a collection of spherical particles whose sizes were distributed similar to those of known water clouds. Laboratory measurements of the infrared refractive index

were used to calculate the cross sections per unit volume for the collection of particles. Figure 2 shows the wave number dependent absorption, scattering, and total cross sections per unit volume. Because of the increased emphasis on the absorption and reemission of radiation in the infrared, the absorption cross section plays a dominant role. The slope in the 750 to 950 cm^{-1} of the previous figure was found to correspond to the strong change in the absorption cross section in the same wave number window.

The question still remained as to why this feature was not observed for all liquid water clouds. To answer this question we took the reciprocal of the cross section per unit volume. This new quantity is the photon mean free path, the average depth from which a photon can be emitted in a cloud and be detected at the satellite. Photons emanating from this depth are emitted at the temperature of that level.

Figure 3 shows the relationship between the photon mean free path in kilometers and the number density of cloud particles for six different wave numbers in the window region. If the cloud contains 100 particles per cubic centimeter, then the 950 cm^{-1} brightness temperature will be that of 0.2 kilometers depth in the cloud, and the 700 cm^{-1} brightness temperature will be that of 0.1 kilometers depth in the cloud. However, if the number density is 10 particles per cubic centimeter then the 950 cm^{-1} temperature will be that of a depth of 2 kilometers in the cloud, and the 700 cm^{-1} temperature will be that of 1 kilometer in the cloud. The temperature increases with depth in most clouds, and thus the 950 cm^{-1} brightness temperature will be higher than the 700 cm^{-1} brightness temperature which was observed in Figure 1. Thus, only those clouds whose number densities are small enough to allow for an appreciable temperature difference over the 700 to 950 cm^{-1} penetration depths will show the peculiar feature.

Using the analysis above and an assumption as to the cloud internal temperature distribution, we used the measured slope in the brightness temperature plots to derive the number density of particles in the measured spectra. Those spectra displayed in Figure 1 were found to have about ten particles per cubic centimeter.

The analysis made yielded two important results which should be of use to future investigations. First, cloud-top altitude determination can be corrected for emission from lower levels in the cloud if an estimate can be made of the number density of particles. Second, using the wave number dependent brightness temperature in 700 to 950 wave number region, estimates of the cloud number density can be made. These cloud number density determinations are of interest in studies of the physical nature of clouds.
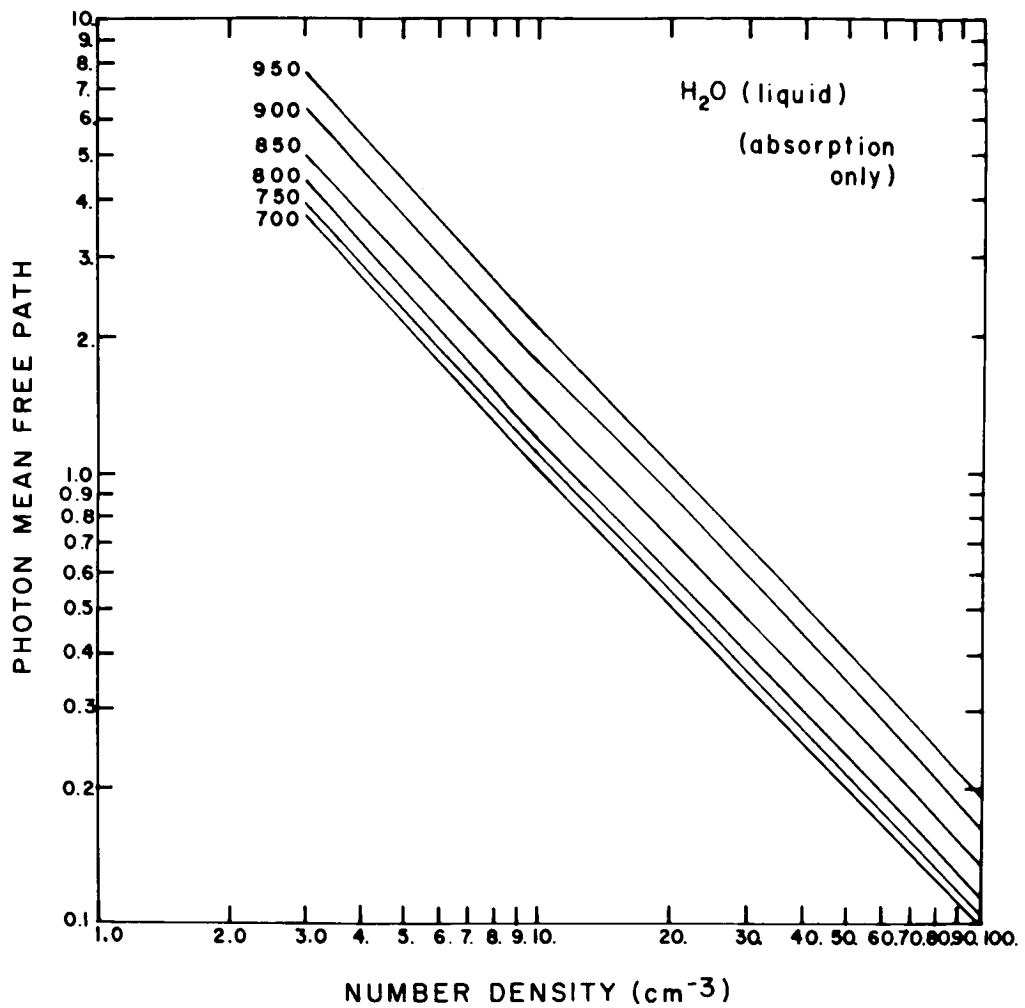
Figure 3. Photon mean free path in kilometers as a function of number density of cloud particles for six different wave numbers in the infrared-window region.

TIDES IN THE UPPER ATMOSPHERE – A CONTROVERSY RESOLVED?

John S. Theon

Since the amplitudes of atmospheric tides are small in the troposphere, they are neglected for most purposes. Such is not the case for the stratosphere and mesosphere, where tides produce significant changes in the temperature, pressure, density, and circulation. The tides in the upper atmosphere are driven by the heating resulting from the absorption of solar energy by ozone near the stratopause and water vapor in the troposphere. This periodic heating was, until 1967, believed to produce a diurnal temperature variation in the upper atmosphere which closely followed the heat input; that is, a maximum temperature near local noon and a minimum temperature in the early morning hours before sunrise.

Unfortunately, the early rocket measurements, which were made utilizing thermistor temperature sensors, reflected this simple-minded concept (Figure 1). These curves are
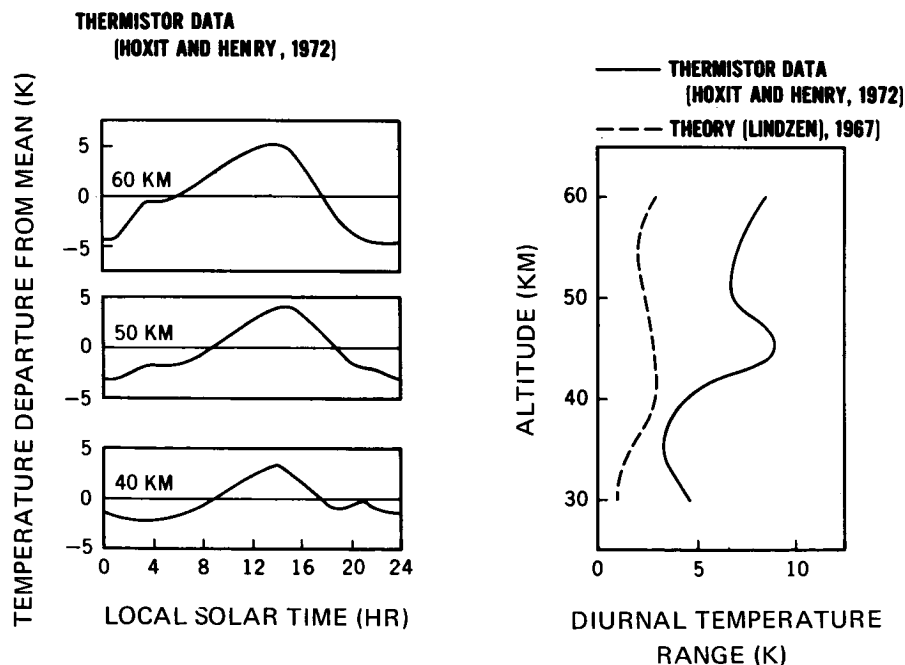

Figure 1. Early rocket temperature measurements utilizing thermistor sensors.

based on an analysis by Hoxit and Henry of 1720 thermistor instrumented rocket soundings obtained during the years 1964-69 from three middle latitude sites. On the left, the

temperature departure from the mean is plotted as a function of local solar time for three altitudes: 40, 50, and 60 km. Note the similarity of the three curves. Each is a sinusoidal wave form; the amplitudes grow with altitude; and the times of maximum and minimum temperature (or phase) remain nearly constant with altitude. The plot at the right shows the amplitude as a function of altitude for the thermistor data compared with the appropriate results from a theoretical model of the thermally driven tides developed by Lindzen in 1967. The observations exceed the theory by a factor of at least two everywhere except near 40 kilometers. When comparing the phase of the observations with the theory, the discrepancy becomes even more obvious. Note the nearly constant phase with altitude of the thermistor results.

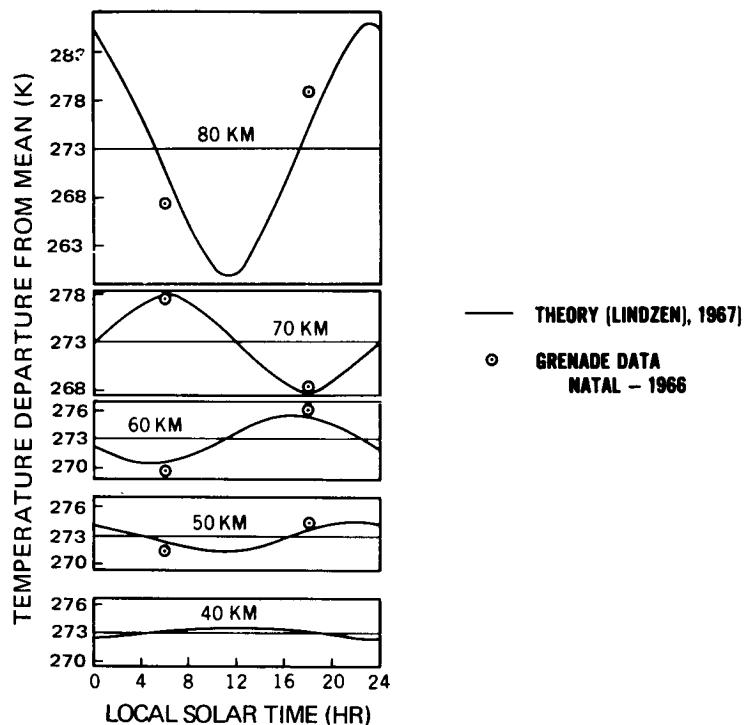The variable nature of the phase predicted by the theory can best be seen in Figure 2.

Figure 2. Theoretical versus measured temperatures.

Here the theoretical temperature variations are given as a function of time for 40, 50, 60, 70, and 80 kilometers. Note how the time of the maximum temperature varies from 1100 hours at 40 kilometers; to 2200 hours at 50 kilometers; to 1700 hours at 60 kilometers; to 0600 hours at 70 kilometers; to 2300 hours at 80 kilometers.

We attempted to clarify these discrepancies by utilizing the acoustic grenade technique, but economic and operational considerations limited the quantity cf data we were able to

206

obtain. With a very limited data sample one cannot rely on statistical techniques to remove the unwanted synoptic and seasonal variations from the data, so we chose to conduct our experiments in the tropics, where these factors would be minimal. Data from a pair of grenade soundings conducted 12 hours apart are plotted with the theoretical curves. These results and several other pairs of similar soundings tended to confirm the theory, especially in regard to the variation of phase with altitude. But the controversy remained because of large numbers of thermistor soundings on one side and the theory supported by fragmentary results from grenades on the other.

It was not until last year that a comprehensive set of acoustic grenade soundings was conducted in an attempt to resolve the apparent differences between the thermistor and grenade results. In an experiment unprecendented in Nike Cajun class meteorological rockets, 13 grenade soundings were launched during a 56-hour period in September 1971, from Kourou, French Guiana. The preliminary results of that experiment are shown in Figure 3.
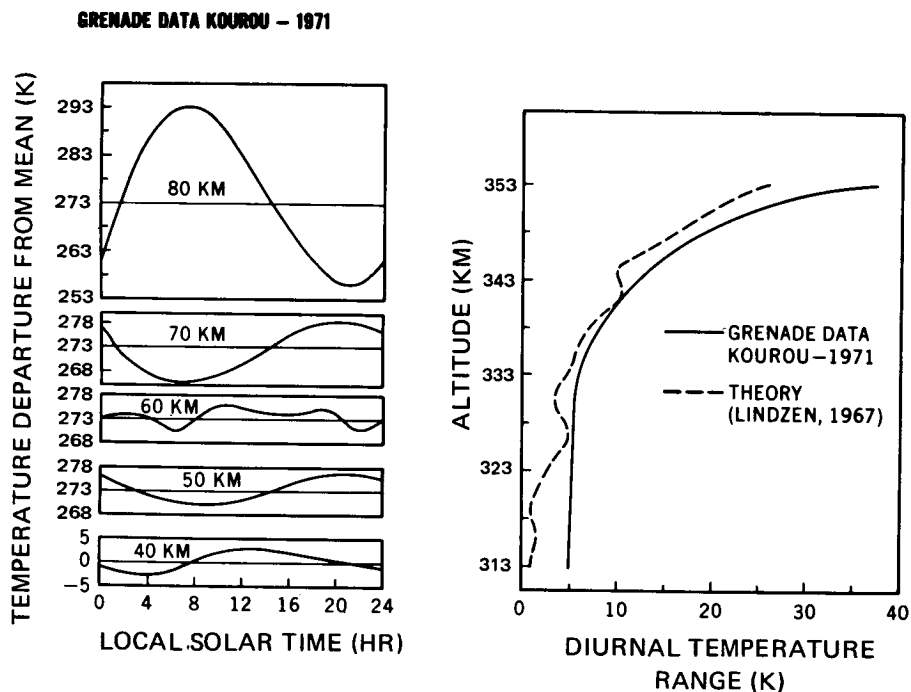
Figure 3. Results of acoustic grenade soundings.

The smoothed observed temperature departures from the mean for the two-day period are plotted at left. Note how the phase changes with altitude in agreement with the theory, although the times of maximum and minimum are not aligned at all altitudes. The amplitudes of the tide as a function of altitude are given in the plot at the right for both the theory and the grenade results. For all altitudes above 50 kilometers, there is remarkable agreement.

The 1971 Kourou grenade data, representing the most complete in situ results ever obtained, will likely be the last such attempt to resolve the tidal questions in the foreseeable future, since the program which supported this work has now been effectively terminated.

SECTION V

EARTH PHYSICS

OVERVIEW

Friedrich O. von Bun

We have been involved over the last four years with NASA Headquarters, developing a new program in the applications area; namely, the Earth and Ocean Physics Applications Program (EOPAP). This program is directed toward the development and the validation of four major applications objectives: First is earthquake hazard assessment and alleviation; second is the prediction of general ocean circulation, surface currents, and thus heat transport (due to the mass transport); third is the monitoring of transient phenomena of the ocean surface, such as sea state and wave conditions, the wind — surface wind particularly — and storm searches; and fourth is to refine global geoid, the gravity and magnetic fields of the earth, to satisfy the user requirements.

At present there are two geodetic spacecraft in orbit, namely GEOS-1 and -2, and in addition there are five other spacecraft in orbit which carry laser corner reflectors. These can and are being used for some experiments which will lead us to the solution of the tasks I have just outlined. We also have fixed and portable high-precision lasers, as well as other tracking systems at our disposal, to help us in this effort.

The next three papers will describe some of the results of our preliminary work in the area of earth and ocean dynamics. The first paper, given by Jim Marsh, is related to both earth and ocean dynamics, and describes a geoid which we constructed utilizing satellite as well as ground-based data.

Why do we need a geoid? For instance, if we want to determine geostrophic currents, we will have to measure the ocean surface tilt caused by the Coriolis acceleration. To give you a feel for it, the Gulf Stream over a 50-kilometer distance (perpendicular to the water flow) has a tilt of $3p.10^5$ (1.5 meters). If we want to detect this 1.5-meter variation we have to get an idea of what the geoid is, because the geoid undulations are much larger than the 1.5 meters.

The second and third papers relate more to solid earth dynamics such as earthquake phenomena. Ron Kolenkiewicz will address himself to an experiment we finished some time ago, where we are taking a new approach to determine the motion of the pole, by using lasers. He will show that, in six hours, we were able to determine the motion of the pole to within one meter.

Finally, Dr. H. Liu will discuss a theoretical model which tries to explain why certain earthquakes occur at certain depths, based on elastic plate theory.

A DETAILED GRAVIMETRIC GEOID OF NORTH AMERICA, THE NORTH ATLANTIC, EURASIA, AND AUSTRALIA

James G. Marsh

During the past year we have computed a detailed gravimetric geoid covering North America, the North Atlantic, Eurasia, and Australia. This geoid is based upon a combination of satellite and surface gravity data and represents the first gravimetric geoid which has been computed on this global scale.

First I would like to define a few of the terms I'll be using in my discussion (Figure 1). The geoid is defined as the equipotential surface which most nearly corresponds to mean sea level. The geoid is a somewhat irregular surface; therefore, for some applications it's desirable to represent the earth as an ellipsoid.

The undulations of the geoid with respect to the ellipsoid are called the geoid heights. The geoid can be either above or below the ellipsoid, and the geoid heights range from about plus 100 meters to minus 100 meters. The Skylab and GEOS-C satellites to be launched in the near future will carry altimeters which will be used to establish the shape of the geoid in the ocean areas. Our independently derived gravimetric geoid will be very valuable for the comparison, evaluation, and interpretation of the new data from these satellite altimeter experiments, especially with respect to studies of phenomena such as tides and currents.
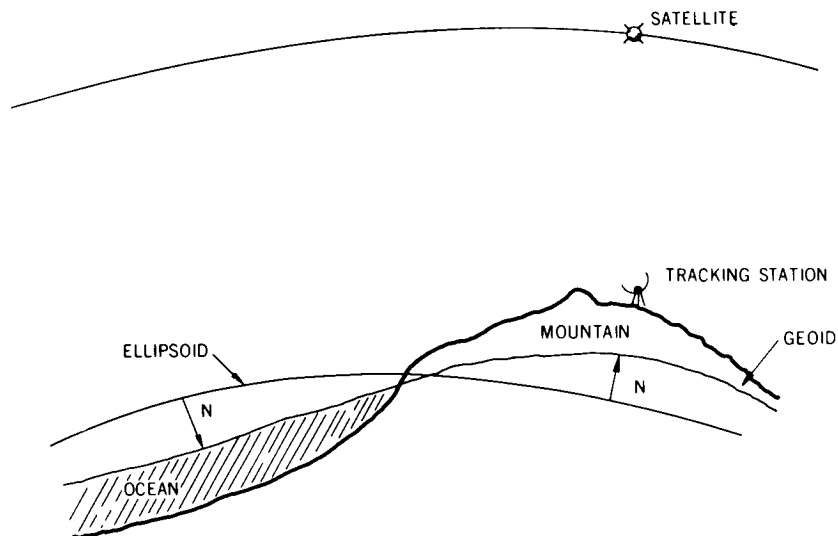

Figure 1. Definition of terms.

212

Another application is in the area of the coordinates of our tracking stations. The conventional surveyors provide us with the height of the tracking station above the geoid. In order to perform orbit calculations, we require that the coordinates for the station be referred to the center of mass of the earth. However, if we have an accurate geoid height at the station, we can calculate a radius vector from the center mass of the earth to the tracking station. The geoid also forms the basis for other geophysical studies of the earth.

The satellite gravity fields provide information on the broad features of the geoid. However, the ground-based data give us information on the details. In our work, we've combined the satellite gravity data with the surface data. Figure 2 presents geoid profiles at 35 degrees north latitude, extending from San Francisco across Eurasia.

The dashed line represents the geoid corresponding to the Smithsonian Astrophysical Observatory 1969 Standard Earth satellite gravity model. The accuracy of this geoid is about 10 meters. In our work, we have combined this satellite solution with the surface data to provide what we call a detailed geoid, which is represented by the solid line. The accuracy of this detailed geoid is on the order of about 2 meters in the land areas, and possibly 2 to 5 meters in areas where we had less accurate surface data.
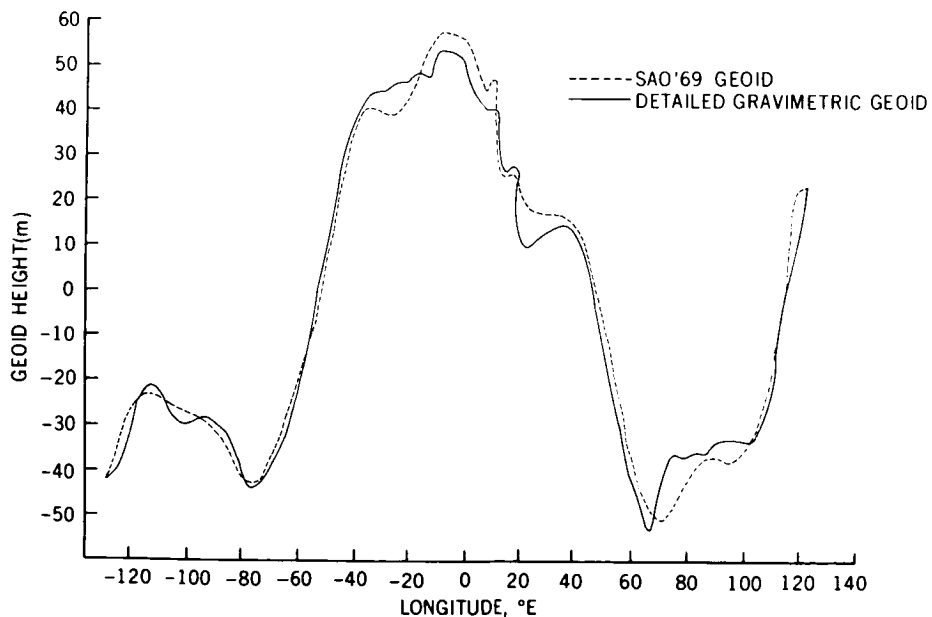
Figure 2. Detailed gravimetric geoid and SAO 1969 geoid at latitude 35° N.

Figure 3 presents a geoid map, or a contour map of the geoid heights, as shown in Figure 1, for the North America-North Atlantic region. Similar maps have been prepared for Eurasia and Australia.

In summary, during the past year we have developed a computer program for the calculation of a geoid based upon a combination of satellite and surface gravity data. Using this program we have derived a detailed gravimetric geoid of North America, the North Atlantic, Eurasia, and Australia.
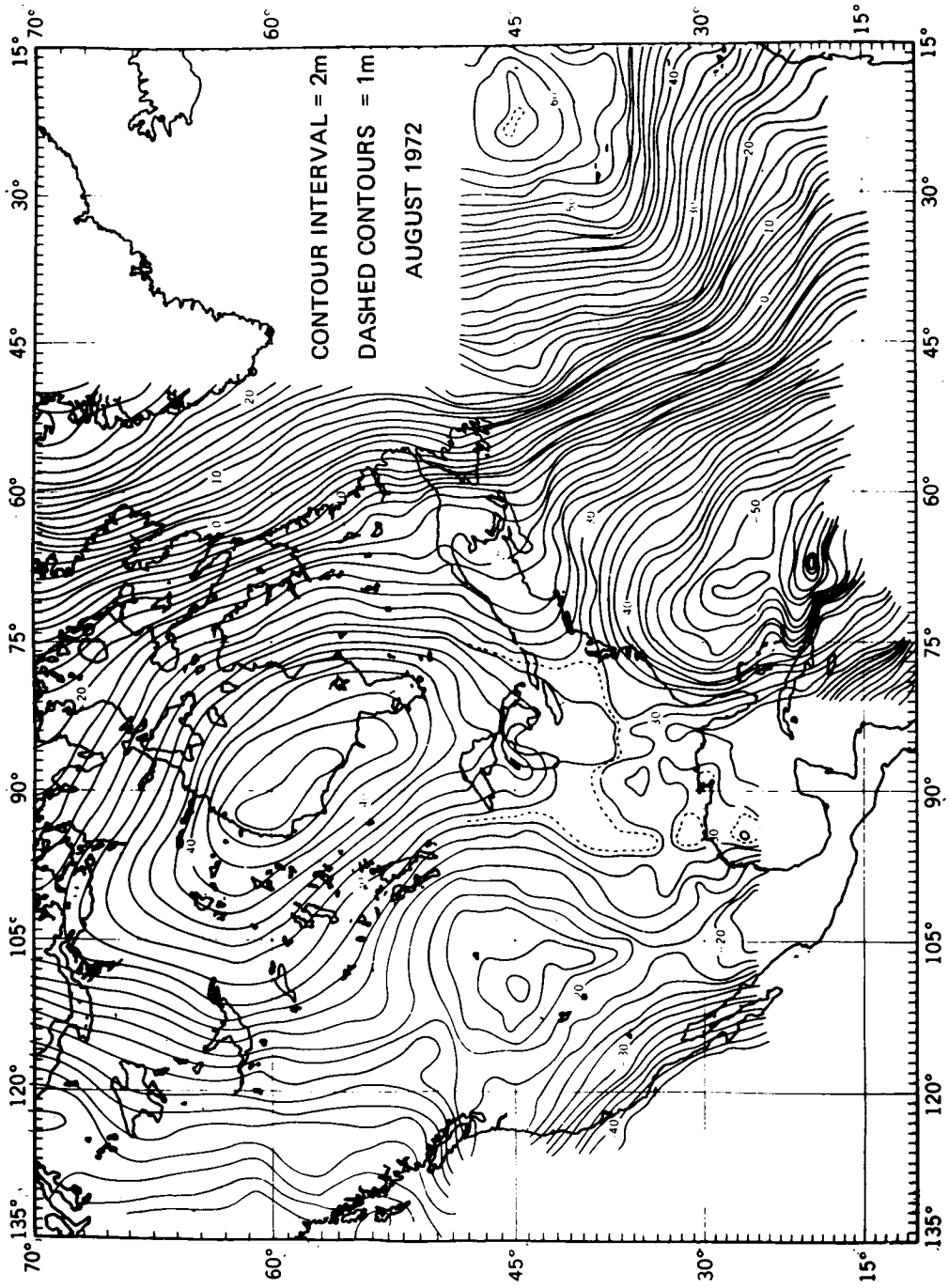
CONTOUR INTERVAL = 2m

DASHED CONTOURS = 1m

AUGUST 1972

Figure 3. Detailed North America/Atlantic gravimetric geoid.

215

POLAR MOTION

Ronald Kolenkiewicz

Today I'm going to talk about polar motion and the solid earth tide. In 1970, Goddard Space Flight Center conducted an experiment utilizing its precision laser tracking system to track the Beacon Explorer-C satellite. The purpose of this experiment was to see how well we could measure some parameters of geophysical significance.

These parameters are the polar motion and a measure of the solid earth tide. In Figure 1, I've indicated a typical Beacon Explorer-C ground track, latitude and longitude. The Goddard laser is located at the Goddard optical facility, and is capable of seeing four passes of this orbit in a single day.

The point of maximum latitude is the point which we wish to measure very precisely. This, incidentally, is also the inclination of the orbit which is about 41 degrees. The first thing we can find by measuring this point is the effect of the solid earth tide, which is due to the fact that the sun and the moon pull on the earth – which is elastic – and this force redistributes the mass of the earth. This mass redistribution perturbs the inclination of the orbit, or the point of maximum latitude.
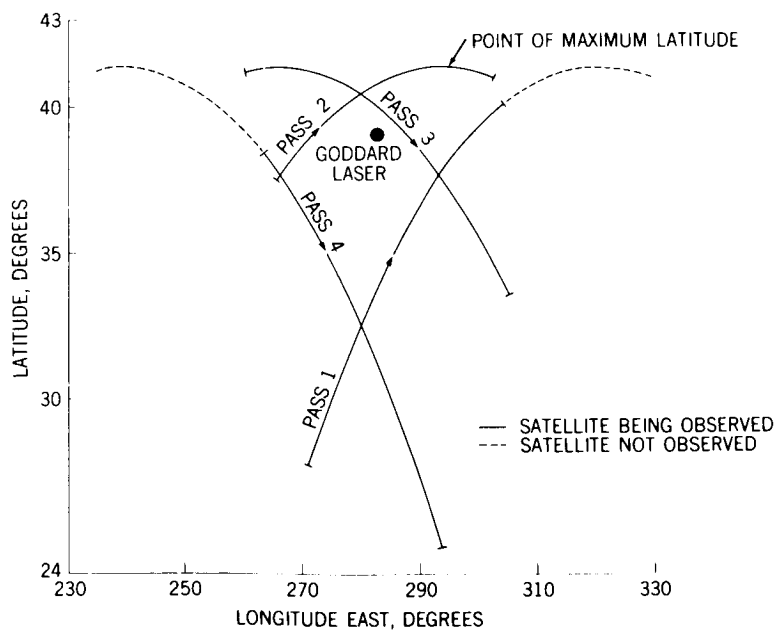

Figure 1. A typical Beacon Explorer-C ground track.

216

Having modeled for this effect in our orbit calculations, we can then get a very precise orbit, and we can find the position of the Goddard laser with respect to the point of maximum latitude. This then is the polar motion part of the experiment. Polar motion is sometimes known as variation in latitude, and arises because the intersection of the instantaneous axis spin of the earth does not remain fixed with respect to the earth's crust. In other words, the earth wobbles.

In Figure 2 I've indicated the solid earth tide portion of this experiment. The tidal perturbation of the Beacon Explorer-C latitude is shown plotted as a variation in maximum latitude in seconds of arc, or meters on the earth's surface as a function of the date.

The open points are the laser data, and the solid line is for a Love's number of 0.25. Now, Love's number is a measure of the elasticity of the earth; it's a dimensionless quantity which would have a value of one if the earth were perfectly elastic — that is, a fluid — and it would be zero if the earth were perfectly rigid.
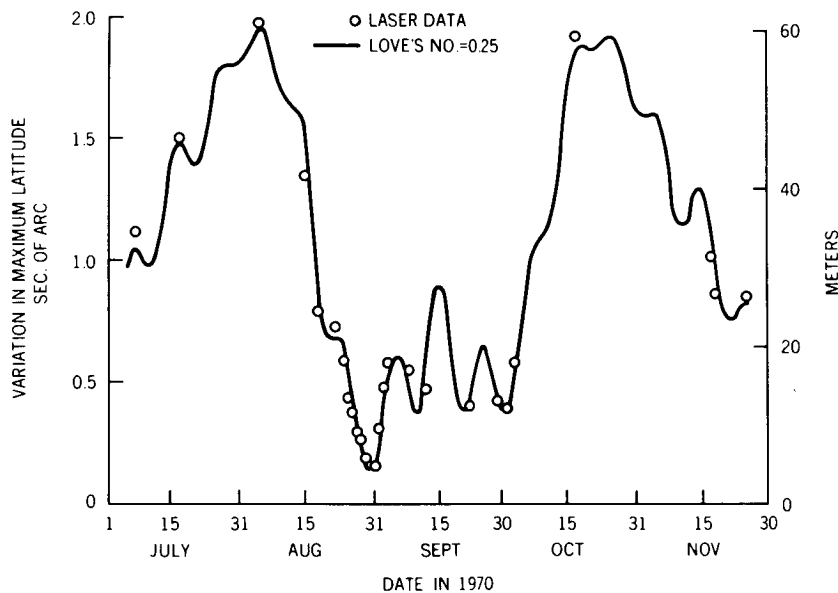

Figure 2. Tidal perturbation of the Beacon Explorer-C latitude.

We see for the actual earth it's more like 0.25. This value of 0.25 seemed to fit our data better than other values we tried. The significance of this is that this is the first time Love's number has been obtained by laser ranging to a satellite. We've obtained it to an order of a magnitude better than that previously obtained by satellite.

More important to our experiment is the fact that by modeling this effect into our perturbation equations for the orbit we can get a very precise orbit. This enables us to use the

orbit as a reference and measure long baselines with this reference. If we put two lasers at a distance of several hundred kilometers apart from each other we could measure the strain buildup along the fault by monitoring the motion of the lasers. This strain buildup is a measure of the energy that would be released should an earthquake occur.

In Figure 3 I've indicated the variation in latitude of the Goddard laser. This is the polar motion part of the experiment. Polar motion is shown by plotting the variation in latitude in seconds of arc, or meters along the earth's surface, as a function of the date.

You'll note that the polar motion had the effect of moving the Goddard station south by about 12 meters during the five-month period shown. The open circles are the laser data, plotted in six-hour averages, six hours being the time from the beginning of the first pass to the end of the fourth pass during a single day's tracking of Beacon Explorer-C.

The smooth line, labeled here BIH smoothed is from the Bureau International de l'Heure, an international agency which monitors polar motion on a routine basis by observing the stars as they cross the meridians. This line looks very smooth. However, the raw data is rather crude, and in order to get such a smooth line the BIH obtains raw data from some 40 latitude stations, rejects some, and averages the rest statistically. BIH takes five-day averages and then draws a smoothing curve through these averages.

The BIH curve is just meant as a reference curve, and we see that the laser data fits the BIH data to within 97 centimeters. The important significance of this result is that we can
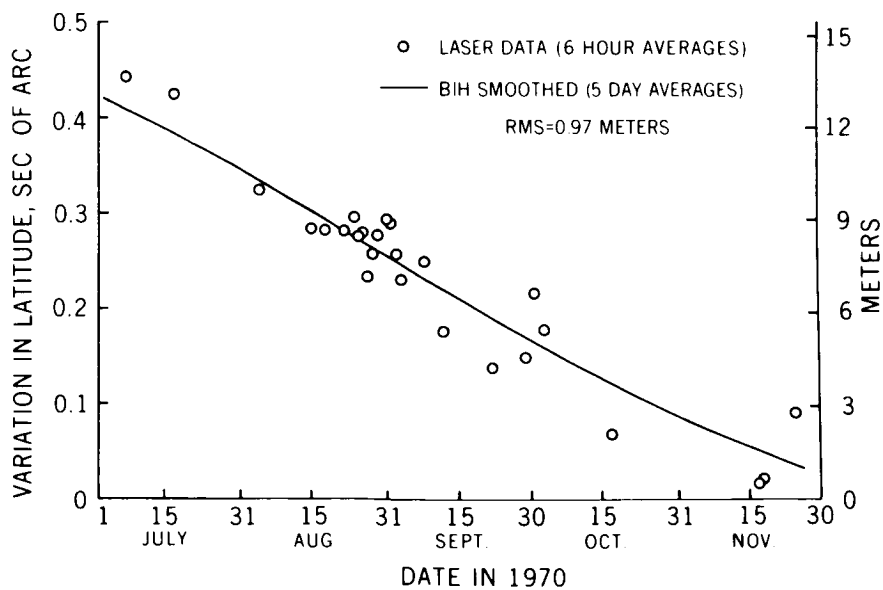

Figure 3. Variation in latitude of the Goddard laser.

218

obtain polar motion from laser tracking data to a time resolution of under a day, and this is extremely important if we are to understand the earthquake mechanism.

Some authors, in recent papers, have indicated a correlation between earthquakes and polar motion, the idea being that before an earthquake there would be a shift in inertia of the earth. This would be followed by a strain buildup along a fault, causing the pole to move (which we would be able to observe with a satellite), and shortly thereafter there would be a major earthquake. If this hypothesis is true, polar motion by laser ranging could lead to prediction of major earthquakes.

DR. PIEPER:

Do the individual fluctuations in the unsmoothed BIH data show a similar distribution to the points that you have?

MR. KOLENKIEWICZ:

The raw five-day average?

DR. PIEPER:

No, the daily unsmooth, raw.

MR. KOLENKIEWICZ:

The noise is too large in the single station BIH raw data to be able to distinguish any trend similar to the one shown on Figure 3.

MEMBER OF AUDIENCE:

On the previous chart, Figure 2, on the solid earth tides, I'm not quite clear on how you got the solid line shown.

MR. KOLENKIEWICZ:

We have the solid earth tide modeled in our orbit computation. First we use a value of Love's number of 0.25 and calculate an orbit for the satellite recording the daily values of the maximum latitude. We then repeat this orbit computation for Love's number zero. Taking the difference in values of the maximum latitudes for these two cases will result in the solid line labeled Love = 0.25.

MEMBER OF AUDIENCE:

We can predict the inclination; and we assume for the polar motion, that the plane of the orbit stands still, and that the earth wobbles.

THE ORIGIN OF INTERMEDIATE AND DEEP FOCUS EARTHQUAKES

Han-Shou Liu

The origin of intermediate and deep focus earthquakes is one of the mysteries of nature. Geophysicists have been forced to give explanations, but no satisfactory theory exists. The purpose of my presentation is to describe the elastic theory of tectonic plates which we have developed here at Goddard as a possible explanation.

The earth is covered by about eight tectonic plates including the American plate, Pacific plate, and Eurasian plate, as shown in Figure 1. Each plate has relative motions. The lower portion of Figure 1 is a block diagram of plate motions.

Physicists have measured that along the plate boundary lines, two plates are moving against each other. In other words, under these lines the Pacific plate, Indian plate, and African plate may thrust under the Eurasian plate and American plate.

Seismologists have determined that the intermediate and the deep earthquakes are located along these lines. Therefore it is possible that the origin of these earthquakes is closely related to the instability of the underthrusting lithospheric plates.

In order to correlate the depth of the instability of these plates with the depth of these earthquakes, let us discuss the depth distribution of the intermediate and the deep earthquakes. As seen in Figure 2, the depths of the intermediate earthquakes in Romania, New Zealand, Kermadec, and Izu-Bonin are centered about 150 kilometers or 450 kilometers below the surface of the earth. The depth of the deep earthquakes in Sunda, South America, Tonga North, New Hebrides, and the Philippines is about 600 kilometers. At a depth of about 300 kilometers there is no seismic activity.

Now, two questions must be answered: Why is there no seismic activity in this region? Why is the distribution of the intermediate and deep earthquakes restricted to these three levels? These are basic and fundamental questions in earth physics which we have to answer.

Here is our elastic plate model (Figure 3). Two plates are moving against each other, one plate thrusting under the other. The depth of the underthrusting is about 600 kilometers. If this plate is elastic, then our problem of tectonic plate instability is simplified to a problem of the deformation of plate structure.

According to the theory of elasticity, the deflection of the plate is shown at **A** and **B** on the figure, which are regions of maximum curvature in which buckling of the plate may occur. **C** is a neutral region in which there is no deformation. Therefore the depth distribution of the intermediate earthquakes is restricted to the regions of instability in **A** and **B**, and the absence of seismic activity at **C**, 300 kilometers below the surface of the earth, can be explained in terms of plate deflection.

220
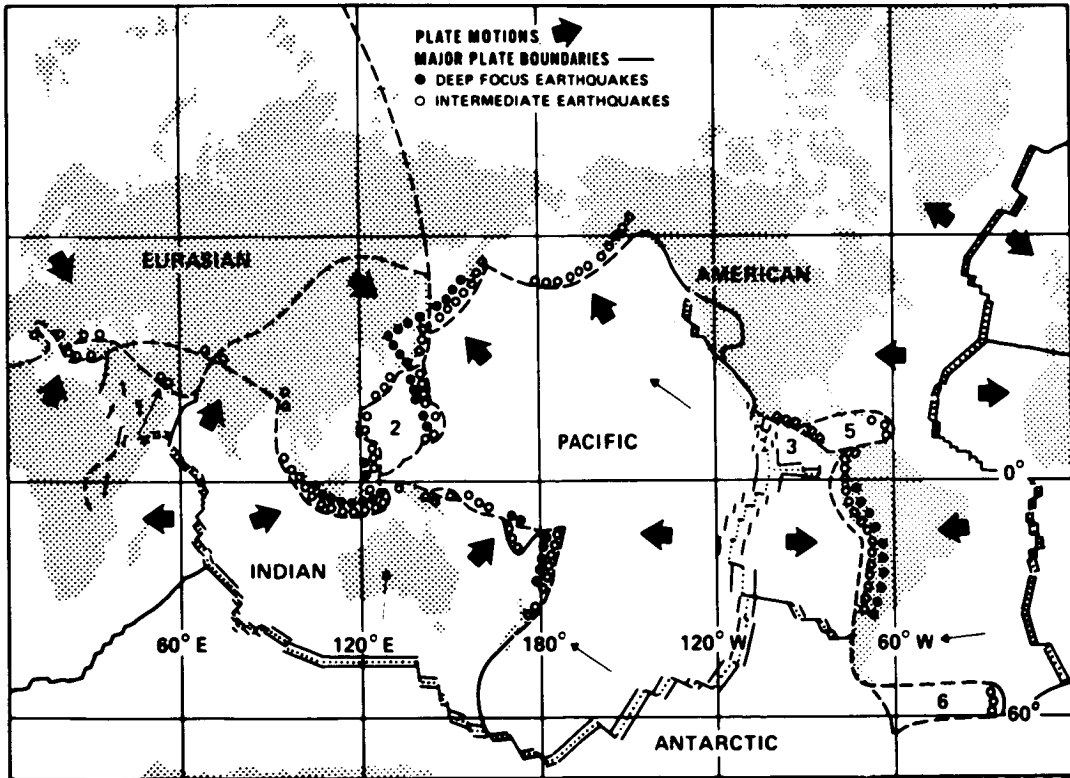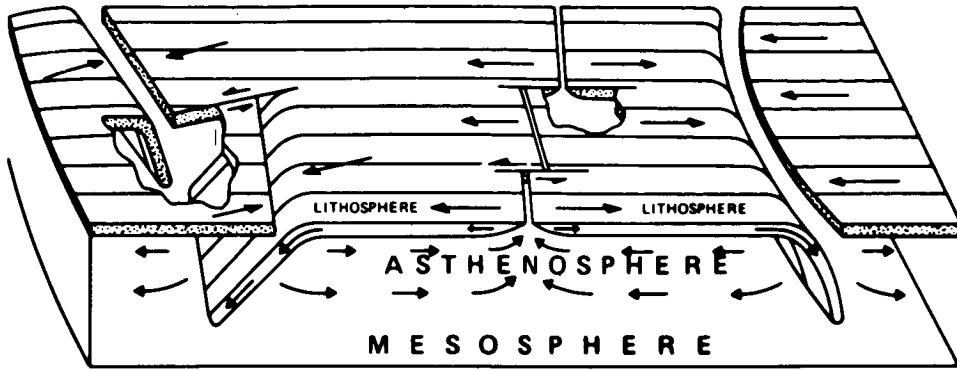
MAJOR TECTONIC PLATES

Figure 1. Seismology and global tectonics.

If the plate continues to thrust into the mesosphere, its buoyancy will act against it because the density of the mesosphere is greater than the density of the asthenosphere. Under this condition, the leading edge of the plate will be deformed with a parabolic profile. So it is possible that the deformation or buckling of the plate in the region of instability **D** is the cause of deep earthquakes.
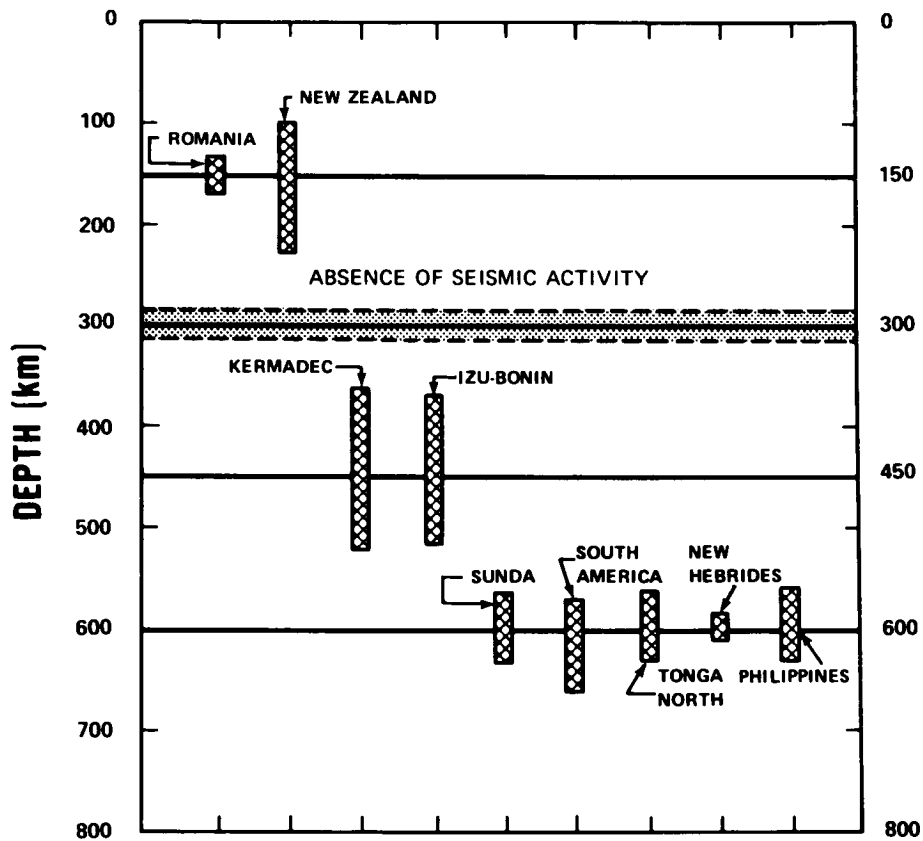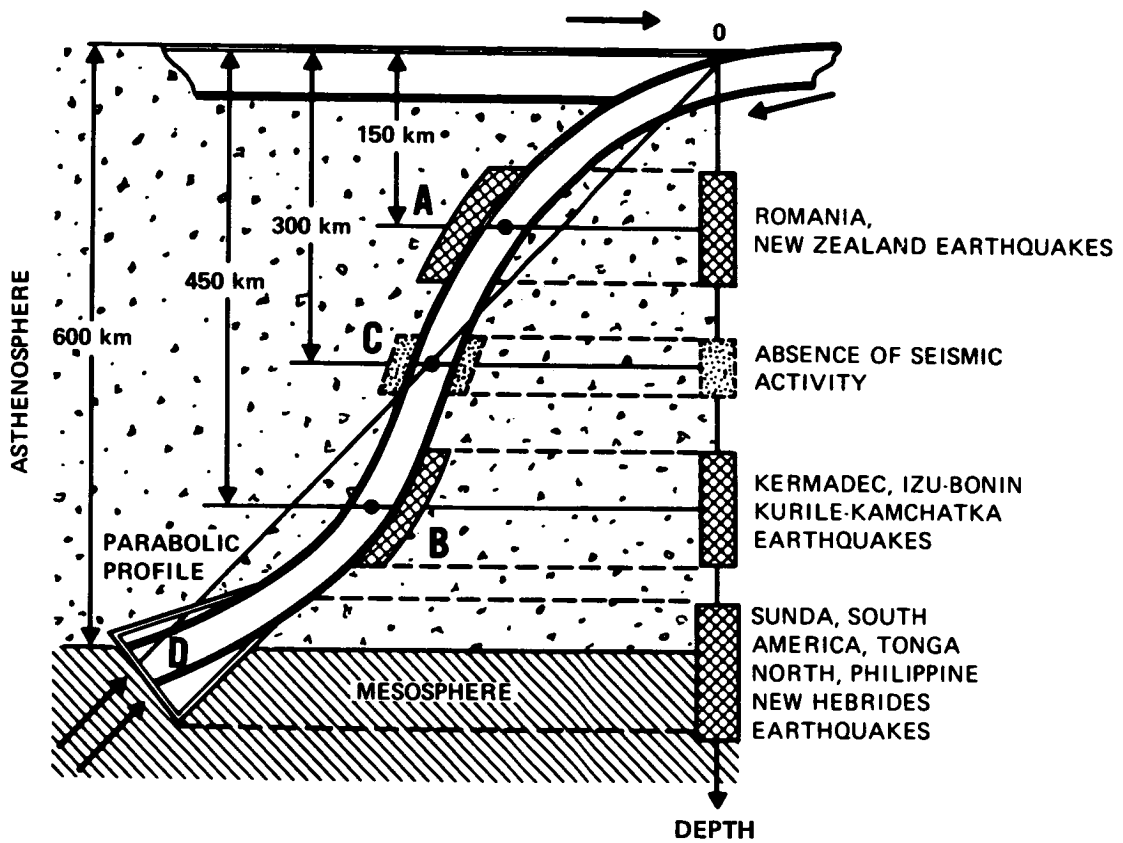

Figure 2. Depth of seismic activity.

Figure 3. Underthrusting lithospheric plate.